HIGH RESOLUTION X-RAY SCATTERING STUDIES OF STRUCTURAL PHASE TRANSITIONS

THESIS

submitted by

THOMAS WILLIAM RYAN

for the degree of

DOCTOR OF PHILOSOPHY

UNIVERSITY OF EDINBURGH

1986

Except where otherwise stated, the research undertaken in this thesis was the unaided work of the author. Where the work was done in collaboration with others, a significant contribution was made by the author.

ACKNOWLEDGEMENTS

I would like to express my gratitude to all of my colleagues, friends and family who have helped make this work possible. In particular;

Dr R.J.Nelmes and Professor R.A.Cowley for their constant encouragement and support;

Dr S.Andrews, Dr H-J. Bleif and Mr A.Gibaud with whom I spent many frustrating, sometimes exciting but always enjoyable hours in the laboratory;

the technical staff of the Physics Department, who helped with the construction of the instrument;

the two boys, Alistair and Graham, who have coped with a part-time father for long enough now;

and my wife, Hazel, to whom this work is dedicated.

ABSTRACT

This thesis is concerned with the application of very high-Q-resolution x-ray scattering techniques to the study of structural phase transitions in crystalline solids. By the use of perfect crystals to define the collimation of the incident and diffracted beam in a scattering experiment, a reciprocal space resolution of the order of 10^{-4}Å^{-1} can be achieved. This is some two orders of magnitude higher resolution than is available through conventional x-ray, or neutron, diffraction techniques. A high-resolution x-ray spectrometer, based on this principle, has been constructed and the x-ray optical factors determining the resolution of the instrument are discussed.

Experimental studies of structural phase transitions in three materials, Ag_3AsS_3, $BaMnF_4$ and $RbCaF_3$, are presented. In each case, the uniquely high resolving power of the triple-crystal spectrometer has revealed new, and in some cases surprising, information on the nature of the phase transition in these materials. In particular, it is evident that defects, even in very low concentrations, play a significant role in determining the behaviour of crystals close to the phase transition temperature.

Table of Contents

CHAPTER ONE

Introduction

The past decade has seen a minor renaissance in diffuse x-ray scattering studies of structural phase transitions (see, for instance, Moncton and Brown 1983). In part, the resurgence of interest was prompted by the emergence of reliable, high-flux rotating anode x-ray sources in the mid-1970's, with the promise of dedicated synchrotron sources to follow in the 1980's. Each advance has permitted the study of progressively weaker and more subtle structural properties in systems as diverse as 2-d melting transitions in liquid-crystals (Brinkman, Fisher and Moncton 1982), charge-density-wave conductors (Fleming, Moncton, Axe and Brown 1984) and the topography of single-crystal surfaces (Andrews and Cowley 1985).

A further, and very important, impetus to the development of high-resolution x-ray scattering was the remarkable advance in the theory of critical phenomena which took place in the late 1960's, culminating in the concepts of Universality, Scaling and the Renormalisation Group (Wilson 1971).

Classical theories predict that, close to a phase transition, certain physical properties of the system should vary with a temperature dependence described by a simple power law. For instance, the quantity by which the structure of the low temperature phase differs from that of the high temperature phase is known as the 'order parameter' of the low temperature phase. Landau theory predicts that this should vary as

$$\xi = c(T_c - T)^{\beta}$$

where c is some constant and β, the 'critical exponent' of the order parameter is predicted to be $\beta=0.5$. Similarly, critical exponents can be assigned to a number of other physical properties of the system above and below T_c. Landau theory attributes a universal quality to all phase transitions, in all materials and at all temperatures. In other words, for any system, identify the order parameter and it should always be found to vary as $(T_c-T)^{0.5}$.

In practice, however, a bewildering array of measured critical exponents

were found but, curiously, a pattern emerged amongst apparently dissimilar systems (Fisher 1968).

The somewhat confusing situation existing in phase transition research in the early 1970's was, to a large extent, clarified by the emergence of the new theoretical descriptions, linking the critical behaviour to the dimensionality of the system and the number of degrees of freedom of the order parameter. The theoretical groundwork was laid for Physicists to calculate critical exponents in an enormous variety of systems.

X-ray scattering, by dint of the inherent summation over all phonon frequencies in the measured quantity $S(\mathbf{Q})$, is uniquely capable of measuring two quantities in the spectrum of scattered radiation from a crystal in the region of a structural phase transition. These are the static correlation length and the static susceptibility, and the temperature dependence of these quantities, described by the critical exponents ν and γ respectively. Both ν and γ can be predicted from renormalisation group theory and x-ray scattering provides a sensitive test of theoretical predictions.

An accurate measurement of ν and γ is however, far from simple, demanding very high wavevector and temperature resolution combined with a very weak scattering signal from the sample. The modern generation of high-$\mathbf{Q}$-resolution triple-crystal x-ray spectrometers mounted on high-intensity sources are ideally suited to this task.

In 1979, the department of Physics, Edinburgh University, was awarded a grant by the Science and Engineering Research Council to construct a triple-crystal x-ray spectrometer on a rotating anode x-ray source, the first such instrument to be constructed in the U.K. The component parts of the instrument were delivered to Edinburgh in 1980 and the instrument was commissioned in 1981. This thesis describes part of the author's scientific involvement in the development, understanding and use of the instrument.

The thesis is organised as follows.

Chapter 2 is concerned with the theory of x-ray and neutron scattering from crystalline solids and the complementary information available from each technique. It concludes with a brief review of current theories of structural phase transitions. In chapter 3, a comprehensive review of recent developments in the field of high-$\mathbf{Q}$-resolution x-ray scattering studies of structural phase

transitions is presented

The remaining chapters, 4 to 8, describe the author's main scientific contributions to the experimental study of structural phase transitions using this technique and the thesis is concluded with a collection of the author's published work to date.

Chapter 4 discusses, at some length, the instrumental resolution. The approach adopted is designed to describe the role of each of the individual x-ray optical elements in a triple-crystal x-ray spectrometer in determining the instrumental resolution. With this knowlege, the experimenter can 'tailor' the resolution, by appropriate choice of x-ray optics or scattering geometry, to suit a particular measurement.

The experimental measurements, presented in chapters 5 to 8, concentrate on three materials, Ag_3AsS_3 (Proustite), $BaMnF_4$ and $RbCaF_3$. Although the preceding introductory paragraphs emphasised the importance of the x-ray scattering technique in measurements of the static critical exponents β,ν and γ, the experimental works discussed in this thesis are primarily concerned with exploiting the uniquely high **Q**-resolution of the instrument to study the subtle lattice distortions or departures from commensurability which can occur as the symmetry of the prototype phase is reduced at T_c. Many of the results contained in this thesis are simply not accessible through any other experimental technique.

Proustite has recently attracted considerable attention because of its potential application in the fields of non-linear optics and acousto-electronics (O'Hara et al 1982). It is also of interest as one of the reaction products in the photodissolution reaction of the chalcogenide glass As_2S_3 and silver (Ag). This has potential applications as a resist for sub-micron photolithography. Proustite was known to undergo a series of structural phase transitions at low temperatures. Despite considerable experimental effort (reviewed by Ewen 1983) the nature of, and even the existence of, the low temperature phases remained unclear. A neutron scattering study (Nelmes et al 1984 and appendix 1) revealed a modulated phase between ~61K and ~27K. Chapter 4 describes a subsequent x-ray scattering study which confirmed the modulated structure below ~61K and revealed a new, incommensurate phase below ~49K.

$BaMnF_4$, on the other hand, is an intensively studied and well characterised material which undergoes a second-order phase transition to an

incommensurably modulated phase at $T_c = \sim 247K$ (Scott 1979(review), Cox et al 1979, Cox et al 1983 and appendix 1). Chapters 6 and 7 describe an experimental study of the phase transition in $BaMnF_4$, originally conceived to confirm the monoclinic symmetry of the low-temperature phase, to measure the monoclinic distortion angle and the critical exponents β, ν and γ. In fact, the experiment developed into a study of the role of defects and revealed remarkable, and unexpected, similarities between the 'defect-influenced' behaviour of this structurally incommensurate material and the, much studied, dilute site-random magnetic Ising systems (Cowley et al 1984, Birgeneau 1985).

The final material to be examined, $RbCaF_3$, is structurally isomorphous with $SrTiO_3$ and so is of experimental interest as one of the simplest conceivable examples of a unit-cell doubling, displacive structural phase transition. The experiment has revealed a wealth of new information on the nature of the phase transition but, of particular interest, is the observation of large (circa. 2000Å) pre-cursor clusters of the low-temperature phase above T_c. The occurence of these clusters is related to the defect concentration of the sample crystal and their effect on experimental measurements of critical phenomena near T_c is profound. Once again, the defect influenced behaviour closely resembled the magnetic Ising systems and, of course, the behaviour of $BaMnF_4$.

Significantly, this 'defect-influenced' behaviour is observed in sample crystals which, by any normal experimental standards, would be described as 'perfect'!

CHAPTER TWO

X-rays, Neutrons and Structural Phase Transitions.

The quantity directly measured in a scattering experiment is the partial differential cross section

$$\frac{d^2\sigma}{d\Omega dE'} \tag{1}$$

which describes the fraction of incident particles (of energy E) scattered into a volume element of solid angle dΩ with an energy E′ between E′ and dE′.

An integration over energy gives the differential cross section

$$\frac{d\sigma}{d\Omega} = \int_0^\infty \left(\frac{d^2\sigma}{d\Omega dE'}\right) dE' \tag{2}$$

Van Hove(1954) showed that within the first Born approximation (i.e. that, in the scattering process, the perturbation on the incident wave is small) the partial differential cross section for the scattering of an incident plane wave with wave-vector $\mathbf{k}_o$ and energy E into a plane wave with wave-vector $\mathbf{k}$ and energy E′ by a monatomic system can be written

$$\frac{d^2\sigma}{d\Omega dE} = \frac{\underline{k}}{\underline{k}_o} \sum_{nm} p_m \left|\langle n| \sum_l b_l \exp\left(i\underline{Q}.\underline{r}(l)\right)|m\rangle\right|^2 \delta\left(\hbar\omega + E_m - E_n\right) \tag{3}$$

Where m and n are the initial and final states of the system, p_m is the probability distribution of the initial states of the system, b describes the interaction between the incident particles and the atoms comprising the system, the sum in l is over all of the atoms in the system and the δ function describes the energy distribution of the scattered particles.

For neutrons, the interaction is described in terms of a scattering length, b(l), which is a rather difficult to calculate property of the nucleus and for x-rays a form factor, f(l), directly related to the number of electrons in the atom.

In the neutron case, there is an inherent randomness in b(l) which depends upon isotope and nuclear spin distribution. This randomness gives rise

to, so-called, incoherent scattering. It is possible to separate (3) into coherent and incoherent parts by separating the coherent and incoherent scattering lengths

$$b_c = \frac{1}{N}\sum_{\ell} b_\ell \quad \text{or the average scattering length} \tag{4}$$

$$b_i^2 = \frac{1}{N}\sum_{\ell}\left(b_\ell^2 - b_c^2\right) \tag{5}$$

and the coherent and incoherent scattering cross sections become

$$\frac{d^2\sigma}{d\Omega dE}(c) = \frac{k}{k_0} b_c^2 \sum_{nm} P_m \left|\langle n \sum_{\ell} e^{(i\underline{Q}\cdot\underline{r}(\ell))} | m\rangle\right|^2 \delta(\hbar\omega + E_m - E_n) \tag{6}$$

$$\frac{d^2\sigma}{d\Omega dE}(i) = \frac{k}{k_0} b_i^2 \sum_{nm} P_m \sum_{\ell} \left|\langle n | e^{(i\underline{Q}\cdot\underline{r}(\ell))} | m\rangle\right|^2 \delta(\hbar\omega + E_m - E_n) \tag{7}$$

We are interested only in the coherent part of the total scattering cross section. For neutrons, the incoherent scattering results in an essentially uniform background. For x-rays there are no significant isotope or spin effects and consequently no incoherent scattering.

Eqn.(6) can be re-written

$$\frac{d^2\sigma}{d\Omega dE}(c) = \frac{k}{k_0} b_c^2 \, S(\underline{Q},\omega) \tag{8}$$

The quantity $S(\underline{Q},\omega)$ is known as the Van Hove scattering function and it depends <u>only</u> upon the positions and motions of the atoms within the scattering medium. The information describing the actual interaction of the incident photons or neutrons and the atoms of the system is contained in the first part of eqn(8), i.e. outside the scattering function. In other words, the quantity $S(\underline{Q},\omega)$ is an intrinsic property of the scattering system and is independent of the probe used to examine it.

For x-rays, eqn(8) can be re-written

$$\frac{d^2\sigma}{d\Omega dE} = \left(\frac{e^2}{mc^2}\right)^2 (\zeta_o \zeta_s)^2 \left|f(\underline{Q})\right|^2 S(\underline{Q},\omega) \tag{9}$$

Where e^2/mc^2 is a constant and the symbols have their usual meanings. $(\zeta_o\zeta_s)$ is a polarisation factor and $f(\underline{Q})$ is the atomic form factor.

The quantity $S(\underline{Q},\omega)$ in the x-ray case is identical to $S(\underline{Q},\omega)$ in the neutron case - the formulae for the differential cross sections differ only in the preceding group of constants.

BRAGG SCATTERING

In the case of Bragg scattering the scattering is totally elastic and there is no interchange of energy between the scattered particle and the sample. The quantity measured is, therefore S(Q,0) and eqn(9) reduces to

$$\frac{d\sigma}{d\Omega} = \frac{e^2}{mc^2}\left(\zeta_0\,\zeta_s\right)^2 \left|f(\underline{Q})\right|^2 \left|\sum_{\ell} e^{(i\underline{Q}\cdot\underline{r}(\ell))}\right|^2 \qquad (10)$$

(once again, this is for a monatomic crystal).

For a crystal composed of N unit cells with n atoms per unit cell we replace the form factor f(Q) by a structure factor F(Q) where

$$F(\underline{Q}) = \sum_{b} f(b)\, e^{(i\underline{Q}\cdot\underline{r}(b))} \qquad (11)$$

and each atom is at a site r(l)+r(b) where (l) denotes the cell site and (b) denotes the atom within the cell.

The formula for the differential cross section can be written

$$\frac{d\sigma}{d\Omega} = \frac{e^2}{mc^2}\left(\zeta_0\,\zeta_s\right)^2 \left|\sum_{b} f(b) e^{(i\underline{Q}\cdot\underline{r}(b))}\right|^2 \left|\sum_{\ell} e^{(i\underline{Q}\cdot\underline{r}(\ell))}\right|^2 \qquad (12)$$

constant : structure factor : cell factor

The cell factor can be written in the form

$$e^{(i\underline{Q}\cdot\underline{r}(\ell))} = \frac{(2\pi)^3}{V_0} \sum_{G} \delta(\underline{Q} - \underline{G}) \qquad (13)$$

where V_0 is the volume of the unit cell and G is a reciprocal lattice vector.

The condition Q=G is the Bragg condition and dσ/dΩ is only non zero when this condition is satisfied. The Bragg condition provides a direct determination of the crystal symmetry and of the lattice constants. The magnitude of dσ/dΩ is related to the structure factor F(Q) (or more correctly to $|F(Q)|^2$ and, thereby, to r(b), the positions of atoms within the cell, and f(b), their form factors.

Eqn(12), therefore, forms the basis of structural crystallography.

In a real crystal, the atoms are not fixed at their lattice sites but

vibrate thermally. To accomodate the effect of this vibration, an additional factor is introduced. The form factor, f(b), must be replaced by

$$f(b,\underline{Q}) = f(b)\, e^{(-W(b,\underline{Q}))} \tag{14}$$

where

$$W(b,\underline{Q}) = \frac{1}{N} \sum_{l} \langle \tfrac{1}{2} (\underline{Q} \cdot \delta \underline{r}(lb))^2 \rangle \tag{15}$$

and $\delta r(lb)$ labels the displacement of the bth atom in the lth unit cell and N is the number of unit cells.

The factor e^{-W} is known as the Debye-Waller factor.

ONE PHONON SCATTERING

The above section considered the case of Bragg scattering and showed that this, elastic scattering, was concentrated at reciprocal lattice points but its intensity could be reduced by the effect of lattice vibrations (the Debye-Waller factor).

The atomic displacements also result in coherently scattered x-ray (or neutron) waves and, as shown by Cochran (1963), the cross section for scattering from a lattice vibration mode can be written

$$\frac{d\sigma}{d\Omega}(\text{mode}_j\ \underline{q}) = N v_z \sum_{G} \delta(\underline{Q}+\underline{q}-\underline{G}) \left| \sum_{b} f(b,\underline{Q})(\underline{Q}\cdot\underline{U}_j(b\underline{q}))\, e^{(i(\underline{Q}+\underline{q})\cdot\underline{r}(b))} \right|^2 \tag{16}$$

and the intensity from this wave appears at the point **G=Q+q**

The expression can be re-written in terms of the energy $E_j(\mathbf{q})$ of the mode

$$\frac{d\sigma}{d\Omega} = \frac{v_z E_j(\underline{q})}{m \omega_j^2(\underline{q})} \sum_{G} Q^2 |F_j(\underline{Q})|^2 \delta(\underline{Q}+\underline{q}-\underline{G}) \tag{17}$$

The quantity $F_j(\mathbf{Q})$ is known as the structure factor of the mode, in analogy with $F(\mathbf{Q})$, the structure factor for Bragg scattering.

Summing over all modes with wave-vector **q** we find

$$\frac{d\sigma}{d\Omega} = \frac{NQ^2}{m} \sum_{j} \frac{E_j(\underline{q})}{\omega_j^2(\underline{q})} |F_j(\underline{Q}|^2 \tag{18}$$

and this, of course, is the differential cross section measured in an

x-ray scattering experiment.

Eqn(17) results in a δ function in reciprocal space. A group of adjacent modes will, however, produce a continuous distribution of scattering in reciprocal space, and hence the term, diffuse scattering. It is important to note that this scattering is entirely due to modes of low frequency. Close to a second-order phase transition one of the modes, j, goes soft and its frequency tends towards zero. As it does so, its contribution to Eqn(18) totally dominates the scattering spectrum and produces the phenomenon of critical scattering. Cochran (1969) examined the relationship between the scattering cross section and the properties of ferro- and anti-ferroelectric crystals in the region of a structural phase transition. The static susceptibility, χ, measures the response of the crystal to some externally applied mechanical field. In the case of a lattice vibration mode the field, $E=E'\exp(i\mathbf{K}.\mathbf{r})$, varies in time with the frequency, ω, of the vibration mode.

The analysis demonstrated that

$$\chi(\underline{Q}) \propto \frac{1}{\omega^2_{(\underline{q})}} \propto S(\underline{Q}) \qquad (19)$$

and so the differential scattering cross section is a direct measurement of the static, wave-vector-dependent susceptibility of the system.

PROPERTIES OF $S(\mathbf{Q},\omega)$.

$S(\mathbf{Q},\omega)$, the Van-Hove scattering function, is the quantity actually measured in a scattering experiment. (Once all of the appropriate corrections have been made for instrumental resolution, background, form factors, scattering length, polarisation etc.) It is entirely a property of the system undergoing investigation in the scattering experiment.

$S(\mathbf{Q},\omega)$ is the fourier transform with respect to both lattice and time of the time-dependent pair-correlation function $G(\mathbf{r},t)$

$$S(\underline{Q},\omega) = \int\int G(\underline{r},t)\, e^{(i\underline{Q}.\underline{r}-\omega t)}\, d\underline{r}\, dt \qquad (20)$$

Whereas $S(\mathbf{Q},\omega)$ is a Fourier space quantity, $G(\mathbf{r},t)$ is a direct space quantity and it contains information on the spatial and temporal relationships which exist between atoms within a sample.

What is the physical interpretation of $G(\mathbf{r},t)$?.

If we take a system, a crystal perhaps, in a state of thermal equilibrium, and locate the exact position of an atom at a time t_0, $G(\mathbf{r},t)$ tells us the probability of finding another atom, at some distance r from the original position of the first atom, at a time t later. In other words, if the atoms in the crystal are thermally excited and the displacements of the atoms from their mean lattice sites are described by plane waves propagating through the crystal (phonons), $G(\mathbf{r},t)$ tells us about the direction and frequency of those waves.

It is possible to make other types of measurements. For instance, we have already discussed the case $S(\mathbf{Q},0)$, or elastic Bragg scattering, when the atoms are fixed at their lattice sites and there is no interchange of energy between the scattered particle and the scattering system. In this case, the Fourier transform of $S(\mathbf{Q},0)$ is $G(\mathbf{r},\infty)$ and this is the well known Patterson function or infinite time pair-correlation function. $G(\mathbf{r},\infty)$ tells us about the relative positions of pairs of atoms within the unit cell and is of enormous importance in the early stages of a crystallographic structural determination.

A further possibility is to measure $S(\mathbf{Q},\omega)$ at a fixed $\mathbf{Q}$ but to sum over all ω and thereby measure $S(\mathbf{Q})$.

$$S(\underline{Q}) = \int_{-\infty}^{\infty} S(\underline{Q},\omega)\, d\omega \tag{21}$$

This is equivalent to measuring the differential cross section

$$\frac{d\sigma}{d\Omega} = \int_{-\infty}^{\infty} \frac{d^2\sigma}{d\Omega\, dE}\, dE \tag{22}$$

The Fourier transform of $S(\mathbf{Q})$ is $G(\mathbf{r},0)$.

$G(\mathbf{r},0)$ is the instantaneous pair-correlation function and it tells us the probability, at any instant in time, of finding another atom at a distance r from our original atom. It measures, therefore, the range within the crystal lattice over which the motions of individual atoms remain correl ated.

In principle, it is possible to measure all three of the above quantities, $S(\mathbf{Q},\omega)$, $S(\mathbf{Q})$ and $S(\mathbf{Q},0)$, by neutron scattering. By definition, thermal neutrons have energies very similar to the energies of lattice vibration phonons and, by a happy coincidence, the wavelength of a thermal neutron is similar to the interatomic spacings within a solid and neutrons are, therefore, diffracted by crystalline solids. The techniques to carry out energy analysis of scattered

neutrons at a fixed wave-vector transfer, and thereby measure $S(\mathbf{Q},\omega)$ are highly developed.

$S(\mathbf{Q},0)$, or elastic Bragg scattering, can readily be measured by neutron or X-ray scattering techniques. The choice depends upon the nature of the sample, the nature of the structural information which the experimentalist wishes to extract from the measurement and the relative availability of neutron and x-ray scattering instruments. It is possible to measure $S(\mathbf{Q})$ using neutrons but the experimental integration over ω at fixed $\mathbf{Q}$ is both difficult and unreliable. In contrast, by dint of the enormous difference between the energy of an x-ray photon (~8KeV) and a lattice phonon (~several meV), the energy exchanged in an inelastic collision is negligible. X-ray scattering performs the integration over ω automatically. Also, by virtue of the much higher flux available from an x-ray source in comparison with a neutron source, x-rays permit a direct measurement of $S(\mathbf{Q})$ with much higher $\mathbf{Q}$ resolution than is possible with neutrons.

All three properties, $S(\mathbf{Q},\omega)$, $S(\mathbf{Q},0)$ and $S(\mathbf{Q})$, are of fundamental importance in understanding the static and dynamic behaviour of crystalline solids. $S(\mathbf{Q},0)$ because it examines the structure of the crystal, $S(\mathbf{Q},\omega)$ because it examines the lattice dynamics of the crystal and $S(\mathbf{Q})$ because modern theories of structural phase transitions predict how the quantities measured by $S(\mathbf{Q})$ vary in the region of a second-order structural phase transition.

STRUCTURAL PHASE TRANSITIONS.

The classical picture of a displacive structural phase transition in a crystalline solid is encapsulated in the 'soft-mode' concept, proposed by Cochran in 1960. A displacive transition is one from one (ordered) crystal to another (ordered) crystal structure of lower symmetry. At T_c, the phase transition temperature, the atoms of the higher symmetry phase move, relative to each other, by a small amount. The amount by which the lower symmetry phase differs from the higher symmetry phase is known as the 'order parameter' of the lower symmetry phase. If the displacement is continuous as the temperature is lowered through T_c the transition is of second-order but if there is a discontinuity in the displacement (and, therefore, the order parameter) the transition is of first-order.

The 'soft-mode' picture considers the normal modes of vibration of the crystal lattice in the high-temperature high-symmetry phase. As T_c is approached from above, one of the vibrational modes becomes unstable, i.e. the phonon frequency tends towards zero, and, at T_c, the positional fluctuations associated with the mode 'freeze out' into the static displacements of the low-temperature structure.

The location of the soft mode within the first Brillouin zone of the prototype, high-temperature phase can be described by the total momentum transfer

$$\mathbf{Q} = \mathbf{G} + \mathbf{q} \qquad (23)$$

where **G** is a reciprocal lattice vector. If **q**=0, the condensation of the soft-mode takes place at the centre of the Brillouin zone and the wavelength of the soft-mode is very long, leading to an identical displacement of the atoms in adjacent unit cells. If the concomitant reduction in symmetry is from a centrosymmetric to a non-centrosymmetric space group the transition is to a ferroelectric phase and the crystal will develop a spontaneous polarisation along one direction, the polar axis. The order parameter of the low-temperature, ferroelectric phase can be obtained from measurements of the spontaneous polarisation or from scattering measurements.

If **q**=0.5, the soft mode condenses at the boundary of the Brillouin zone, The wavelength of the soft-mode is very short, two unit cells, and this corresponds to oppositely directed displacements of the atoms in adjacent unit cells with a resultant doubling of the lattice repeat distance and the appearance of new Bragg reflections in reciprocal space. In this case, the transition is said to be to an anti-ferroelectric phase and no spontaneous polarisation develops. The intensity of the new Bragg reflections is directly related to the atomic displacements and so provides a measure of the order parameter.

Within the last ten years, new families of materials have been discovered in which the soft-mode condenses at an apparently arbitrary position within the Brillouin zone. i.e. $\mathbf{q}=\xi$, where ξ is not a rational fraction. In this case, the wavelength of the soft mode, or the frozen-in distortion of the low-temperature phase, is not a rational multiple of the high-symmetry phase lattice repeat distance and so, in adjacent unit cells, the atoms are displaced from their mean positions by different amounts. In effect, translational periodicity, one of the fundamental features of the crystalline state, has been

lost in at least one direction within the crystal lattice. These materials, which are described as being incommensurate, or more correctly incommensurably modulated, are of considerable current experimental and theoretical interest.

Current theoretical models of structural phase transitions predict that the temperature dependence of certain physical properties of the system can be described by a simple power law behaviour. For instance the order parameter of the low temperature phase is expected to follow the relationship

$$Q = (T_c - T)^{\beta} \qquad (24)$$

where β is the critical exponent of the order parameter. In classical theories, the exponent $\beta = 0.5$, but in real systems it can vary quite significantly.

Two other critical properties can be measured by scattering techniques, the static susceptibility (χ) and the correlation length (ξ) of the system. Both quantities are obtained from a measurement of $S(\mathbf{Q})$ and so, although both can be measured by the use of inelastic neutron scattering, the most direct and accurate method of measurement is x-ray scattering.

Once again, these quantities are described by simple power-law relationships.

$$\chi = C\,(T - T_c)^{-\gamma} \qquad (25)$$

and

$$\xi = A\,(T - T_c)^{-\nu} \qquad (26)$$

where classical theories predict values of $\gamma = 1.0$ and $\nu = 0.5$. as in the case of the order parameter exponent β, the values of γ and ν vary considerably in practice.

By the 1960's critical exponents had been measured at a large variety of phase transitions - both structural and magnetic as well as systems as diverse as water and superfluid 4He - and it had become apparent that the classical theories were quite inadequate. Furthermore, experimental evidence suggested that, in materials which were superficially quite dissimilar, the measured critical exponents could be remarkably similar (Fisher 1968). In fact the connection turned out to be in the spatial dimensionality of the system and the number of components of the order parameter. Materials with the same

critical dimensionality and the same number of components in their order parameter are said to belong to the same 'Universality Class', (Griffiths 1970), and exhibit similar critical exponents. For example, a ferromagnet is a 3-dimensional system which can be magnetised in any one of the 3 spatial dimensions and has, therefore, a 3-component order parameter. i.e. It is a d=3, n=3 system. A fluid, however, is a 3-dimensional system which, because it is isotropic, has only a one component order parameter. i.e. It is a d=3, n=1 system.

Universality brought some semblance of order to the plethora of measured exponents and the contemporary concept of scaling showed that certain fixed relationships existed between critical exponents but it was the development of Renormalisation Group Theory, in the early 1970's (Wilson 1971) which, at last, allowed a quantitative prediction of critical exponents to be made.

In particular, for structural phase transitions, the theory predicts the exponents γ, ν and β, and these are accesible through x-ray scattering measurements.

As discussed above, the static susceptibility is derived from measurements of the temperature dependence of the intensity of the scattering at some value of $\mathbf{q}$, whilst the correlation length is derived from measurements of its wave-vector width. In a second order transition, both quantities diverge very rapidly as T_c is approached. In other words the peak intensity increases very rapidly whilst the wave-vector width decreases very rapidly. To make sensible measurements of $S(\mathbf{Q})$, and thereby γ and ν, in the temperature range close to T_c, very high wave-vector and temperature resolution are demanded. The modern generation of triple-crystal x-ray spectrometers are uniquely able to satisfy those demands.

CHAPTER THREE

A Review of Recent Developments in High-Q-Resolution X-Ray Scattering.

1) INTRODUCTION

In their seminal paper on high-Q-resolution x-ray scattering Eisenberger, Alexandropolous and Platzman (1972), working at Bell Laboratories, demonstrated the ability of a triple-crystal x-ray spectrometer to probe the reciprocal space of a sample crystal with a momentum resolution as small as 10^{-4}Å^{-1}. This represented a very significant technical advance with profound implications for the study of static and dynamic departures from perfection in crystalline systems. Such static phenomena (e.g. dislocations, defects, grain boundaries, inhomogeneities) or dynamic phenomena (e.g. phonons) give rise to extended, diffuse scattering in the sample reciprocal space. Previously, x-ray and neutron scattering investigations of diffuse scattering had been limited to resolutions of approximately 10^{-2}Å^{-1}, corresponding to correlation lengths of a few hundreds of Angstroms. The enormously improved resolution of the triple-crystal x-ray spectrometer permitted the detailed study of features with correlation lengths of many thousands of Angstroms, thus opening up new areas of Physics to experimental study.

Although, in the case of x-rays, the optical techniques necessary to obtain the very highest-Q-resolution had been understood since the earliest days of x-ray scattering (Darwin 1914) and by the 1930's those techniques had been raised to a fine art in the pioneering work of J.W.DuMond (1937) and Allison and Williams (1930) the techniques were not applied to the study of diffuse scattering for four decades. This was partly due to the lack of sufficiently intense sources and partly because early experimental attention was focussed on measurement of the widths of Bragg reflections (rocking curves) in an effort to examine crystal perfection or on measurements of the characteristic x-ray wavelengths and lineshapes. For a review of the latter see Merril and DuMond (1961).

In the late 1950's and 1960's interest in the information available from

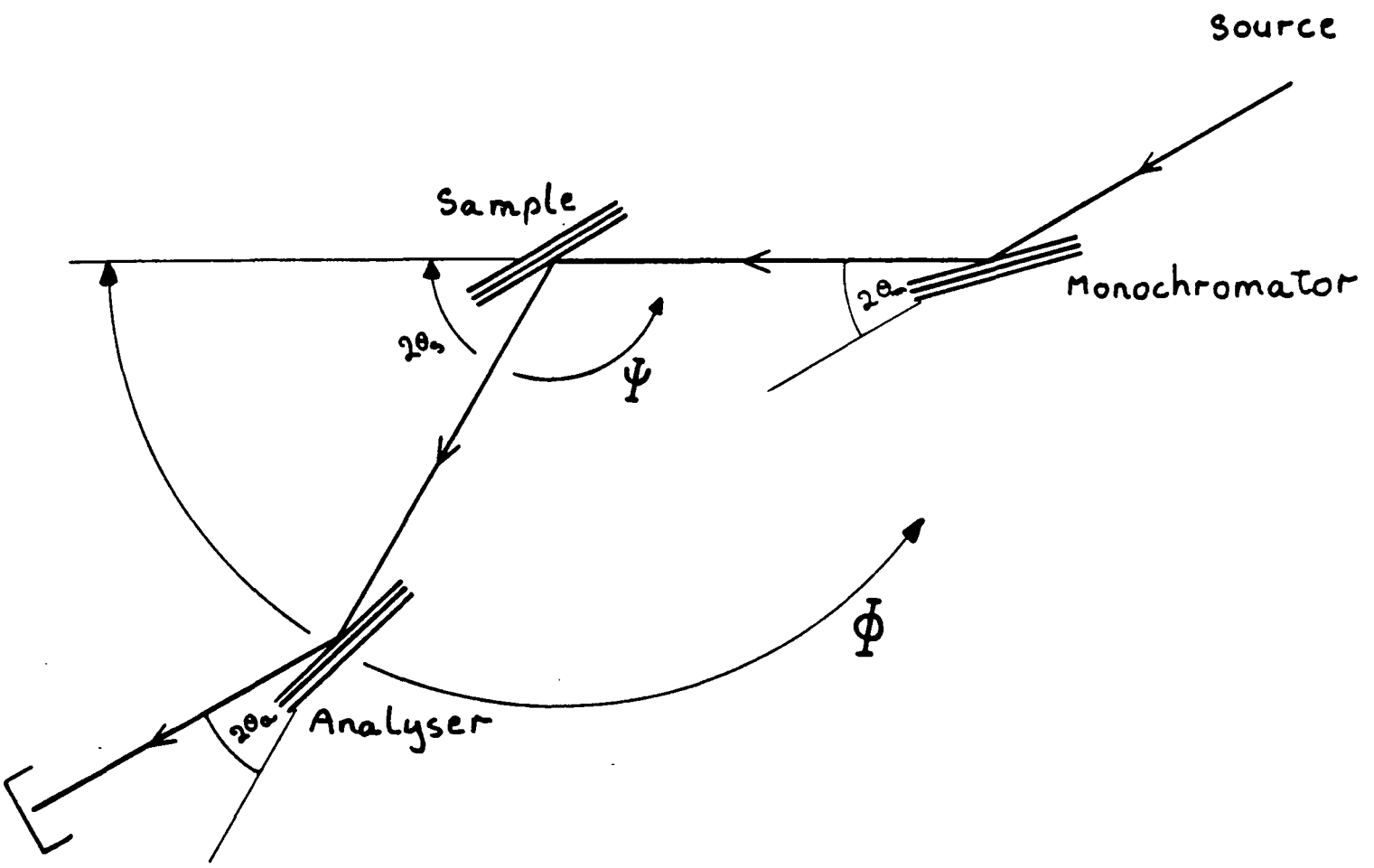

Figure 3.1 – The essential elements of a triple-crystal x-ray spectrometer.

diffuse x-ray and neutron scattering grew with the rising interest in radiation damage in metals and the lattice dynamics and structural phase transitions in crystalline solids.

A considerable amount of work was carried out with low-**Q**-resolution x-ray scattering techniques but it was expected that the extensive background produced by elastic Bragg scattering, i.e. the characteristic tails of the so-called Darwin profile of a Bragg reflection from a perfect crystal, would effectively obscure any inelastic thermal diffuse scattering (TDS), or elastic scattering from defects (Huang scattering - HDS) and make measurements at small **q** (i.e. $< 10^{-2}A^{-1}$) impossible.

The breakthrough in high-**Q**-resolution x-ray scattering studies heralded by Eisenberger et al. was the realisation that the elastic scattering forming the 'tails' of a Bragg reflection from a perfect crystal is not isotropically distributed in reciprocal space around the reciprocal lattice point but is localised into a well defined streak. In a triple-crystal x-ray spectrometer the elastic scattering tails associated with perfect monochromator and analyser crystals similarly form well-defined localised streaks in the sample reciprocal space. In contrast, because there are phonons (or in the case of HDS - defects) in all directions and of all wavelengths within the sample crystal, the diffuse scattering is distributed more or less isotropically around reciprocal lattice points. By an appropriate choice of scattering geometry the monochromator, analyser and sample streaks can be arranged to lie in such a way as to allow measurement of diffuse scattering to be made at positions very close to Bragg peaks (i.e. at **q** approaching 10^{-4}Å^{-1}).

For a complete discussion of the reciprocal space resolution of a triple-crystal x-ray spectrometer the reader is referred to chapter four of this thesis.

Figure(3.1) shows the essential elements of a triple-crystal x-ray spectrometer. It comprises an x-ray source followed by a monochromator crystal producing a primary beam with some wave-vector spread defined by the characteristics of source and monochromator. The sample crystal is mounted on a rotation axis, conventionally called Psi(Ψ) whilst an analyser crystal and detector are mounted on a second rotation axes, conventionally called Phi(Φ), concentric with Ψ. Ψ and Φ are the two experimental variables and normally must have setting accuracies better than 0.001°.

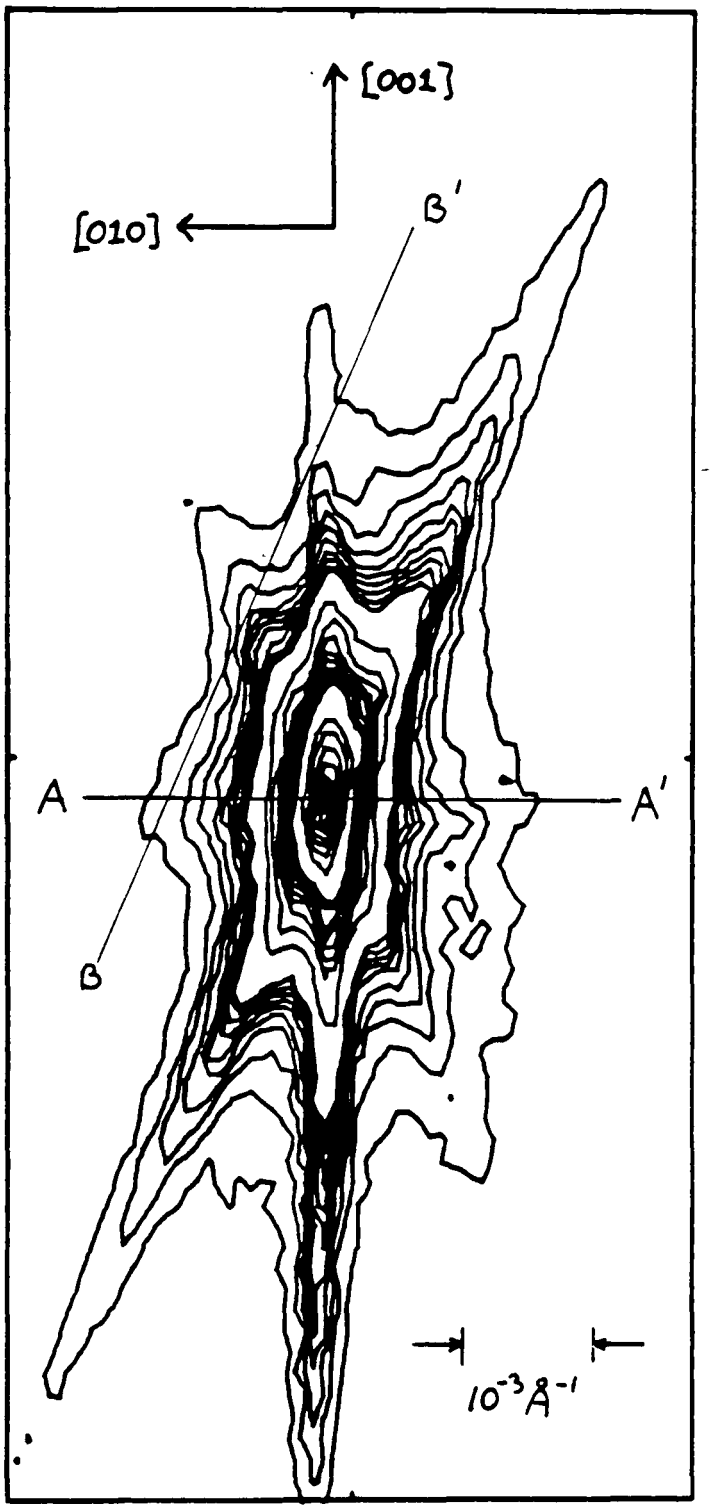

Figure 3.2 - An iso-intensity contour plot of the x-ray scattering in the vicinity of a typical Bragg reflection, recorded using the Edinburgh triple-crystal x-ray spectrometer.

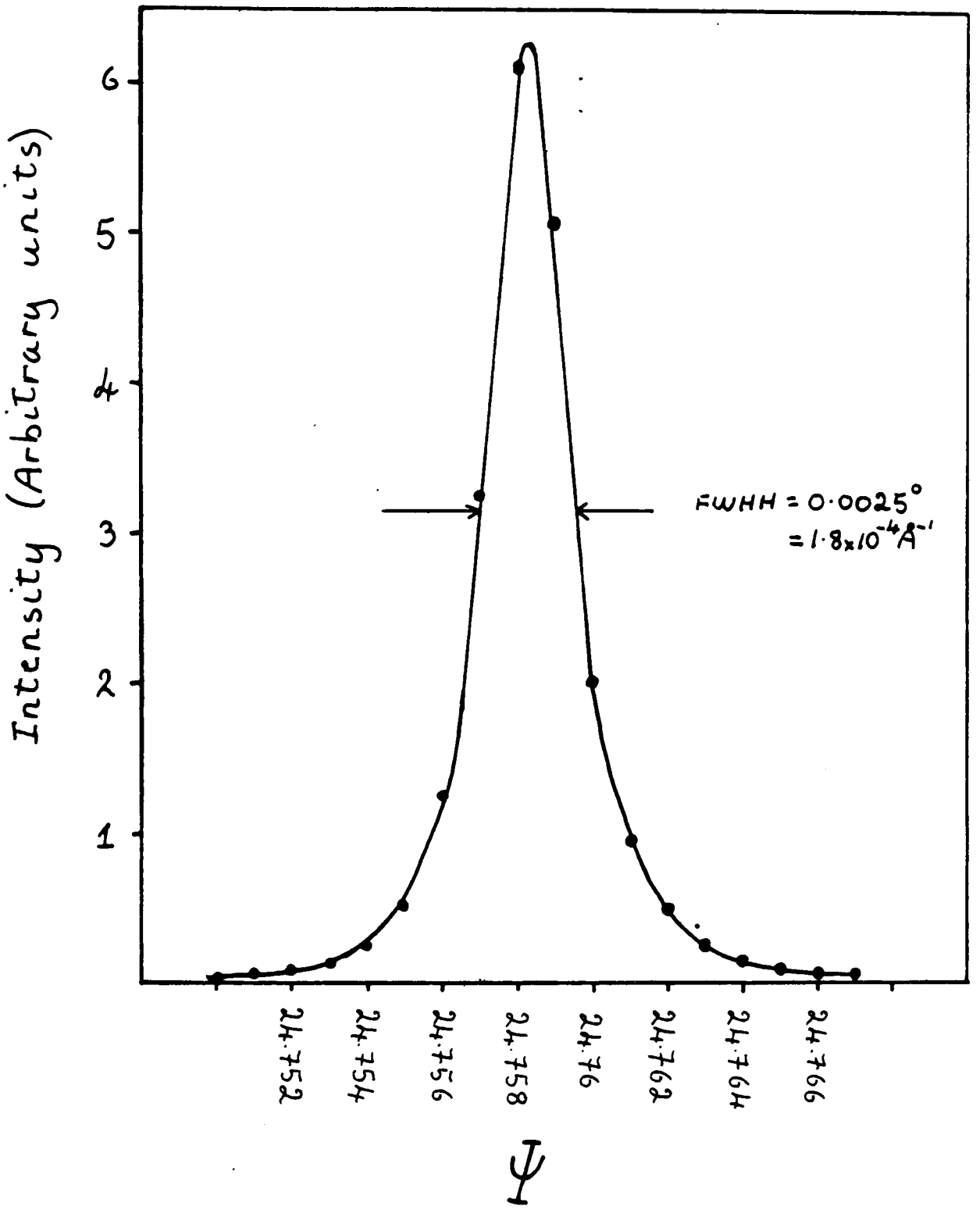

Figure 3.3 – The intensity distribution along section AA' (figure 3.2). A Ψ scan, or rocking curve.

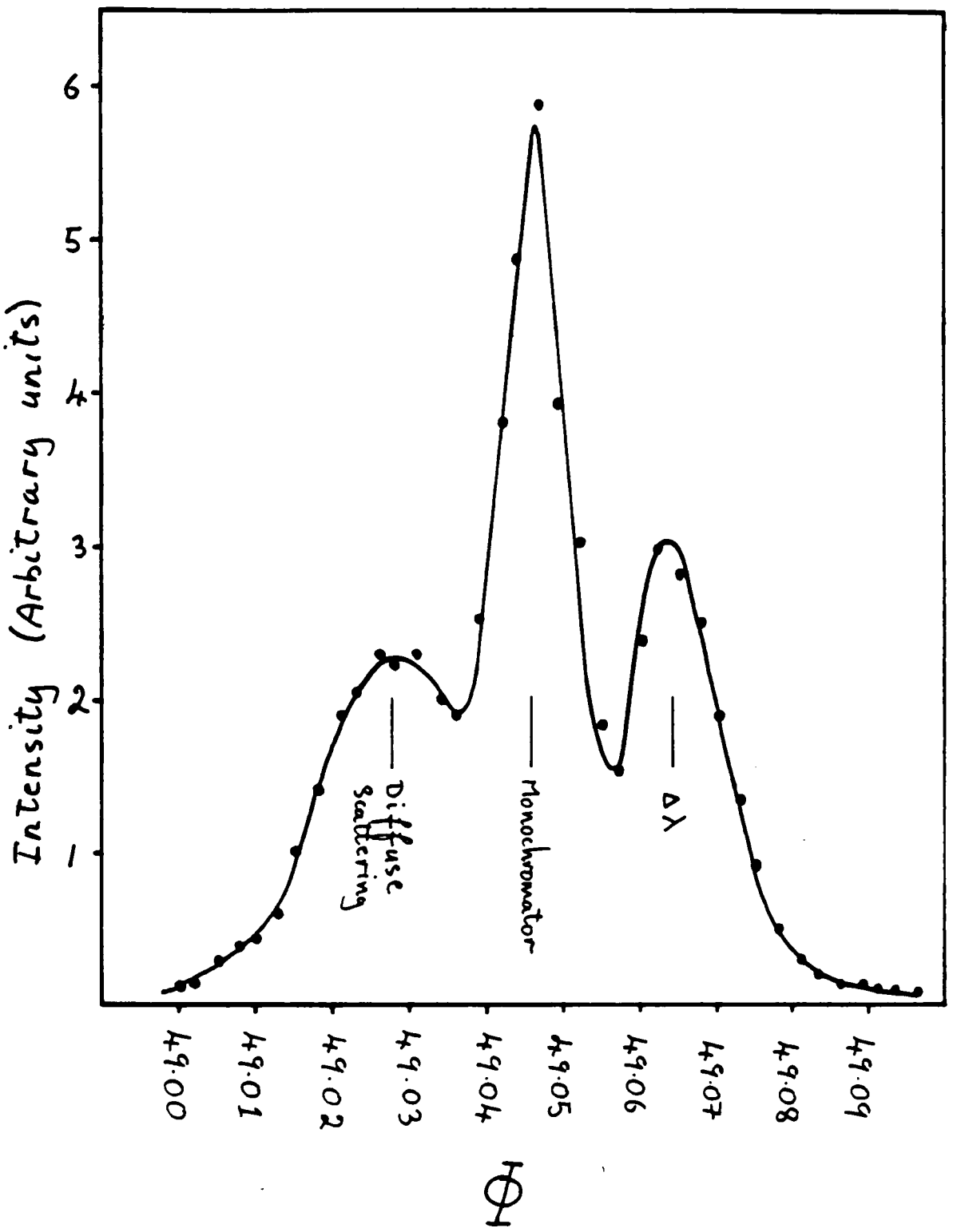

Figure 3.4 - The intensity distribution along section BB' (figure 3.2). A Φ scan with Ψ offset from the Bragg position by 0.03°.

The iso-intensity plot of Fig(3.2) shows the distribution of x-ray scattering in the vicinity of a typical Bragg reflection. This measurement was recorded using the Edinburgh triple-crystal spectrometer with $CuK\alpha_1$ x-rays from a rotating anode source and flat Si(111) monochromator and analyser crystals. The sample crystal was KH_2PO_4 and the measurement shows the (400) reciprocal lattice point (Θ_s=24°). The measurement was made in Bragg geometry, in reflection from an extended face sample crystal. The contours are arranged on a quasi-logarithmic scale, 0.1% to 1%, 1% to 10% and 10% to 100%. Three streaks are clearly visible, corresponding to elastic scattering tails from the monochromator and analyser crystals and a superposition of the elastic scattering tail from the sample crystal and spectral dispersion. TDS is clearly visible as an isotropic bulge centered on **q**=0. Note that the streaks are only in evidence at the 1% level.

The instrumental resolution element is conventionally thought of as that volume of reciprocal space enclosed by the 50% intensity contour level. It is possible to both calculate (Pynn, Fujii and Shirane 1983, This work Chapter four) and empirically measure this quantity which, in general, is an ellipse with its axes directed parallel and perpendicular to the momentum transfer, **Q**. In the example shown the resolution is 1.8×10^{-4}Å^{-1} perpendicular to **Q** and 7×10^{-4}Å^{-1} parallel to **Q**.

The intensity distributions along section AA′ - a Ψ scan through the Bragg peak - and BB′ - a Φ scan with Ψ offset by some 0.03° from the Bragg peak - are shown in Figures(3.3) and (3.4), respectively. Figure(3.3) illustrates the remarkable **Q** resolution of the triple-crystal technique; and the equally remarkable quality of the sample crystal. The full width at half height of the Bragg peak is some 0.0025°, corresponding to a **Q** resolution of 1.8×10^{-4}Å^{-1}. Figure(3.4) is very similar to Figure(2) of Eisenberger et al(1972) and shows the broad, diffuse scattering peak and the considerably sharper monochromator and sample (or $\Delta\lambda$) peaks. Eisenberger et al pointed out the possibility of eliminating the monochromator and analyser streaks by the use of monolithic, channel-cut crystals, as described by Bonse and Hart (1965). By using a three reflection channel-cut crystal the $\mathbf{q}^{-2}$ dependence of the streaks from a single reflection crystal can be reduced to $\mathbf{q}^{-6}$ with only a 15% loss in peak intensity.

Dramatic improvements in resolution (in this case from 10^{-2}Å^{-1} to 10^{-4}Å^{-1}) are, of course, only won at the expense of signal in a scattering experiment. The emergence of a new generation of high-intensity

rotating-anode x-ray sources in the mid 1970's and the promise of dedicated synchrotron sources by the 1980's provided the stimulus for the construction of a number of triple-crystal x-ray spectrometers. The combination of a high-intensity source and a triple-crystal spectrometer operating in a low-Q-resolution mode provides, of course, an unprecedentedly powerful tool for the study of weak scattering effects.

In the eight years since the first of these instruments became operational the technique has made a significant impact in several areas of research. In the field of structural phase transitions a number of groups have been active in examining the establishment of order in two-dimensional structures. The attraction of studying two-dimensional melting is that, in contrast to the three-dimensional case, current theories predict that the transition should be of second-order. In the mid 1970's these theoretical predictions were entirely untested. High-Q-resolution x-ray scattering is an ideal tool with which to examine this problem. Research groups centred on Bell Laboratories and M.I.T. have concentrated on phase transitions in low-dimensional structures such as physisorbed monolayers, liquid crystals and graphite intercalates. At Riso, in Denmark, similar work has been carried out on liquid crystals and physisorbed monolayers and the technique has been developed to examine the structure of liquid crystal surfaces.

Meanwhile, in Edinburgh, a more traditional approach has been adopted and the technique has been used to study critical phenomena in a variety of zone-centre, zone-boundary and incommensurate phase transitions in bulk, crystalline solids such as KH_2PO_4, $SrTiO_3$, and $BaMnF_4$, with a growing emphasis on the role of of competing interactions and defects.

At Bell Laboratories the incommensurate-commensurate phase transitions in the charge-density-wave conductors 2H-$TaSe_2$ and $NbSe_3$ have also been studied.

Outside the field of phase transitions, the technique has been applied by groups in Japan, USSR and E.Germany to the study of process induced defects in semiconductor crystals and, by the Edinburgh group, to examine the topography of crystal surfaces and the structure of internal interfaces.

These applications will be discussed in detail in section 2.

In a remarkable development of the triple-crystal x-ray spectrometer

technique, once again conceived at Bell Laboratories, Marra, Eisenberger and Cho (1979) demonstrated that at glancing angles of incidence, when the incident x-ray beam is totally externally reflected from the sample surface, conventional x-ray diffraction can take place within a surface layer only a few tens of Angstroms thick. Although several well developed techniques exist for studying surface structures (e.g. low energy electron diffraction (LEED), reflection high energy electron diffraction (RHEED) and ion scattering spectroscopy - to name but three) grazing incidence x-ray diffraction offers two advantages. Firstly, the Bragg intensities obtained are less badly affected by multiple scattering than is the case with the above techniques and are thus more readily interpretable and secondly, the technique can be used to study the structure of buried interfaces.

Grazing incidence x-ray diffraction has, for instance, been used to study the structure of the interface between epitaxially grown Al on a GaAs substrate (Marra, Eisenberger and Cho,1979), the Ge(001) reconstructed surface (Eisenberger and Marra,1981), Pb monolayers on Cu(110) (Marra, Fuoss and Eisenberger,1982), the Au(110) reconstructed surface (Robinson,1983) and most recently, the structure of the InSb(111)2x2 reconstructed surface (Bohr, Feidenhans'l, Neilsen, Toney, Johnson and Robinson,1985). It is expected that, over the next few years, this technique will make a significant impact on surface structural studies and, eventually, the study of surface structural phase transitions.

In this section we will present a brief review of some of the main areas of application of high-Q-resolution x-ray scattering. A large number of workers have used lower resolution x-ray diffuse scattering techniques to study an enormous range of subjects. Clearly, the distinction between high- and low-resolution is somewhat arbitrary - to a worker using x-ray photographic techniques to study diffuse scattering a resolution of 10^{-2}Å^{-1} is high - whereas, in terms of state of the art triple-crystal spectrometry, it is very poor resolution indeed! To make this review manageable it is restricted to those groups of workers endevouring to work at the highest attainable Q resolution, $\sim 10^{-4}$Å^{-1}, although relevant work performed over the whole resolution range is also described.

2) PHYSISORBED MONOLAYERS.

High-Q-resolution x-ray scattering techniques have been applied, with considerable success, to the study of phase transitions, particularly melting transitions, in two dimensional systems - and the changes in the nature of these transitions as the dimensionality increases from two to three. The rare gases Ar, Kr and Xe, absorbed on a graphite substrate, provide a very good experimental realisation of two-dimensional solids.

Graphite is a particularly suitable substrate material for these studies because of the easy availability of basal plane (0001) faces with suitable sites for absorption. Furthermore, exfoliated graphite, which consists of stacks of thin (100 - 300Å) sheets some 2000Å wide with a Gaussian distribution of planar orientations, is readily available (Union Carbide UCAR-ZYX). This material has a specific surface area of 1-3m^2/g: the large area available for absorption dramatically increases the signal in a scattering experiment on absorbed monolayers.

Monolayer coverages are established by first heating the substrate under vacuum to some 900°C to drive off contaminants. Once clean, the substrate is loaded into a sample cell, still under vacuum, attached to a cryostat. A controlled amount of rare gas is admitted to the sample chamber and, as the sample is cooled to roughly 100K, the gas condenses on the substrate surface.

The Lennard-Jones diameters of the rare gases are very similar to the

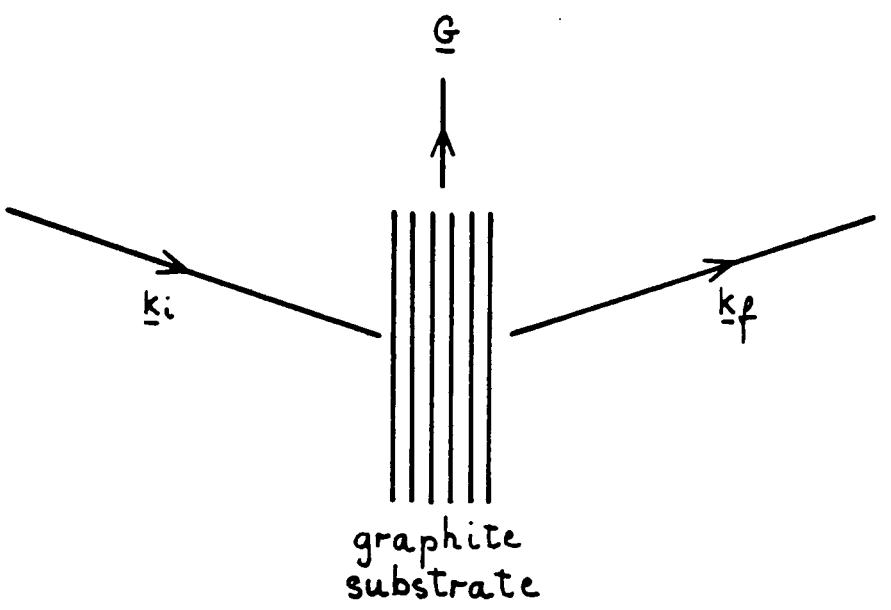

Figure 3.5 - The scattering geometry employed in studies of physisorbed monolayers. Correlations within the plane of the graphite substrate are probed.

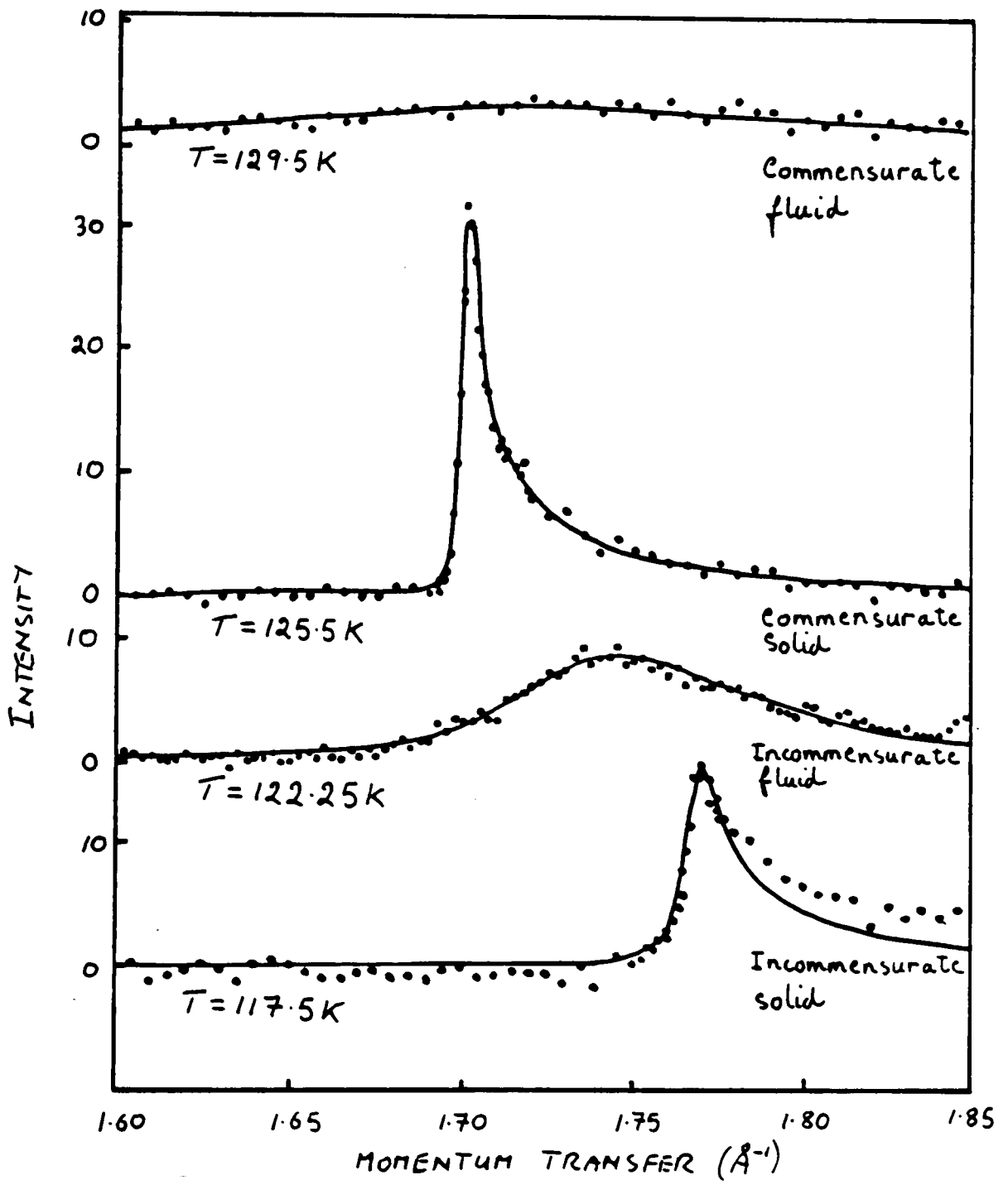

Figure 3.6 - Typical scattering data for monolayer Kr on a graphite substrate showing the evolution from a fluid phase, with a correlation length of ~20Å, through a commensurate solid phase and an incommensurate fluid phase to a stable solid phase, incommensurate with the substrate. (After Specht et al. 1984)

separation of the minima in the potential of the graphite (0001) substrate. In fact, the diameters for Ar, Kr and Xe are, respectively, some 8% less than, almost equal to and some 8% more than the separation of the graphite minima. As a function of temperature, or of pressure, the absorbed gas forms 2-D fluid, incommensurate solid or commensurate solid phases. X-ray scattering measurements are performed in transmission geometry (figure 3.5) and thus correlations within the plane of the graphite surface are probed.

The first such film to be studied was submonolayer Kr on graphite (Horn, Birgeneau, Heiney and Hammonds, 1978) using a triple-crystal instrument with pyrolytic graphite monochromator and analyser crystals on a Rigaku 12KW rotating anode x-ray generator at M.I.T. This low-Q-resolution ($\sim 10^{-2}$Å^{-1}) experiment confirmed the $\sqrt{3}$ x $\sqrt{3}$ triangular krypton lattice structure, commensurate with the graphite substrate, and demonstrated the feasibility of the x-ray technique to study the melting transition. Stephens, Heiney, Birgeneau and Horn (1979), in a further low-Q-resolution experiment, observed a sequence of phase transitions from a fluid, through a commensurate solid phase to an incommensurate phase.

The experiment was subsequently repeated, by Moncton, Stephens, Birgeneau, Horn and Brown (1981), using the Bell Laboratories triple-crystal spectrometer which had recently been installed at the Stanford Synchrotron Radiation Laboratory (SSRL). This instrument used a double Ge(111) monochromator and a single Ge(111) analyser crystal to give a resolution of 3.5×10^{-4}Å^{-1} FWHH parallel to **G**, the scattering vector, corresponding to a correlation length of some 9000Å. The improved resolution, made possible by the high x-ray flux from the synchrotron source, allowed a detailed lineshape analysis to be carried out as the sample was cooled through the sequence of phase transitions. Figure (3.6) shows some typical data; in fact, obtained from a later study of the same system by Specht, Sutton, Birgeneau, Moncton and Horn (1984).

As the sample temperature is decreased the condensed gas layer evolves from a fluid phase to a 2-D solid phase characterised by a powder averaged, Gaussian scattering profile. The Kr atoms, in this phase, are in registry with the potential minima in the graphite substrate and the correlation length is limited only by the finite graphite crystallite size. The asymmetric profile, with excess scattering at larger wave-vectors, is characteristic of 2-D powders (Warren 1941, Kjems et al 1976) and results from a combination of the 2-D

nature of the Kr layers, the orientational disorder of the graphite crystallites about their (0001) axes and the mosaic distribution of the graphite crystallites.

On further cooling, the Kr-Kr interaction begins to predominate over the Kr-C interaction and there is a phase transition to a fluid-like phase, incommensurate with the substrate, with no long range order. Finally, an incommensurate phase is established in which the scattering is described by a combination of Lorentzian and Lorentzian squared forms and the correlation length is some 300Å, - much shorter than the mean substrate crystallite size but substantially larger than a conventional fluid.

Monolayer films of Xe on graphite (Heiney, Birgeneau, Brown, Horn, Moncton and Stephens 1982: and Heiney, Stephens, Birgeneau, Horn and Moncton 1983) and monolayers of Ar on graphite (McTague, Als-Nielsen, Bohr and Nielsen 1982) have also been studied by this technique. Both Ar and Xe form 'free-floating' incommensurate structures and do not form the $\sqrt{3} \times \sqrt{3}$ commensurate structure, stabilised by the substrate potential, which is observed in the Kr films.

The detailed information provided by the high-Q-resolution x-ray scattering technique (and hitherto, unobtainable) has provided important insights into the nature of phase transitions in two dimensions. Experimental attention is now being focussed on absorbed monolayers of more complicated molecules such as methane (Kjaer, Nielsen, Bohr, Lauter and McTague 1982) or ethylene (Mochrie, Sutton, Birgeneau, Moncton and Horn 1984) and to coverages of more than one layer (Specht, Sutton, Birgeneau, Moncton and Horn 1984).

Very recently, the technique has been developed to study the structure of a Kr monolayer absorbed on a single crystal graphite substrate (as opposed to the exfoliated graphite conventionally used) by D'Amico, Moncton, Specht, Birgeneau, Nagler and Horn (1984). Despite the substantial reduction in intensity, the authors were able to measure linewidths, in the commensurate phase, of 0.0005Å^{-1}, corresponding to correlation lengths of about 1 micron! Below the re-entrant, commensurate to incommensurate transition, the evolution from a hexagonal, commensurate domain structure to a weakly modulated structure, rotated by several degrees from the substrate lattice, was followed. An impressive experiment - performed on a single atomic monolayer!

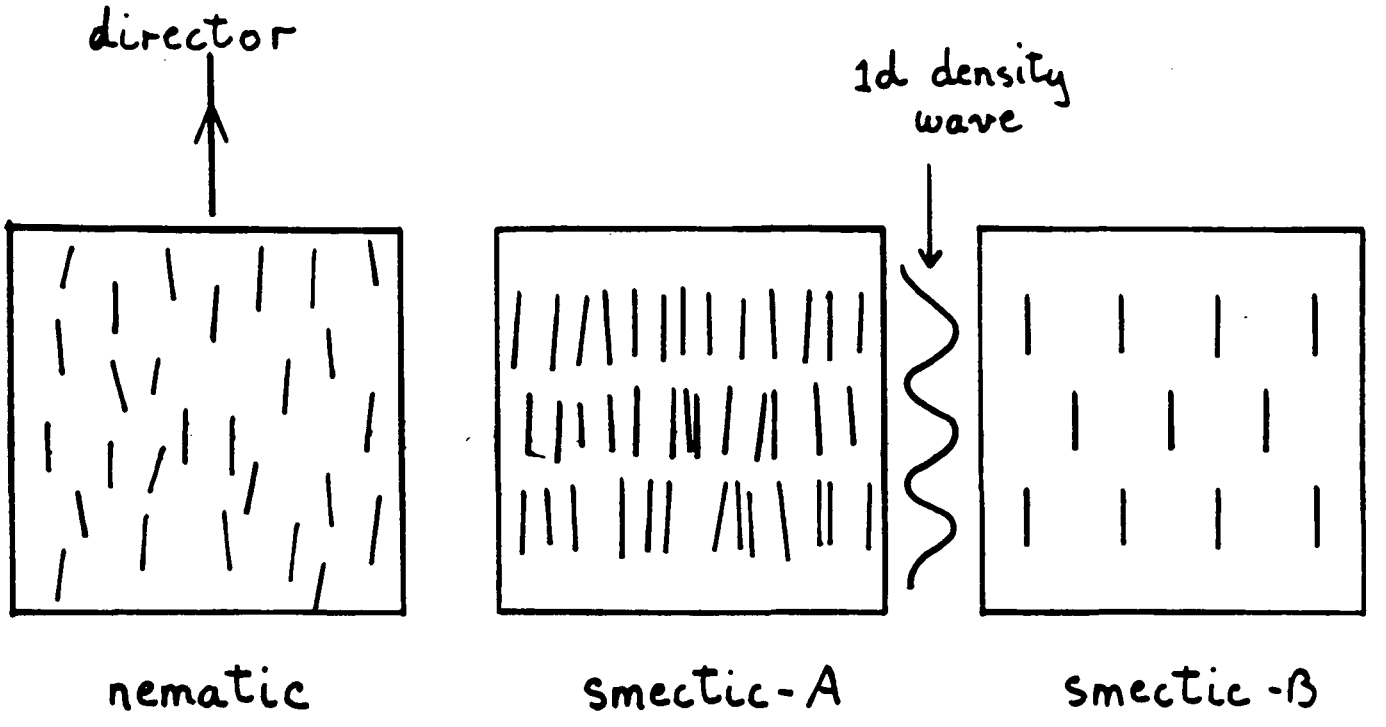

Figure 3.7 - The important types of liquid-crystal ordering; nematic, smectic-A and smectic-B.

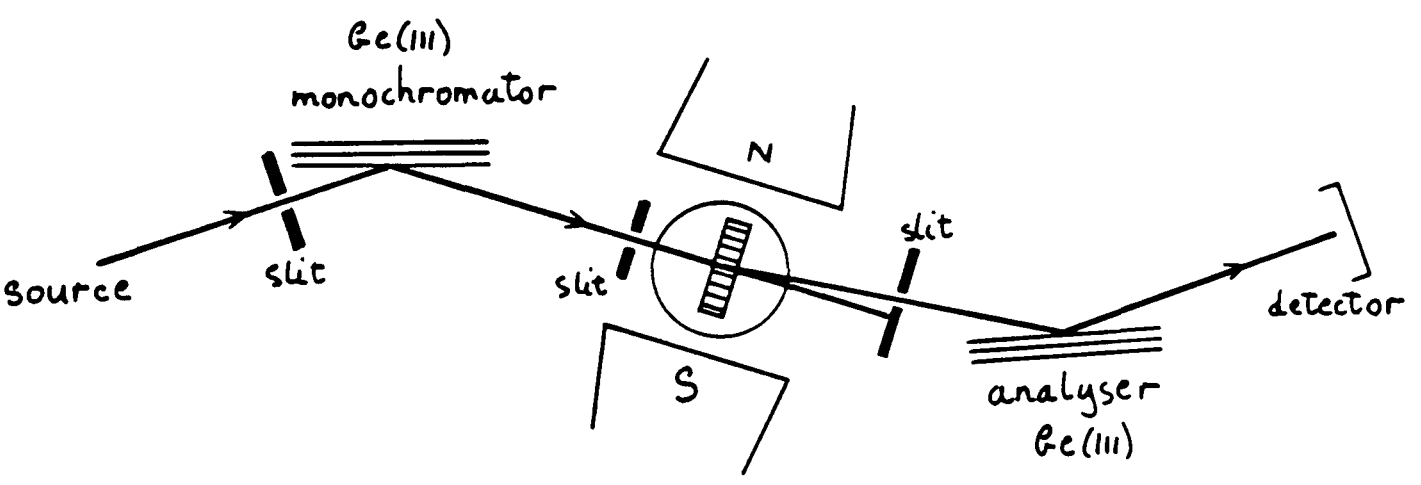

Figure 3.8 - A schematic view of a triple-crystal spectrometer configured to study ordering in liquid-crystals.

2) LIQUID CRYSTALS.

High-Q-resolution x-ray scattering has also been used to study the rich variety of structural phase transitions exhibited by liquid crystals. Broadly, liquid crystals can be classified as Isotropic, Nematic, Smectic and Cholestric (P.D.De Gennes 1974 and Figure 3.7). The Isotropic phase is a liquid in which the molecules are randomly oriented with no long range positional correlations. In the Nematic phase, the rod-like molecules are aligned parallel to one another and the alignment direction is known as the 'director'. This phase still lacks any long-range positional order.

The Smectic phases are characterised by the establishment of a one-dimensional density wave parallel to, or inclined at some small angle to, the director.

The simplest Smectic phase, Smectic-A, is best described as a one-dimensional density wave in a three dimensional nematic fluid with the density wave along the director. Within the sheets, perpendicular to the director, the structure is liquid-like. There are several further variations on the Smectic phase - including the Smectic-B (or hexatic) phase in which a six-fold symmetry is established within the sheets. This phase is more properly described as a lammellar crystal with true long-range order in three dimensions.

Of particular experimental interest is the Nematic to Smectic-A transition. This is thought to be one of the simplest examples of solidification in nature and, furthermore, the transition is almost perfectly second-order. This transition was first studied, using low-Q-resolution x-ray scattering techniques, by McMillan(1971) and subsequently by Als-Nielsen, Birgeneau, Kaplan, Litster and Safinya (1977) using the M.I.T. high-Q-resolution triple-crystal spectrometer. The experimental configuration used in this experiment (which is essentially identical to that used in all subsequent work on liquid crystals) is shown in Fig(3.8).

The liquid crystal was contained within a flat vessel, some 1.5mm thick, with Be or Kapton windows and was aligned in the Nematic phase by an applied magnetic field. The sample vessel was contained within a temperature controlled oven.

Ge(111) monochromator and analyser crystals were used to collimate

the incident and scattered beams, providing a resolution of $\sim 4 \times 10^{-4} \text{Å}^{-1}$ in the direction of momentum transfer (normal to the Smectic layers) and a remarkable $2 \times 10^{-5} \text{Å}^{-1}$ in the perpendicular direction.

The Smectic ordering manifests itself as a peak centred at $(0,0,Q_o)$ where $Q_o \simeq 0.2 \text{Å}^{-1}$, depending on the particular sample under examination. The critical scattering, close to T_c in the Nematic phase, is ellipsoidal in shape and the ratio of the width in the $\mathbf{q}_{pr}$ direction to the $\mathbf{q}_{pl}$ direction is roughly 6:1. Longitudinal $(\mathbf{q}_{pl})$ and transverse $(\mathbf{q}_{pr})$ scans are measured as a function of temperature. The line widths narrow and the peak height grows as T_c is approached and so the temperature dependence of the longitudinal and transverse correlation lengths and the Smectic susceptibility can be measured directly.

In this first experiment, the critical exponents γ and ν, describing the divergence of the susceptibility and correlation length respectively, were ,measured and the transition was shown to be second-order.

In a second experiment (Als-Nielsen, Birgeneau, Kaplan, Litster and Safinya 1977) attention was focussed on the structure of the Smectic-A phase. Theory predicted that, in some low dimensional systems - such as the one-dimensional density wave established in the Smectic-A phase, long-range correlations should exist without the long-range-order characteristic of the three-dimensional crystalline state. Thus, instead of a Bragg peak (a δ function in reciprocal space) the scattering should take the form of a cusp and in the $\mathbf{q}_{pl}$ direction the intensity should be proportional to $\mathbf{q}^{-2+x}$ whilst, in the $\mathbf{q}_{pr}$ direction the intensity should be proportional to $\mathbf{q}^{-4+2x}$, where x is small, of the order 0.1.

The experimental problem is to distinguish between this 'Landau-Peierls' scattering profile and a true Bragg reflection in the presence of thermal diffuse scattering and (difficult to quantify) instrumental resolution effects. This experiment, in fact, failed due to an insufficiently clear understanding of the instrumental resolution effects. The particular experimental configuration employed resulted in the monochromator and analyser dynamical streaks (which show a $\mathbf{q}^{-2}$ intensity dependence) lying along the direction of the $\mathbf{q}_{pl}$ scan, effectively obscuring the predicted $\mathbf{q}^{-2}$ tails of the 'Landau-Peierls' scattering profile.

Subsequently, the experiment was repeated (Als-Nielsen, Litster, Birgeneau, Kaplan, Safinya, Lindegaard-Andersen and Mathieson 1980) using the

recently constructed triple-crystal spectrometer at Riso, in Denmark, with channel-cut, Bonse-Hart, monochromator and analyser crystals to attenuate the dynamical streaks by several orders of magnitude. This time, the experiment sucessfully confirmed the 'Landau-Peierls' structure of the Smectic-A phase; the first experimental observation of such behaviour in a low-dimensional system.

Similar techniques have been applied to the study of the Nematic to Smectic-A transition in a large variety of liquid crystals (e.g. Davidov et al 1979, Safinya et al 1980, Ocko et al 1984) and the phenomenology is now reasonably well understood.

To study the structure of, and the correlations within, the Smectic planes, a novel sample preparation technique, developed at Harvard in the late 1970's, was adopted to obtain free-standing, liquid crystal films between two and several hundred molecular layers thick. This technique eliminates two problems associated with field-aligned samples, the influence of the sample cell walls and the orientational disorder about the layer normal, and also permits the nature of the ordering within the planes to be studied as the dimensionality of the system is reduced from 3 to 2.

In the first reported x-ray scattering study of liquid crystal thin films, Moncton and Pindak (1979) examined the structure of a Smectic-B phase as a function of temperature and layer number using the Bell Laboratories triple-crystal spectrometer with pyrolytic graphite monochromator and analyser crystals. The in-plane resolution was approximately 10^{-2}Å^{-1}. The experiments were performed in transmission geometry with **G**, the scattering vector, in the plane of the Smectic layers.

Within the limits of the experimental resolution, it was shown that the thin Smectic-B films form two-dimensional crystals and that the thick (~100 layers) films have conventional long-range order with the interlayer ordering consisting of a hexagonal close packed structure.

Having established the crystalline nature of the Smectic-B phase in two-dimensions (thin films) and in three-dimensions (thick films) attention was then focussed on the Smectic-B to Smectic-A melting transition in films of varying thickness (Moncton, Pindak, Davey and Brown 1982). The two-layer film is believed to provide the only example of an experimentally viable, two-dimensional, substrate free melting transition and is, therefore, of considerable interest. The experiments were performed using the SSRL

triple-crystal spectrometer with Si(111) monochromator and analyser crystals for high-Q-resolution studies of the solid Smectic-B phase and Graphite crystals for lower resolution studies of the Smectic-A liquid phase.

The two-layer films were found to melt by a strongly first-order transition with a ~1K hysteresis, in contrast to the current theories which predicted a continuous two-dimensional melting. The three-layer films melted by two phase transitions with a remarkable, and quite unique, intermediate phase lacking long-range positional order but with bond-orientational order and with a correlation length decreasing as the temperature is lowered. The development of interlayer ordering was studied in thin films of increasing thickness.

The x-ray scattering technique has also been applied to the study of more exotic Smectic-B phases (Davey, Budai, Goodby, Pindak and Moncton 1984) and to the study of surface structures in Smectic-A liquid crystals (Als-Nielsen and Pershan 1983).

4) GRAPHITE INTERCALATES.

Just as the physisorbed monolayers and liquid crystals provide experimentally realisable systems for the study of melting transitions in two-dimensions, the graphite intercalates are ideally suited for the study of commensurate to incommensurate transitions in two-dimensional solids.

Intercalants are formed by the insertion of guest atoms or molecules between layers of a host material, such as graphite. (Dresselhaus and Dresselhaus 1981). An enormous variety of intercalants (several hundred species) from alkali metals, such as Li, to compounds such as $FeCl_3$ and $SbCl_5$ have been inserted into the graphite host lattice but, from the point of view of phase transition research, the most important intercalants are the halogens, in particular Br_2.

Br_2 is introduced from the vapour in a furnace. By varying the conditions under which intercalation takes place it is possible to control the number of layers of the host material between each of the intercalate layers, a phenomenon known as 'staging'. A stage one intercalation compound has alternating host and guest layers, whereas a stage four compound has one guest layer for each four host layers. Thus, the degree of interaction between intercalate layers can be controlled.

Structural phase transitions within the basal-plane layers occur as a result of differential thermal expansion. Graphite exhibits almost no, in plane, thermal expansion whereas, the intercalate layers generally show a significant thermal expansion. Thus, if the intercalate atoms are, at one temperature, in positions commensurate with the graphite lattice as the temperature is increased or decreased the intercalate lattice can move out of registry with the host lattice, i.e. to an incommensurate phase. On further heating, some intercalates, including Br_2, undergo a two-dimensional melting transition.

High-Q-resolution X-ray scattering techniques are routinely used to determine the staging index and to study the size of intercalate domains (Hardcastle, Misenheimer and Zabel 1983) but the technique is also use to study the crystal structure of the two-dimensional intercalate layers and the dynamics of the two-dimensional melting transitions. (Kortan, Erbil, Birgeneau and Dresselhaus 1982: Erbil, Kortan, Birgeneau and Dresselhaus 1983).

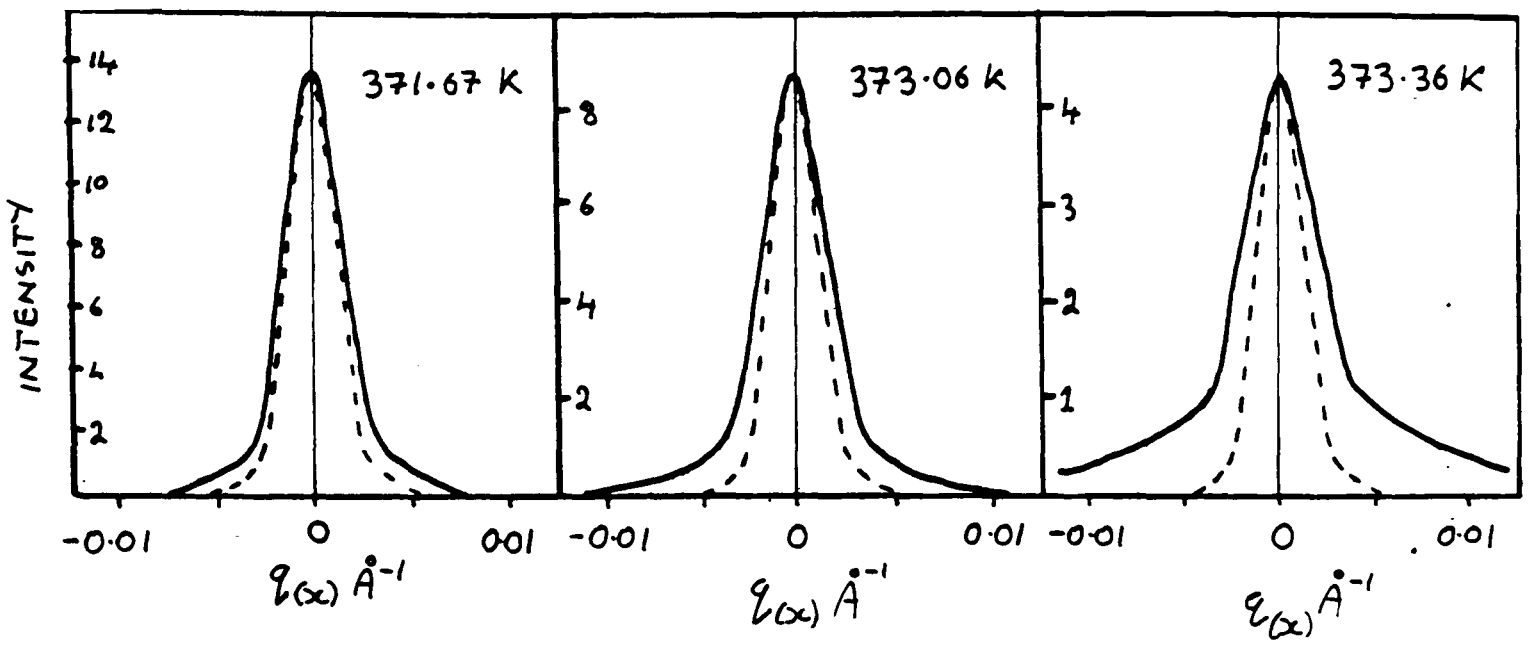

Figure 3.9 – Br_2 intercalated in a graphite host. Line shapes of a scattering peak in the incommensurate phase. The dashed line is the instrumental resolution, the full line is a power law fit to the observed data. $T_m \simeq 373.56K$. (After Erbil et al. 1983)

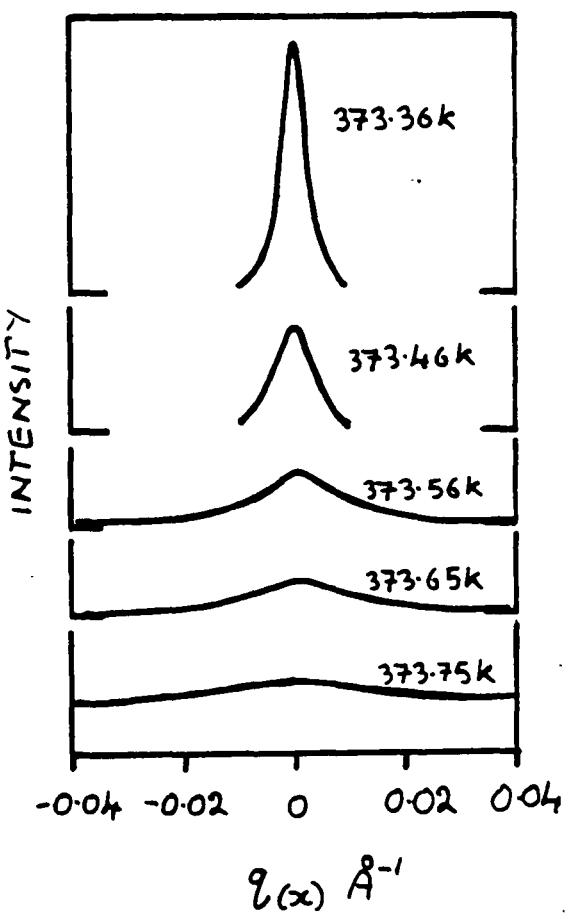

Figure 3.10 – Br_2 in graphite. Line shapes of a scattering peak at the incommensurate melting transition. (After Erbil et al. 1983)

The phase transition work was carried out using the M.I.T. triple-crystal spectrometer with MoKα_1 radiation from a 12KW rotating anode source. As with the physisorbed monolayers, the experiments were carried out in transmission geometry, using graphite platelets some 0.1mm thick, to examine correlations within the intercalate layers. Low-Q-resolution studies, with graphite monochromator and analyser crystals, showed that the Br_2 molecules formed a $\surd$3x7 commensurate structure with the sevenfold axis directed along a graphite [110] direction. As the sample temperature was increased, thermal expansion within the Br_2 layer resulted in a transition to an incommensurate phase. Interestingly, the Br_2 superlattice remained commensurate with the host along the $\surd$3 direction but became incommensurate only along the sevenfold direction.

Analysis of the low-resolution diffraction profiles in the incommensurate phase showed that the structure of the Br_2 superlattice could not be described by a uniform expansion along the sevenfold direction, rather, the structure was better described by a domain wall model in which locally commensurate regions are separated by displacement slips or discommensurations. Thus, a stripe domain phase is formed.

High-Q-resolution measurements, with Ge(111) monochromator and analyser crystals, were used to study the lineshapes of the diffraction peaks in the commensurate and incommensurate phases. In the commensurate phase, the Bragg peaks were found to be resolution limited Gaussians, showing that long-range order existed and that the domain sizes were larger than 10^4A (or one micron).

In the incommensurate phase, the Br_2 intercalate layers have continuous, rather than discrete symmetry. In common with the other two-dimensional systems, physisorbed monolayers and liquid crystal Smectic phases, the scattering is expected to be described by a power law singularity rather than a δ function (as in the Bragg case). This was indeed found to be the case. Figure (3.9), from Erbil et al (1983), shows the lineshape of an incommensurate phase peak as the sample temperature is increased. The dotted line shows the Gaussian, resolution limited lineshape characteristic of the commensurate phase and the solid line shows a power law fit to the experimental data. The slightly increased FWHH and greatly increased scattering in the wings are characteristic of systems with continuous symmetry.

The two-dimensional melting transition was also investigated by lineshape analysis, Figure (3.10). In this case the power law singularity of the incommensurate phase almost disappears at the melting transition, to be replaced by a broad Lorentzian form corresponding to an exponential decay of positional correlations in the intercalate layers, characteristic of a liquid. Interestingly, in the region of T_m, the melting transition temperature, the linewidth increased rapidly and continuously but anisotropically in the directions corresponding to the $\sqrt{3}$ fold and sevenfold directions. At T_m+0.5K, however, the scattering was isotropic once again. This behaviour is possibly indicative of some kind of intermediate, two-dimensional Smectic liquid crystal phase, a phenomenon predicted by theory but never experimentally realised.

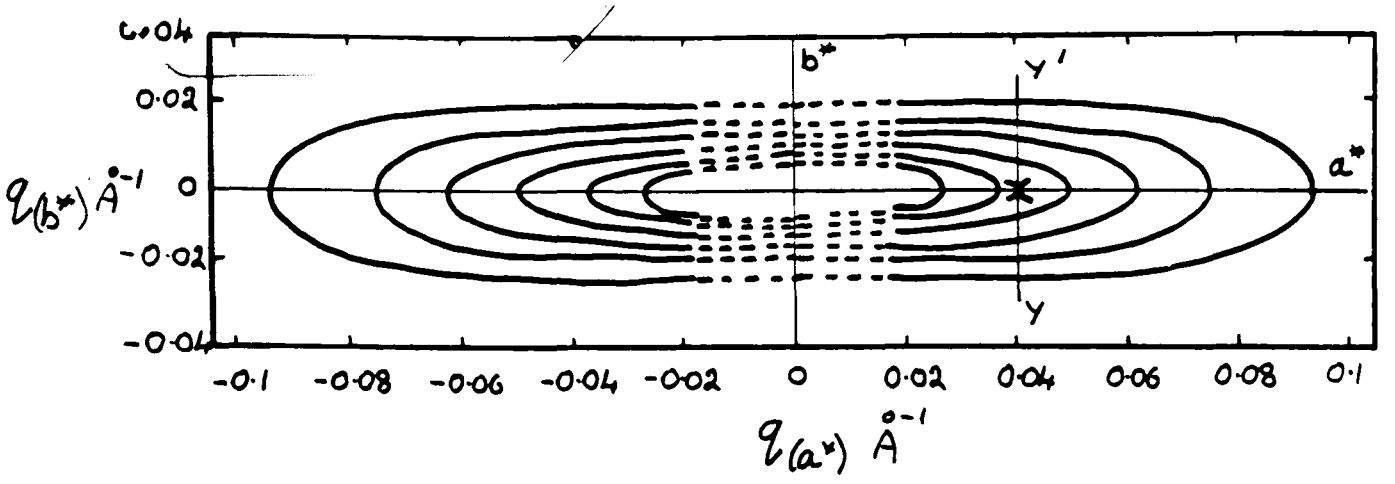

Figure 3.11 - Tri-glycine sulphate (TGS). The intensity distribution of critical scattering around a typical Bragg peak in the a*b* plane. (After Fujii and Yamada 1971)

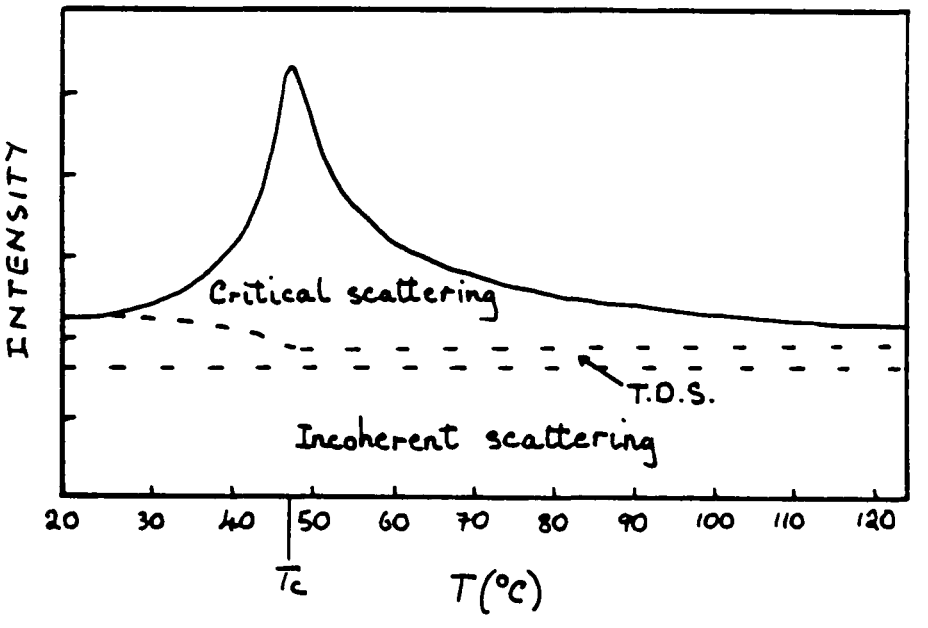

Figure 3.12 - TGS. Diffuse scattering intensity at the point 'x' (figure 3.11) as a function of temperature. (After Fujii and Yamada 1971)

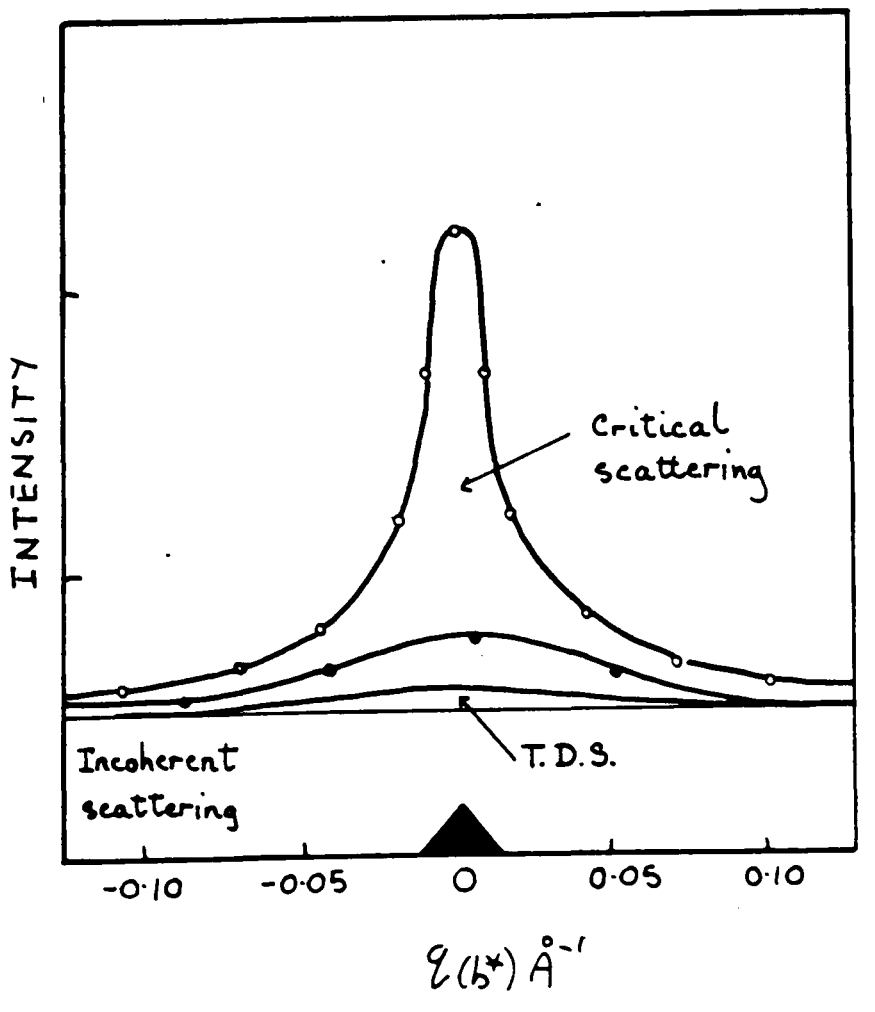

Figure 3.13 - TGS. Diffuse scattering intensity along the section yxy' (figure 3.11) at T_c + 0.1K. (After Fujii and Yamada 1971)

5)STRUCTURAL PHASE TRANSITIONS IN CRYSTALLINE SOLIDS.

JAPAN. Perhaps surprisingly, in view of the large amount of experimental effort applied to inelastic neutron scattering studies of structural phase transitions in the 1960's and 1970's, the literature contains comparatively few quantitative x-ray studies of critical scattering. In notable exception to this rule are the series of experimental studies of critical x-ray scattering in order-disorder ferroelectrics by the Osaka University group under Y.Yamada. (e.g. Yamada and Yamada 1966, Fujii and Yamada 1971, Terauchi and Yamada 1972, Terauchi, Takenaka and Shimaoka 1975).

In particular, the 321K ferroelectric phase transition in tri-glycine sulphate (TGS) was examined (Fujii and Yamada 1971). TGS, along with KH_2PO_4 and $NaNO_2$, is one of the most thoroughly studied examples of an order-disorder ferroelectric (for a review, see Lines and Glass (1977), Chapter 9). TGS is a particularly attractive subject because it is one of the few, second-order zone-centre structural phase transitions.

Using a relatively simple diffraction apparatus with a low-power conventional x-ray source, a LiF monochromator and slit to select $CuK\alpha_1$ radiation and a scintillation counter to detect the scattered x-rays, a number of text-book critical scattering measurements were carried out. Figure (3.11) shows the intensity distribution of the critical scattering at T_c+0.1K in the **a***b* plane. TGS is a uniaxial ferroelectric; at T_c, a spontaneous dipole moment develops along the monoclinic **b*** axis but, in the critical temperature region, the macroscopic electric fields associated with the development of the polarisation supress the ferroelectric fluctuations along the **b*** axis.

This interaction results in the characteristically anisotropic critical scattering distribution shown in Fig(3.11).

Figure(3.12) shows the temperature dependence of the diffuse scattering intensity at the point (3.04,4,0), marked 'x' on Fig(3.11). The critical scattering, which peaks sharply at T_c, is superimposed upon a largely temperature independant background of incoherent (Compton) scattering and thermal diffuse scattering (TDS) from long wavelength acoustic modes. Figure(3.13) shows the intensity distribution along the section yxy' in Figure(3.11) at T_c+0.1K. Once again, the critical scattering is seen to be

superimposed on a background of TDS and Compton scattering.

From this data it was possible to measure the intensity divergence in the a* direction and thus the correlation length critical exponent, ν, which was found to be ν=0.502. Mean field theory predicts a value of ν=0.5 for systems, such as TGS, dominated by long-range dipole forces. The correlation range, κ, in the 'a' direction was found to extend over 24, 11 and 3 unit cells at T_c+0.2K, 1.0K and 10K respectively.

BELL LABS. In the late 1970's the Bell laboratories group, initially using a triple-crystal instrument mounted on a rotating anode source and subsequently the SSRL triple-crystal spectrometer, examined the incommensurate charge-density wave in the transition metal chalcogenides 2H-$TaSe_2$ and $NbSe_3$ (Fleming, Moncton and McWhan 1978, McWhan, Fleming, Moncton and DiSalvo 1980, Fleming, Moncton, McWhan and DiSalvo 1980, Fleming, Moncton, Axe and Brown 1984). In these materials, at sufficiently low temperatures, a periodic positional modulation of the lattice can arise as a result of an interaction between the lattice and the Fermi surface of the crystal.

By exploiting the high intensity of the synchrotron source the period of the lattice modulation and wave-vector width of the sattelite peaks were measured with a Ω resolution of $\sim 10^{-4}$ Å^{-1}.

2H-$TaSe_2$ was shown to undergo a sequence of phase transitions on cooling between 122K and 85K, from a normal phase, through an incommensurate phase to a commensurably modulated phase. The incommensurate phase is characterised by three wave-vectors $\mathbf{q}_i=(\frac{1}{3}\mathbf{a}^*-\mathbf{d})$ where $\mathbf{a}^*$ is a reciprocal lattice vector and d is a measure of the incommensurability. The behaviour of the structural modulation was found to be quite different on warming, with the formation of an intermediate, 'stripe-domain' phase in which one of the modulation wave-vectors remains locked-in to the commensurate value of $\frac{1}{3}$.

The electrical conductivity of CDW materials is believed to be influenced by the presence of defects, which pin the phase of the wave. This pinning is expected to limit the correlation length of the wave and should result in a broadening of the incommensurate sattelites. The high-Ω-resolution x-ray scattering measurements of Fleming et al (1984), however, showed that the

correlation length of the modulation wave was many thousands of Ångstroms in a sample of $NbSe_3$ which, from the evidence of conductivity measurements, was expected to show significant pinning. The conclusion to be drawn from these experiments is that the behaviour of CDW materials is considerably more subtle than was previously expected.

EDINBURGH. At Edinburgh University, using a triple-crystal instrument mounted on a 15KW rotating-anode source, work has concentrated on three classes of structural phase transitions in crystalline solids; the classic order-disorder ferroelectrics KH_2PO_4(KDP) and KD_2PO_4(DKDP), the antiferrodistortive perovskites $SrTiO_3$, $KMnF_3$ and $RbCaF_3$ and transitions to incommensurably modulated phases in, for example, Rb_2ZnCl_4, $BaMnF_4$ and Ag_3AsS_3. To broadly summarise the conclusions of these studies before examining some of the work in more detail, it has become apparent that, close to T_c, current theories fail to predict the detailed behaviour of real systems. Very tiny quantities of defects or impurities can significantly alter the critical properties of materials in quite unexpected ways and much of the more recent Edinburgh work has been concerned with examining the role of defects, competing interactions, impurities and random fields at structural phase transitions.

UNIAXIAL FERROELECTRICS.

KDP and DKDP are uniaxial ferroelectrics with transition temperatures 123K and 229K respectively. They display critical behaviour very similar to that of TGS (see 4.1). As well as containing information on the correlation range and static susceptibility of a system undergoing a structural phase transition, the critical scattering contains information on the atomic motions involved in the softening mode (or, in KDP and DKDP, the ferroelectric fluctuation). Inelastic neutron scattering measurements have been used with some sucess to determine the atomic motions in, for example, $KTaO_3$ (Harada, Axe and Shirane 1970) and KD_2PO_4 (Skalyo, Frazer and Shirane 1970) but an inconsistency between the ferroelectric mode motions in DKDP proposed by Skalyo et al and the atomic displacements of the ferroelectric phase determined by Nelmes, Meyer and Tibballs (1982), from high resolution elastic neutron scattering data, prompted a re-examination of the ferroelectric mode motions using diffuse x-ray scattering data (Bleif, Cowley and Nelmes 1982, Cowley, Bleif, Andrews and Nelmes 1983, Andrews and Cowley 1986).

An alternative model for the atomic motions, incorporating a local fluctuation of the centre of mass of the unit cell, was proposed; the resulting atomic motions were found to be in remarkable agreement with the thermal vibration amplitudes of the K, P and O atoms above T_c deduced from further elastic neutron scattering measurements by Nelmes, Kuhs, Howard, Tibballs and Ryan (1985).

INCOMMENSURATES.

Andrews and Mashiyama (1983) carried out a detailed study of critical scattering in Rb_2ZnCl_4, which undergoes a second-order normal to incommensurate phase transition at ~303K and a subsequent lock-in transition to a commensurably modulated phase at ~190K. The critical exponents γ and ν were obtained from measurements of the intensity and width of the critical scattering above T_c=303K whilst β, the order parameter exponent, was obtained from the temperature dependence of the intensity of a first-order sattelite peak in the incommensurate phase. The measured exponents were in good agreement with theoretical predictions (LeGuillou and Justin 1980).

Subsequent attempts to perform similar measurements on the incommensurates $\{N[CH_3]_4\}_2CoCl_4$ (TMATC-Co for short) and $BaMnF_4$ encountered serious reproducibility problems. It became clear that in TMATC-Co (Fjaer, Cowley and Ryan 1985), radiation damage was induced in the sample throughout the course of the measurement, resulting in local pinning of the modulation wave at damage sites. In $BaMnF_4$ (Ryan 1986, Ryan, Cowley and Andrews 1986, this thesis Ch7), differences between samples from various sources and, indeed, within single samples, confirmed that the behaviour of the system is strongly influenced by the presence of intrinsic defects.

A detailed lineshape analysis of the incommensurate satellite reflections in two samples of $BaMnF_4$, with different defect concentrations, revealed behavior which was remarkably similar to that seen in the site random Ising antiferromagnets which have attracted considerable experimental and theoretical interest over the past five years (Cowley et al 1984, Birgeneau et al 1985).

PEROVSKITES.

The 105K second-order displacive transition in $SrTiO_3$ (Fleury et al 1968) was thought to represent one of the simplest possible cell-doubling

transitions and, as such, has been the object of continued interest since the first (inelastic neutron scattering) observation of a zone-boundary soft-mode condensation (Shirane and Yamada 1969). Despite the apparent simplicity of the transition, subsequent experimental work posed a number of unexpected questions which exposed serious inadequacies in contemporary theory and which, to a large extent, are still unanswered. (see e.g. Bruce and Cowley 1981)

In particular, the observation, by inelastic neutron scattering, of a quasi-elastic scattering peak at the zone-boundary in the cubic phase - the so-called 'central-peak' - was entirely unexpected (Riste et al 1971, Shapiro et al 1972). This feature was visible some 70K above T_c and completely dominated the scattering spectrum within 10K of T_c. The inelastic neutron scattering measurements showed that the scattering was, within error, elastic and suggested a correlation length of the same order as that of the soft mode.

Subsequent x-ray and Mossbauer scattering experiments (Darlington et al 1975, 1976) showed a very strong, quasi-elastic scattering component just above T_c which appeared to be surface and sample history related.

Andrews(1986), at Edinburgh, used very high-**Q**-resolution x-ray scattering techniques to examine the wave-vector width of the 'critical' scattering in $SrTiO_3$ for the first time, and saw two components in the scattering spectrum; a broad feature corresponding to critical scattering from the soft mode and a very narrow, Bragg like feature superimposed upon the diffuse scattering. The Bragg component was first observable at $\sim T_c$+6K and grew rapidly in intensity as T_c was approached. Its width was resolution limited, corresponding to a correlation length of several thousands of Ångstroms. Andrews extracted the correlation length exponent, ν, from the diffuse (critical) scattering and also discussed the possible origins of the Bragg component, arriving at no firm conclusion.

In a series of follow-up experiments, attention was turned to the isomorphous perovskite $RbCaF_3$ (this thesis Ch8, Ryan, Nelmes and Gibaud 1986, Gibaud and Ryan 1986, Cowley, Mitchell and Gibaud 1986). Several samples were examined and similar features were observed although, in contrast to $SrTiO_3$, the Bragg component was not resolution limited and its correlation length diverged as T_c was approached. Significantly, the occurence of the Bragg feature appeared to be related to the sample quality, lending force to the conjecture that it is an extrinsic feature, caused by the presence of defects.

That the presence of defects should influence the critical behaviour of materials is not in itself surprising and is, in fact, widely appreciated. What is surprising is that the quality of the crystals examined in the above experiments was, by most normal standards, very good (i.e. rocking curve widths of the order of 0.01° FWHH).

6) DEFECTS,SURFACES and INTERFACES.

Although the theme of this review is to provide an overview of recent work in the field of high-Q-resolution x-ray scattering studies of structural phase transitions, it is important to consider other phenomena which can give rise to measurable features in the scattering spectra.

Defects, dislocations, interstitials, impurities, grain boundaries, the surface of the crystal itself and the myriad of other imperfections which are inevitably present in a real crystal all result in local displacements of atoms from their ideal lattice sites. The elastically scattered, diffuse x-ray scattering from a real crystal containing such imperfections was first considered by Huang(1947) and the theory was subsequently refined by Cochran and Kartha(1956).

The Huang scattering technique is of considerable technological interest as it provides one of the best experimental techniques for studying, for example, radiation damage in metals and ionic crystals (Ehrhart and Schilling 1973, Guerard, Grasse and Peisel 1980) or process induced defects in materials for semiconductor manufacture (Patel 1975, Lomov, Zaumseil and Winter 1985). As befits such an important subject, the literature is extensive but a good introduction to theory and experiment is given by Dederichs(1971).

Briefly, the intensity of the Huang diffuse scattering is related to the number and type of defects present in the crystal and its topology is related to the symmetry of the displacement field around the defect. At small **q** the Huang intensity is determined by the long-range displacement field of the defects and varies as $\mathbf{q}^{-2}$ but, at larger **q**, the intensity is influenced by the heavily distorted regions close to the centre of the defect and falls off as $\mathbf{q}^{-4}$. The crossover from $\mathbf{q}^{-2}$ to $\mathbf{q}^{-4}$ dependence is related to the average defect, or defect cluster, size.

If the defects are small, the Huang scattering can be studied by conventional, low-Q-resolution x-ray scattering methods. In many materials of technological importance, however, defect clusters with dimensions of up to 1 micron can be present. To study these the high-Q-resolution of a perfect-crystal, triple-crystal spectrometer is required.

Iida and Kohra(1979) and Iida(1979) used a triple-crystal instrument

with Bonse-Hart monochromator and analyser crystals in the (1,-1,1) configuration to study diffusion induced defects in silicon. In samples diffused with copper, lithium and gold it was possible to measure Huang scattering corresponding to defect diameters of up to one micron.

Using a similar triple-crystal instrument, previously described by Zaumseil and Winter(1982), Lomov, Zaumseil amd Winter(1985), examined process induced defects in silicon prepared for device fabrication and, once again, measured defect cluster diameters of the order of one micron.

Although, as far as the study of critical scattering at structural phase transitions is concerned, Huang scattering simply contributes to a temperature independant background effectively indistinguishable from TDS, the above papers are of considerable interest to the experimentalist as they represent the most serious attempt, to date, to exploit the suggestions of Eisenberger, Alexandropolous and Platzman and to measure diffuse scattering with extremely high wave-vector resolution at $\mathbf{q} \sim 10^{-4}\text{Å}^{-1}$.

Very recently, Andrews and Cowley (1985) and Robinson (in press) have reported the observation of extended, diffuse streaks in reciprocal space, perpendicular to the plane of the crystal surface. The streaks have been shown to arise from the abrupt termination of the crystal lattice at the surface. The **q** dependence of the intensity of the streak is strongly related to the surface roughness, on an atomic scale, - allowing highly sensitive surface roughness measurements to be made.

CHAPTER FOUR

The Resolution of a Triple-Crystal X-Ray Spectrometer

1) INTRODUCTION

A thorough understanding of the optical effects determining the instrumental resolution is of fundamental importance to the sucessful outcome of any attempt to quantitatively measure the distribution of scattered intensity in a neutron or x-ray diffraction experiment. As such, the subject has attracted considerable interest since the inception of computer controlled x-ray and neutron diffractometers in the mid 1950's.

Broadly speaking, diffraction experiments, and the instruments used to carry out these experiments, can be split into two categories; those designed to measure the integrated intensity of Bragg reflections and those designed to study the distribution of diffuse scattering between the Bragg reflections. In each case an understanding of the instrumental resolution is required but the reasons for that understanding differ significantly.

When the objective of the experiment is to measure the integrated intensities of Bragg reflections (e.g. for a crystallographic structural determination) it is important that scan widths and aperture sizes are chosen to be sufficiently large to allow the instrument to record all of the intensity scattered by the sample crystal but, at the same time, not excessively large as this may result in a disproportionately high background and inefficient use of the instrument. The development of automatic single-crystal four-circle diffractometers in the mid 1950's prompted a lively discussion of the relative merits and demerits of the various possible scan types and coupling ratios of crystal and detector rotations made possible by sophisticated computer control (Alexander and Smith 1962,1964a,1964b, Burbank 1964, Ladell and Spielberg 1966, Werner 1972). Remarkably, in view of the superficially simple nature of the x-ray diffraction procedure, the controversy over scan types and aperture sizes has rumbled on to the present day (Mathieson 1982,1983a,1984,1985).

The contemporary discussion was stimulated, in part, by the development of linear position sensitive x-ray detectors (PSD). Instead of producing an integrated intensity as a function of a single rotational parameter ($\Delta\omega$ - the crystal rotation) the PSD produces a two-dimensional map of the scattered intensity as a function of $\Delta\omega$ and position along the detector axis - $\Delta 2\Theta$ (Schoenborn 1983, Mathieson above and 1983b). The distribution of scattered intensity in $\omega/2\Theta$ space (or in reciprocal space when the correct transformation has been made) is found to be determined by a complex and often subtle interplay of such parameters as the wavelength spread of the incident beam $\Delta\lambda$, beam collimation, source size and shape, sample crystal size and shape, sample crystal mosaic spread, absorption of the beam in the sample and monochromator crystals and detector resolution.

If the experimental objective is the measurement of the intensity distribution of diffuse x-ray (or neutron) scattering it is important to understand the spatial dimensions of the volume of reciprocal space sampled in a particular measurement. From these dimensions an instrumental resolution function can be derived and this can be used to apply a correction to the measured data and obtain the true intensity distribution.

In contrast to the neutron scattering case, in which the instrumental resolution can be described very sucessfully in terms of a Gaussian convolution of each of the resolution degrading effects (Cooper and Nathans 1967, Stedman 1968, Bjerrum-Moller and Neilsen 1969), the resolution function of x-ray scattering instruments has received scant attention.

Reid (1981) has discussed the factors influencing the resolution of a low-Q-resolution two-crystal x-ray spectrometer comprising a curved crystal monochromator, an extended face sample crystal and a detector receiving aperture defined by a simple slit (essentially the same experimental configuration as that described by Mathieson). The only published work specifically devoted to the resolution of a high-Q-resolution triple-crystal x-ray spectrometer is by Pynn, Fujii and Shirane (1983). In this work the formalism of Bjerrum-Moller and Neilsen was applied to the case of a perfect crystal 3-crystal spectrometer and the calculated resolution function was compared with experimental measurements of the peak shapes of Bragg reflections from a perfect Germanium crystal. Although the work is undoubtedly a step in the right direction towards establishing a general formula for calculating the resolution function of a real triple-crystal spectrometer, the method is conceptually

opaque and is of limited value to the practising experimentalist interested in understanding the role of the individual x-ray optical components comprising the instrument and their contributions to the experimental resolution.

The present work discusses the role of each of these optical components in a real triple-crystal instrument. At first sight, the reader familiar with the work of Mathieson, Reid or Schoenborn, discussing resolution effects in a two-crystal x-ray (or neutron) instrument, may guess that the introduction of an additional x-ray optical element, the analyser crystal, would introduce a further complication into the resolution function. Surprisingly, this is not the case. Far from introducing a complication, the analyser crystal introduces a significant simplification and many of the resolution degrading effects with which the aforementioned authors concern themselves at some length simply disappear.

The remainder of this chapter is organised as follows. In section 2 the direction and magnitude of each of the resolution degrading effects is isolated and discussed in both instrumental space (with orthogonal co-ordinates $\Delta\omega$ and $\Delta 2\Theta$ or, as we shall call them, $\Delta\Psi$ and $\Delta\Phi$) and in reciprocal space. This will lead to a general description of the instrumental resolution for any spectrometer configuration. Section 3 presents experimental measurements of the instrumental resolution for a variety of typical spectrometer configurations and real sample crystals. In section 4 the characteristics of a number of alternative monochromator and analyser arrangements are examined with a view to tailoring or optimising the instrumental configuration for specific experimental requirements.

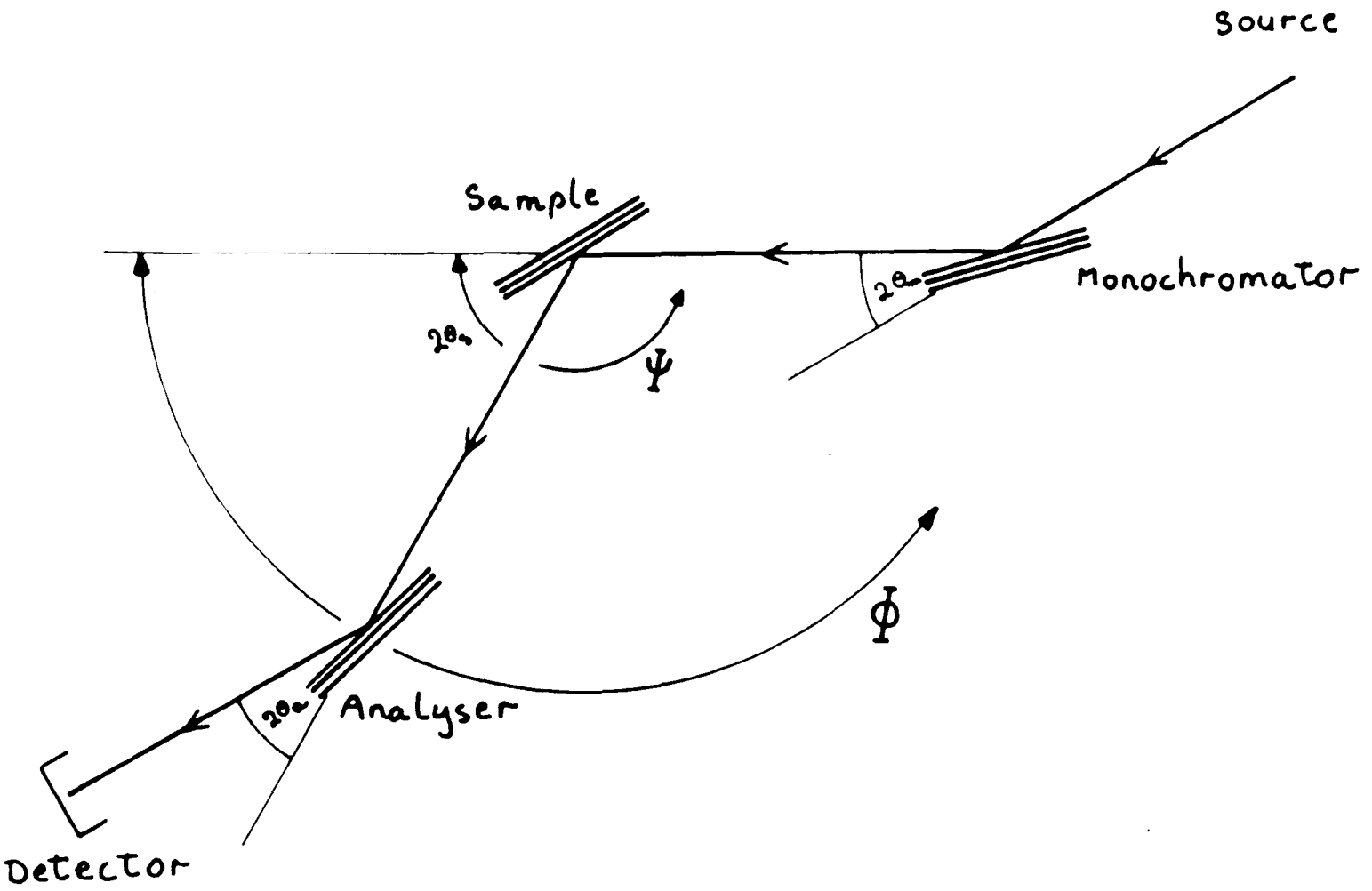

Figure 4.1 - The essential elements of a triple-crystal x-ray spectrometer.

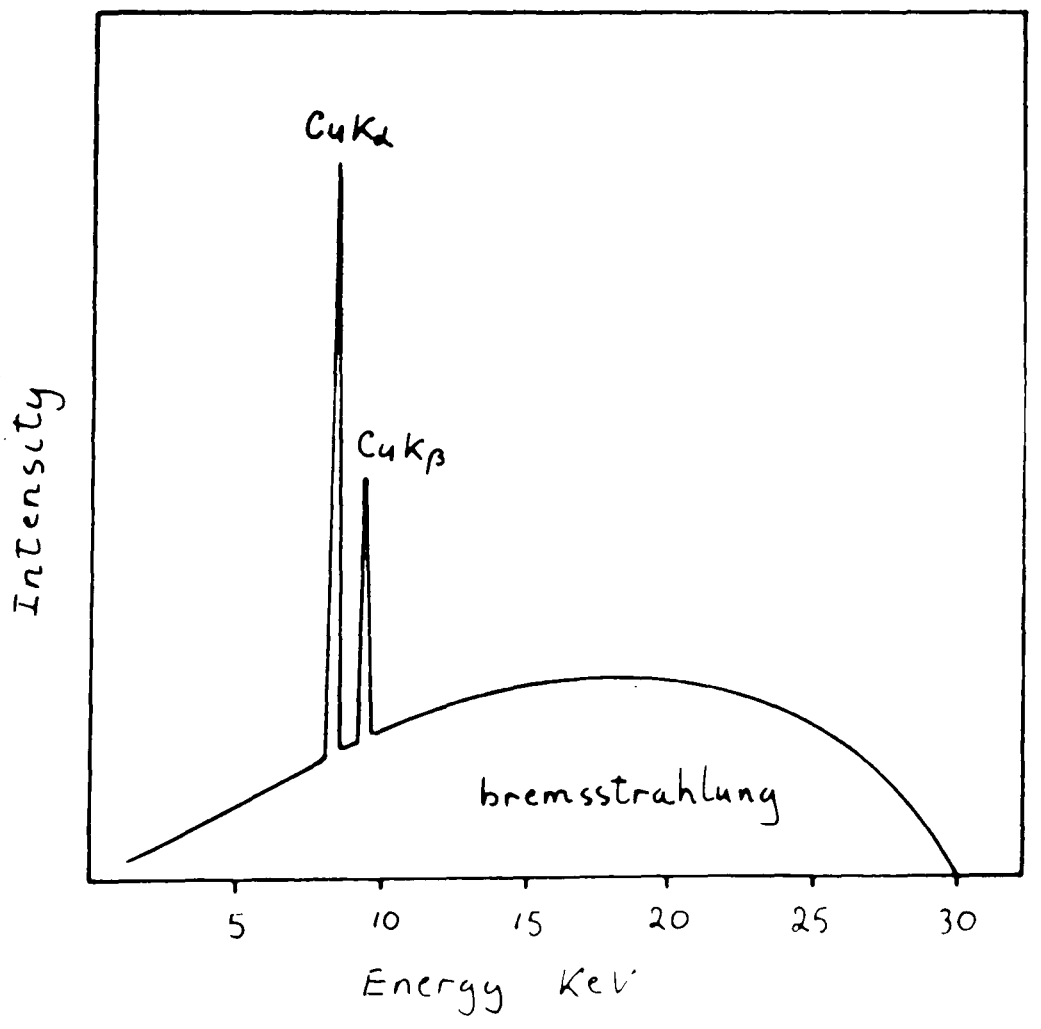

Figure 4.2 - The spectral distribution of a Cu target excited by 30KeV electrons.

2) THE RESOLUTION OF A TRIPLE-CRYSTAL X-RAY SPECTROMETER.

2.1) A DESCRIPTION OF THE INSTRUMENT.

Figure (4.1) shows a schematic picture of a triple-crystal x-ray spectrometer in the (+M,-S,+A) configuration. M, S and A refer to the monochromator, sample and analyser crystals respectively and the signs to the sense of scattering at each crystal. Conventionally, the sense of scattering at the monochromator crystal is always denoted '+'. The setting angles Θ_m, Θ_s and Θ_a are not necessarily equal although, normally, the spectrometer is configured with $\Theta_m = \Theta_a \neq \Theta_s$. This would be denoted the (+1,-S,+1) configuration. The special case $\Theta_m = \Theta_a = \Theta_s$, denoted (+1,-1,+1), will be considered at length later.

The two instrumental variables are Ψ, the crystal setting angle, and Φ, the analyser/detector setting angle. Θ_m, the monochromator setting angle, and Θ_a, the analyser setting angle, remain fixed throughout a measurement.

The x-ray source may be a conventional sealed x-ray tube, a rotating anode tube or a synchrotron source. Throughout this work we shall deal with a rotating anode source with a copper target. The basic arguements apply equally well to a sealed tube source and to a synchrotron source with minor adjustments to account for the special characteristics of this source. The spectral distribution of a Cu target excited by 30KeV electrons is shown in Fig (4.2). It is composed of a bremsstrahlung continuum with a number of characteristic lines superimposed upon it; the most important being the Cu$K\alpha_1\alpha_2$ doublet at roughly 8KeV. The exact wavelengths of the $K\alpha_1$ and $K\alpha_2$ lines are

$$K\alpha_1 = 1.540511\text{Å},\ \Delta\lambda = 0.00058\text{Å} : K\alpha_2 = 1.544551\text{Å}$$

The intensity ratio $K\alpha_1$:$K\alpha_2$ is almost exactly 2:1 and, under normal x-ray tube operating conditions, the intensity of the $K\alpha_1$ line is roughly 100 times greater than the bremsstrahlung continuum.

The monochromator crystal may be a mosaic crystal, such as pyrolytic graphite, or it can be a perfect crystal, perhaps silicon or germanium. Additionally, it may be flat, bent in the scattering plane or doubly bent, both in and perpendicular to the scattering plane. In some cases the monochromator

may be composed of several crystals or may involve several reflections from the same crystal. These options will be discussed in detail in section 4. The common feature of all of these monochromator systems, however, is that the beam which is incident upon the sample crystal is *never* perfectly monochromatic, nor is it ever perfectly collimated. A specific monochromator arrangement is chosen to define the degree of collimation of the incident beam (which we shall call $\Delta\Theta_m$) and the degree of monochromatisation (which we shall call $\Delta\lambda$). In practice, the range of $\Delta\Theta_m$ available is enormous - from one or two thousandths of a degree using flat silicon or germanium crystals through a few tenths of a degree using pyrolytic graphite to several degrees with a curved crystal mocochromator. The choice, in terms of the wavelength composition of the incident beam, is generally between inclusion or exclusion of the $K\alpha_2$ component although the $\Delta\lambda$ contained in the inevitable bremsstrahlung component can prove to be a serious complication in many experimental situations.

The sample crystal is always flat, may be perfect or mosaic and, most importantly, must be large enough to intercept all of the incident beam. As with the monochromator crystal, the sample crystal will satisfy the Bragg condition over a range of setting angles which we shall call $\Delta\Theta_s$. This may range from thousandths of a degree in very perfect crystals to tenths of a degree in highly mosaic crystals.

Similarly, the analyser crystal must be flat, may be perfect or mosaic and must be sufficiently large to intercept all of the beam diffracted by the sample. It too will satisfy the Bragg condition over a range of setting angles, denoted $\Delta\Theta_a$. The detector, normally a NaI(Tl) scintillation counter or a $Xe(CH_4)$ proportional counter, must have an active area larger than the beam passed by the analyser crystal and must have an energy window considerably larger than the range of energies defined by $\Delta\lambda$ but sufficiently narrow to discriminate against higher harmonics of λ (principally $\lambda/2$=16KeV) which may be passed by the spectrometer.

The proportional counter, with an energy window of 1.3KeV FWHH at 8KeV, is ideally suited to this task but for technical and financial reasons (sealed proportional counters have a limited useful life and Xe ges for a continuous flow counter is prohibitively expensive) a scintillation counter, with an energy resolution of 4KeV FWHH, is often preferred.

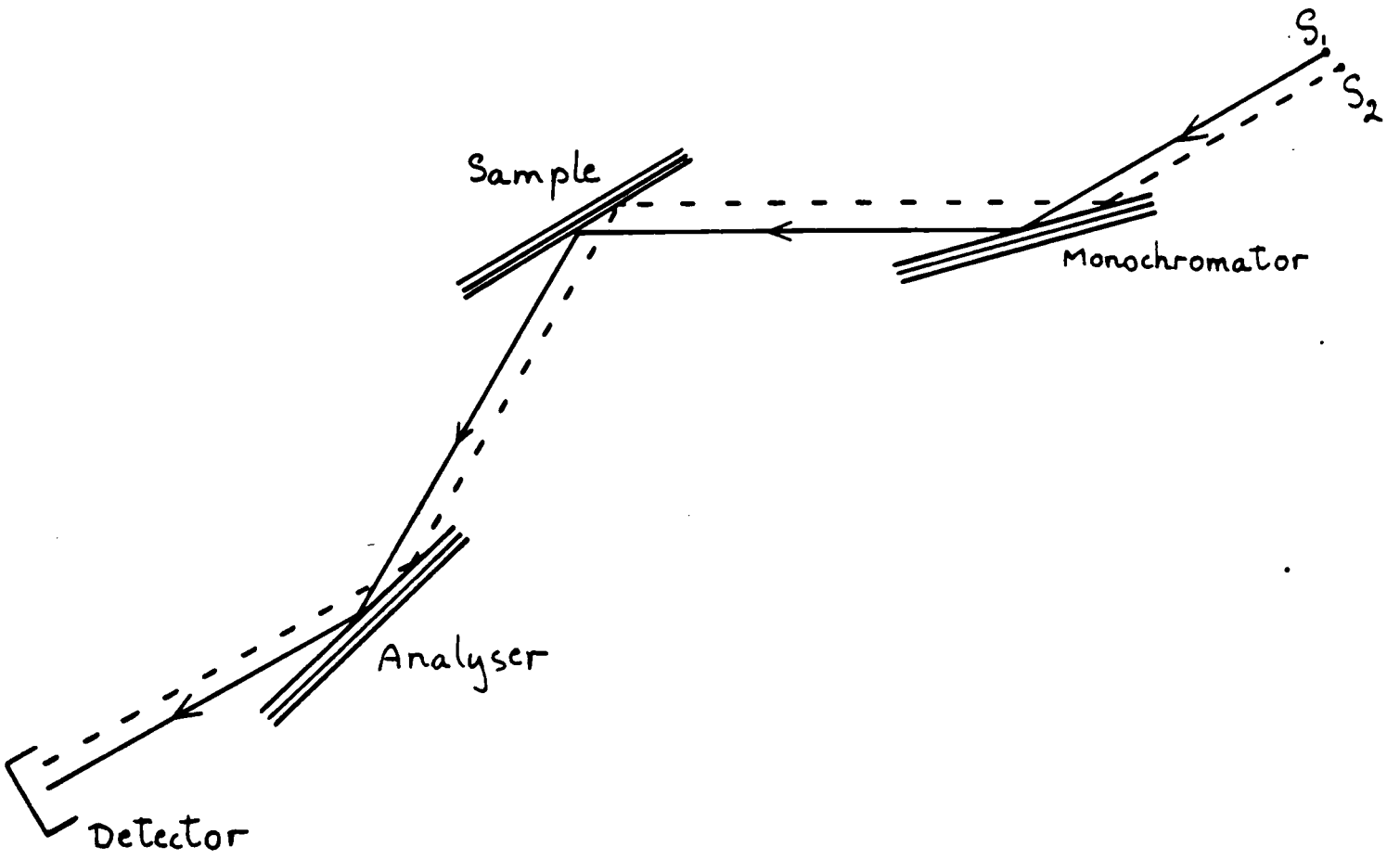

Figure 4.3 - As figure 4.1 but with the single source replaced by a double source, at S_1 and S_2. X-rays from both sources pass through the instrument identically.

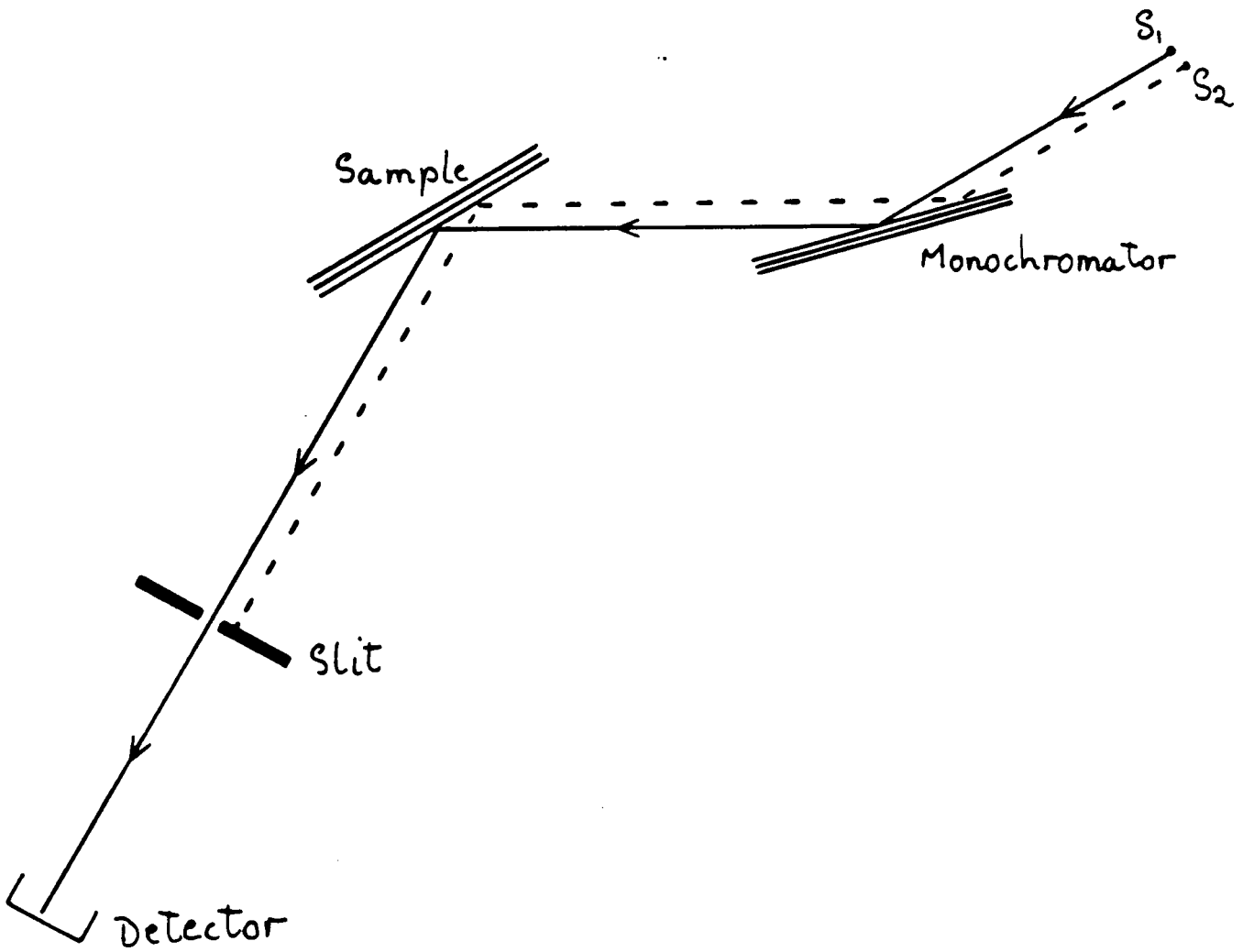

Figure 4.4 - As figure 4.3 but the analyser crystal has been replaced by a simple slit giving, nominally, the same **q** resolution. X-rays from source S_2 are obscured by the slit edge.

So far, we have considered the instrument in only two-dimensions and have ignored the vertical divergence of the x-ray beam. In practice, it is usual to limit this divergence to $\sim 0.5°$ by the use of a simple slit before the sample.

At this point, we should consider the essential difference between a two-crystal spectrometer (in other words a conventional diffractometer as described by Mathieson, Schoenborn or Reid) and the three-crystal spectrometer. Figure(4.3) is essentially the same as Figure(4.1) but shows the point source of Figure(4.1) replaced by two point sources, S_1 and S_2. The full and dashed lines represent beam paths through the instrument for rays from S_1 and S_2 respectively. Fig (4.4) shows the same instrument with the analyser crystal replaced by a simple slit - subtending an angle $\Delta\Theta_a$ at the centre of the instrument and thus with nominally the same resolution in Φ as the analyser crystal.

The rays from S_1 and S_2 pass through the triple-crystal instrument identically but, in the two-crystal instrument the ray from S_2 is obscured by one edge of the slit.

The essential feature of the triple-crystal spectrometer is that it is sensitive only to the *direction* and *energy* of the scattered x-ray beam. In other words the instrument probes *wavevector* space. The two-crystal instrument, however, is also sensitive to the *position* of the scattered beam and the resolution of the instrument depends upon a complex interplay of wavevector space (or reciprocal space) effects and direct space effects. These direct space effects - finite source size and intensity distribution within the source, x-ray beam penetration within the monochromator and sample crystals, sample size and shape effects and beam path lengths - simply vanish with the adoption of an analyser crystal.

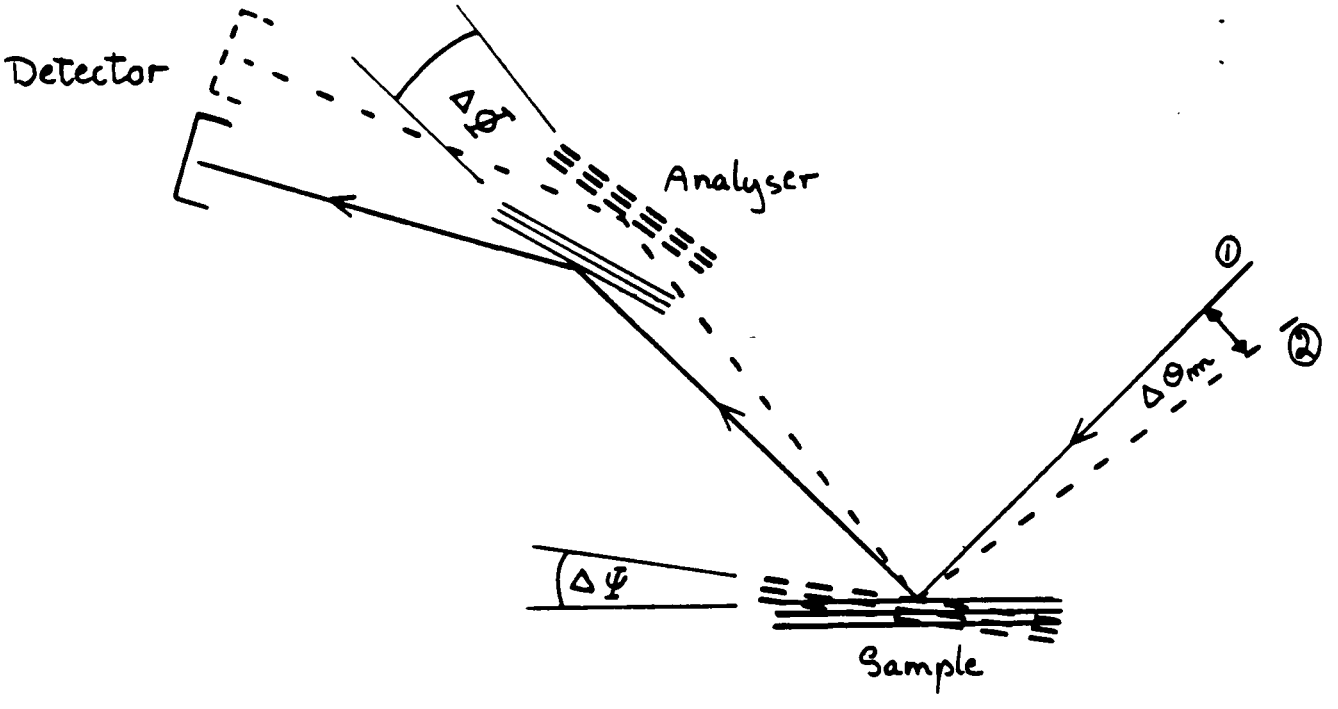

Figure 4.5 - The effect of $\Delta\Theta_m$. Both Ψ and Φ must rotate through $\Delta\Theta_m{}^\circ$ to pass the range of wave-vectors contained in the incident beam.

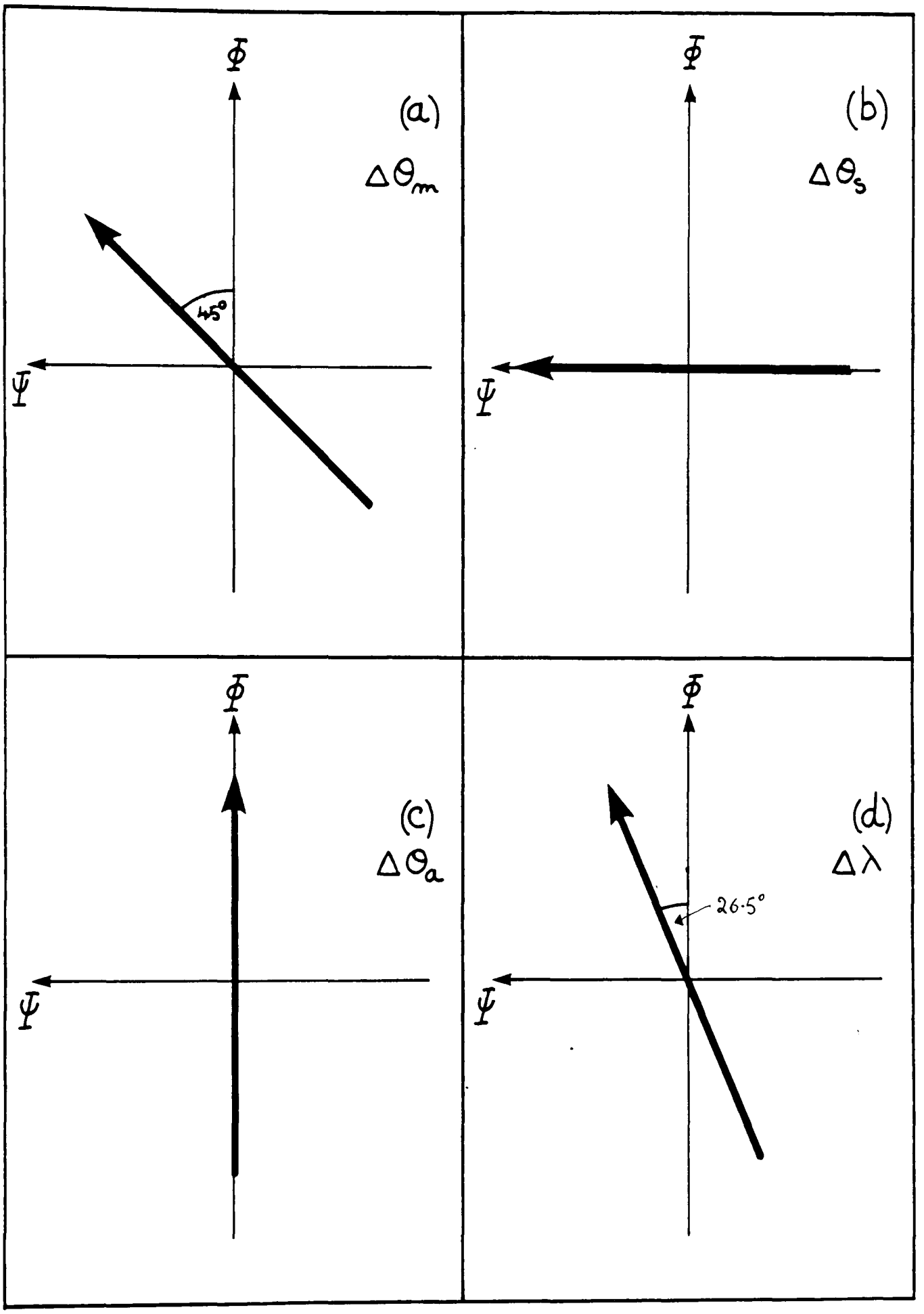

Figure 4.6 - The loci of the main resolution degrading effects in ΨΦ space.

2.2) THE RESOLUTION

We have now identified the resolution degrading effects of a triple-crystal x-ray spectrometer to be

- $\Delta\Theta_m$, the angular spread of any single wavelength component of the incident beam.
- $\Delta\lambda$, the wavelength spread of the incident beam.
- $\Delta\Theta_s$, the angular range through which the sample crystal can satisfy the Bragg condition.
- $\Delta\Theta_a$, the angular range through which the analyser crystal can satisfy the Bragg condition.
- $\Delta\Theta_v$, the vertical divergence of the x-ray beam which is defined by a simple slit to be $\sim 0.5^\circ$ and which we shall now ignore.

and we will now proceed to examine the loci of each of the above effects in instrument space (as a function of the setting angles Ψ and Φ) and in reciprocal space.

2.2.1) $\Delta\Theta_m$, $\Delta\Theta_s$ and $\Delta\Theta_a$.

The loci of $\Delta\Theta_m$, $\Delta\Theta_s$ (for a mosaic crystal) and $\Delta\Theta_a$ are intuitively obvious. Fig (4.5) illustrates the effect of $\Delta\Theta_m$. The source is presumed to be perfectly monochromatic and both sample and analyser are assumed to be perfect. Clearly, to satisfy the Bragg condition for beams 1 and 2 both Ψ (the sample) and Φ (the analyser) must rotate through $\Delta\Theta_m{}^\circ$. Therefore $\Delta\Psi=\Delta\Phi$ and the locus of $\Delta\Theta_m$ in Ψ/Φ space is a straight line with gradient 1. Figure(4.6a).

$\Delta\Theta_s$, for a mosaic crystal, reflects a range of orientations of the mosaic blocks comprising the crystal and a corresponding uncertainty in the direction of the scattering vector. Thus, for a perfectly monochromatic and perfectly collimated incident beam, the crystal can satisfy the Bragg condition as it is rotated through a range of setting angles, $\Delta\Psi$, whilst the angle Φ is constant and well defined. Fig (4.6b) shows the locus of $\Delta\Theta_s$ in Ψ/Φ space.

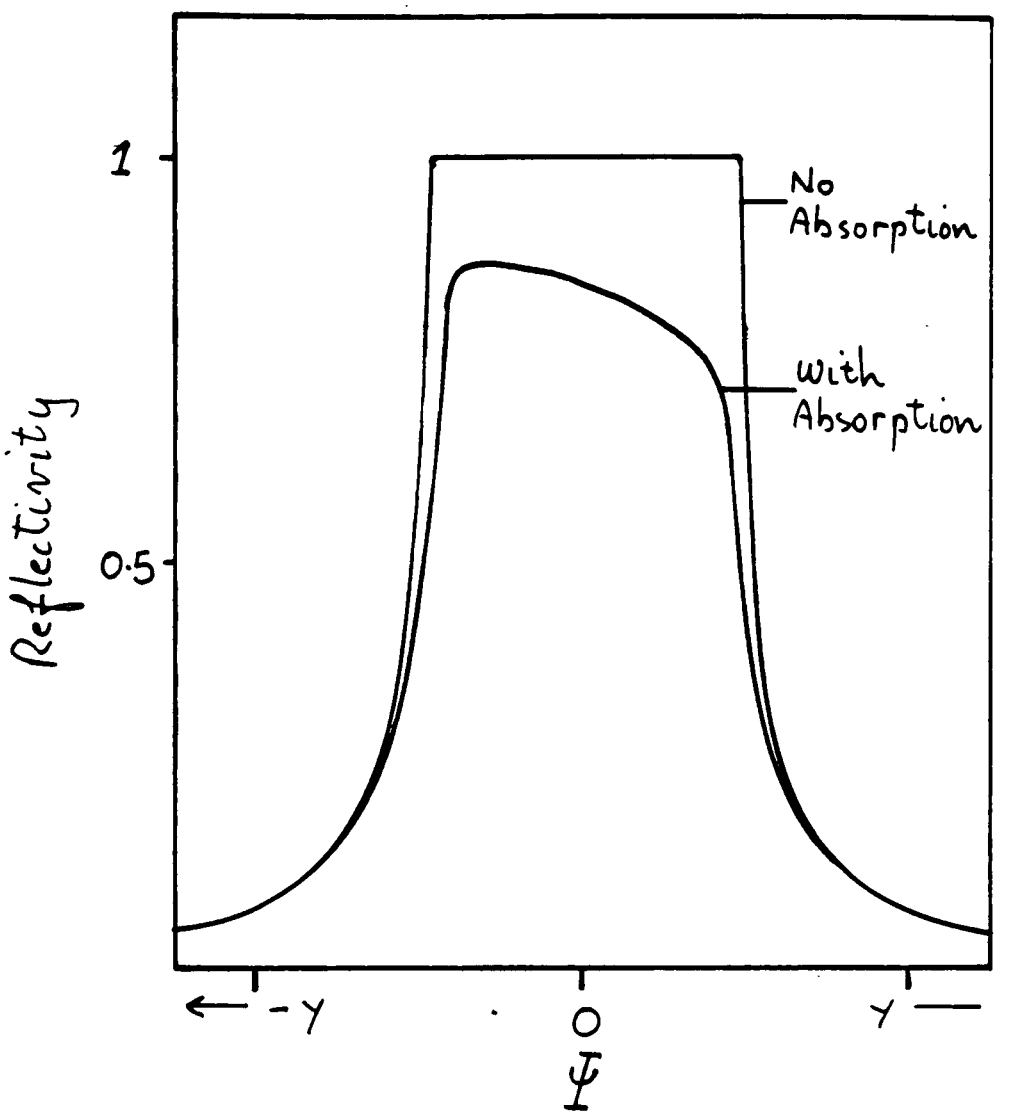

Figure 4.7 – The theoretical 'Darwin' profile for diffraction from a perfect crystal. The range of total reflectivity is, typically, a few seconds of arc and is related to F_{hkl}, the structure factor.

$\Delta\Theta_a$ simply defines the acceptance angle of the detector system and its locus is, therefore, directed along Φ, as shown in Figure(4.6,c).

The loci of $\Delta\Theta_s$, in the case of diffraction by a highly perfect crystal, and of $\Delta\lambda$ require more careful consideration.

2.2.2) $\Delta\Theta_s$ FOR A PERFECT CRYSTAL.

If the sample crystal is highly perfect and $\Delta\Theta_m$, $\Delta\Theta_a$ and $\Delta\lambda$ are arranged to be negligibly small we must consider resolution effects which either do not exist or are too tiny to be of consequence in the case of scattering by a mosaic crystal. At the root of these effects are refraction of the incident and diffracted x-ray beams as they pass through the air (or vacuum) to crystal interface, extinction of the incident beam within the crystal and the abrupt termination of the crystal lattice at the surface of the crystal. Dynamical scattering theory, as described at length by James(1949), Zacharaisen(1945), and Cowley(1981), describes x-ray scattering by a perfect crystal and incorporates the above effects. The treatment is complex and the physical meaning often hard to grasp but the essential result is encapsulated in the well known 'Darwin curve' or reflection curve for a perfect crystal without absorbtion. Figure(4.7).

A relatively simple conceptual model can be constructed which serves to bring out the essential physics of x-ray scattering from a perfect crystal.

An x-ray beam, assumed to be perfectly monochromatic and perfectly collimated, is incident upon an extended face of a perfect sample crystal. The crystal is of infinite extent in the plane of the surface and of infinite depth below the surface. The refractive index of solids for x-rays wavelengths is less than 1 by a few parts in 10^6 and so the incident beam is refracted to a slightly shallower angle of incidence as it enters the crystal. This has the effect of displacing the apparent Bragg angle from the true Bragg angle by a few thousandths of a degree. At incidince angles far from the Bragg angle the x-ray beam suffers reflection from each of the lattice planes it traverses as it passes through the crystal but the reflected beams interfere destructively and no energy is transferred to a diffracted beam. The penetration depth of the incident beam within the crystal is limited by photoelectric absorbtion and may be,

typically, 10's to 100's of microns.

If the incidence angle satisfies the Bragg condition then the reflected waves interfere constructively and energy is transferred to a diffracted beam which then emerges from the crystal, suffering further refraction as it passes through the surface. The intensity of the incident beam is depleted by the transfer of energy to the diffracted beam as a function of the number of lattice planes traversed and so the penetration depth is reduced dramatically. This is the phenomenon of Primary Extinction. Under these conditions the penetration depth is inversely related to the reflectivity of the lattice planes or, more precisely, to $|F|$, the structure factor. For a strong reflection, the beam may be reduced to half of its original intensity after traversing only a few thousand lattice planes, corresponding to a penetration depth of several thousand Å. A weak reflection, however, may only reduce the intensity by half after many tens of thousands of lattice planes. (James 1948 pp 60-62)

The shape of the crystal volume sampled in the diffraction experiment is, therefore, defined by two effectively infinite lengths within the plane of the surface and, perpendicular to the surface by the abrupt discontinuity of the surface and an exponential decay of the intensity of the extinguished beam within the crystal.

In reciprocal space (or Fourier transform space) the diffraction maxima are described by δ functions in the directions parallel to the plane of the crystal surface. Perpendicular to the surface, however, the widths of the diffraction maxima are inversely related to the penetration depth (and so directly related to $|F|$, the structure factor). Furthermore, extensive tails perpendicular to the crystal surface arise from the Fourier transform of the step function in the electron density at the crystal surface .

The important point to emerge from this qualitative discussion is that the scattering in reciprocal space is resolution limited in the plane of the crystal surface but is extended in a direction normal to the surface. As discussed by Andrews and Cowley (1986) and separately by Robinson (1986) this so called 'surface streak' or 'crystal truncation rod' contains important information on the topography of the crystal surface or, more correctly, on how abruptly the crystal lattice terminates at the crystal surface.

The locus of the surface streak is well defined in reciprocal space but less well defined in Ψ/Φ space, depending as it does on the geometrical

relationship between the scattering vector and the crystal surface.

2.2.3) $\Delta\lambda$ (OR SPECTRAL DISPERSION.)

Unlike $\Delta\Theta_m$, $\Delta\Theta_s$, and $\Delta\Theta_a$ the locus of spectral dispersion, $\Delta\lambda$, in a triple-crystal x-ray spectrometer with $\Theta_m \neq \Theta_s \neq \Theta_a$ is not intuitively obvious and must be calculated.

Diffraction of x-rays from a crystal lattice is described by Bragg's law

$$\lambda = 2d \sin\Theta$$

by differentiation

$$d\lambda = 2d \cos\Theta \, d\Theta$$

and

$$\frac{d\lambda}{\lambda} = \cot\Theta \, d\Theta$$

and the dispersion introduced by the first crystal is

$$d\Theta_1 = \frac{d\lambda}{\lambda}\tan\Theta_1$$

$d\Theta_2$, the angle through which the second crystal must be rotated to diffract the full range of $\Delta\lambda$ passed by the first crystal is the sum of the dispersion introduced by the first and the second crystals

$$d\Theta_2 = \frac{d\lambda}{\lambda}(\tan\Theta_1 - \tan\Theta_2)$$

the negative sign is a consequence of the sense of scattering at the second crystal in the (+M,-S,+A) configuration.

Similarly, $d\Theta_3$, the angle through which the third crystal must rotate to diffract the full range of $\Delta\lambda$ passed by the first and second crystals is the sum of the dispersion, $d\Theta_2$, introduced by the first two crystals and the dispersion introduced by the third crystal

$$d\Theta_3 = d\Theta_2 + (-\frac{d\lambda}{\lambda}\tan\Theta_2 + \frac{d\lambda}{\lambda}\tan\Theta_3) = \frac{d\lambda}{\lambda}(\tan\Theta_1 - 2\tan\Theta_2 + \tan\Theta_3)$$

In terms of the setting angles Ψ and Φ

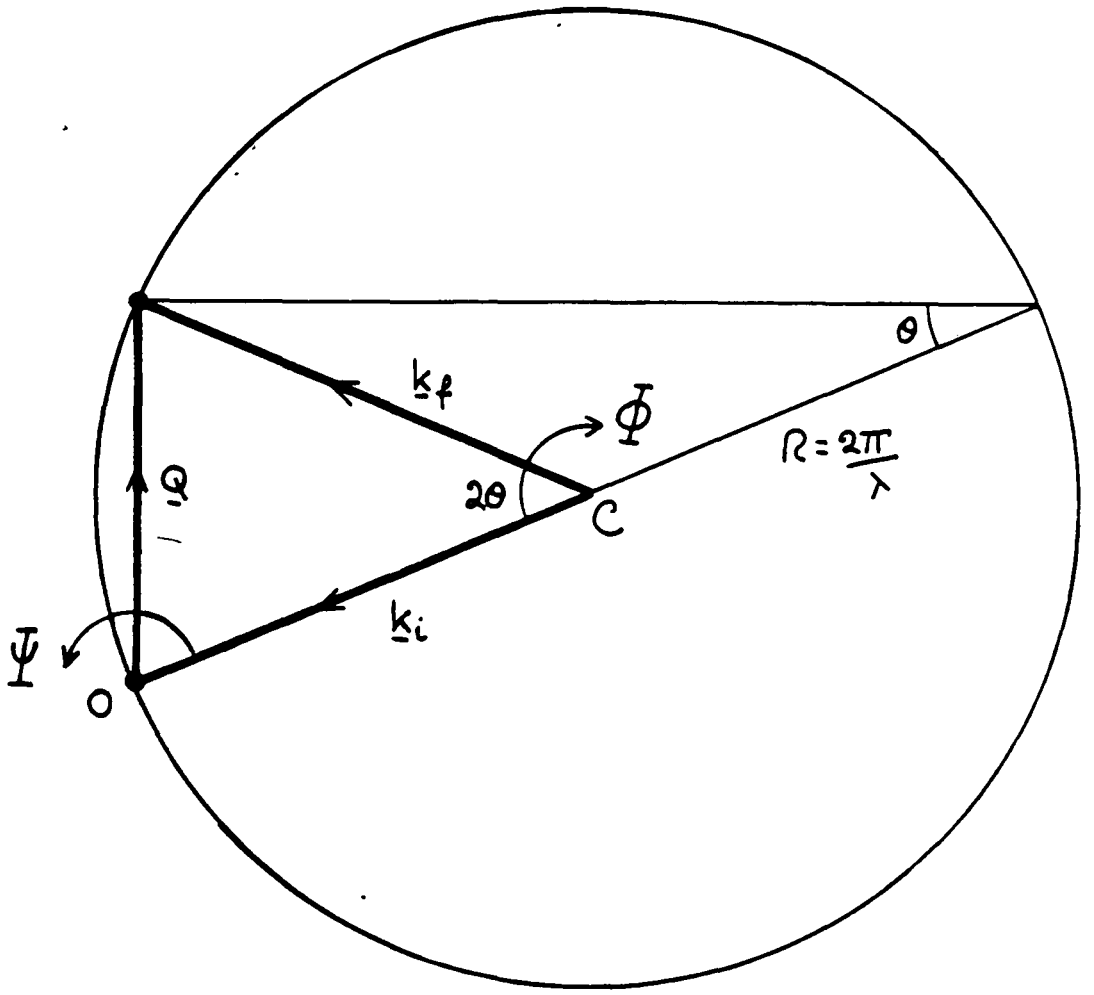

Figure 4.8 – The exact Bragg condition, illustrated by the Ewald sphere construction. $\mathbf{k}_i$ and $\mathbf{k}_f$ are the incident and scattered wave-vectors and are of length $2\pi/\lambda$. $\mathbf{Q}$ is the scattering vector and is of length $2\pi/d$, where d is the appropriate lattice spacing. The directions of positive rotation for Ψ and Φ are indicated.

$$d\Theta_2 = \frac{d\lambda}{\lambda}(\tan\Theta_1 - \tan\Theta_2) = d\Psi$$

$$d\Theta_3 = \frac{d\lambda}{\lambda}(\tan\Theta_1 - 2\tan\Theta_2 + \tan\Theta_3) = d\Phi$$

These relationships define the locus of $\Delta\lambda$ in Ψ/Φ space for any triple-crystal spectrometer configuration. In practice, the most commonly used spectrometer configuration is the (+1,-S,+1) configuration, or $\Theta_m = \Theta_a$.

This introduces an important simplification into the dispersion relationships, namely

$$d\Psi = \frac{d\lambda}{\lambda}(\tan\Theta_1 - \tan\Theta_2)$$

$$d\Phi = 2\frac{d\lambda}{\lambda}(\tan\Theta_1 - \tan\Theta_2) = 2d\Psi$$

Thus, the locus of $\Delta\lambda$ in Ψ/Φ space is constant for any Θ_s and is described by the ratio

$$d\Psi : d\Phi = 1:2$$

and on the Ψ/Φ diagram the locus of $\Delta\lambda$ is a straight line inclined at [illegible] to the Φ axis. Figure(4.6d).

In the situation $\Theta_m = \Theta_s = \Theta_a$; $\tan\Theta_1 = \tan\Theta_2$ and the magnitudes of both $d\Psi$ and $d\Phi$ reduce to zero. In other words, the spectral dispersion vanishes. This spectrometer configuration is known as the (+1,-1,+1), or focussing, configuration and, for obvious reasons (the total elimination of one of the most serious resolution degrading elements) it is very widely used.

2.3) TO TRANSFORM FROM Ψ/Φ SPACE TO RECIPROCAL SPACE.

Having established the loci of each of the resolution degrading effects in diffractometer, or Ψ/Φ space we must now consider the relationship between Ψ/Φ space and reciprocal space.

Figure(4.8), using the Ewald construction, shows a reciprocal space representation of the exact Bragg condition. $\mathbf{k}_i$ and $\mathbf{k}_f$ represent, respectively, the incident and scattered wavevectors and are of length $\frac{2\pi}{\lambda}$, where λ is the wavelength of the incident beam, and the scattering is elastic. $\mathbf{Q}$ is a reciprocal lattice vector and is of length $\frac{2\pi}{d}$, where d is the appropriate direct lattice

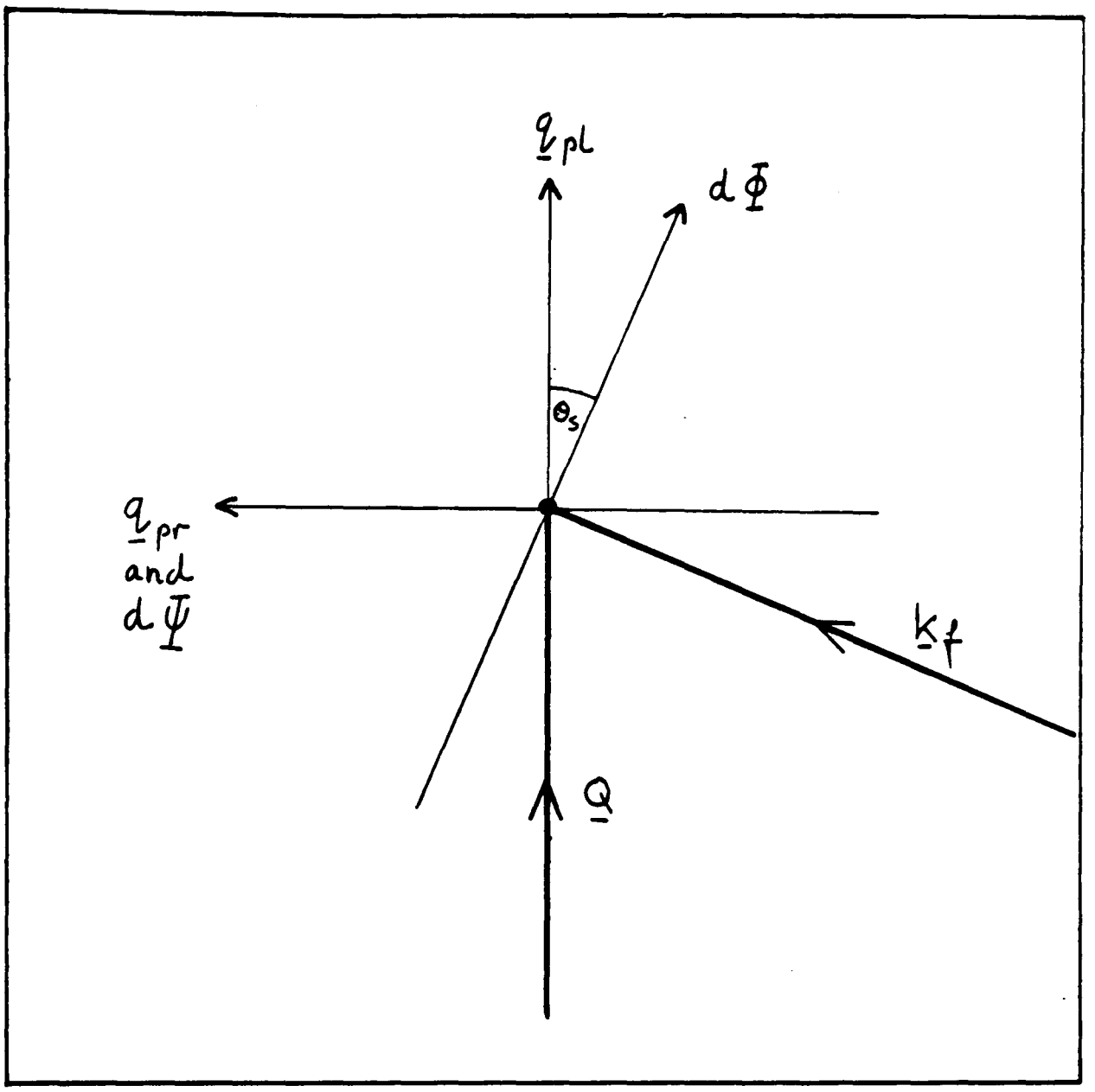

Figure 4.9 - The relationship between the oblique axes of $\Psi\Phi$ space and the rectangular reciprocal space axes with unit vectors $\mathbf{q}_{pl}$ and $\mathbf{q}_{pr}$.

spacing. The Bragg condition is satisfied when a reciprocal lattice point lies on the surface of the Ewald sphere and

$$\mathbf{k}_f = \mathbf{k}_i + \mathbf{Q}$$

A conventional, equatorial plane, x-ray diffractometer (and this includes the triple-crystal x-ray spectrometer) has two variable setting angles

- Ψ (or ω) the crystal setting angle
- Φ (or 2Θ) the detector setting angle

The incident x-ray beam illuminates the volume of reciprocal space defined by the surface of the Ewald sphere (which can be regarded as having a finite thickness governed by the wave-vector spread of the incident beam and the sample crystal mosaic). A Ψ increment rotates the Ewald sphere around the origin of reciprocal space. The Bragg condition is satisfied when a reciprocal lattice point lies on the surface of the Ewald sphere.

The detector aperture (or analyser $\Delta\Theta_a$) defines an acceptance angle for the scattered beam and, together with the above factors which determine the thickness of the Ewald sphere, this determines the volume of reciprocal space sampled in an experiment. In other words, the instrumental resolution. A Φ increment moves the resolution element along the surface of the Ewald sphere.

If the angular increments in Ψ and Φ are small, the directions of $d\Psi$ and $d\Phi$ are approximately tangential to the circles centred on points O and C respectively in Figure(4.8). To transform from Ψ/Φ space to reciprocal space we must relate the oblique axes with unit vectors of length $d\Psi$ and $d\Phi$ to the rectangular reciprocal space axes, $\mathbf{q}_{pl}$ and $\mathbf{q}_{pr}$ with unit vectors of length q_{pl} and q_{pr} which are, respectively, parallel and perpendicular to the scattering vector $\mathbf{Q}$ Figure(4.9).

In the tangential approximation, the directions of $\mathbf{d\Psi}$ and q_{pr} are coincident. The magnitude of $\mathbf{d\Psi}$, in reciprocal space, is related to the length of $\mathbf{Q}$ and, therefore, Θ_s. (See Figure(4.8)). and

$$d\Psi = 2\sin\Theta_s\, q_{pr}$$

$\mathbf{d\Phi}$ is inclined at an angle Θ_s to $\mathbf{q}_{pl}$ and, therefore, has components in both $\mathbf{q}_{pl}$ and $\mathbf{q}_{pr}$

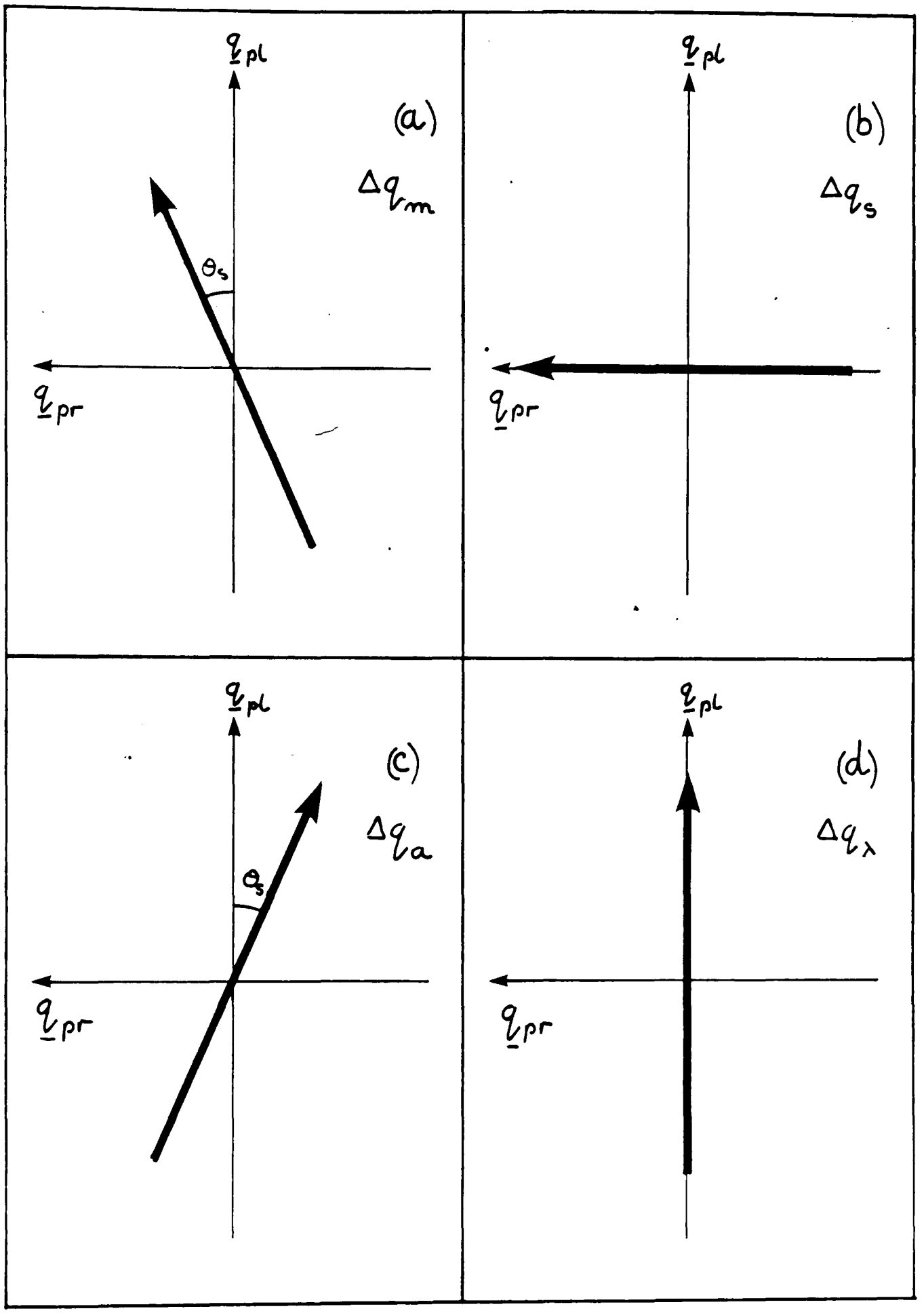

Figure 4.10 – The loci of the main resolution degrading effects in reciprocal space.

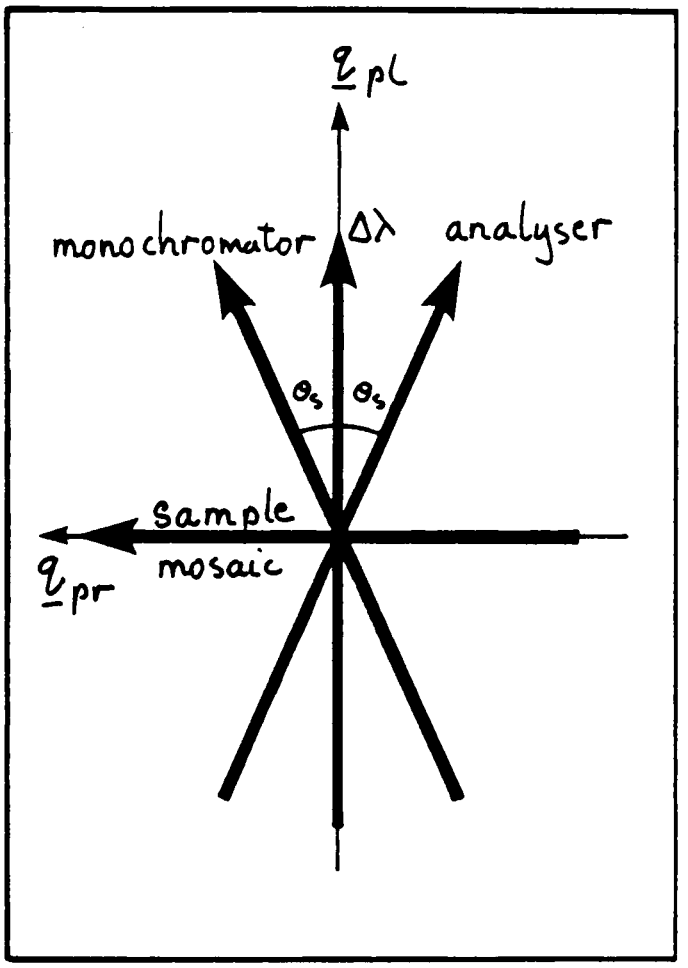

Figure 4.11 - A combined picture of the loci of each of the resolution degrading effects. This 'star(?)' shape is characteristic of the triple-crystal x-ray spectrometer.

$$d\Phi = \cos\Theta_s\, q_{pr} - \sin\Theta_s\, q_{pl}$$

or

$$d\Psi = 2\sin\Theta_s\, q_{pr}$$

$$d\Phi = -\sin\Theta_s \cos\Theta_s\, q_{pl}$$

We can now see that the locus of spectral dispersion in Ψ/Φ space of the triple-crystal spectrometer in the symmetric (+1,-S,+1) configuration,

$$d\Psi + 2d\Phi$$

transforms to

$$2\sin\Theta_s(q_{pr}) + 2(-\sin\Theta_s(q_{pr}) + \cos\Theta_s(q_{pl}))$$

or

$$2\cos\Theta_s(q_{pl})$$

In other words, it is directed along q_{pl} and is therefore radial in reciprocal space.

The locus of $\Delta\Theta_m$, the incident beam divergence, in Ψ/Φ space is

$$d\Psi + d\Phi$$

and this transforms to

$$2\sin\Theta_s(q_{pr}) - \sin\Theta_s(q_{pr}) + \cos\Theta_s(q_{pl})$$

or

$$\sin\Theta_s(q_{pr}) + \cos\Theta_s(q_{pl})$$

which is a straight line inclined at an angle Θ_s to q_{pl}.

Figure(4.10a to d) shows the reciprocal space representation of each of the resolution degrading effects. Figure(4.11) combines the above results to give a general picture of the loci of the instrumental resolution effects in a (+1,-S,+1) triple-crystal x-ray spectrometer. As we shall see in the following section (3), the resolution 'star' of Figure(4.11) is a characteristic feature of this instrument.

It is now a matter of straightforward geometry, given the appropriate instrumental parameters, to calculate the magnitudes of each of the resolution effects in reciprocal space.

These are (in reciprocal Ångstroms)

- $dq_m = \frac{2\pi}{\lambda}\sin\Delta\Theta_m$
- $dq_a = \frac{2\pi}{\lambda}\sin\Delta\Theta_a$
- $dq_s = \frac{4\pi}{\lambda}\sin\Theta_s \sin\Delta\Theta_s$
- $dq_\lambda = \frac{2\pi}{\lambda}\cos\Theta_s \sin(\frac{2\Delta\lambda}{\lambda}(\tan\Theta_m - \tan\Theta_s)$

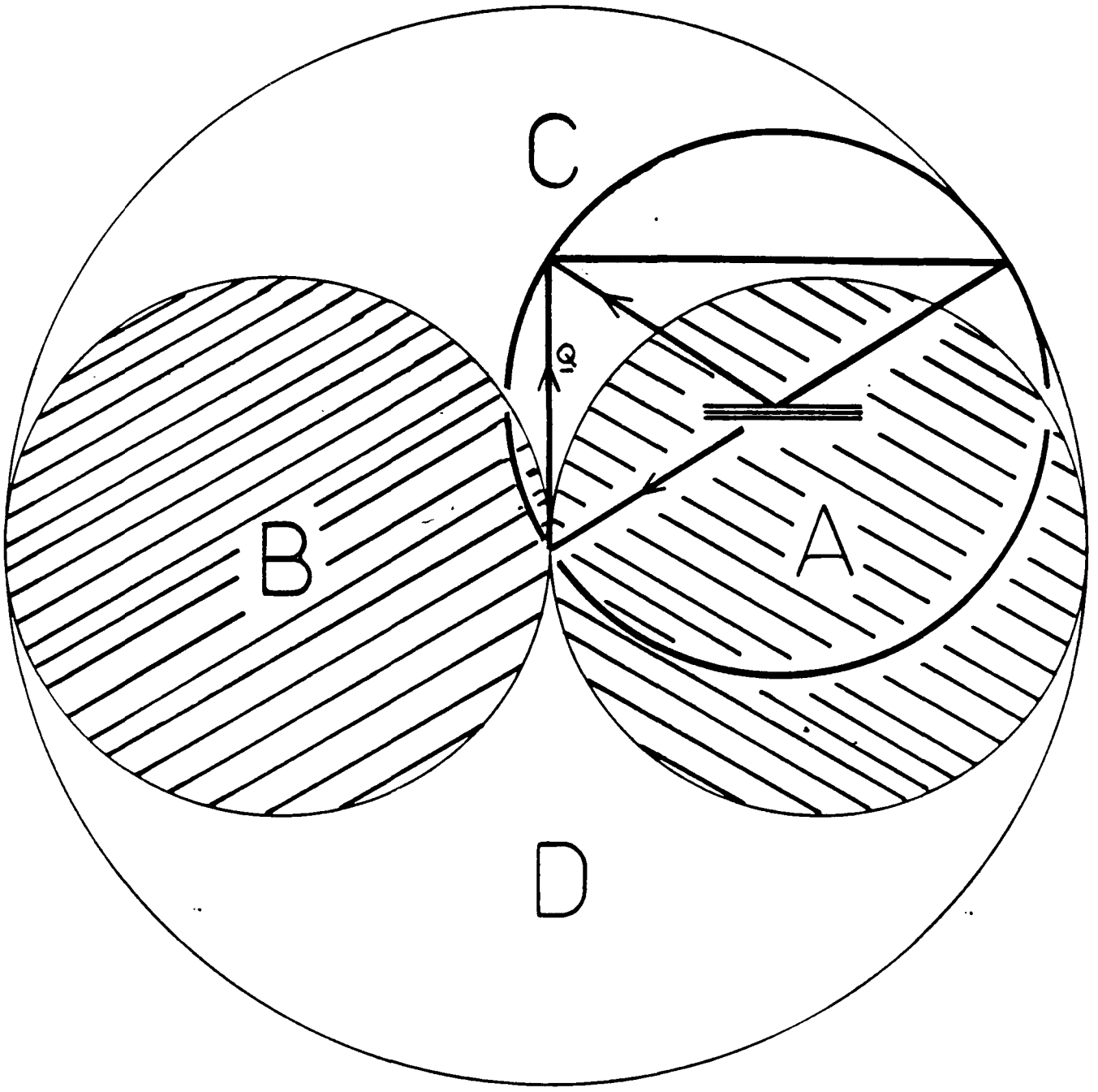

Figure 4.12 - An Ewald sphere diagram illustrating the accessible and forbidden regions of reciprocal space in 'extended-face' scattering geometry. In region A, the incident beam is obscured by the crystal face, as is the diffracted beam in region B. Region D is accessible in (+1,+S,+1) scattering geometry and region C in the conventional (+1,-S,+1) geometry.

3) EXAMPLES

3.1) SCATTERING GEOMETRY AND THE ACCESSIBLE REGIONS OF RECIPROCAL SPACE.

Before examining real examples of the instrumental resolution we should consider the limitations imposed on the accessible regions of reciprocal space by scattering from an extended face and the geometrical relationship between the crystal face, the incident and diffracted beams and the reciprocal lattice.

X-ray diffraction measurements from an extended sample crystal can be carried out in reflection geometry (Bragg case), in which the incident and diffracted beams enter and exit through the same crystal face, or transmission geometry (Laue case), in which the diffracted beam exits through the opposite face of a thin crystal plate. All of the measurements described in this work were carried out in reflection geometry. The adoption of this geometry maximises the available signal in a diffraction experiment as the effect of absorbtion can be minimised. It results, however, in a serious restriction on the accessible region of reciprocal space.

Figure(4.12), based on the familiar Ewald construction, illustrates tha accessible (Bragg) and forbidden (Laue) regions. In region A the incident beam is obscured by the crystal face, as is the diffracted beam in region B. Region C is the Bragg geometry region described by the spectrometer configuration (+M,-S,+A) whilst region D is the Bragg geometry region described by the configuration (+M,+S,+A). The figure also shows the orientation of the crystal face and Ewald sphere when the diffraction condition is satisfied for a reciprocal lattice vector, $\mathbf{Q}$.

3.2) EXAMPLE 1. LOW RESOLUTION: PYROLYTIC GRAPHITE MONOCHROMATOR AND ANALYSER CRYSTALS, SILICON SAMPLE CRYSTAL.

The set of measurements presented here illustrate the resolution of the instrument in its low-resolution mode. The pyrolytic graphite monochromator

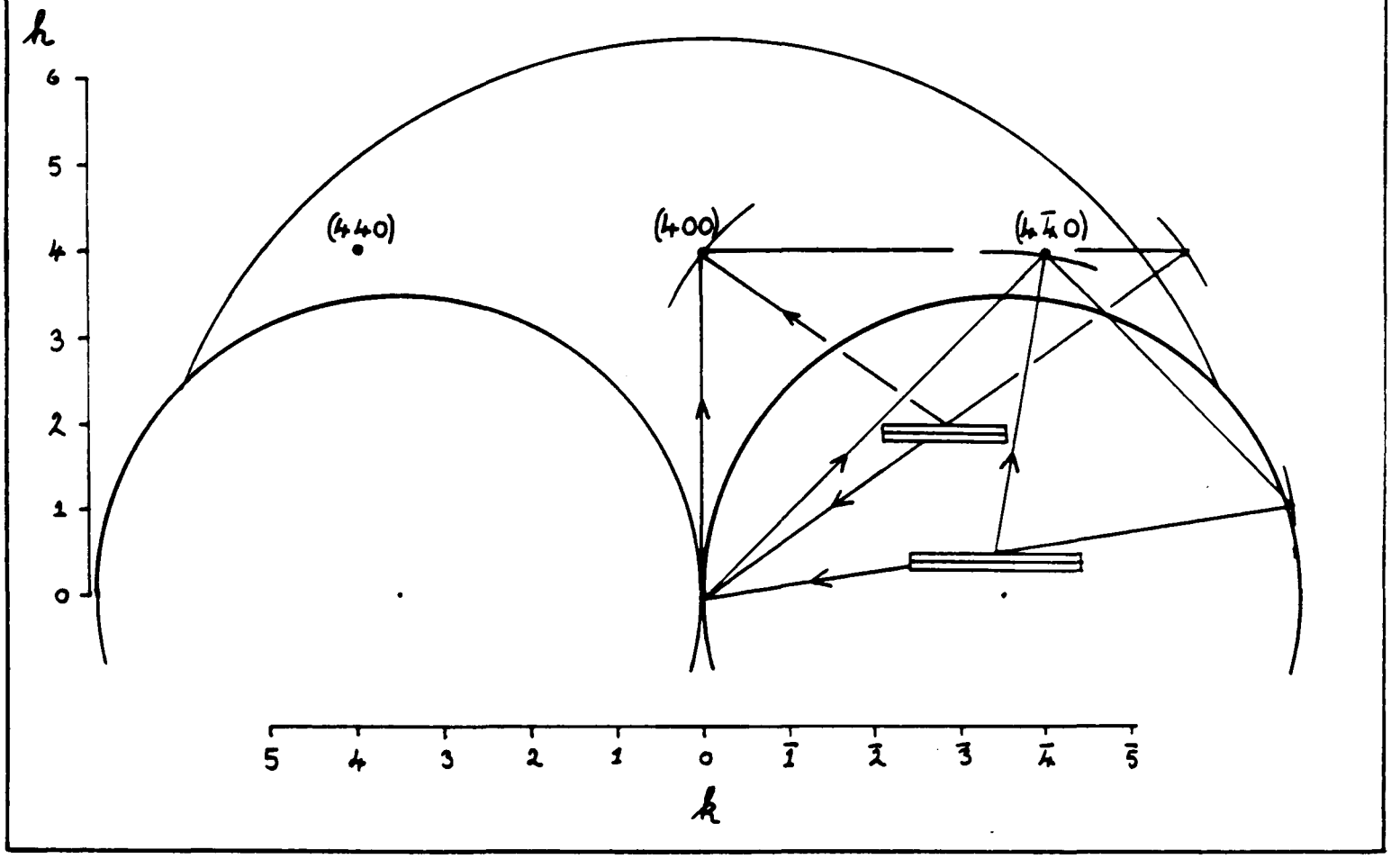

Figure 4.13 - Low resolution, Si sample, graphite monochromator and analyser. The accessible region of reciprocal space and the scattering geometry at two Bragg reflections, (400) and (4-40).

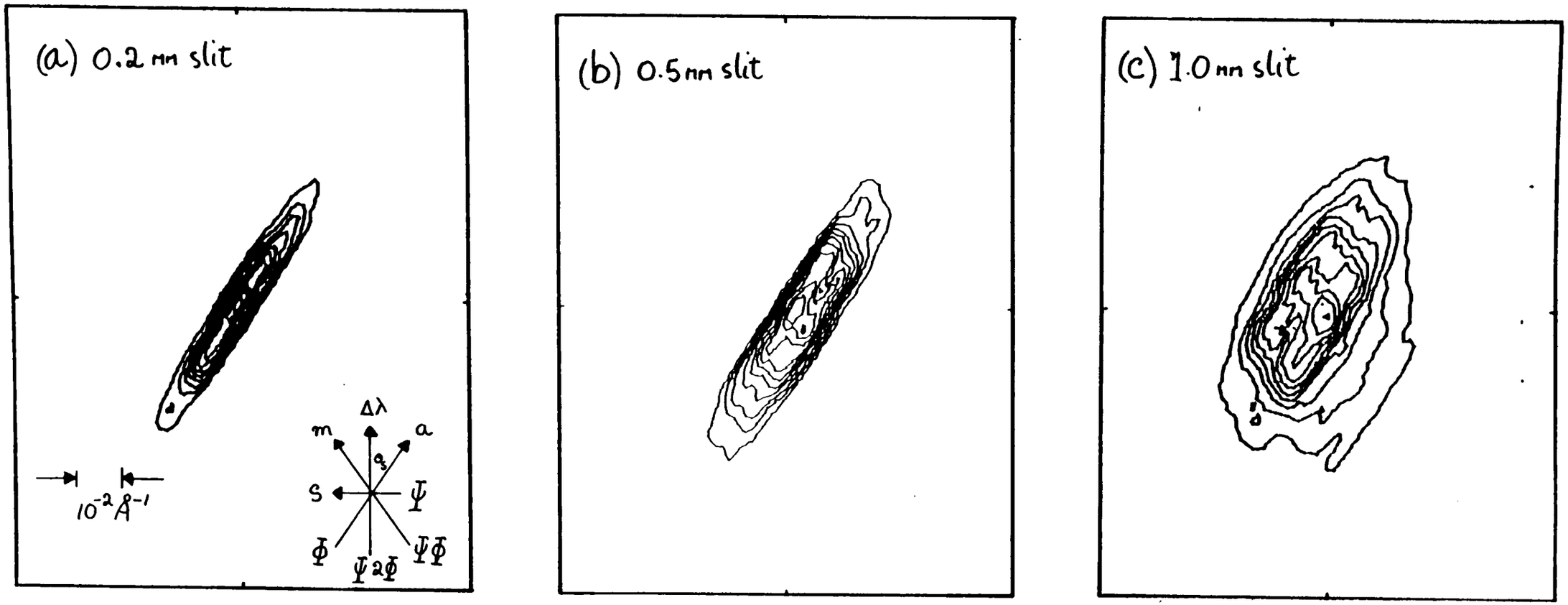

Figure 4.14 - Si(400). The instrumental resolution. Graphite monochromator and analyser. CuKα_1. θ_s = 34.5°. (a) 0.2mm pre-monochromator slit, $\Delta\theta_m$ = 0.06°. (b) 0.5mm slit, $\Delta\theta_m$ = 0.16°. (c) 1.0mm slit, $\Delta\theta_m$ = 0.32°.

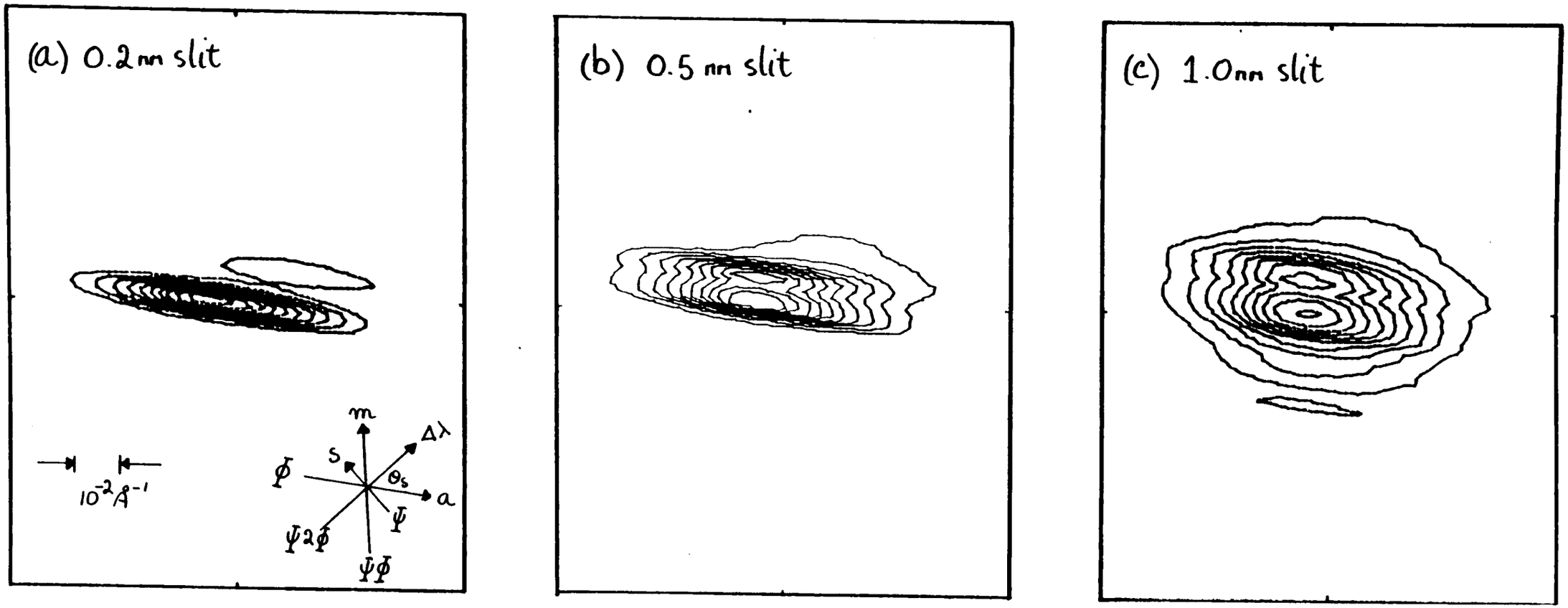

Figure 4.15 – Si(4–40). As figure 4.14 but $\theta_s = 53°$.

TABLE 4.1

Theta(s)	dq(m)	dq(s)	dq(a)	dq(lambda)
2°	0.01138	0.00001	0.02846	0.00067
4°	"	0.00002	"	0.00051
6°	"	0.00003	"	0.00040
8°	"	0.00004	"	0.00029
10°	"	0.00005	"	0.00018
12°	"	0.00006	"	0.00007
14°	"	0.00007	"	0.00004
16°	"	0.00008	"	0.00015
18°	"	0.00009	"	0.00026
20°	"	0.00010	"	0.00037
22°	"	0.00011	"	0.00048
24°	"	0.00012	"	0.00059
26°	"	0.00012	"	0.00069
28°	"	0.00013	"	0.00080
30°	"	0.00014	"	0.00091
32°	"	0.00015	"	0.00101
34°	"	0.00016	"	0.00111
36°	"	0.00017	"	0.00122
38°	"	0.00018	"	0.00132
40°	"	0.00018	"	0.00142
42°	"	0.00019	"	0.00151
44°	"	0.00020	"	0.00161
46°	"	0.00020	"	0.00170
48°	"	0.00021	"	0.00180
50°	"	0.00022	"	0.00189
52°	"	0.00022	"	0.00197
54°	"	0.00023	"	0.00206
56°	"	0.00024	"	0.00214
58°	"	0.00024	"	0.00222
60°	"	0.00025	"	0.00230

Table 4.1 - Resolution widths (fwhh) in reciprocal Ångstroms for a triple-crystal spectrometer operating in the low-resolution mode. CuKα source, pyrolytic graphite monochromator and analyser, 0.5mm pre-monochromator slit, Silicon sample crystal.

and analyser crystals (Union Carbide UCAR grade ZYA) are completely disordered within the hexagonal basal plane but have a mosaic structure with a nominally Gaussian distribution of orientations around the hexagonal 'c' axis [0001]. The mosaic spread is quoted as 0.4(1)° FWHH. CuKα_1 x-rays were used and the focal spot of the rotating anode x-ray tube was a vertical line of height 3mm and width 0.3mm viewed at a take-off angle of 6°. A variable width slit was placed immediately in front of the monochromator crystal and this was used to limit the angular range of the x-ray beam incident upon the monochromator and thus provide control over the parameter $\Delta\Theta_m$.

Figure(4.13) shows the accesible region of reciprocal space and the scattering geometry at the two Bragg reflections investigated, Si(400) and Si(4-40) (Θ_s = 34.3° and 53° respectively). The iso-intensity contour plots of Figures(4.14) and (4.15) show the instrumental resolution at both Bragg reflections with

- (a) a 0.2mm pre-monochromator slit ($\Delta\Theta_m$=0.06°)
- (b) a 0.5mm pre-monochromator slit ($\Delta\Theta_m$=0.16°)
- (c) a 1.0mm pre-monochromator slit ($\Delta\Theta_m$=0.32°).

The resolution is, quite clearly, dominated by $\Delta\Theta_m$ and $\Delta\Theta_a$ and the effects of $\Delta\Theta_s$ and $\Delta\lambda$ are negligible. Note the double peaked distribution of $\Delta\Theta_m$. The 'nominally' Gaussian mosaic distribution of a pyrolytic graphite crystal is seldom perfectly Gaussian when examined carefully.

Table (4.1) shows the results of the calculated magnitudes of each of the resolution effects for a 0.5mm pre-monochromator slit. dq_s and dq_λ are, indeed, negligibly small but the calculated and measured values of dq_m and dq_a agree well.

3.3) EXAMPLE 2. HIGH RESOLUTION: SILICON (111) MONOCHROMATOR AND ANALYSER CRYSTALS, SILICON (111) SAMPLE CRYSTAL.

This is the special case (+1,-1,+1) configuration with three identical Si(111) crystals, often referred to as the focussing, or non-dispersive configuration. In this case dq_λ is reduced to zero. Figure(4.16) shows a contour

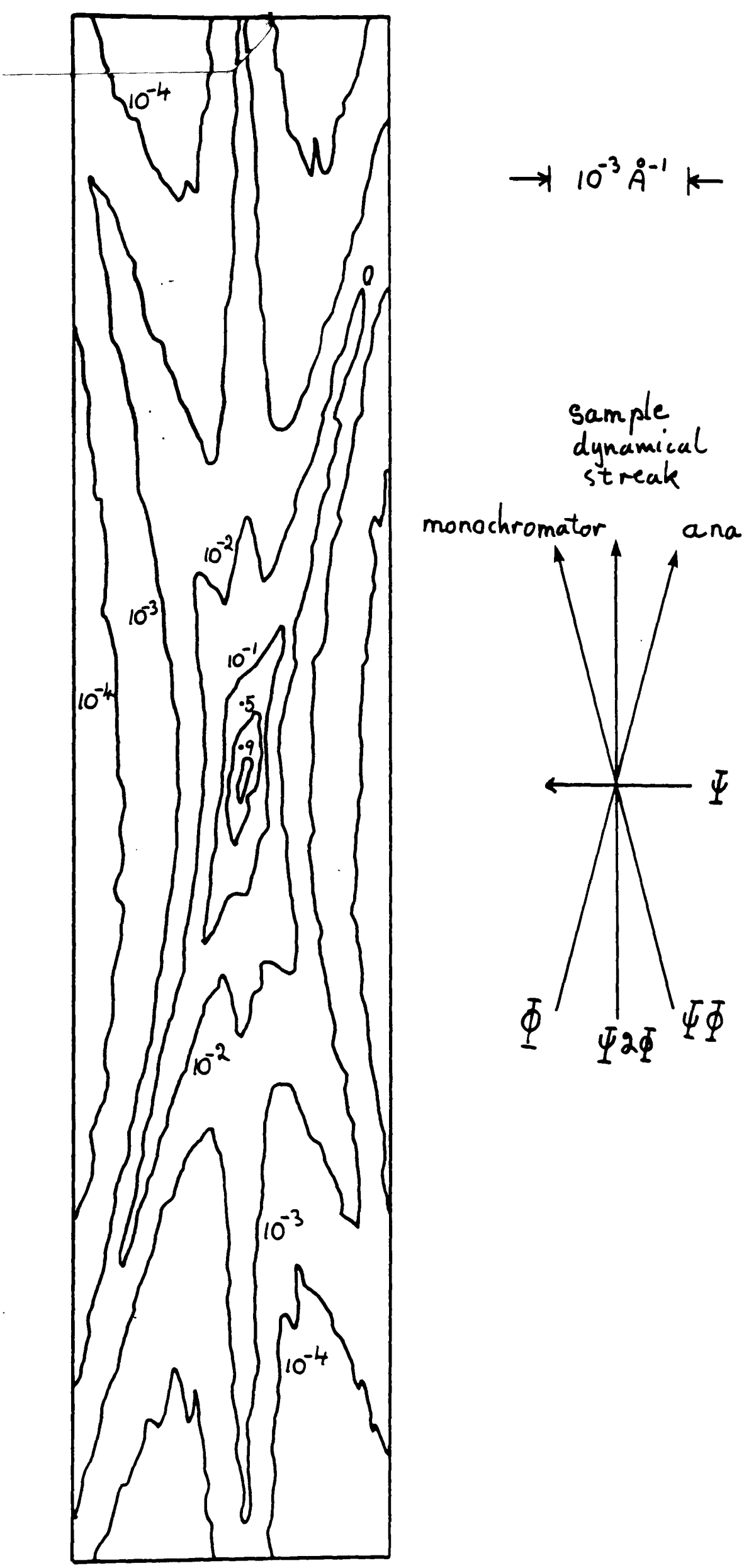

Figure 4.16 – Si(111) monochromator, sample and analyser crystals. The focussing (+1,−1,+1) configuration. CuKα_1, $\Theta_m = \Theta_s = \Theta_a = 14.22°$.

plot of the scattering in the region of the (111) reciprocal lattice point. The contour intervals on this plot are at 90%, 50%, 10%, 1%, 0.1%, and 0.01% of the maximum count and so cover a range of four orders of magnitude in intensity. The instrumental resolution itself is given by the 50% contour and is approximately

- 1.5×10^{-4}Å^{-1} FWHH (q_{pr})
- 5.0×10^{-4}Å^{-1} FWHH (q_{pl})

but these figures are somewhat unreliable as they are approaching the single step size (0.001°) of the Ψ and Φ axes. Of real interest in this figure is the characteristic 'star' shape with the three, well resolved streaks from the monochromator, sample and analyser. Note that, in this spectrometer configuration, the effect of $\Delta\lambda$ is completely eliminated and the scattering streak in the Ψ2Φ direction (q_{pl}) is entirely due to the sample dynamical scattering profile, including the 'surface streak' (Andrews and Cowley 1985). In the direction q_{pr}, the intensity drops off remarkably rapidly - reaching a value of 10^{-4} in less than 10^{-3}Å^{-1}. It is in this region of wave-vector space that it is, in principle, possible to measure critical scattering at very small **q**, corresponding to very large correlation lengths in direct space.

3.4) EXAMPLE 3. HIGH RESOLUTION, SILICON (111) MONOCHROMATOR AND ANALYSER, KH_2PO_4 - 123K TETRAGONAL TO ORTHORHOMBIC PHASE TRANSITION.

This example has been chosen, not only because it illustrates, very clearly, a number of important resolution effects, but it also demonstrates how a detailed knowledge of the instrumental resolution can be exploited to permit a quantitative measurement of diffuse scattering to be carried out at $q<<10^{-2}$Å^{-1}.

KH_2PO_4 (KDP) undergoes a well known structural phase transition from a tetragonal paraelectric phase to an orthorhombic ferroelectric phase on cooling through Tc=123K (Bacon and Pease 1955). In principle, the reduction in symmetry results in the formation of 4 ferroelectric domains within a bulk crystal but, if the crystal is dislocation free, packing considerations favour the

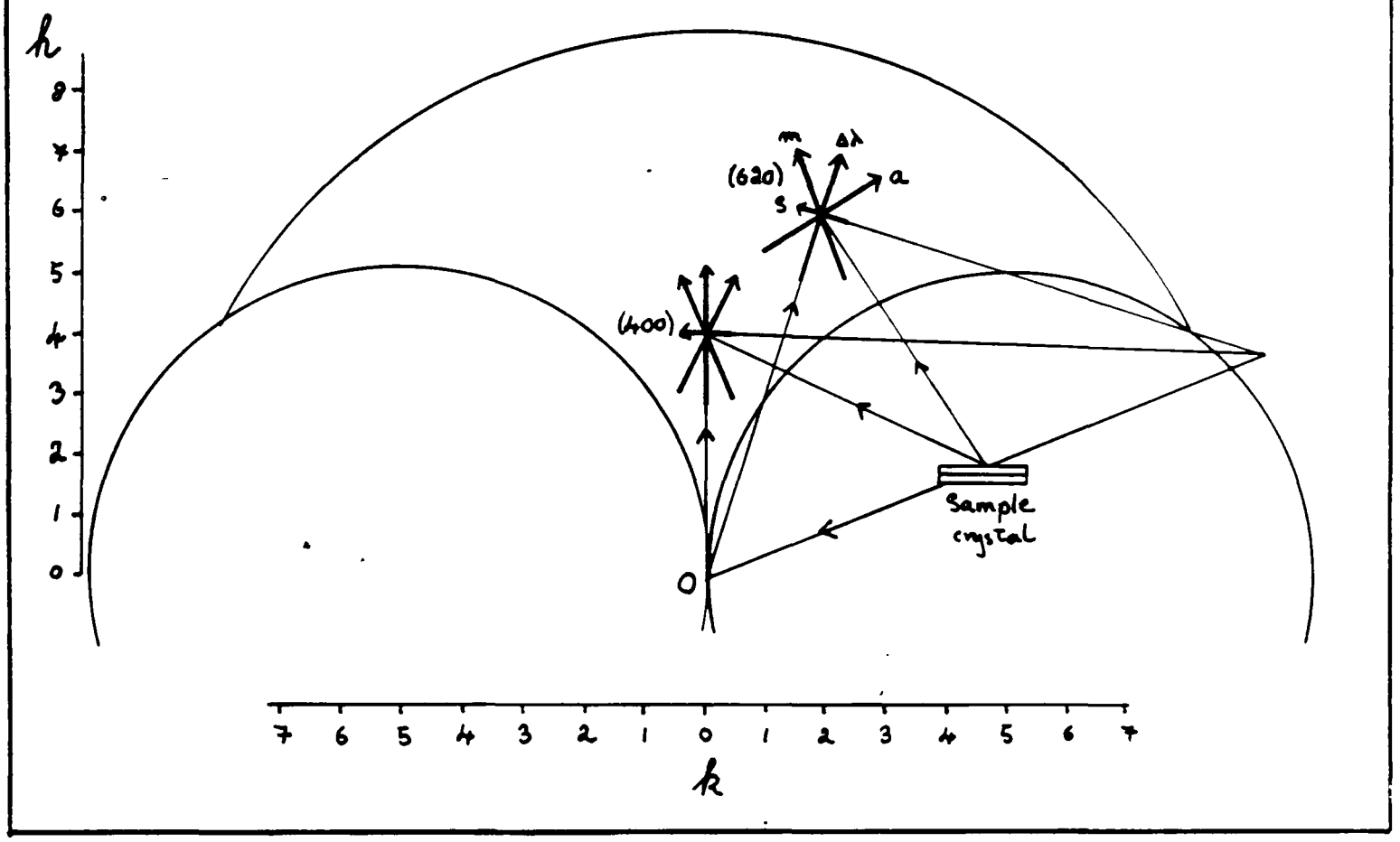

Figure 4.17 – KH_2PO_4 (KDP) sample, Si(111) monochromator and analyser. $CuK\alpha_1$. The accessible region of reciprocal space and the scattering geometry at two Bragg reflections,(400) and (620), and the loci of the resolution degrading effects.

TABLE 4.2

Theta(s)	dq(m)	dq(s)	dq(a)	dq(lambda)
2°	0.00014	0.00001	0.00014	0.00067
4°	"	0.00003	"	0.00056
6°	"	0.00004	"	0.00045
8°	"	0.00006	"	0.00034
10°	"	0.00007	"	0.00023
12°	"	0.00009	"	0.00012
14°	"	0.00010	"	0.00001
16°	"	0.00012	"	0.00010
18°	"	0.00013	"	0.00021
20°	"	0.00015	"	0.00032
22°	"	0.00016	"	0.00043
24°	"	0.00017	"	0.00054
26°	"	0.00019	"	0.00065
28°	"	0.00020	"	0.00076
30°	"	0.00021	"	0.00086
32°	"	0.00023	"	0.00097
34°	"	0.00024	"	0.00107
36°	"	0.00025	"	0.00118
38°	"	0.00026	"	0.00128
40°	"	0.00027	"	0.00138
42°	"	0.00029	"	0.00148
44°	"	0.00030	"	0.00157
46°	"	0.00031	"	0.00167
48°	"	0.00032	"	0.00176
50°	"	0.00033	"	0.00185
52°	"	0.00035	"	0.00194
54°	"	0.00035	"	0.00203
56°	"	0.00036	"	0.00211
58°	"	0.00036	"	0.00219
60°	"	0.00037	"	0.00227

Table 4.2 - Resolution widths (fwhh) in reciprocal Ångstroms for a triple-crystal spectrometer operating in the high-resolution mode. $CuK\alpha_1$ source, Si(111) monochromator and analyser crystals, 0.2mm pre-monochromator slit, KH_2PO_4 sample crystal ($\Delta\theta_s$=0.003°).

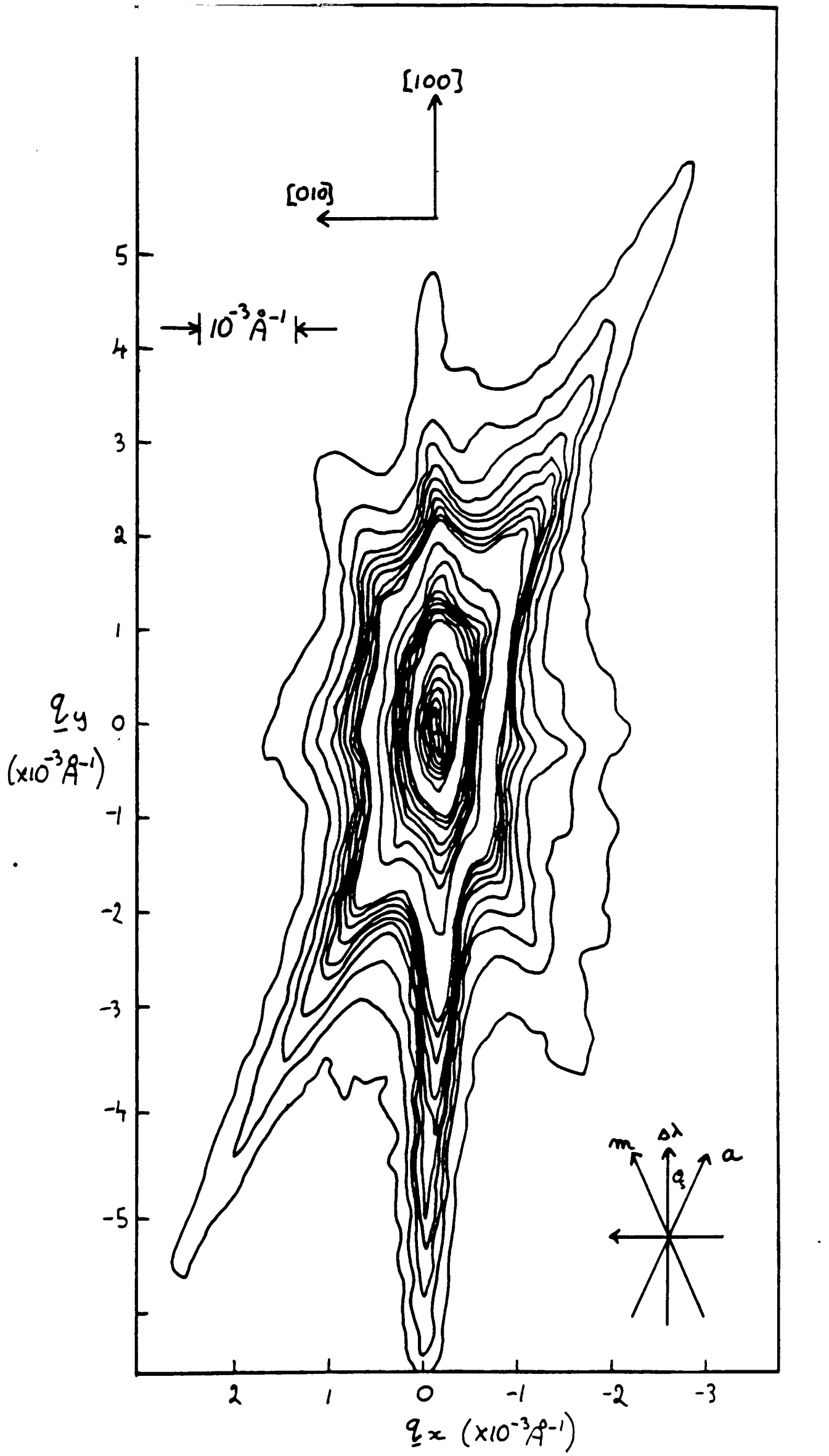

Figure 4.18 - KDP. An iso-intensity contour plot of the scattering around the (400) reciprocal lattice point in the tetragonal phase (T_c + 12K). Θ_s = 34° and well defined $\Delta\lambda$, monochromator and analyser streaks are visible. The contour are arranged on a quasi-logarithmic scale, 0.1% to 1%, 1% to 10% and 10% to 100%.

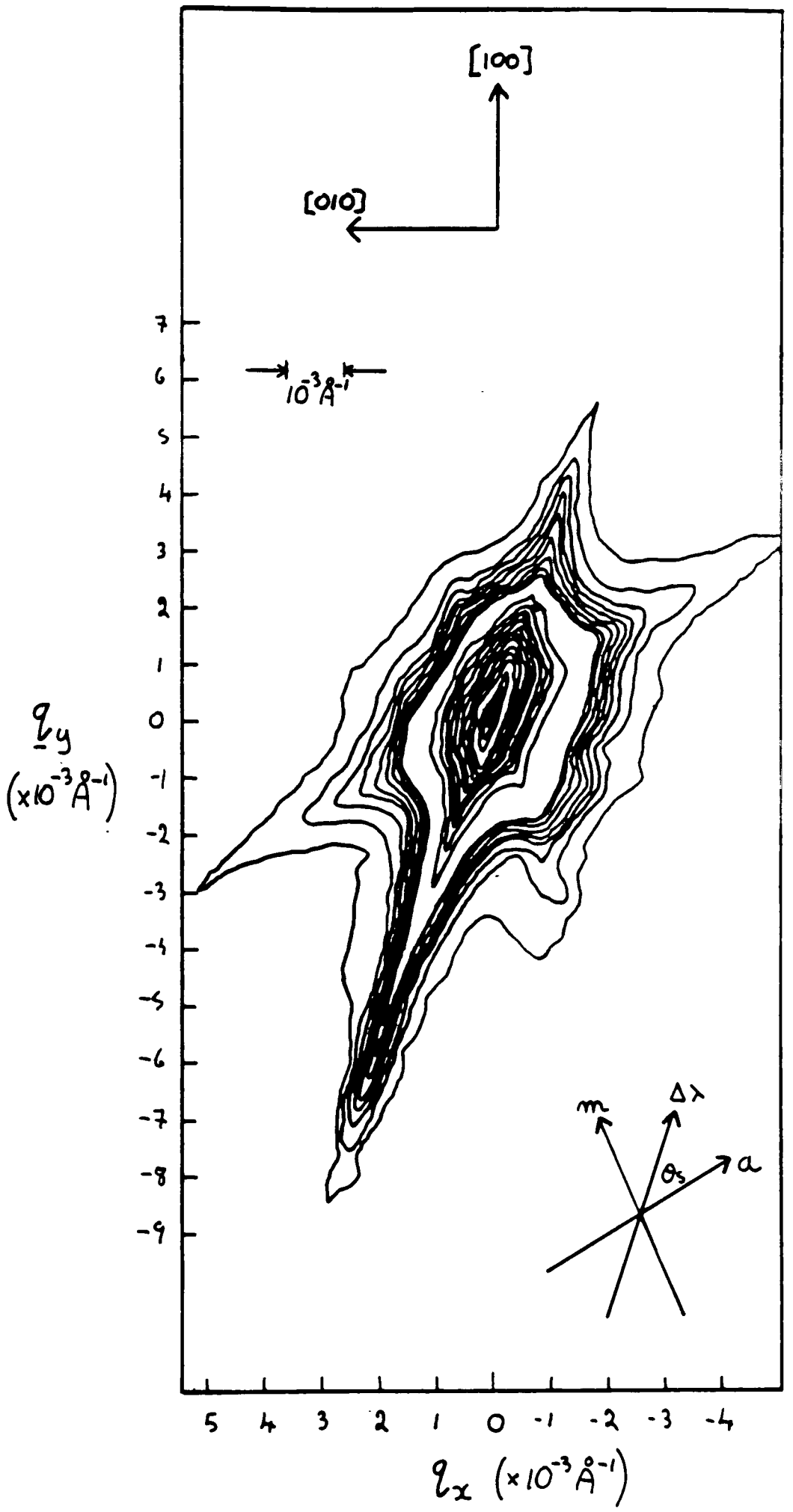

Figure 4.19 – KDP. As 4.18 but the (620) reciprocal lattice point.

formation of only two of the four possible domain orientations. The crystal can form a lamellar structure with the oppositely-poled ferroelectric domains separated by structural discontinuities commonly known as domain walls. In an analogous manner to the production of the crystal surface streak (or truncation rod) described in section 2.2.2 the abrupt termination, at the domain wall, of the particular Fourier component of the electron density distribution giving rise to a Bragg reflection results in the production of extended rods of diffuse scattering in reciprocal space in a direction perpendicular to the domain wall (Andrews and Cowley 1986).

Figure(4.17) shows a map of the (tetragonal phase) **a*b*** reciprocal lattice plane in KDP with the directions of the resolution degrading elements marked for two reciprocal lattice points (400) and (620). Once again Si(111) monochromator and analyser crystals were used with $CuK\alpha_1$ x-rays. The resolution parameters were

- $\Theta_m = \Theta_a = 14.2°$
- $\Delta\Theta_m = \Delta\Theta_a = 0.002°$
- $\lambda = 1.540511Å$
- $\Delta\lambda = 0.00058Å$
- $\Delta\Theta_s = 0.003°$
- pre monochromator slit = 0.2mm
- $\Theta_s(400) = 24.0°$
- $\Theta_s(620) = 41.0°$

and the corresponding widths in reciprocal space can be read off Table (4.2).

Figures(4.18) and (4.19) show contour plots of the scattering at reciprocal lattice points (400) and (620) in the tetragonal phase (135K). The contour levels are arranged on a quasi-logarithmic scale (i.e. 0.1% to 1%, 1% to 10%, 10% to 100%) to display weak scattering effects without over-contouring the main peak. The instrumental resolution, shown by the 50% contour, is dominated by the sample mosaic spread and spectral dispersion. Streaks due to $\Delta\Theta_m$, $\Delta\lambda$ and $\Delta\Theta_a$ can be clearly identified. The $\Delta\lambda$ streak is composed of the intrinsic width of the $CuK\alpha_1$ line and a substantial bremsstrahlung component. There is no sign of a streak perpendicular to the sample surface but this is not

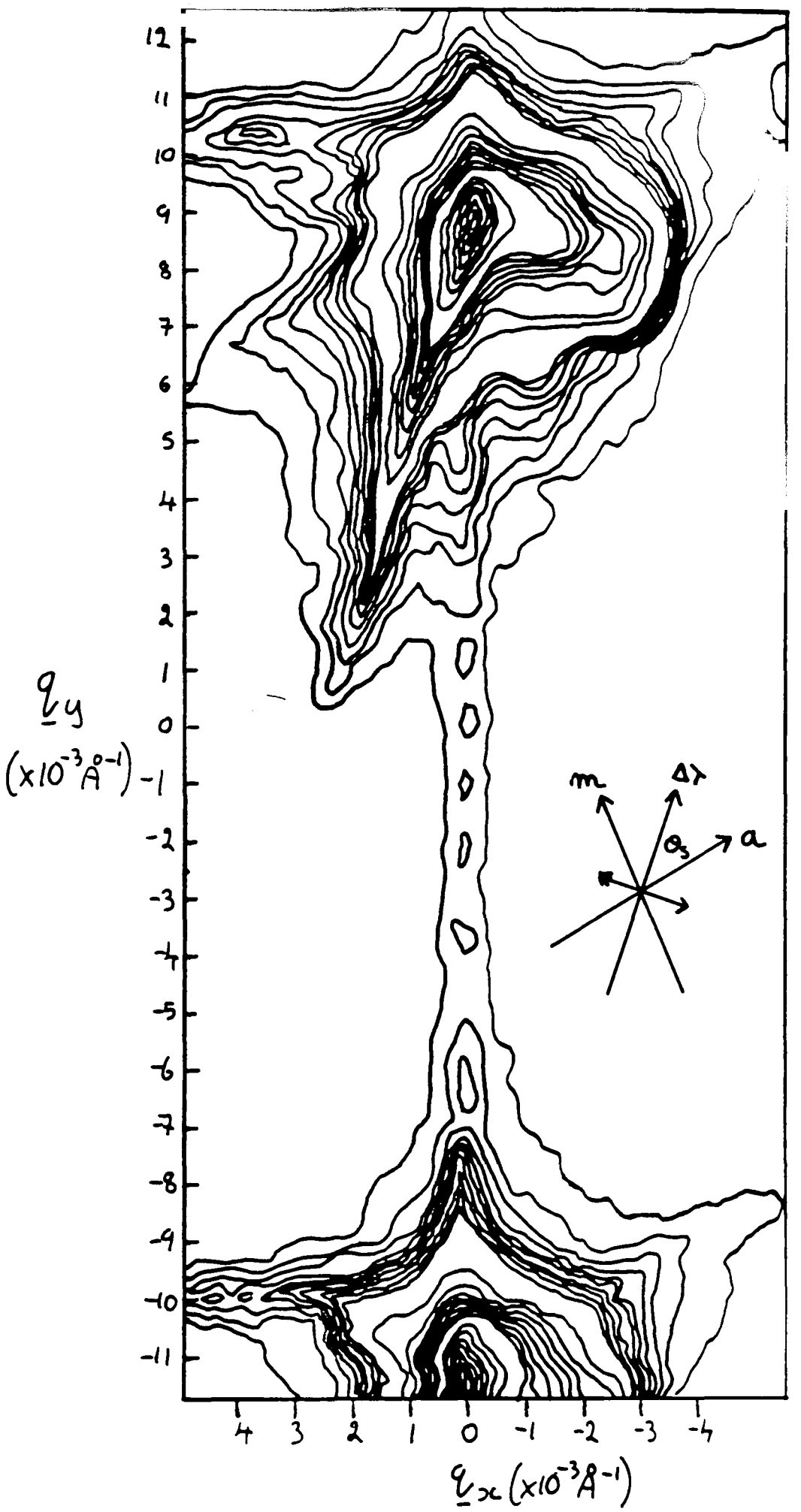

Figure 4.20 - KDP. As 4.19 but at T_c - 10K, in the orthorhombic phase. The single Bragg peak of the tetragonal phase has split into two. Note the increased mosaicity at the <10% level and the diffuse scattering streak joining the two peaks. This is domain-wall scattering.

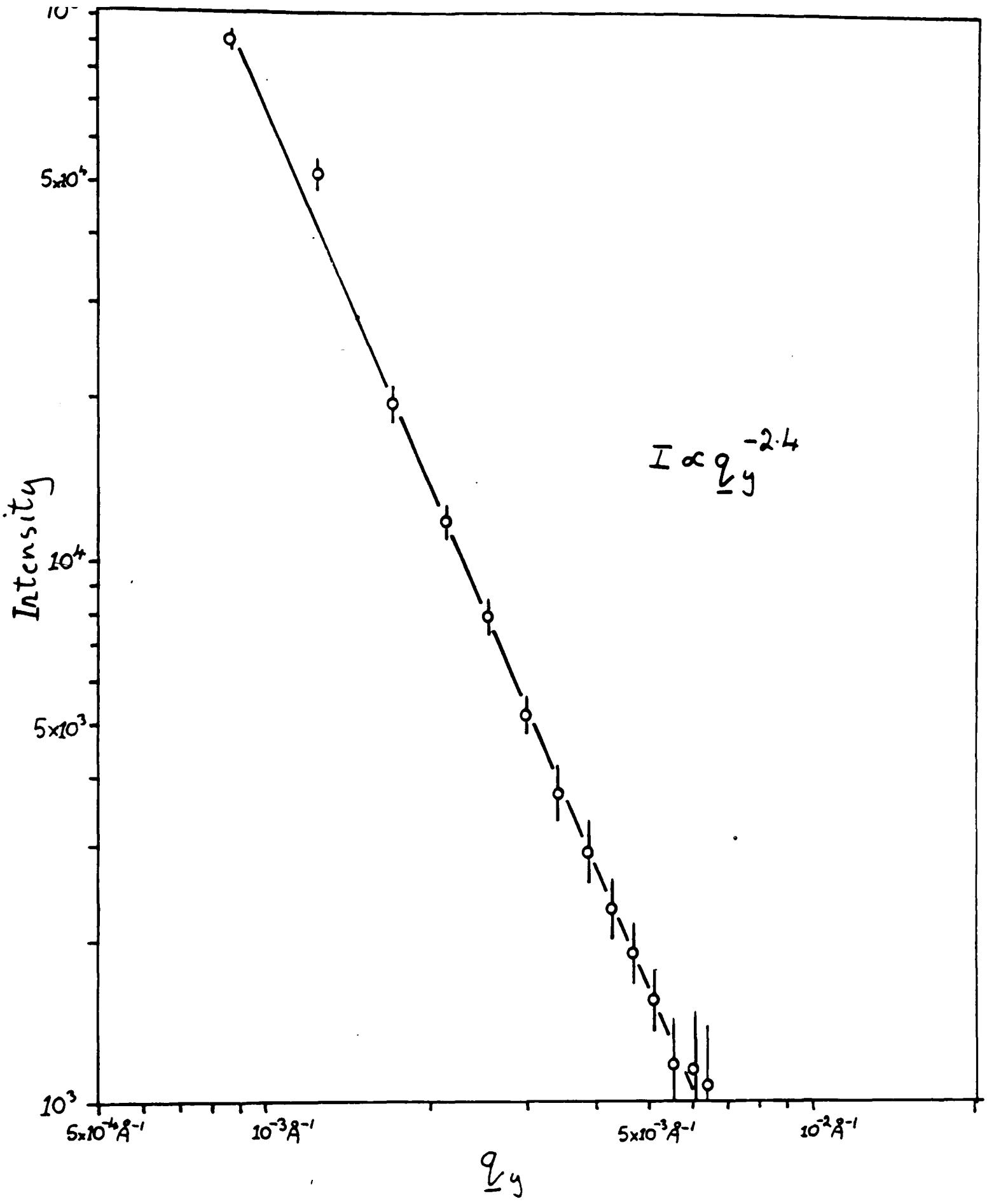

Figure 4.21 - KDP. A log-log plot of the intensity of the domain-wall scattering against wave-vector

surprising. The crystal preparation method (diamond polishing followed by etching in distilled water to remove surface damage) leaves a surface which is far from flat; greatly diminishing the intensity of the surface streak (Andrews and Cowley 1985).

Figure(4.20) shows how the scattering at the position of the (620) tetragonal phase reflection has altered on cooling through T_c into the orthorhobic phase (113K). The single Bragg peak of the tetragonal phase has split into two, well resolved, orthorhombic phase Bragg peaks. The magnitude of the splitting is directly related to the ratio of the lengths of the orthorhombic 'a' and 'b' axes and thus to the amount by which the γ angle of the original tetragonal cell has sheared from 90°. The temperature dependence of the splitting can be regarded as an order parameter of the orthorhombic phase.

It is clear that the mosaic structure of the crystal has altered slightly. Although the FWHH of each Bragg peak has not altered there is evidence of a small amount of crystal misorientated from the bulk by several hundredths of a degree. Most importantly, a narrow ridge of scattering can be seen to have developed between the two Bragg peaks, extending through the Bragg peaks. This is domain wall scattering. By careful choice of Bragg reflection to ensure that the $\Delta\Theta_m$ and $\Delta\Theta_a$ streaks do not interfere with the measurement, and by optimising the monochromator settings to shift the bremsstrahlung streak to one side of the Bragg peak, it is possible to carry out intensity measurements very close to the Bragg peak.

Figure(4.21) shows a log/log plot of the integrated intensity of this scattering against reduced wavevector, **q**. The remarkably straight line obtained, even for points less than 10^{-3}Å^{-1} from the Bragg peak, shows that the intensity is described by a power law

$$I \propto \mathbf{q}^{-2.4}$$

in perfect agreement with the results obtained by Andrews and Cowley (1986) on a sample crystal from the same source and at the same temperature but using a lower resolution spectrometer configuration and in the wavevector range 2×10^{-2} to 4×10^{-1}Å^{-1}.

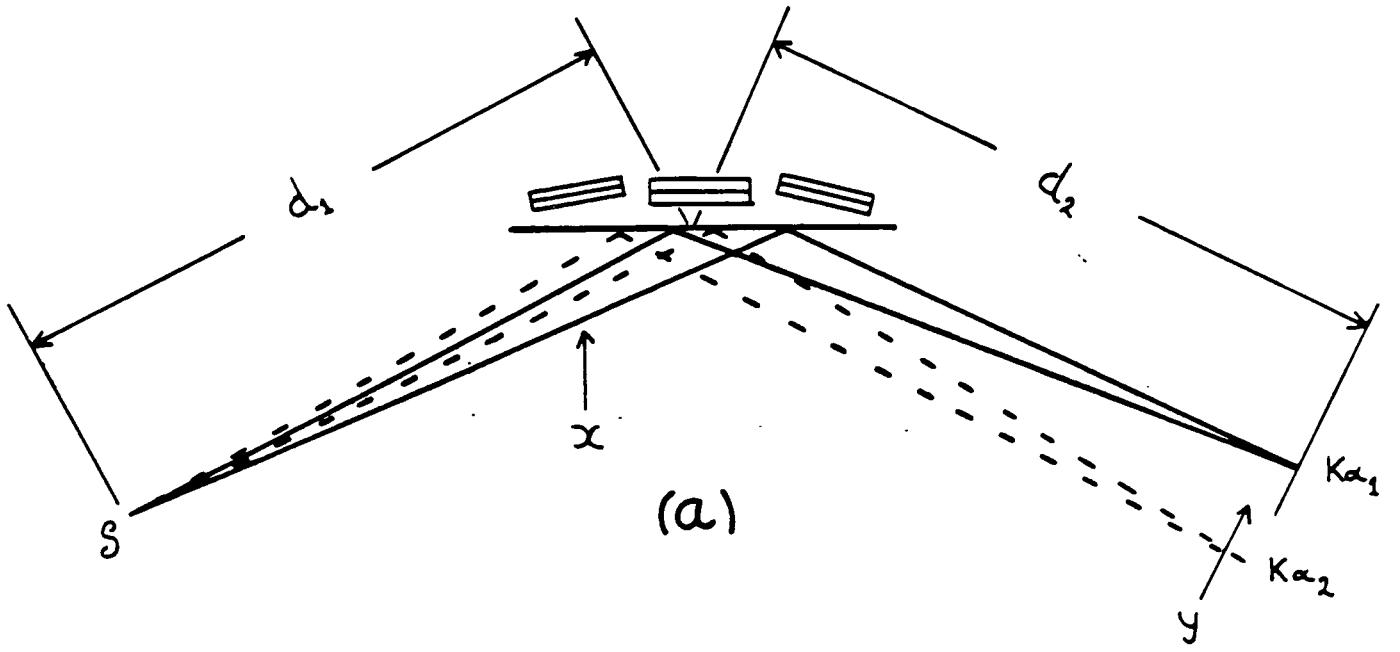

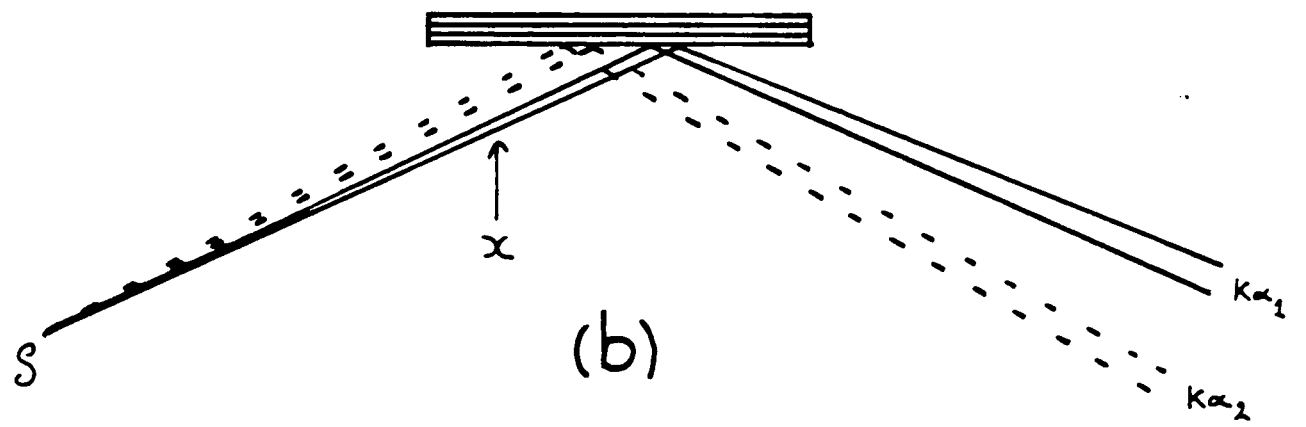

Figure 4.22 – A ray diagram showing a two (spectral) component ($K\alpha_1\alpha_2$) x-ray beam diffracted by (a) a mosaic crystal and (b) a perfect crystal.

4) ALTERNATIVE MONOCHROMATOR AND ANALYSER ARRANGEMENTS.

The role of the monochromator crystal in a triple-crystal x-ray spectrometer is two-fold: to control $\Delta\Theta_m$ and to control $\Delta\lambda$. So far, we have limited the discussion to flat monochromator crystals, either perfect (e.g. silicon) or mosaic (e.g. pyrolytic graphite). Before examining possible alternatives we should consider, in detail, the modus-operandi of the above crystals and identify their shortcomings.

4.1) FLAT MONOCHROMATOR AND ANALYSER CRYSTALS - SILICON AND GRAPHITE.

The arguements put forward in sections 2.2.1 and 2.2.2 to describe $\Delta\Theta_s$ for mosaic and perfect sample crystals apply equally to the monochromator crystal, and the spectral dispersion introduced by the monochromator crystal was discussed in section 2.2.3. Figure(4.22) summarises diagramatically the operation of both types of monochromator in conjunction with a two-component ($CuK\alpha_1$, $K\alpha_2$) point source.

The mosaic monochromator produces a series of spectrally dispersed, focussed images of the source; whereas the perfect monochromator produces a series of spectrally dispersed but slightly de-focussed images of the source. To eliminate the $K\alpha_2$ component we must introduce a further optical element - a knife edge or preferably a narrow slit - at some point where the $K\alpha_1$ and $K\alpha_2$ beams are spatially separated. The obvious place is position Y, where the mosaic crystal produces its focussed images. If $d_1=d_2=200mm$, the separation of the $K\alpha_1$ and $K\alpha_2$ foci is 0.25mm and, with care, it is possible to eliminate the $K\alpha_2$ component. A narrow slit placed at position X, very close to the monochromator crystal can, in the case of a mosaic crystal, be used to control $\Delta\Theta_m$. The effects of such a slit were discussed in section 3.2 Example 1. and shown in Figures (4.14) and (4.15).

In practice, a narrow slit at position X, in conjunction with a perfect monochromator crystal, can be used to eliminate the $K\alpha_2$ component, as shown in Figure(4.23). The spectrometer configuration was a $CuK\alpha$ source, 3mm high by 0.3mm wide viewed at a take-off angle of 6°, a silicon(111) monochromator

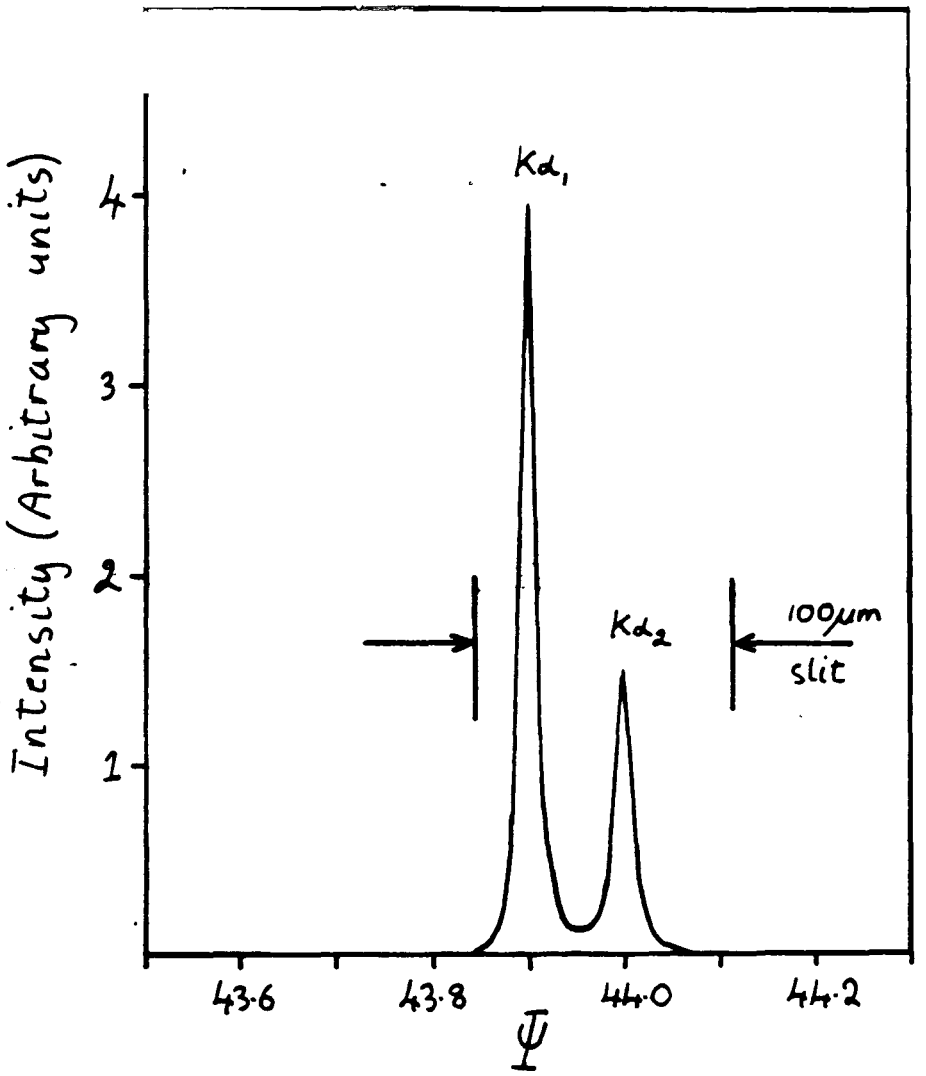

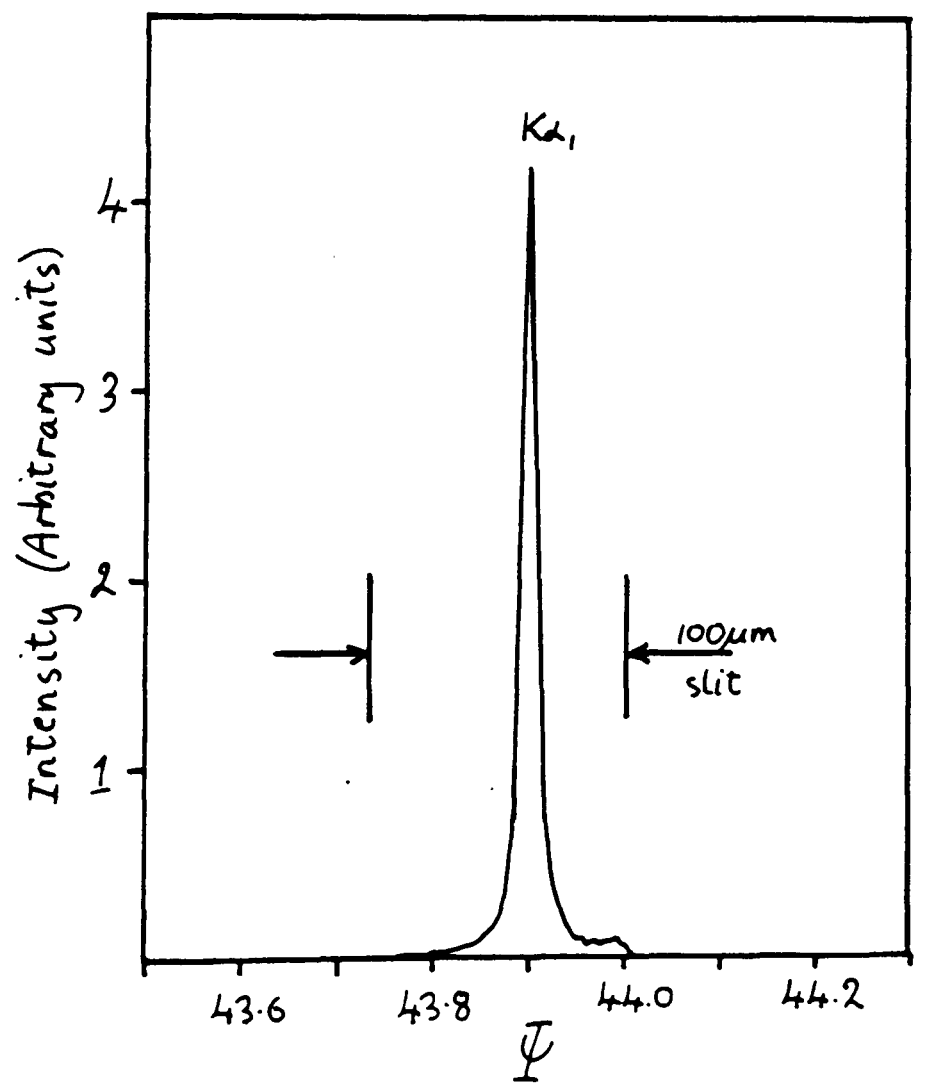

Figure 4.23 - $RbCaF_3$ sample crystal (400), θ_s = 41°. Si(111) monochromator and analyser crystals. CuKα x-rays. A Ψ2Φ scan (i.e. along q_{pl}) showing $K\alpha_1\alpha_2$ splitting and the effect of a 0.1mm pre-monochromator slit. The $K\alpha_2$ component can be eliminated but, inevitably, a small bremsstrahlung component is passed.

at a distance of 200mm from the source with a 0.1mm wide slit immediately in front of the monochromator crystal, an RbCaF3 sample crystal, ((400) reflection, Θ_s=42°) and a silicon(111) analyser.

Figure(4.23a) shows a $\Psi 2\Phi$ scan through the $K\alpha_1$ and $K\alpha_2$ components of the Bragg peak with the slit set to allow both spectral components to pass. In Figure(4.23b) the slit is translated by 0.04mm, effectively eliminating the $K\alpha_2$ component. It is quite clear from these figures that a slit as narrow as 0.1mm will allow a substantial bremsstrahlung component to pass the monochromator, and this component is much in evidence in the contour plots of Figures(4.18, 19 and 20). To eliminate the bremsstrahlung streak would require a tiny slit (<20microns).

To summarise, a flat graphite monochromator combined with appropriate pre- and post-monochromator slits can produce a monochromatic ($K\alpha_1$) incident beam with an angular range, $\Delta\Theta_m$, variable between several hundredths and several tenths of a degree, (i.e. a reciprocal space resolution range of 2×10^{-3} to 2×10^{-2}Å^{-1}). Because of the inadvisability of using slits after the sample crystal, the use of a graphite analyser fixes the reciprocal space resolution in one direction to be $\sim2\times10^{-2}$Å^{-1}.

Flat silicon(111) monochromator and analyser crystals fix $\Delta\Theta_m$ and $\Delta\Theta_a$ to ~0.002°. In other words, a factor of 10^2 smaller than with graphite. Many experimental measurements, however, demand an intermediate resolution and to satisfy this demand we must examine focussing monochromator and analysers or, altenatively, find a suitable crystal with an intermediate mosaic spread. Some experiments, on the other hand, require even higher resolution or, more accurately, the elimination of the most obvious resolution degrading elements - the monochromator and analyser streaks. This requirement is most easily satisfied by the use of monolithic channel cut, or Bonse-Hart, monochromator and analyser crystals.

4.2) THE BONSE-HART, MONOLITHIC CHANNEL-CUT MONOCHROMATOR.

The 'Darwin' curve of Figure(4.7) shows that, over a small angular range, the reflectivity of a perfect crystal is, or at least approaches, unity,

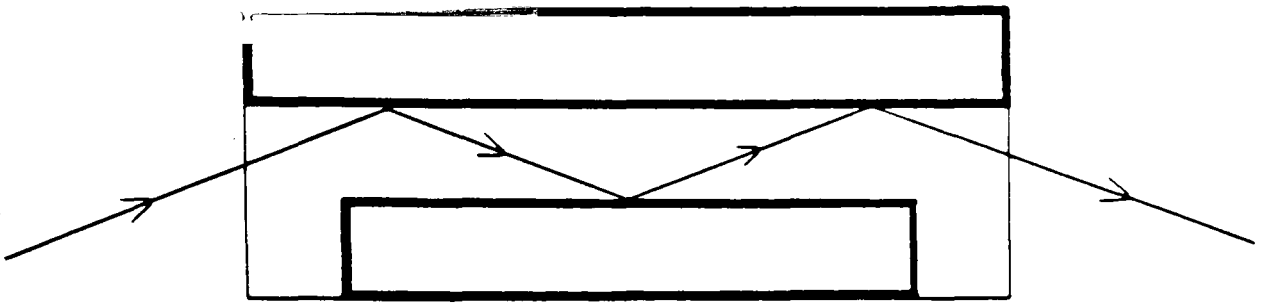

Figure 4.24 - A Bonse-Hart, monolithic channel-cut multiple-reflection monochromator.

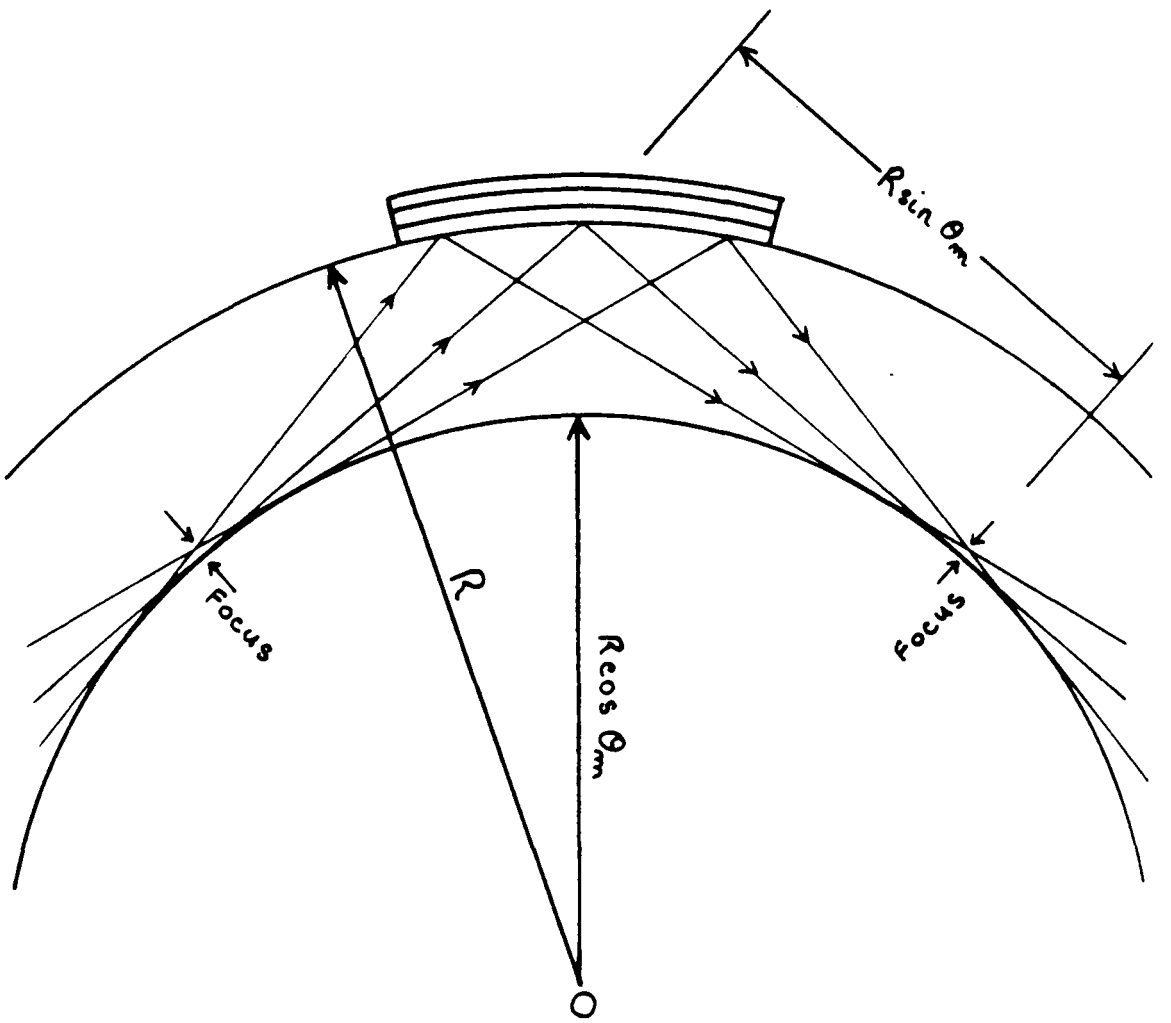

Figure 4.25 - A Johann geometry focussing monochromator.

Outside that range the reflectivity diminishes as $\sim y^{-2}$. Successive reflection from identical crystals will, therefore, result in only a small diminution of the intensity of the diffracted beam over the limited range of high reflectivity but outwith that range the intensity will diminish as $\sim y^{-2n}$, where n is the number of reflections.

Clearly, since the range of total reflectivity is of the order of 0.002° , the relative orientation of each successive crystal must be defined very accurately. To achieve this accuracy, Bonse and Hart (1965) fabricated a multiple reflection monochromator from a monolithic block of dislocation free silicon by the simple expedient of milling a groove in the block parallel to a set of crystallographic planes. The device is shown diagrammatically in Figure(4.24). In practice, a 5 reflection device is sufficient to completely eliminate the monochromator and analyser streaks in a triple-crystal x-ray spectrometer (Zaumseil and Winter, 19).

Bonse-Hart devices are in relatively common use but they do, of course, have disadvantages; for many applications the dramatic improvement in resolution is unnecessary but a certain diminution of the extensive tails is desireable. Recent work at Edinburgh has shown that careful roughening of the crystal surface, without damage to the crystal lattice, can significantly reduce the intensity of the surface streak (Andrews 1986). By way of illustration, note the virtual absence of the monochromator streak in Figure(4.18).

4.3) FOCUSSING OPTICS - THE JOHANN MONOCHROMATOR.

A perfect, flat crystal monochromator, in conjunction with a point source of monochromatic x-rays, satisfies the diffraction condition at only one point along its surface. If the crystal is elastically bent to the correct radius it can satisfy the diffraction condition along its entire surface. For an excellent review of focussing x-ray monochromators, see Witz (1969). Figure(4.25) shows a ray diagram for a cylindrically bent crystal (Johann type). The crystal is bent to a radius R around point O. The diffraction condition is satisfied for all incident and diffracted rays tangential to another circle, the Caustic circle, radius $R\cos\Theta_m$, also centered on O. The distance from the centre of the monochromator to the point of focus is $R\sin\Theta_m$.

A typical source to monochromator distance is 200mm and θ_m for Si(111) and CuKα_1 is 14.22°. This gives a Johann radius of 814.18mm and a corresponding Caustic circle radius of 789.23mm. If the accepance angle of the Johann monochromator is limited to, say, 0.4° then, since the accepted rays are tangential to the Caustic circle, the focus will have a finite width of 0.02mm. For the same geometry, the radius of the CuKα_2 Caustic circle is 789.1mm and the distance between the Kα_1 and Kα_2 foci is, therfore, 0.13mm. If the device is to operate correctly, the tolerance on R, the crystal bending radius, is tiny (+/-0.3mm), The monochromator setting angle must be stable to better that 0.001 , and the position of the crystal relative to the source must be stable to better than 0.01mm.

Clearly, these tolerances are difficult to meet and maintain, a conclusion borne out by two years of experience.

The Johann monochromator is of little use as an analyser as the illuminated area of the sample crystal very often exceeds the focal width of the device.

4.4) ALTERNATIVE CRYSTALS.

To achieve an instrumental resolution intermediate between that obtained using pyrolytic graphite ($\sim 10^{-2}$Å^{-1}) and silicon (or germanium) ($\sim 10^{-4}$Å^{-1}) we must look for a crystal, with a mosaic spread of ~0.04°. Additionally, the crystal must have a high reflectivity, be stable in an intense x-ray beam and be homogeneous over a large surface area. In principle, the above requirements do not sound too demanding, in practice, real crystals tend to be either too perfect or too messy and, despite a prolonged search, the ideal material has proved elusive.

In the absence of suitable, as grown crystals, attempts have been made, with little sucess, to dope, squeeze or thermally shock perfect crystals (Si or Ge) into an ideal mosaic structure.

Recent work in Edinburgh has shown that epitaxially grown PbTe on a BaF_2 substrate is a promising candidate for an intermediate resolution monochromator crystal. Work is currently in progress on this important subject

and it would be premature to discuss the results here.

CHAPTER FIVE

An X-Ray Scattering Study of the Structurally Modulated Phases in Proustite (Ag_3AsS_3).

Preamble

The material presented in this chapter has been published in Journal of Physics C: Solid State Physics (Ryan, Nelmes and Gibaud 1985), as have the results of an earlier neutron and x-ray scattering study (Nelmes, Howard, Ryan, David, Schultz and Leung 1984, See appendix).

Prior to our neutron scattering study, a plethora of phase transitions had been reported in proustite between room temperature and ~27K. Below the first-order transition at ~27K the structure has been shown to be monoclinic, with space group Cc (Allen 1985). Above this temperature, transitions had been reported at ~60K, ~110K and ~210K (as reviewed by Ewen et al. 1983) but, despite considerable experimental effort, the nature of the structural changes at these transitions, and indeed their very existence, remained unclear.

Our neutron scattering experiment was carried out using the single-crystal, time-of-flight diffractometer equipped with an area detector at the Argonne National Laboratory. This revealed no structural changes from room temperature to ~60K and a modulated structure below this temperature.

This low-Q-resolution provided the necessary information to permit a high-Q-resolution measurement of the modulation wave-vector to be carried out in Edinburgh. This x-ray experiment confirmed the existence of a commensurably modulated structure between ~27K and ~49K and revealed a, previously unexpected, incommensurate phase between ~49K and ~60K. Coincidentally, rather similar results were published by a Russian research group (Khasanov et al 1984). This chapter describes a subsequent, and considerably more detailed, study of the structurally modulated phases in proustite.

We have recently reported neutron and X-ray scattering measurements which demonstrate the existence of two modulated phases in proustite (Ag_3AsS_3) in the temperature range ~27K to ~61K (Nelmes et al 1984 and appendix). Our results were generally in agreement with those derived from X-ray scattering measurements carried out separately by Khasanov et al (1984) but seemed to differ significantly in some important details. To obtain more precise information about the modulated phases and to examine the apparent differences between our results and those of Khasanov et al, we have now carried out a further series of high (reciprocal space) resolution X-ray scattering measurements.

The room-temperature structure of proustite was studied by Harker (1936) and, more recently, by Engel and Nowacki (1966), and is known to have space group R3c. Conventionally, the hexagonal setting of the rhombohedral cell is adopted and the room-temperature lattice parameters are $\underline{a}$=10.82Å and $\underline{c}$=8.69Å. Although phase transitions have been reported at ~210K (Smolenskii et al 1981) and ~110K (Semak et al 1975), more recent work indicates that the room-temperature structure is stable on cooling to the well-established second-order phase transition at ~61K (Ewen et al 1983, Nelmes et al 1984, Belyaev et al 1984, Allen 1985). In accord with the evidence first found in NQR spectra by Bondar et al (1983), our previous results showed that the ~61K transition is to an incommensurate phase and that there is a further, abrupt transition at ~49K to a commensurably modulated phase. At ~27K there is known to be a strongly first-order transition to a phase in which the structure is monoclinic with space group Cc (Allen 1985).

The modulated phases are characterised by the appearance in the diffraction pattern of a cluster of up to six satellite peaks around the Bragg peaks of the room-temperature structure (Nelmes et al 1984, Khasanov et al 1984). In the commensurably modulated phase (~27K to ~49K) the satellites are located at the following positions -

$$(hkil) \pm (\tfrac{1}{3},-\tfrac{1}{3},0,\tfrac{1}{3}),$$

$$\pm (0,\tfrac{1}{3},-\tfrac{1}{3},\tfrac{1}{3}) \text{ and}$$

$$\pm (-\tfrac{1}{3},0,\tfrac{1}{3},\tfrac{1}{3})$$

- which all lie in planes parallel to the mirror planes of the point group 3m, as

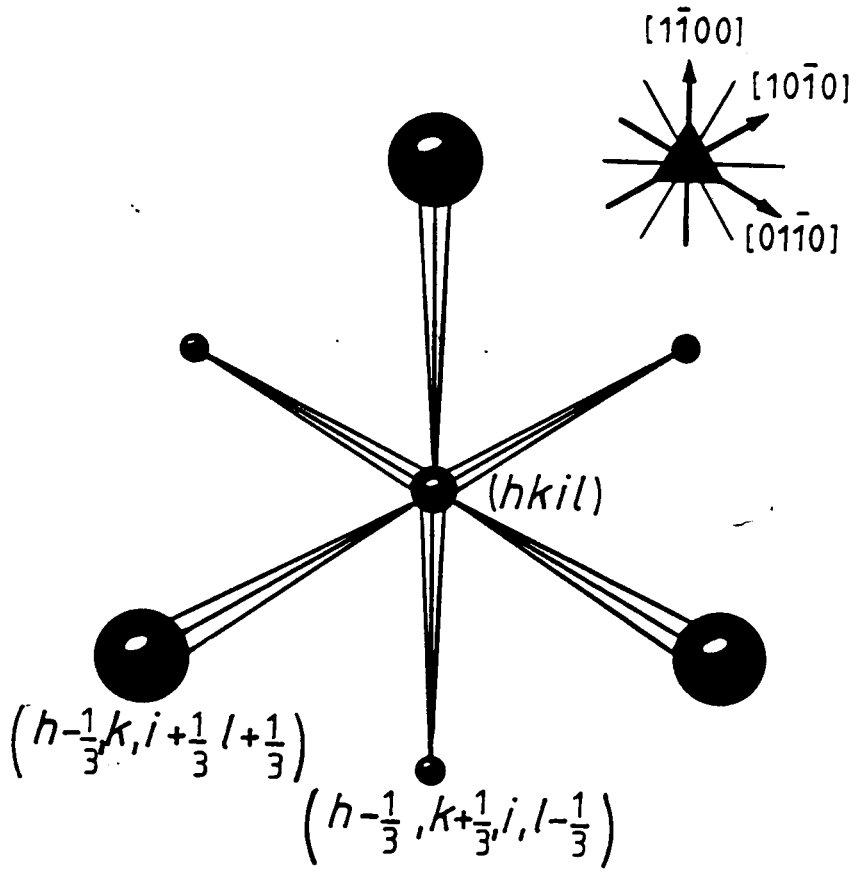

Figure 5.1 – A typical (modulated phase) reciprocal lattice point (hkil) showing the accompanying cluster of six satellite reflections, viewed parallel to the [0001] direction. The insert shows the corresponding orientation of the crystallographic point group elements and the hexagonal axes.

shown in Figure (5.1). Thus the component of the modulation in the (hexagonal) basal plane is $\frac{1}{3}\mathbf{a}^*$ and the component along the z axis is $\frac{1}{3}\mathbf{c}^*$; and the satellite peaks are at one ninth of the distance to the next reciprocal lattice point (see Figure (5.6), below), not one third as suggested by Khasanov et al (1984).

The incommensurate phase is characterised by a wave-vector of magnitude smaller than, and a direction almost coincident with, that of the commensurably modulated phase. Khasanov et al (1984) concluded that the discommensuration was confined to the component of the wave-vector along the $\mathbf{c}^*$ axis (i.e. [000l) and that the basal-plane component remained constant at $\frac{1}{3}\mathbf{a}^*$. The relatively poor reciprocal-space resolution of our previous experiment did not permit us to make a definitive statement about the value of the incommensurate wave-vector; but our results did suggest that the discommensuration was not, in fact, confined to the $\mathbf{c}^*$ direction, although any departure from the commensurate value in the basal plane was clearly very small. An accurate determination of the magnitude, direction and temperature dependence of the modulation wave-vector, in both modulated phases, was the principal objective of these new measurements

The experiment was performed using a high-resolution two-circle diffractometer mounted on an intense, rotating-anode X-ray source. All of the measurements shown were made by reflection from a large and carefully prepared face of the sample crystal, which was oriented with the $h\bar{h}0l$ plane in the (horizontal) scattering plane of the diffractometer: in this (mirror) plane of the reciprocal lattice the R lattice imposes the condition h+l=3n on the hexagonal-cell indices and the c-glide absences are reflections with $l \neq 2n$. The sample crystal was mounted in an isothermal enclosure attached to the cold stage of a closed-cycle cryo-refrigerator. The sample temperature was controlled with a stability and reproducibility of ±0.02K and with an absolute accuracy better than ±0.3K. The primary beam, of Mo$K\alpha_1$ X-rays, was monochromated by the (111) reflection of a flat, symmetrically cut silicon crystal; and the scattered beam was collimated by an identical silicon crystal set in the parallel (non-dispersive) configuration. The wave-vector resolution of the experiment was limited principally by the mosaic spread of the sample crystal which had a measured width of 0.03° FWHH.

To achieve as accurate a measure as possible of the modulation wave-vector, particular care was taken to ensure that any errors attributable to instrumental misalignment were minimised. The measurements were carried out

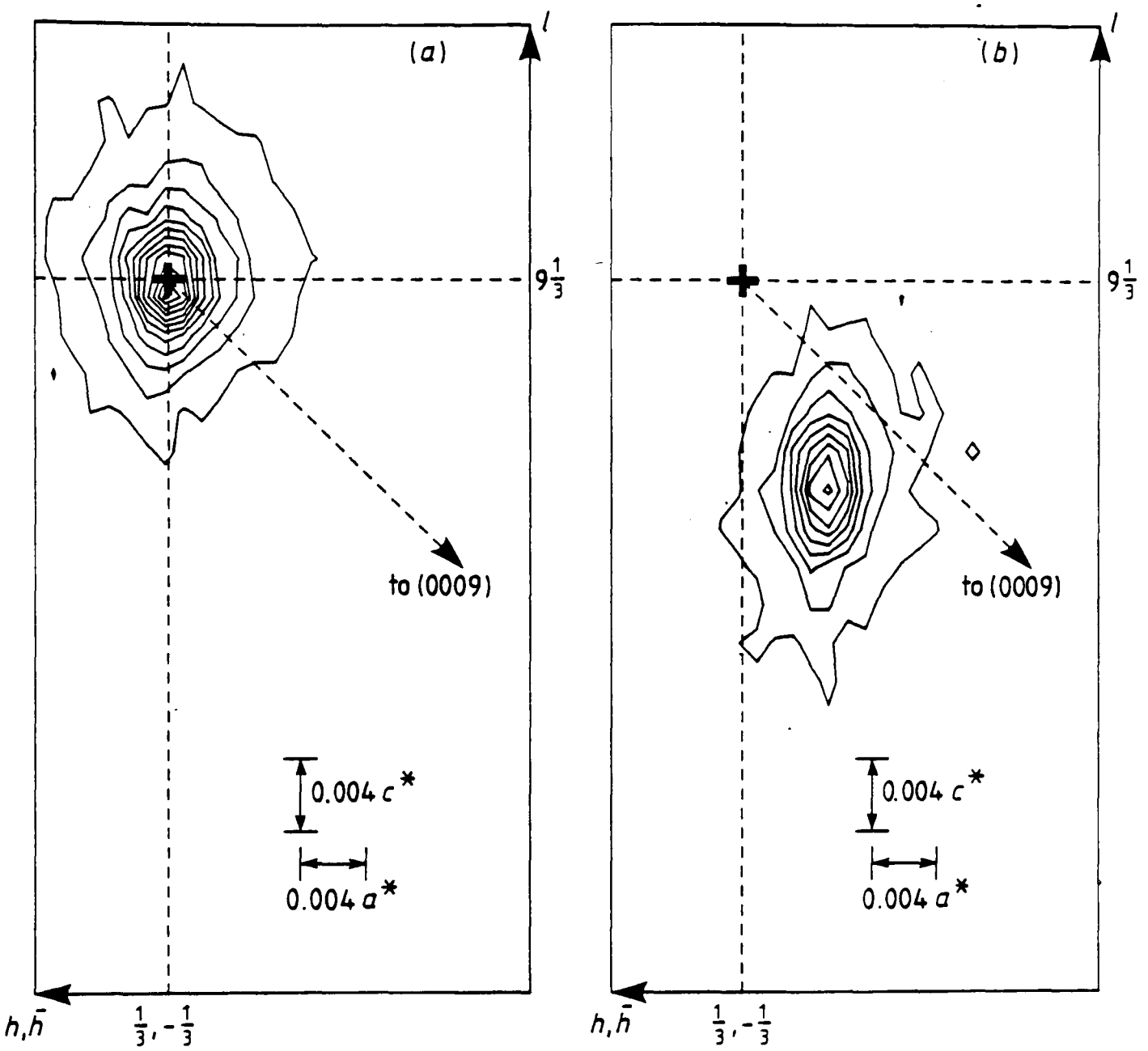

Figure 5.2 - Grid scans showing the recorded X-ray scattering intensity as a function of position in the region of $(\frac{1}{3},-\frac{1}{3},0,9\frac{1}{3})$ at (a) 45K and (b) 51K. The cross marks the commensurate position.

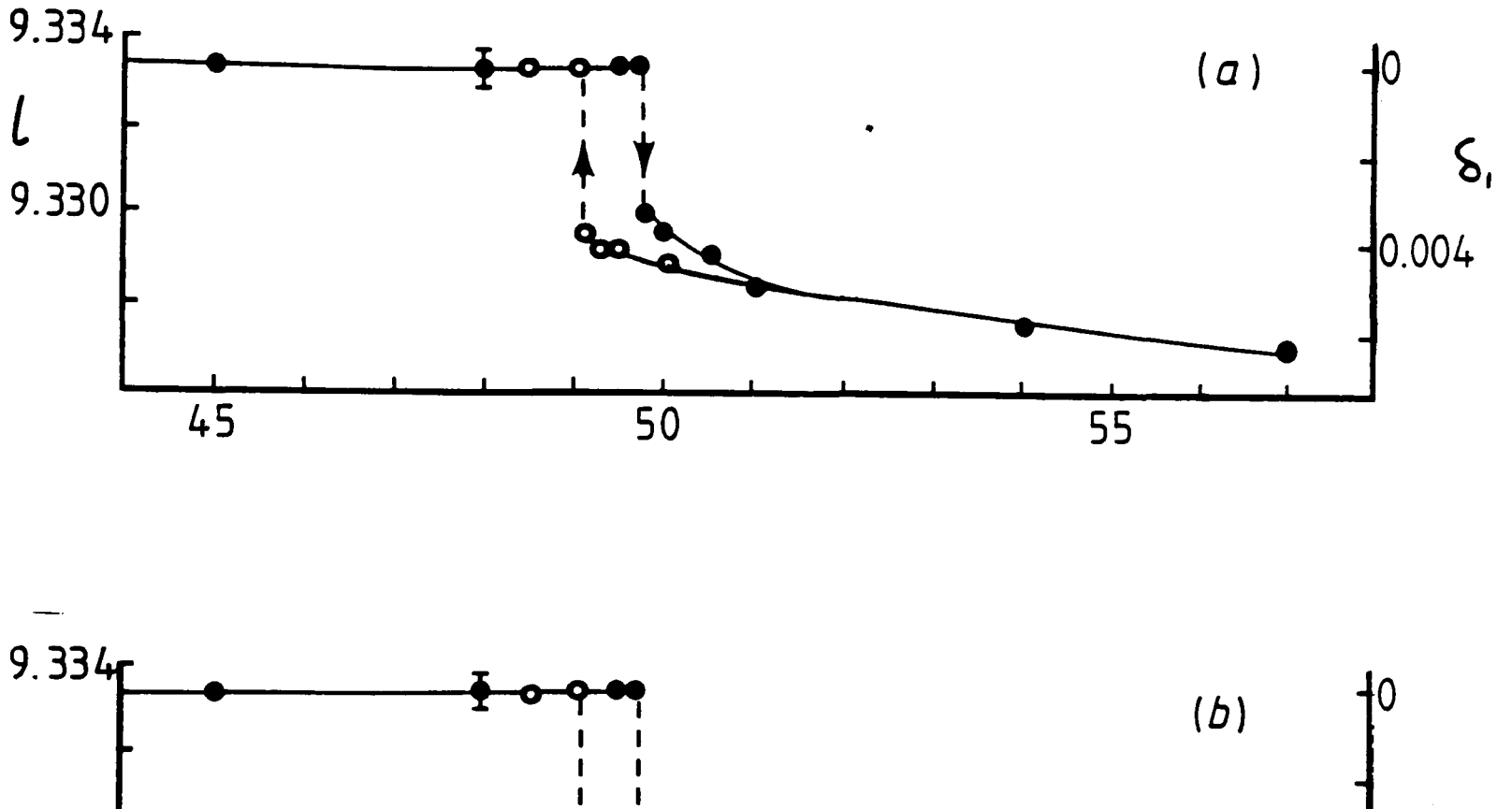

Figure 5.3 - The temperature dependence of the modulation wavevector along (a) the [hh̄00] direction and (b) the ([0001] direction. δ_1 and δ_2 are the deviations from the commensurate value of $h=\frac{1}{3}$ and $l=9\frac{1}{3}$ respectively. Measurements were obtained on warming (●) and on cooling (o). Typical error bars are shown.

on the pair of satellite reflections in the hh̄0l plane associated with the (0009) reciprocal lattice point, namely $(\frac{1}{3},-\frac{1}{3},0,9\frac{1}{3})$ and $(-\frac{1}{3},\frac{1}{3},0,8\frac{2}{3})$. At each temperature the orientation matrix was refined and then checked by scanning a number of Bragg peaks. The precise positions of the two satellite peaks were found by performing a high-resolution grid scan of the area of reciprocal space around the expected position of each one; the components of the wave-vector in the [hh̄00] and [0001] directions were then determined from the difference in position of the two satellites, thus eliminating any absolute setting errors. By this method the value of the wave-vector could be measured with a precision of better than ±0.0003 reciprocal lattice units. Data were accumulated at a rate of one temperature per 12-hour period, allowing ample time for the sample to reach equilibrium at each temperature.

Figure (5.2) shows the results of typical grid scans of the satellite peak at $(\frac{1}{3},-\frac{1}{3},0,9\frac{1}{3})$ recorded in the commensurate phase at 45K and in the incommensurate phase at 51K. The position of the cross marking the commensurate position in this figure was derived from the refined orientation matrix and is subject to an error of ±0.0002 reciprocal lattice units. Clearly, within the limits of the experimental resolution, the satellite lies on the commensurate position at 45K; but at 51K it lies at a position which is incommensurate with respect to both axes. The detailed temperature dependence of the modulation wave-vector in the region of the ~49K phase transition is shown in Figure (5.3).

In this reciprocal lattice plane the incommensurate phase is now seen to be characterised by the pair of wave-vectors

$$q_1=(\tfrac{1}{3}-\delta_1,-(\tfrac{1}{3}-\delta_1),0,\tfrac{1}{3}-\delta_2),\ q_2=-q_1$$

where δ_1 and δ_2 are temperature dependent and vary from values of δ_1=0.0063(3) and δ_2=0.0125(3) at T_c+8K to δ_1=0.0038(3) and δ_2=0.0108(3) on cooling to T_c+0.1K. At T_c=49.1K there is a first-order transition to the commensurably modulated phase ($\delta_1=\delta_2$= zero). On warming, the structure remains commensurate to 49.7K: the magnitude of the observed thermal hysteresis is thus 0.6K. On both warming and cooling there is a small temperature range (±0.1K) over which the commensurate and incommensurate phases co-exist: grid scans in these temperature ranges reveal two

well-resolved satellite peaks, located on the commensurate and incommensurate positions, whose relative locations and intensities appear to be stable over time periods of at least 24 hours. Our past experience of studying structural phase transitions using the same instrument suggests that this is a real effect and is the result neither of temperature gradients nor of thermal oscillations. It is of interest to note that, in the temperature range close to the transition, the magnitude of the wave-vector differs on warming and on cooling - an effect observed in a number of incommensurate systems such as $(N(CD_3))_4ZnCl_4$ (Marion et al 1981) and $BaMnF_4$ (Cox et al 1983).

The results displayed in Figure (5.3) confirm that the departure from commensurability is not confined to the hexagonal $\mathbf{c}^*$ axis and, moreover, appear to show that the incommensurate satellite peaks are displaced in an arbitrary direction within the $h\bar{h}0l$ reciprocal lattice plane. On closer inspection, however, it can be seen that the ratio of $\delta_1:\delta_2$ tends, with increasing temperature, towards 1:2. Indeed, at 57K it <u>is</u> 1:2, within error. The significance of this ratio becomes clearer if the reciprocal lattice is re-indexed in terms of the primitive, rhombohedral cell. Then, for example, the $(\frac{1}{3},-\frac{1}{3},0,9\frac{1}{3})_{hex}$ point becomes $(2\frac{8}{9},3\frac{2}{9},3\frac{2}{9})_{rh}$; the wavector of the commensurate modulation (in our chosen reciprocal lattice plane) is $(-\frac{1}{9},\frac{2}{9},\frac{2}{9})_{rh}$; and the satellite peak is at one ninth of the distance to the next Bragg peak in the $[\bar{1}22]_{rh}$ direction. At 57K the modulation wave-vector (see Figure (5.3)) is $(0.3270, -0.3270, 0, 0.3205_{hex})$ which corresponds to $(-0.1112, 0.2158, 0.2158_{rh})$: whilst 0.2158 is irrational, $0.1112 = \frac{1}{9}$ within error. This suggests that in the region of the ~61K transition the modulation is, or is tending towards being, commensurate in the $[\bar{1}00]_{rh}$ direction with an incommensurate component in the $[011]_{rh}$ direction. Closer to the ~49K transition the component in the $[\bar{1}00]_{rh}$ direction shows a small but significant difference from one ninth.

Prior attempts to measure the temperature dependence of the incommensurate wave-vector, conducted on a considerably shorter timescale (15 minutes per temperature) than the measurements described above, revealed a significantly larger thermal hysteresis (~1.5K) and a larger range of temperature (~2.0K) over which both phases were seen to co-exist. Abdikamalov et al (1978) have demonstrated that the magnitude of the thermal hysteresis at the ~27K phase transition is related to the number of cycles through the transition experienced by the crystal: our initial assessment was that a similar effect occurred at the ~49K transition. For that reason, the measurements presented in Figure (5.3) were made after the crystal had been

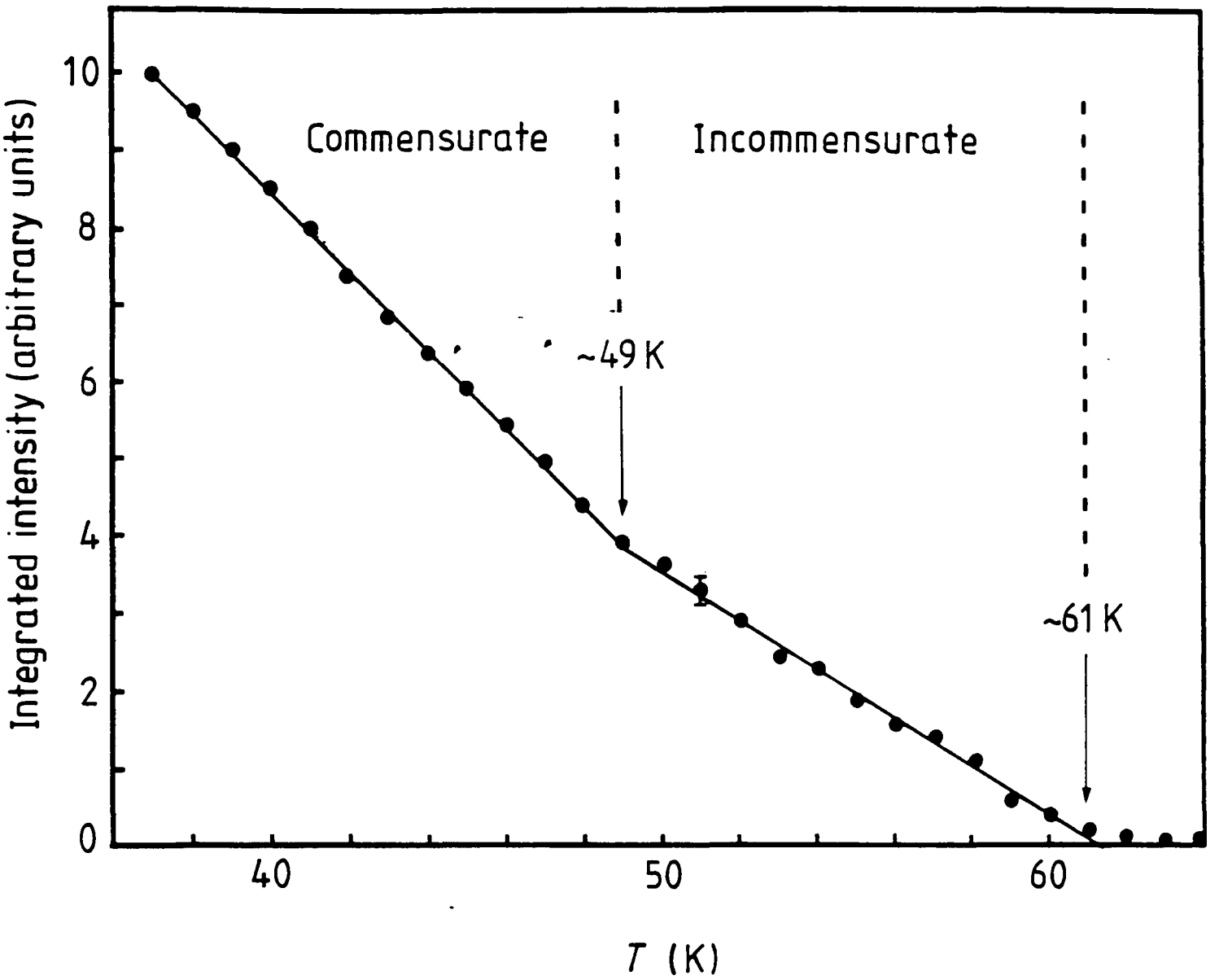

Figure 5.4 - The integrated intensity of the $(\frac{1}{3},-\frac{1}{3},0,9\frac{1}{3})$ satellite reflection as the sample is cooled from 65K at a rate of 4K per hour. A typical error bar is shown.

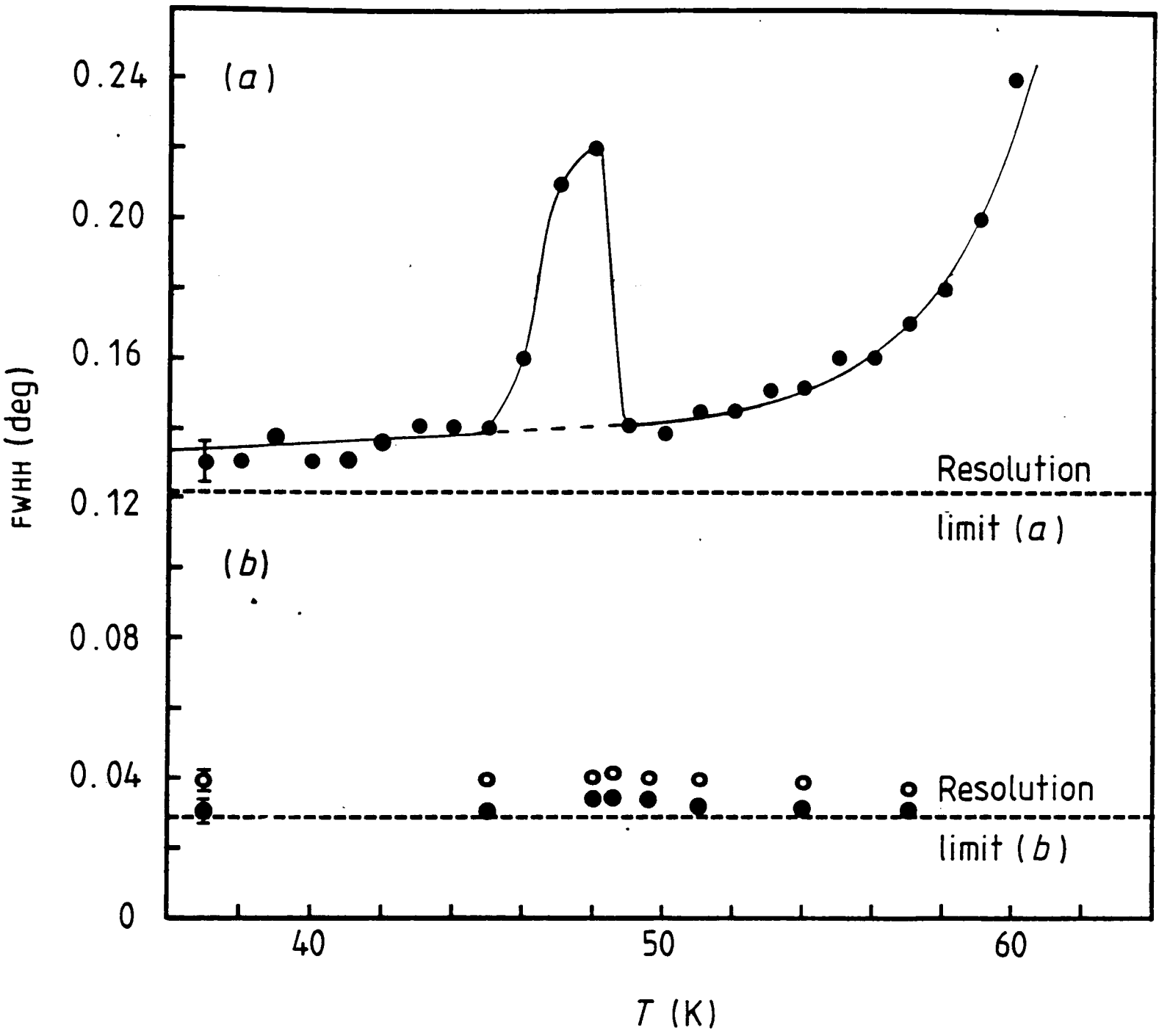

Figure 5.5 - The width (see text) of the $(\frac{1}{3},-\frac{1}{3},0,9\frac{1}{3})$ satellite reflection as the sample is cooled from 65K at a rate of 4K per hour. The resolution limit is for the instrument in its low-resolution configuration. (b) The width (● along [hh̄00] and o along [0001]) of the same reflection derived from grid scans in which the sample had been allowed to reach long-term equilibrium. The resolution limit in this case is for the instrument operating in its high-resolution mode. Typical error bars are shown for (a) and (b).

cycled through the transition a number of times. However, subsequent measurements conducted on a short timescale revealed, once again, the larger thermal hysteresis. Our conclusion is that structural memory effects, such as are in evidence at the ~27K transition, are not observable at the ~49K transition and that the ordering of the structure in this temperature range is simply subject to rather long equilibrium times (of the order of several hours).

Further evidence of the long equilibrium times is seen in the measured temperature dependence of the intensity and width of a satellite reflection shown in Figures (5.4) and (5.5a). To obtain these data the instrument was operated in a lower-resolution mode, as a conventional two-circle diffractometer (i.e. the silicon crystal used to collimate the scattered beam was removed). The integrated intensity was measured using an omega scan (rotating crystal, stationary detector) and the sample was cooled from 65K, through the ~61K and ~49K transitions to 37K, with a rate of change of temperature of approximately 4K per hour. Figure (5.4) shows the measured intensity as a function of temperature. Within the limits of the experimental error it can be seen that there are two temperature regimes, separated by the ~49K phase transition, in each of which the temperature dependence of the intensity is linear; and the rate of change of intensity in the commensurably modulated phase is roughly double that in the incommensurate phase. The linear temperature dependence is unexpected. In transitions to incommensurate phases the first-order satellites are primary order parameters of those phases (Bruce and Cowley 1981) and the relationship

$$I \alpha (T_c - T)^{2\beta}$$

describes the temperature dependence of the integrated intensity of the satellites. A linear temperature dependence corresponds to a β value of 0.5, the classical value of the critical exponent for systems obeying mean field theory. An incommensurate phase with a six-component order parameter (as we have in this case) is not, however, expected to show such classical behaviour; rather, β is expected to be less than 0.5, corresponding to the magnitude of dI/dT increasing as T_c is approached from below. A similarly linear temperature dependence of satellite intensities has been observed recently in at least two other incommensurates, $(N(CD_3))_4ZnCl_4$ (Marion et al 1984) and TMATC-Co (Fjaer et al 1985). In the latter case the (almost) linear temperature dependence of the

satellite intensities was explained in terms of a simultaneous reduction and smearing of the transition temperature as a result of X-ray irradiation damage to the sample. The relatively rapid rate of change of temperature during our measurements appears to introduce a similar reduction and smearing of the transition temperature (see below), and it is suggested that this may account for the unexpectedly linear temperature dependence of the satellite intensities.

Perhaps the most revealing feature to emerge from these measurements is the apparent temperature dependence of the width of the satellite reflection, as shown in Figure (5.5a). Although no instrumental resolution correction has been applied to these data, it is quite clear that the width decreases as the temperature falls throughout the incommensurate phase. The sharply increased width in the region of the ~49K phase transition is due simply to the co-existence of the commensurate and incommensurate phases; the ~3K temperature range of this co-existence, and the shift in the average transition temperature of the bulk crystal from 49.1(1)K to 47(2)K, illustrates the simultaneous smearing and reduction of the transition temperature referred to above. Then, in the commensurably modulated phase, the width of the satellite reflection continues to decrease with falling T but is still not resolution limited, indicating that true long-range order has not been established. Unfortunately, the nature of the instrumental resolution function in its lower-resolution mode does not allow us to determine unambiguously the direction of the additional width. Figure (5.5b) shows the width, along [hh̄00] and [0001], of the same satellite reflection derived from the high-resolution grid scans used to obtain the temperature dependence of the wave-vector. These data - which were obtained over a very much longer timescale than the data of Figure (5.5a) and after the sample had been allowed to equilibriate in the modulated phase for a period of several days - show that the satellite width is virtually independant of temperature. Along [hh̄00] the width is resolution limited within error, but there is a small elongation in the [0001] direction, indicating that true long-range order is not established in that direction even after very long times. It now seems clear that the curve of Figure (5.5a) demonstrates a time-dependent ordering of the structure of proustite in the modulated phases rather than a temperature-dependent width effect. This ordering process appears to have a time constant of several hours and even then remains incomplete.

In addition to the above measurements, considerable effort was directed towards searching for higher-order satellites. A systematic search, at 31K, of the region of reciprocal space illustrated in Figure (5.6) revealed no

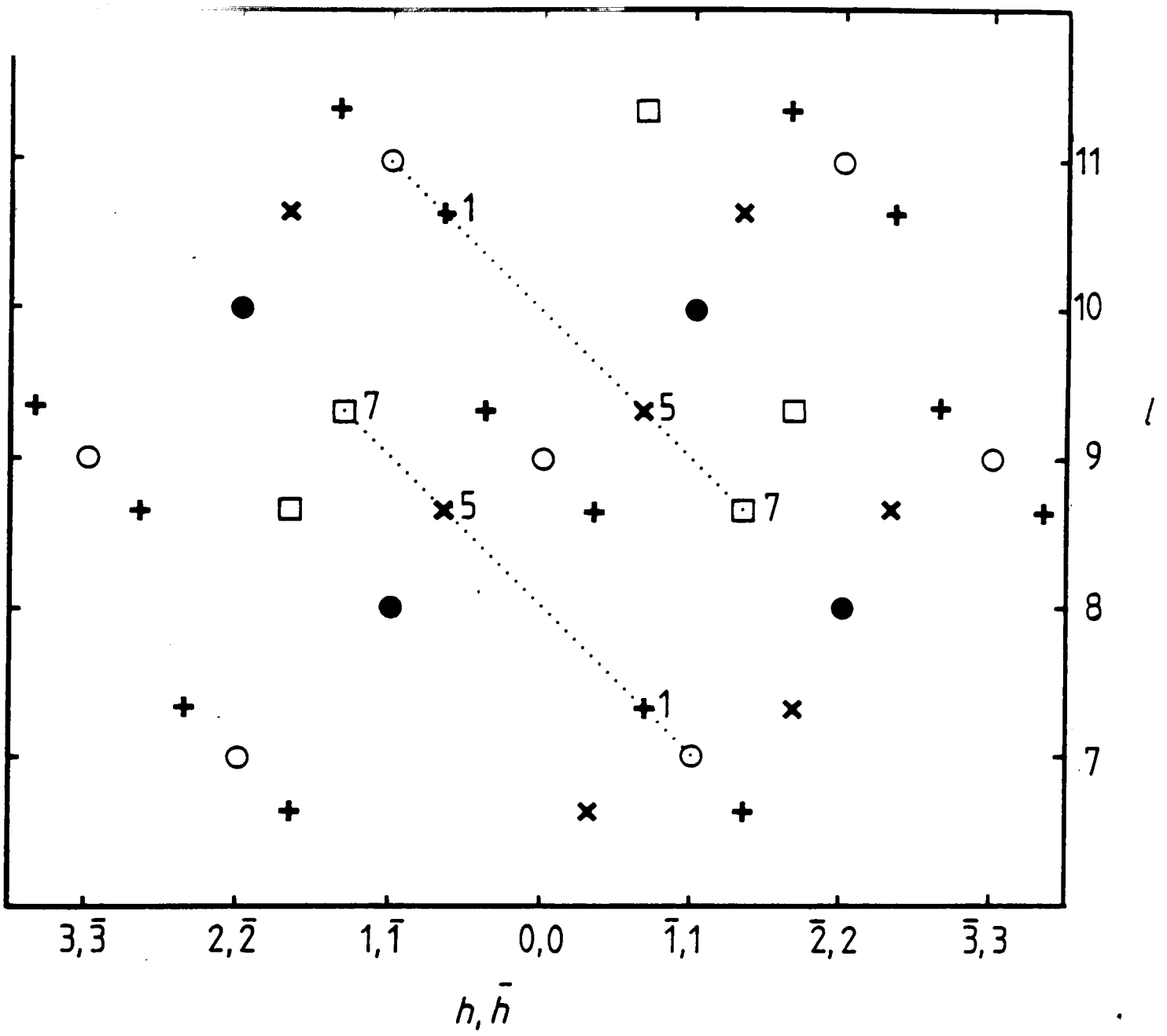

Figure 5.6 - Part of the (hh̄0l) reciprocal lattice plane examined in this experiment showing:- ●= the allowed reflections of R3c (h+l=3n), o= the c-glide absences (l ≠ 2n), += first-order satellites, x= fifth-order satellites, ⊡= seventh-order satellites as labelled for two particular cases. Note the absence of first-order satellites associated with the reflections (l=2n) in this reciprocal lattice plane (Nelmes et al 1984).

evidence of second-order satellites; but significant scattering was found at a number of positions corresponding to fifth and seventh-order satellites. The intensities of the strongest fifth and seventh-order satellites were found to be roughly 10% of the intensities of strong first-order satellites. The sequence of odd-order satellites was broken by the absence of third-order satellites. The intensities of all of the measurable fifth and seventh-order satellites were found to decrease to zero on warming to the ~49K phase transition. The systematic search also confirmed the observation, reported in our previous paper, that satellites associated with reciprocal lattice points with l=2n are either absent or are too weak to be observed in this plane (Nelmes et al 1984).

As we discussed in our previous paper, in relation to scattering observed at reciprocal lattice points forbidden by the c-glide extinction rule (in this plane, l≠2n), multiple-scattering effects must be considered. In principle, reflections corresponding to second, fifth and seventh-order satellites can be generated by combinations of two first-order satellite reflections. Although we were unable to carry out a direct test to eliminate multiple-scattering as a possible source of these reflections, we believe that there are three arguments against it. Firstly, we were unable to find any scattering at the second-order satellite positions; secondly, the intensities of the observed higher-order satellites are considerably larger than would be expected from multiple scattering originating from the coupling of two first-order satellites; and finally, the disappearance of all of the observed fifth and seventh-order satellites at ~49K suggests that they are a real feature of the commensurably modulated phase.

To summarise, our results show that the incommensurate phase between ~49K and ~61K in proustite is described by the six wave-vectors

$$q_1=(\tfrac{1}{3}-\delta_1,-(\tfrac{1}{3}-\delta_1),0,\tfrac{1}{3}-\delta_2),\ q_2=-q_1$$

$$q_3=(0,\tfrac{1}{3}-\delta_1,-(\tfrac{1}{3}-\delta_1),\tfrac{1}{3}-\delta_2),\ q_4=-q_3$$

$$q_5=(-(\tfrac{1}{3}-\delta_1),0,\tfrac{1}{3}-\delta_1,\tfrac{1}{3}-\delta_2),\ q_6=-q_5$$

where $\delta_1 \neq \delta_2$ and both δ_1 and δ_2 are temperature dependent. The modulation is, therefore, doubly incommensurate with components in the hexagonal $\mathbf{a}^*$ and $\mathbf{c}^*$ directions. On cooling there is a first-order lock-in

transition at 49.1(3)K to a commensurably modulated phase in which $\delta_1=\delta_2$=zero. This transition is accompanied by a thermal hysteresis of approximately 0.6K. Described in terms of the primitive-rhombohedral axes, the modulation wave-vector in the incommensurate phase has components in both the $[\bar{1}00]_{rh}$ and the $[011]_{rh}$ directions; but as the temperature increases towards the ~61K transition the $[\bar{1}00]_{rh}$ component approaches a commensurate value of $\frac{1}{9}$ whilst the $[011]_{rh}$ component remains clearly incommensurate. The ordering of the structure in proustite in the region of the ~49K transition is subject to very long time-constants (of the order of several hours) and future experimental studies of proustite must be designed with this in mind. Higher-order satellites (odd-orders only) were found in the commensurably modulated phase but their intensities decreased to zero on warming through the ~49K phase transition.

CHAPTER SIX

A High-Resolution X-ray Scattering Study of Monoclinic Incommensurate $BaMnF_4$

Preamble to chapters six and seven

The following chapters, six and seven, have been accepted for publication in Journal of Physics C: Solid State Physics. Chapter six (Ryan), as a full paper, and chapter seven (Ryan, Cowley and Andrews) as a letter to the editor. Both form part of a longstanding (and continuing) Edinburgh involvement with this material. $BaMnF_4$ is of interest because of its second-order phase transition to an incommensurably modulated phase, characterised by a four-component order-parameter. In principle, then, it should be possible to experimentally test the theoretically predicted critical exponents, γ, ν and β, in an n=4, d=3 system by studying this material. In practice, however, such a measurement is found to be complicated by a number of factors; in particular, the formation of domains below T_c and the role of defects above T_c. It is with these two factors that the following chapters are concerned.

INTRODUCTION

Following the discovery of its incommensurate phase (Shapiro et al 1976) the material $BaMnF_4$ has been the object of continuing interest, both theoretical and experimental. At room temperature its structure is known to be orthorhombic with space group $A2_1am$ (Keve et al 1969). The lattice parameters of the orthorhombic phase are **a**=5.998Å, **b**=15.098Å and **c**=4.22Å. On cooling through the second-order phase transition at ∿247K a distortion characterised by a wave-vector **q**=(0.39,0.5,0.5) appears, corresponding to an incommensurate modulation along the polar **a**-axis accompanied by a unit cell doubling in the **bc** plane. The modulation is unusual in that the incommensurate component remains virtually independent of temperature on further cooling with no 'lock-in' transition to a commensurate value.

Cox et al (1979) proposed two alternative structures for the incommensurate phase: type (i), in which the average structure retains the 2mm point group symmetry of the orthorhombic phase and the modulation is characterised by two symmetry related pairs of wave-vectors

$\mathbf{q}_1$=(0.39,0.5,0.5), $\mathbf{q}_2$=- $\mathbf{q}_1$ and $\mathbf{q}_3$=(0.39,-0.5,0.5), $\mathbf{q}_4$=- $\mathbf{q}_3$

or type (ii), in which the symmetry of the average structure is reduced from orthorhombic to monoclinic and the crystal forms twin domains with modulations characterised by only one of the above pairs of wavectors in each domain. The authors suggested that solution (i) appeared to be more likely. The type (ii) solution, however, is in closer agreement with theoretical analyses of the phase transition which predict a lowering of the point group symmetry from 2mm to 2 (Scott 1979, Dvorak and Fousek 1980, Golovko et al 1983).

More recently, Cox et al (1983) have reported further X-ray and neutron scattering studies which show that systematic absences amongst second-order satellite reflections are consistent with a type (ii) structure. As no direct evidence of the monoclinic distortion could be found its magnitude was concluded to be very small.

Further evidence of the reduction in symmetry was seen in the results of optical polarimetry measurements by Pisarev et al (1983). Once again, however, the technique provided no quantitative measure of the monoclinic distortion angle. The first direct indication of its magnitude was obtained from

X-ray scattering measurements by Barthes-Regis et al (1983). A systematic broadening of Bragg peaks parallel to the $\mathbf{b}^*$ direction was interpreted in terms of a departure of the angle α, between **b** and **c**, from 90° in each of the twin domains which presumably make up the sample crystal in the incommensurate phase. Although the instrumental resolution was insufficiently good to resolve the twinned Bragg peaks, the observed broadening corresponded to a departure of roughly 0.03° in the angle α from 90° at T_c-100K.

This chapter describes, and discusses the implications of, two X-ray scattering measurements performed on a high-resolution triple-crystal X-ray diffractometer mounted on a GEC Avionics high-brilliance rotating-anode source. The first was designed to confirm the existence of monoclinic domains in the incommensurate phase and to provide a direct measurement of the monoclinic distortion angle. The second demonstrates that the distribution of domains within a sample crystal is not necessarily homogeneous and that the inhomogeneity can seriously complicate quantitative X-ray scattering measurements on this material.

EXPERIMENT 1.

In this experiment MoKα_1 X-rays were used and the primary beam was monochromated by the (111) reflection of a flat, symmetrically cut silicon crystal. A pre-monochromator slit system was used to eliminate the Kα_2 component. The wave-vector spread of the incident beam was determined by the intrinsic width of the MoKα_1 spectral line (FWHH=0.00029Å) and the dynamical width of the Si(111) Bragg reflection (approximately 0.002°). This beam was incident on an extended face of the sample crystal, a cuboid of dimensions 5x2x2 mm corresponding to the **a**, **b**, and **c** axes. The crystal was grown at Bell Laboratories from zone melted materials and was from the same source as the crystals examined by Cox et al (1979,1983).

Careful preparation of the sample face is of utmost importance in all high-resolution X-ray scattering measurements performed in reflection from an extended face sample crystal. In this case the face was lapped with 0.25μm diamond paste to give a flat and optically perfect finish and then etched in concentrated orthophosphoric acid to remove sub-microscopic surface damage induced by the polishing process. At room temperature the etching reaction proceeds only very slowly. At 120°C a total reaction time of about 25 minutes was required to remove the damaged surface layer. Rocking curve measurements were used to assess the crystal quality and, ultimately, a width of 0.006° was achieved.

The prepared sample was then mounted, in an isothermal enclosure, on the cold stage of a closed-cycle cryo-refrigerator allowing temperature control over the range 10K to 300K with a stability of ±0.02K and an absolute accuracy of ±0.3K. To permit a direct measurement of the unit cell angle α the crystal was oriented with the $\mathbf{b}^*$ and $\mathbf{c}^*$ axes in the scattering plane and with the $\mathbf{c}^*$ axis normal to the crystal face.

A second Si(111) crystal was used to collimate the scattered beam. This crystal, which was identical with the monochromator crystal, was set in the non dispersive (+1,-n,+1) configuration and limited the angular acceptance of the detector system to approximately 0.002°.

Figure (6.1) shows the results of high-resolution grid scans in the neighbourhood of the (006) Bragg reflection as the sample is cooled from 250K,

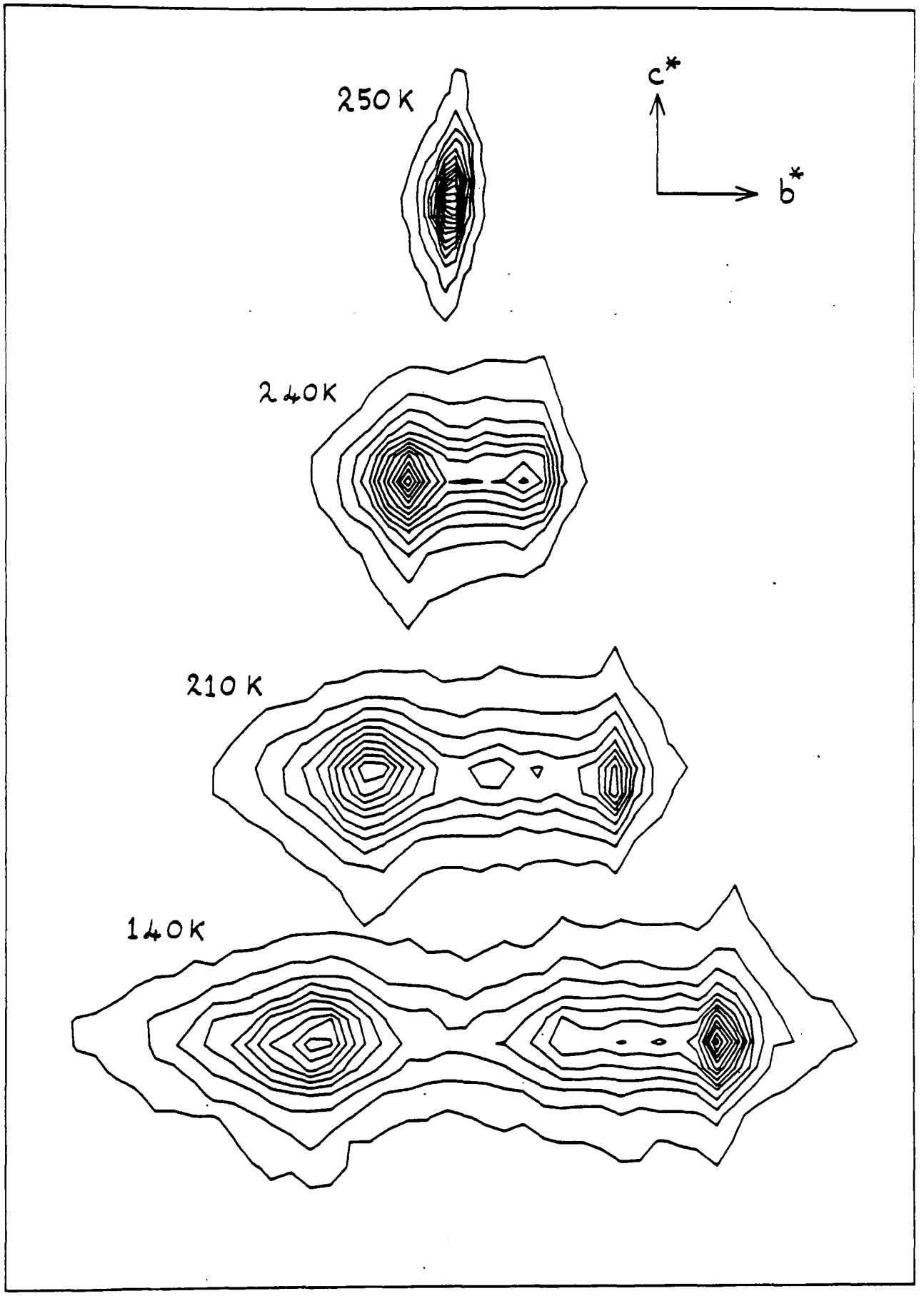

Figure 6.1 - Isointensity contour plots of X-ray scattering intensity in the region of the (006) (orthorhombic phase) reciprocal lattice point showing the development of twin, monoclinic phase Bragg peaks as the sample is cooled through the ~247K transition.

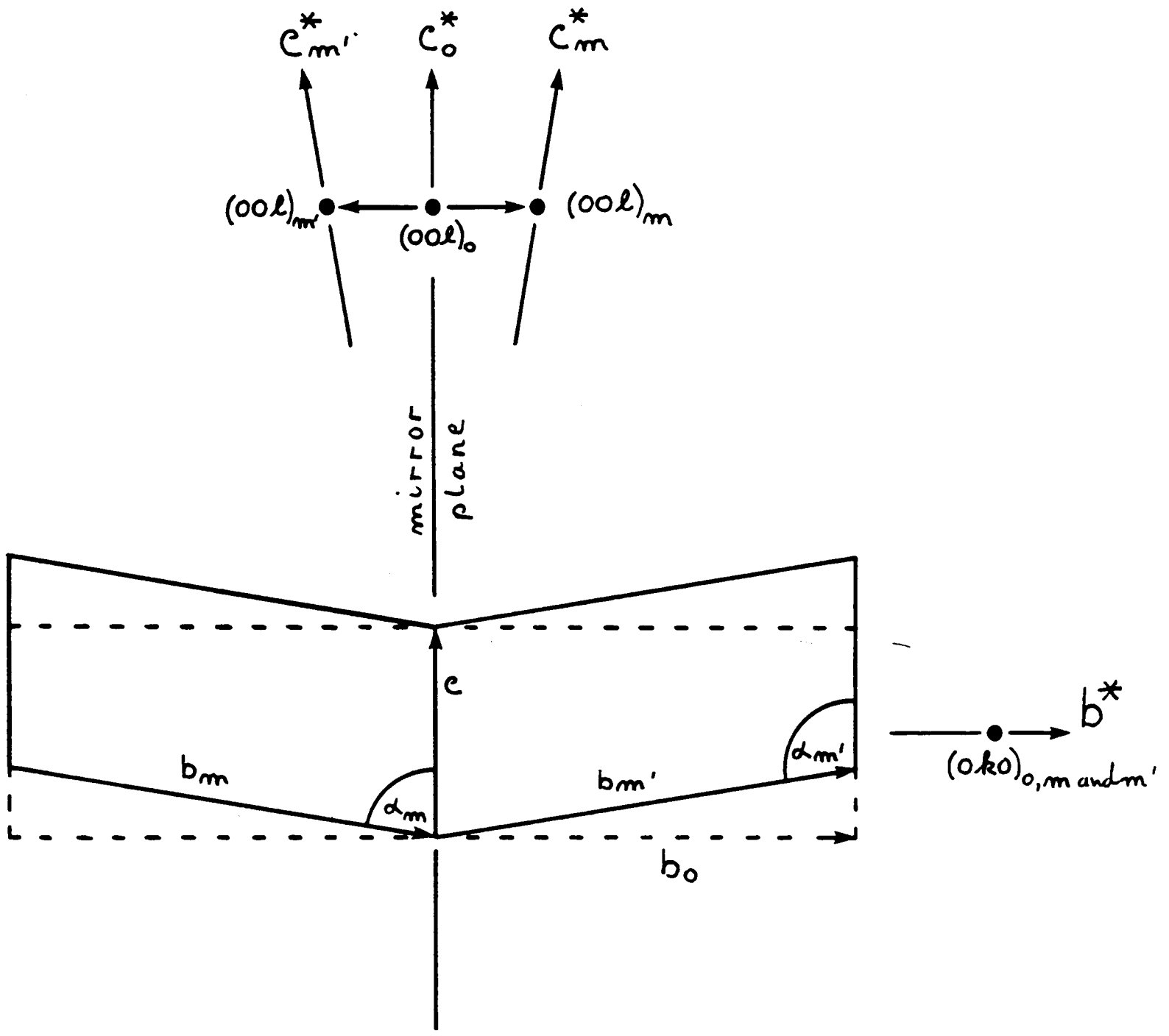

Figure 6.2 – The relationship between the orthorhombic phase unit cell and reciprocal lattice (identified by the subscript o) and the twin monoclinic unit cells and reciprocal lattices (identified by the subscripts m and m'). The mirror twin plane is perpendicular to $\mathbf{b}^*$.

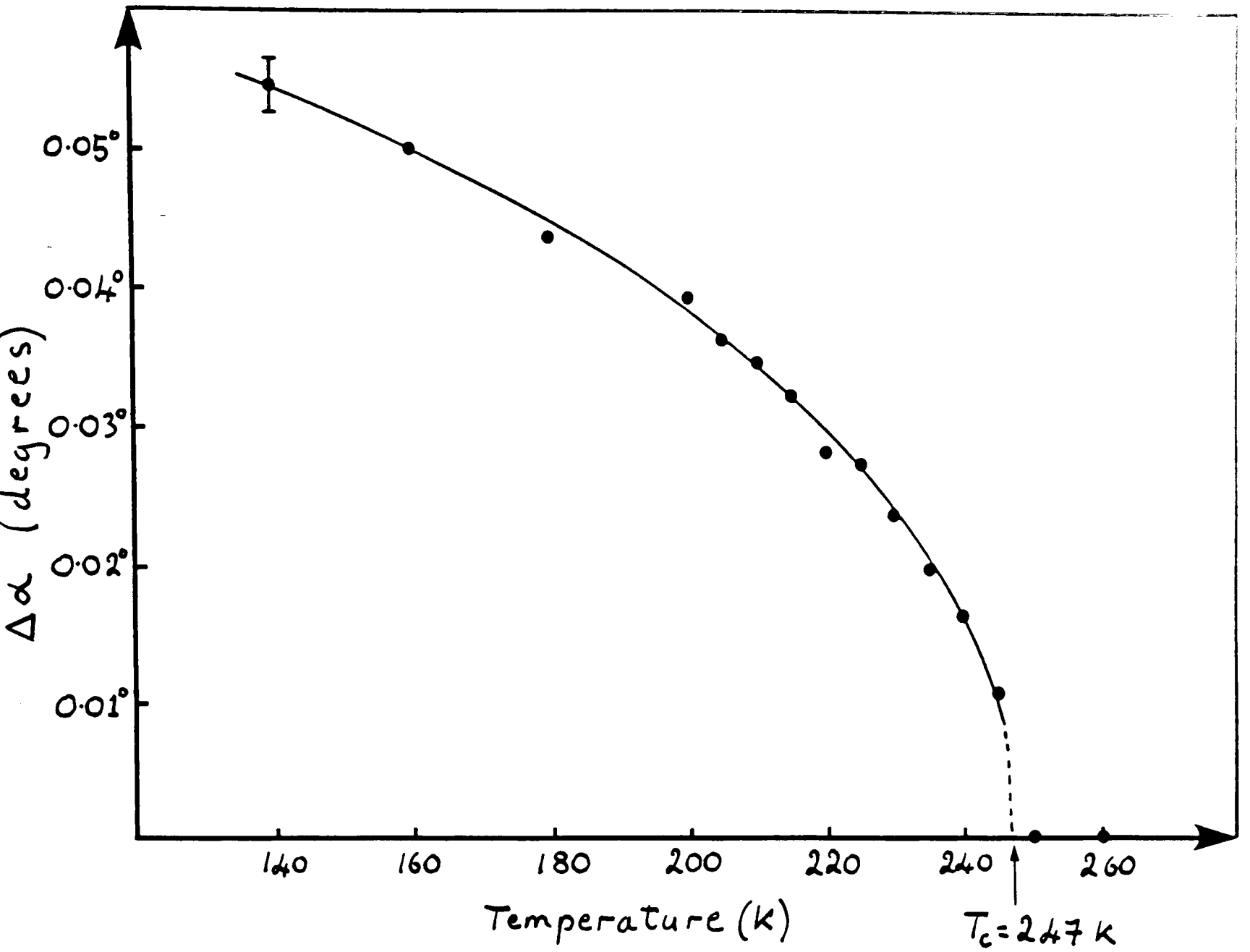

Figure 6.3 - The temperature dependence of $\Delta\alpha$, the departure of the unique angle α from 90°.

through the phase transition (at ~247K) to 140K. The instrumental resolution is well illustrated by the plot of the orthorhombic phase Bragg reflection at 250K. To a very good first approximation the width perpendicular to the scattering vector is dominated by the mosaic spread of the sample crystal (approximately 0.006° FWHH) and parallel to the scattering vector by the spectral dispersion due to the intrinsic linewidth of the MoKα_1 line (approximately 0.01° FWHH at the (006) Bragg angle of 30.4°).

As the crystal is cooled through the transition, the single Bragg peak of the orthorhombic phase clearly splits into two; confirming the coexistence of two distinct domains in the incommensurate phase. Similar scans, performed at general points in the reciprocal lattice, show that the magnitude of the splitting is consistently proportional to the distance from the $\mathbf{b}^*$ axis and that the direction of the splitting is always parallel to the $\mathbf{b}^*$ axis. The observed splitting is, therefore, entirely consistent with the formation of monoclinic domains related by mirror symmetry as illustrated in Figure (6.2). A reciprocal lattice point, $(hk\ell)_o$, of the orthorhombic phase splits into two reciprocal lattice points, $(hk\ell)_m$ and $(hk\ell)_{m'}$, where the subscripts m and m′ refer to the monoclinic cells with $\alpha=(90°-\Delta\alpha)$ and $\alpha=(90°+\Delta\alpha)$ respectively. The angular separation of the $(00\ell)_m$ and $(00\ell)_{m'}$ Bragg reflections is equivalent to $2\Delta\alpha$, where $\Delta\alpha$ is the departure from 90° of the unit cell angle α.

Figure (6.3) shows the temperature dependence of $\Delta\alpha$ as the sample crystal is cooled from 260K through the phase transition to 140K. As anticipated, the magnitude of $\Delta\alpha$ is very small: indeed at T_c−100K it is only 0.05° and just below T_c it is less than 0.01°. A log-log plot of $\Delta\alpha$ against reduced temperature (T_c−T) reveals that the behaviour of $\Delta\alpha$ is well described by a power law and the value of the exponent is found to be 0.46±0.02. The very small size of $\Delta\alpha$ means, of course, that in a conventional X-ray or neutron diffraction experiment with a reciprocal space resolution of, typically, 10^{-2}Å^{-1} the adjacent monoclinic phase Bragg peaks are unresolved.

The monoclinic shear results in the loss of the mirror planes perpendicular to the $\mathbf{b}^*$ and $\mathbf{c}^*$ axes. Weissenberg photographs and scans using a four circle diffractometer have shown that reflections $(hk\ell)$ with $k+\ell$ odd which are forbidden by the A-face centered lattice in the orthorhombic phase are also absent below T_c (Ryan and Amin, unpublished). In principle, the incommensurate modulation along the **a** axis destroys translational periodicity in that direction but the average structure can be regarded as retaining the 2_1

screw diad (Scott 1979). The most likely space group of the average structure in the low temperature phase is, therefore, $P2_1$. The full symmetry of the incommensurate structure cannot, of course, be described by one of the 230 3-dimensional space groups (Janner and Janssen 1977).

Having established that the crystal does, indeed, form monoclinic domains in the incommensurate phase it is of interest to consider how the twinning affects the interpretation of X-ray (or neutron) diffraction data. In general, reflections $(hk\ell)_m$ and $(hk\ell)_{m'}$ are not related by the point group symmetry of the monoclinic cell. Their observed intensities will be determined by their respective structure factors and by the relative proportions of each of the two domains sampled in the experiment (i.e. the twin fraction). Reflections $(hk\ell)_m$ and $(h\text{-}k\ell)_{m'}$ are, however, related by the mirror twinning operation and their relative intensities are related by the twin fraction (ignoring extinction effects and assuming that absorbtion is correctable). Thus, the very high reciprocal space resolution of the present experiment permits a direct measurement of the twin fraction and the collection of a limited set of intensity data from each of the two monoclinic domains, but the geometry of the instrument precludes the collection of a full crystallographic data set.

The variability of the twin fraction as a function of sample temperature is well illustrated in Figure (6.1). In this case the relative intensities of the two Bragg reflections $(006)_m$ and $(006)_{m'}$ are determined by the twin fraction and it is obvious that this alters dramatically as the sample is cooled, even although the portion of the sample crystal examined in this experiment remained, in principle, the same throughout the measurement. This is not wholly unexpected as similar behaviour has been reported in, for instance, the tetragonal phase of the perovskite $RbCaF_3$ (Maetz et al 1978). The variable twin fraction, of course, introduces an additional uncertainty into any experiment which is sensitive to the domain structure.

In a conventional X-ray or neutron diffraction experiment the adjacent, twin Bragg peaks are inseparable. To correct such data for the effects of twinning an accurate knowlege of the twin fraction (which must differ significantly from 50:50) is required (Rees 1983). Interestingly, this information is accessible in the first-order satellites.

Each fundamental Bragg reflection, $(hk\ell)_{m \text{ or } m'}$, is accompanied by two first-order satellite peaks at $(hk\ell)_m$ or $_{m'} \pm \mathbf{q}_i$ and by two second-order satellite

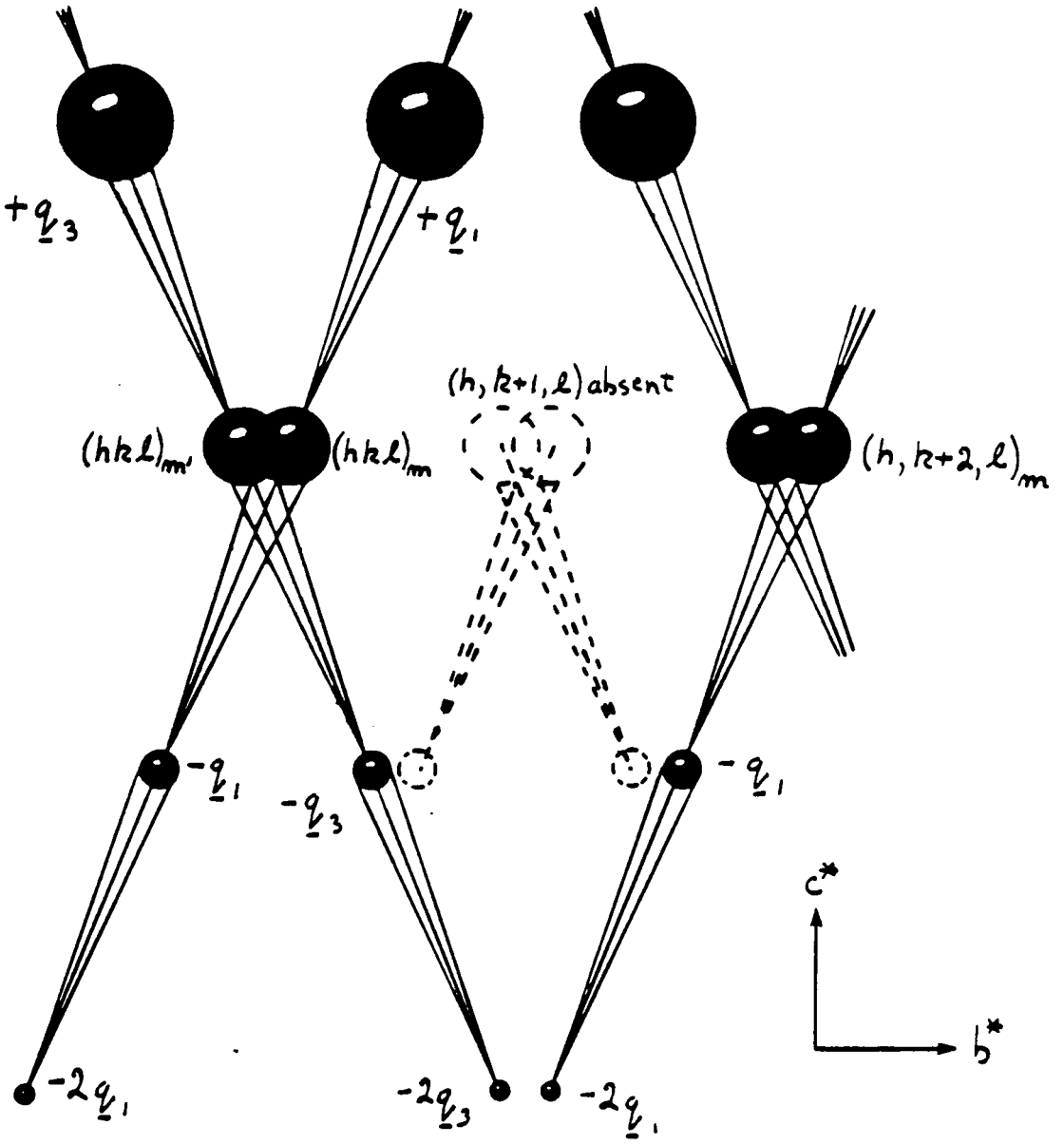

Figure 6.4 – A schematic view of a representative part of reciprocal space showing the relative positions of typical Bragg, first- and second-order satellite peaks in the incommensurate (monoclinic) phase. Note that although Bragg peaks and second-order satellite peaks are effectively superimposed upon peaks originating in the twin domain, first-order satellites are not.

peaks at $(hk\ell)_{m \text{ or } m'} \pm 2\mathbf{q}_i$ where $\mathbf{q}_i$ is either $\mathbf{q}_1=(0.39,0.5,0.5)$ or $\mathbf{q}_3=(0.39,-0.5,0.5)$. Unfortunately, the relationship between the modes $\mathbf{q}_1$ and $\mathbf{q}_3$ and the monoclinic domains with $\alpha=(90°+\Delta\alpha)$ and $\alpha=(90°-\Delta\alpha)$ is uncertain and further experimental work is required to resolve this question. For the present discussion, the mode $\mathbf{q}_1$ has been arbitrarily assigned to the domain m with $\alpha=(90°-\Delta\alpha)$. Figure (6.4) shows, schematically, the relative locations of Bragg, first- and second-order satellite peaks in a representative volume of reciprocal space. The (incommensurate) $\mathbf{a}^*$ axis is normal to the plane of the diagram and the $\mathbf{b}^*$ and $\mathbf{c}^*$ axes lie within the plane of the diagram.

The relationship between the Bragg peaks,$(hk\ell)_m$ and $(hk\ell)_{m'}$ has already been discussed. Considering the typical first-order satellite peak $(hk\ell)_{m'}-\mathbf{q}_3$, it can be seen to lie adjacent to the position at which one might expect to find the first-order satellite $(h,k+1,\ell)_m-\mathbf{q}_1$, were it not forbidden by the A face-centered lattice. First-order satellite peaks are, therefore, <u>not superimposed</u> in a conventional diffraction experiment: i.e. the incommensurate reciprocal lattice point $(hk\ell)_{m \text{ or } m'} \pm \mathbf{q}_i$ cannot be generated by any other combination of (allowed) $(hk\ell)_{m \text{ or } m'}$ and $\mathbf{q}_i$. Consequently it is possible to collect two, distinct monodomain sets of first-order satellite intensities and, by comparison of the intensities of satellites related by the mirror twinning operation, extract an unambiguous measure of the twin fraction.

The typical second-order satellite reflection $(hk\ell)_{m'}-2\mathbf{q}_3$ lies adjacent to the second-order satellite reflection $(h,k+2,\ell)_m-2\mathbf{q}_1$ which is allowed by the space group and originates in the twin domain. Their separation is identical to that of the Bragg peaks and they are, therefore, inseparable in a conventional diffraction experiment. In principle, as with Bragg reflections, an analytical separation of the intensities of superimposed second-order satellites is possible: but their low intensities (at least a factor of 10^{-3} down on typical Bragg reflections) probably makes this impracticable.

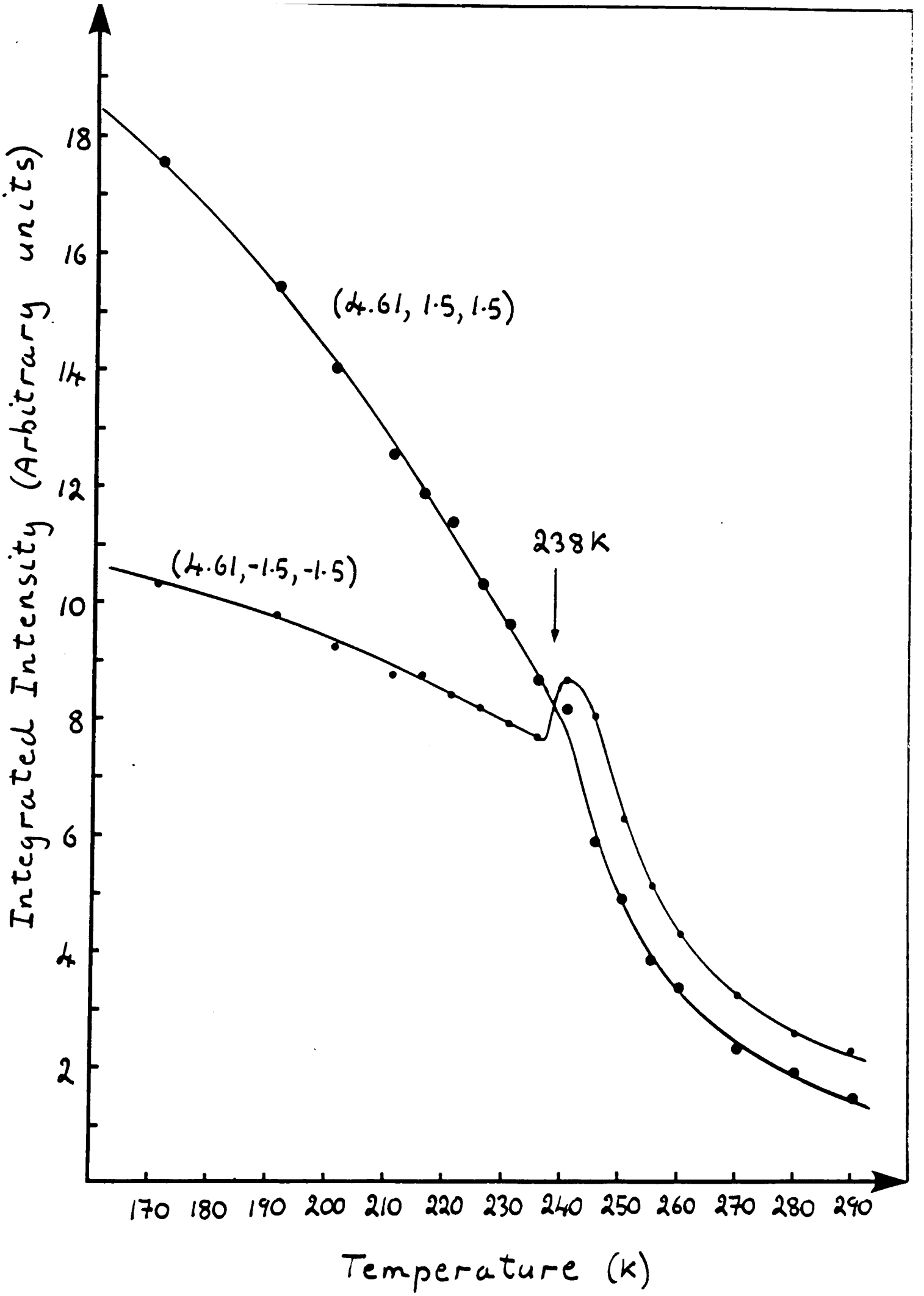

Figure 6.5 - The temperature dependence of two typical first-order satellite peaks showing the anomalous behaviour at ~238K.

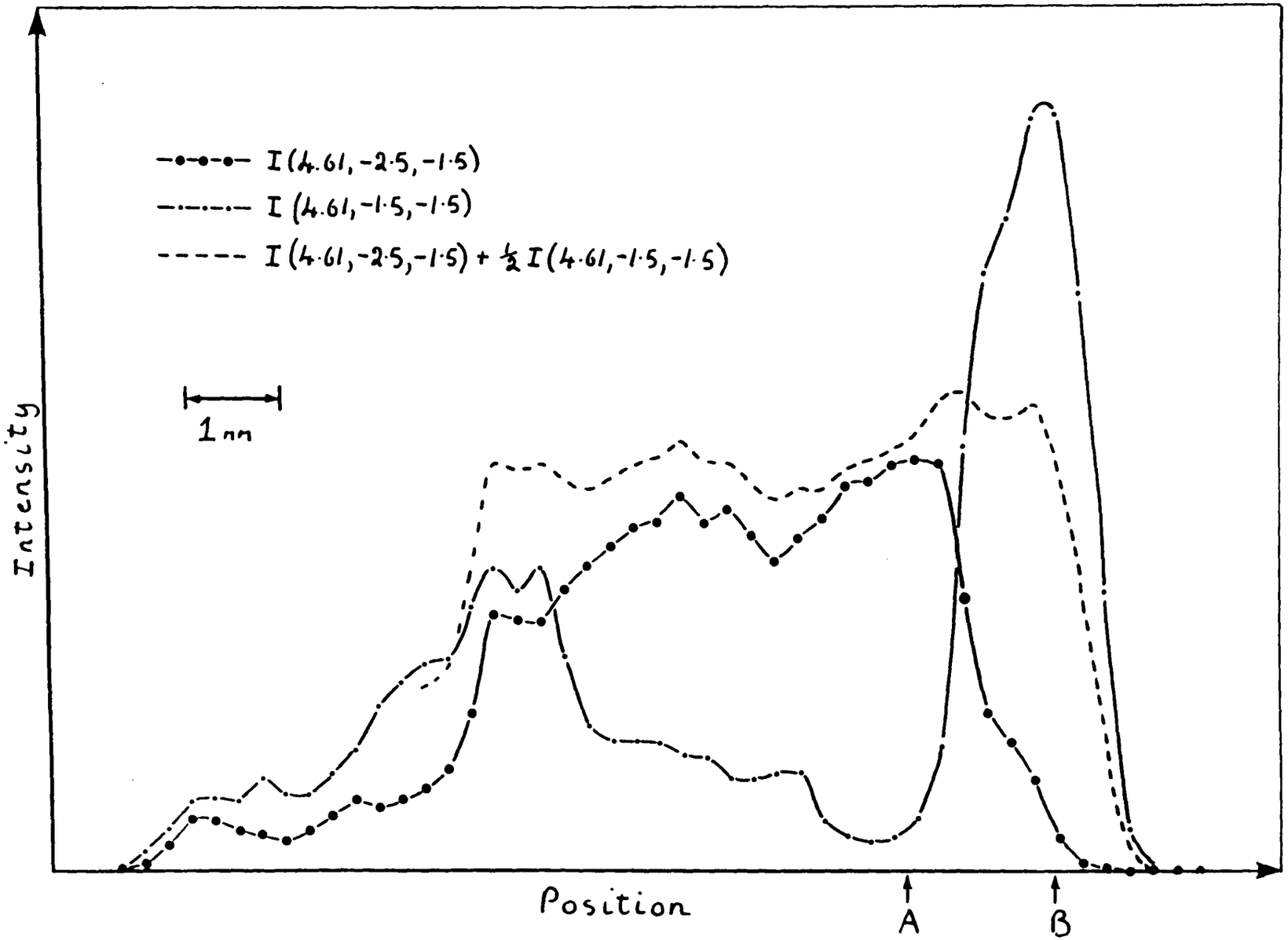

Figure 6.6 – The integrated intensities of two first-order satellite reflections as a function of position on the sample face. Each satellite originates in a different twin domain and their relative intensities provide a clear indication of the relative proportions of the twin domains in the sampled volume. The dotted line is a weighted sum of the two intensities.

EXPERIMENT 2.

The second experiment was performed using a different $BaMnF_4$ sample crystal, grown in the Clarendon Laboratory, University of Oxford, and was designed to study the critical behaviour of $BaMnF_4$ at the commemsurate-incommensurate phase transition in a sample with random impurities. The results will be described in detail in chapter 7. In the course of the experiment, however, several features were observed which are of relevance to the present discussion.

The sample face was prepared as described for experiment 1 and the crystal was mounted with the (100) and (011) axes in the scattering plane and with the (100) axis normal to the crystal face. The wave-vector $\mathbf{q}_1$=(0.39,0.5,0.5) lies within this reciprocal lattice plane, making access to Bragg, first- and second-order satellite peaks possible. CuKα X-rays were used with flat, pyrolytic graphite monochromator and analyser crystals to give a reciprocal space resolution of approximately 5×10^{-3}Å^{-1} in the scattering plane. Briefly, whilst attempting to measure the X-ray scattering intensity at the positions of a number of first-order satellites as the sample temperature was lowered through T_c, anomalous but reproducible results were obtained, as illustrated in Figure (6.5). The pronounced dip in the intensity of one of the satellite reflections at ∿238K was entirely unexpected. Further measurements showed that the occurence and magnitude of the dip were related to the position of the incident X-ray beam on the sample face.

To test the suspected connection between this anomaly and the domain distribution within the sample we performed a simple topograph of a horizontal strip of the sample crystal, approximately 1mm high and 8mm long with a horizontal resolution of approximately 0.2mm. This was accomplished by measuring the integrated intensities of two first-order satellite reflections, (4.61,-1.5,-1.5) and (4.61,-2.5,-1.5), as the sample was translated in steps of 0.25mm parallel to the crystal face. The (4.61,-1.5,-1.5) reflection originates in one of the two monoclinic domains and lay within the horizontal, scattering plane of the instrument (i.e. the zero-layer). Following the convention of Figure (4) this reflection is $(5,-1,-1)_m-\mathbf{q}_1$. The (4.61,-2.5,-1.5) reflection (or $(5,-3,-1)_{m'}-\mathbf{q}_3$) originates in the other domain and lay in the first-layer, with almost identical setting angles but with an inclination angle of 5.6° in normal beam Weissenberg geometry. Thus, by moving the detector out of the

horizontal plane by an appropriate amount to find the first-layer reflection, it was possible to measure the intensity of each of the two satellite reflections whilst sampling the same area of the crystal face. The results are shown in Figure (6.6).

Clearly, the relative proportion of each of the two monoclinic domains varies dramatically as a function of position on the sample face; indeed large parts of the crystal appear to be almost completely monodomain. Taking the intensity of (4.61,-2.5,-1.5) at position A and that of (4.61,-1.5,-1.5) at position B (i.e. the two most completely monodomain points on the topograph) it can be seen that the ratio of their intensities is almost exactly 1:2. The almost flat topped result obtained by plotting the sum, I(4.61,-2.5,-1.5)+0.5xI(4.61,-1.5,-1.5), as a function of position fully confirms the domain distribution hypothesis.

The origin of the anomalous dip in Figure (6.5) is now more obvious. Both softening modes, $\mathbf{q}_1$ and $\mathbf{q}_3$, are present in equal proportions in the orthorhombic phase. As the crystal is cooled through T_c the modes condense and the crystal forms distinct domains in which the modulation is characterised by only one of the modes, either $\mathbf{q}_1$ or $\mathbf{q}_3$. The domains, or perhaps clusters of domains, appear to form on a macroscopic scale (in this case on a scale considerably larger than the sampled area of the crystal) and the observed dip in the integrated intensity occurs at T_c if the sampled area forms predominantly the 'wrong' domain.

The formation of large domains at, or possibly just below, T_c with a consequent effect on measurements sensitive to the domain distribution may offer a possible explanation for the apparent occurence of two phase transitions in some samples of $BaMnF_4$ observed by a number of authors (Levstik et al 1975, Scott et al 1982, Hidaka et al 1984).

The lower transition temperature (∿238K as opposed to ∿247K in the previous sample crystal) is characteristic of incommensurate phases in which the modulation is pinned by defects or impurities. Lavrencic et al (1981) have demonstrated that T_c in a $BaMnF_4$ sample is highly sensitive to the presence of defects. They observed a 10K reduction in T_c after extended heat treatment and interpreted this effect in terms of an increasing concentration of fluorine vacancies as a result of fluorines 'boiling off' the sample surface.

CONCLUSIONS

The existence of twin, monoclinic domains in the incommensurate phase of $BaMnF_4$ has been confirmed by X-ray scattering and the magnitude of the monoclinic distortion as a function of temperature has been directly measured for the first time. At T_c-100K $\Delta\alpha$, the deviation from 90° of the angle α is approximately 0.05°. This result is in agreement with theoretical predictions and with previous experimental work and resolves a longstanding uncertainty. The close nature of the twinning means that twinned Bragg peaks are effectively superimposed in any conventional X-ray or neutron scattering experiment. First-order satellite peaks do not, however, overlap, and a comparison of the intensities of satellites related by the twinning operation affords an unambiguous measure of the twin fraction. In principle, at least, it is possible to use this information to separate analytically the twinned Bragg peaks but the variability of the twin fraction as a function of temperature and of position within a sample crystal poses a number of potentially serious problems.

X-ray scattering experiments are particularly vulnerable to this variability. The very high absorbtion of $BaMnF_4$ for the commonly used X-ray wavelengths (for CuKα μ=108.3mm^{-1} and for MoKα μ=14mm^{-1}) means that, unless an impractically tiny sample crystal is used, the experiment does not uniformly probe the entire sample crystal in any given scattering geometry. Thus, as Figures (6.5) and (6.6) show, changes in temperature or in scattering geometry may correlate with changes in the twin fraction and, as a result, an additional complication may be introduced into experimental measurements of quantities sensitive to the domain distribution.

CHAPTER SEVEN

An Experimental Study of the Effect of Random Fields in $BaMnF_4$: a Material with Continuous Symmetry

The application of randomly directed fields has a drastic effect on the properties and phase transitions of systems. Imry and Ma (1975) considered the effect of a site random magnetic field on the ordering of a ferromagnet and, by comparing the energy gained by reversing a domain with the energy needed to produce a domain wall, showed that the long range ferromagnetic order would be destroyed in systems with dimensionality, d, less than d_c, where d_c was 2 for Ising systems and 4 for systems with continuous spin symmetry. By using the suggestion of Fishman and Aharony (1979), that a uniform magnetic field applied to a random Ising antiferromagnet produces a random staggered field, there have now been many experimental studies made of Ising systems in 2 and 3 dimensions, as reviewed by Cowley et al (1984), Birgeneau et al (1984) and reported subsequently (Cowley et al, 1985, Yoshizawa et al, 1985, Belanger et al, 1985, and Birgeneau et al, 1985). The results show behaviour considerably more complex than predicted by Imry and Ma, in that, when the systems are cooled in a random field, there is a well defined transition below which the system has many metastable states and long range order is achieved only when the random field is removed. These properties are still not understood in detail and a review of the theory is given by Villain (1985).

Very little experimental work has been performed on systems with continuous spin symmetry because applying a uniform field to an antiferromagnet with continuous symmetry produces a spin-flop phase, when the random fields no longer influence the ordering. The behaviour of systems with a continuous symmetry can, however, be studied by the introduction of impurities into incommensurably modulated phases. The impurities then act as local fields which pin the phase of the incommensurate modulation and the resulting properties are described by the same Hamiltonian as that which describes the effect of site random magnetic fields on a continuous spin system.

This chapter describes detailed measurements of the structural phase transition to an incommensurately modulated phase in two samples of $BaMnF_4$ containing different defect concentrations. The results are qualitatively very similar to the experimental results found in the Ising systems, which is surprising in view of the difference expected by the arguments of Imry and Ma. There is a well defined transition, below which long range order is not established and the scattering is characterised by a Lorentzian squared lineshape.

$BaMnF_4$ has an orthorhombic crystal structure at room temperature and, on cooling to ~ 247K, undergoes a second-order phase transition to an incommensurably modulated phase (Cox et al, 1979). Somewhat unusually, the material remains incommensurate down to the lowest temperatures, and the phase transition is associated with 4 wavevectors

$$\mathbf{q}_1=(0.39, 0.5, 0.5),\ \mathbf{q}_2=-\mathbf{q}_1$$
$$\mathbf{q}_3=(0.39.-0.5, 0.5),\ \mathbf{q}_4=-\mathbf{q}_3$$

The low temperature structure is described by monoclinic domains associated with either the wavevectors $\mathbf{q}_1$ and $\mathbf{q}_2$, or $\mathbf{q}_3$ and $\mathbf{q}_4$ (Cox et al, 1983, Barthes-Regis et al, 1983 and this thesis, chapter 6).

Two crystals were used in this work. One was grown by H.J. Guggenheim at Bell Laboratories from zone melted materials in the same way as those used earlier by Cox et al (1979, 1983), whereas the other was grown by the crystal growing group at Oxford University. The former crystal was optically clear and had a mosaic spread of 0.006° while the latter was optically cloudy and had a mosaic spread of 0.022°, showing that the Bell crystal contained far fewer defects. The surfaces of the crystals were carefully prepared as described in chapter 6, and then the crystals were mounted in a closed cycle cryostat on a triple crystal X-ray diffractometer with the [100] and [011] axes in the scattering plane. The temperature could be controlled with a stability of ±0.02K and measured to an absolute accuracy of ±0.3K.

The X-ray source was a GEC Avionics rotating-anode generator. $CuK\alpha_1$ X-rays were selected and collimated by reflection from either a flat Si(111) crystal or a flat pyrolytic graphite (0002) crystal. In the former case the scattered beam was collimated either by a simple slit or by an identical Si(111)

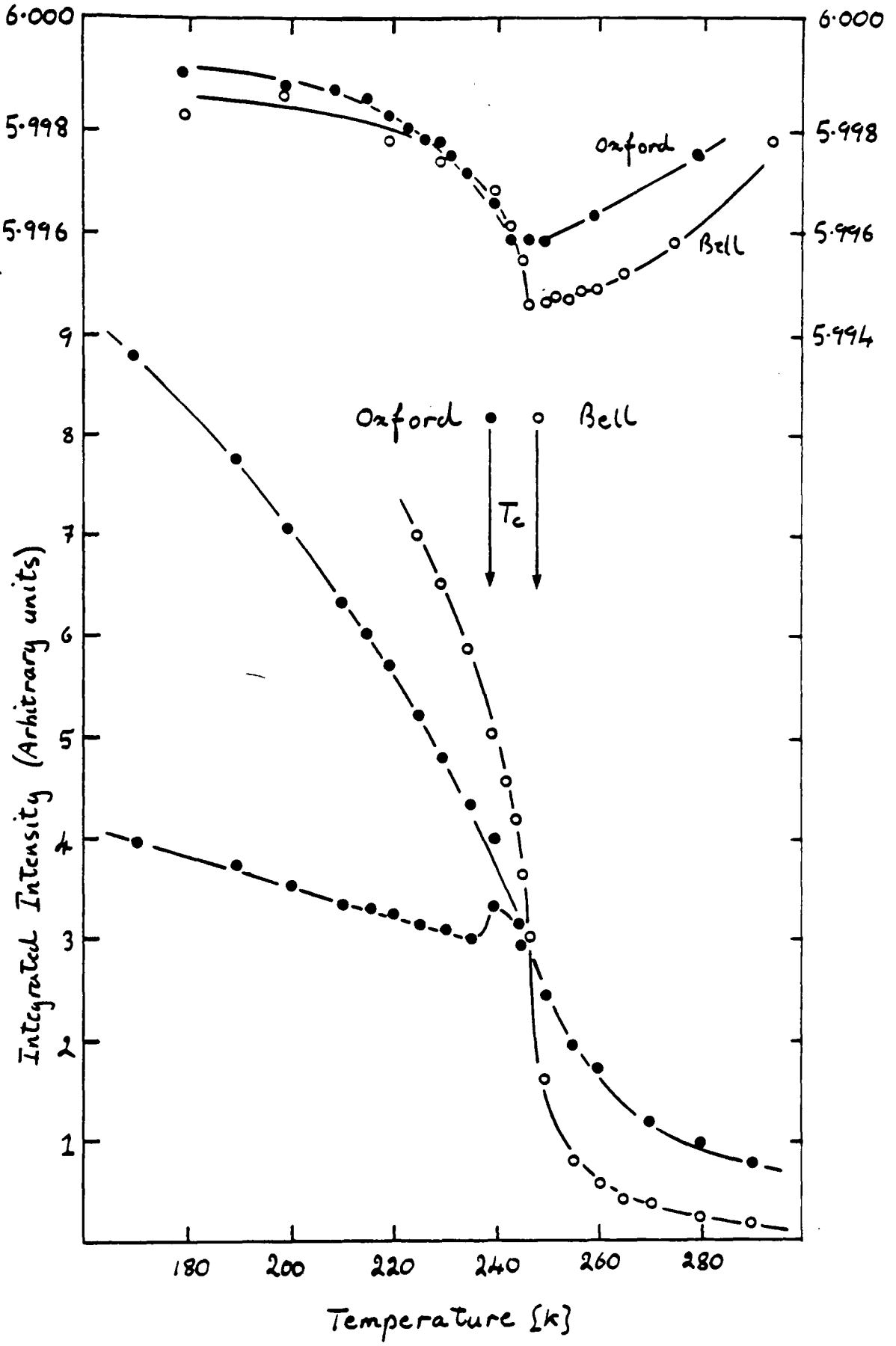

Figure 7.1 - The temperature dependence of the integrated intensity of the incommensurate reflections. The results for two different parts of the Oxford crystal are shown by circles and have been scaled at high temperatures. Below 238K the curves differ because of the formation of macroscopic domains. The upper part of the figure shows the temperature dependence of the 'a' lattice constant for both crystals.

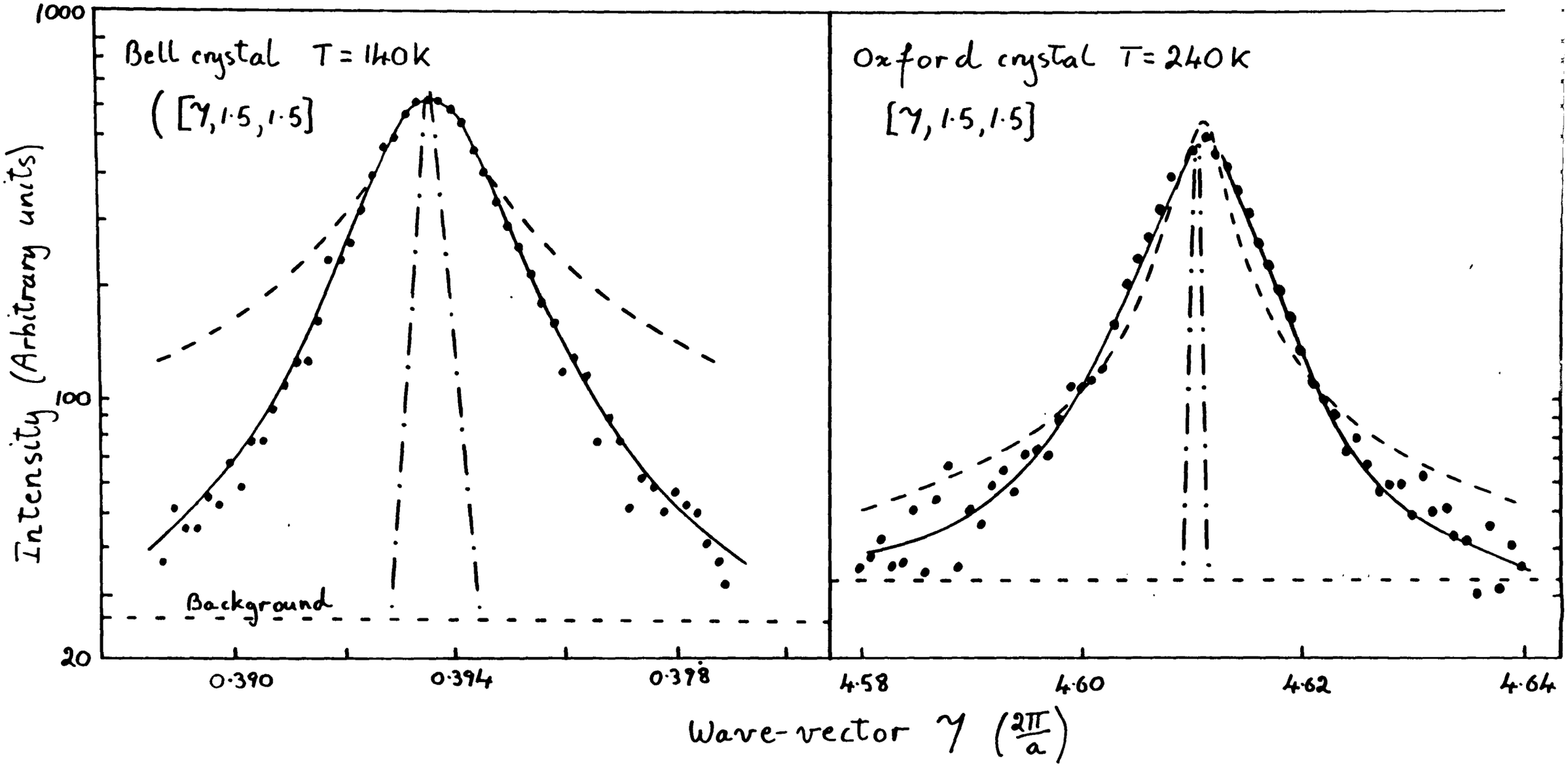

Figure 7.2 – The scattered intensity for a wavevector transfers along (ξ,1.5,1.5) from a) Bell crystal at 140K and b) the Oxford crystal at 240K. The solid line is a best fit of a Lorentzian squared profile and the dotted line of a Lorentzian profile. The dot-dash line gives the resolution function.

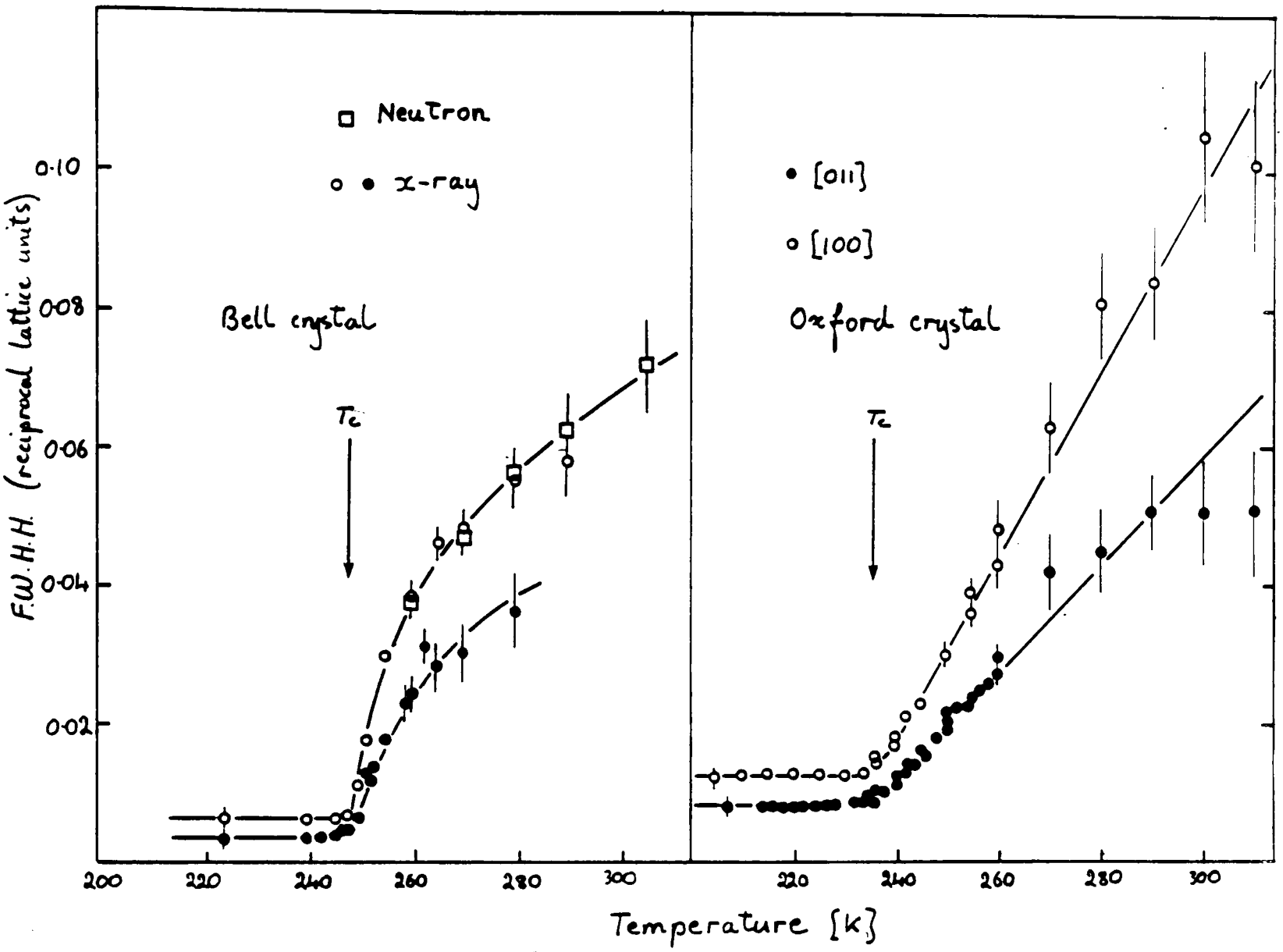

Figure 7.3 - The measured full half-widths at half maximum of the scattering for both crystals as a function of temperature.

analyser crystal. A pyrolytic graphite analyser crystal was always used in combination with the graphite monochromator. The resolution of the instrument is then dependent on the wavevector transfer, as discussed in chapter 4, but in the scattering plane it is typically (Si-Si)$5x10^{-2}$Å^{-1} and (PG-PG)10^{-2}Å^{-1}. For the (Si-Slit) arrangement the resolution was 10^{-3}Å^{-1} perpendicular to the surface of the Ewald sphere and $2x10^{-2}$Å^{-1} parallel to the surface. Perpendicular to the scattering plane the resolution was $5x10^{-2}$Å^{-1}.

The temperature dependence of the integrated intensity around the incommensurate reflections was measured and the results are shown in Figure (7.1). In the case of the Bell crystal the transition temperature was determined from the temperature dependence of the 'a' lattice constant, also Figure (7.1), as 247.0±0.5K, and this temperature is at least roughly consistent with the onset of order as determined by the integrated intensity when allowance is made for the critical scattering included in the intensity above T_c. The integrated intensity obtained from different parts of the Oxford crystal could be scaled to one another for temperatures above 240K, but below this temperature there was a break in the temperature dependence and the scaling no longer applied. As explained in detail in chapter six, this behaviour is due to the formation of the two different types of monoclinic domains having macroscopic dimensions. The temperature at which these macroscopic domains occur is 238.0±1.0K and is the signature of a well defined transition. An unexpected feature of the results is that the transition temperature in the Oxford crystal coincides neither with the onset of appreciable integrated scattering, Figure (7.1), nor the broad dip in the 'a' lattice parameter, but occurs at a considerably lower temperature when the integrated intensity has already reached a large fraction of its low temperature value. Above 250K the Oxford crystal also gives relatively much more scattering than the Bell crystal. We believe that these differences arise because the Oxford crystal contains many more defects than does the Bell crystal.

The wavevector dependence of the scattering was studied in detail for both crystals above and below T_c. Scans were performed along the [100] and [011] directions through a number of incommensurate reflections. Two typical scans are shown in Figure (7.2). They both show widths which are considerably larger than the experimental resolution. Figure (7.3) shows that the observed full width of the scattering at half maximum steadily decreases as the temperature decreases for both crystals. In the case of the nearly pure Bell crystal the width below T_c is only slightly larger than the experimental resolution and at high temperatures the widths are consistent with those of Cox

et al (1979). These results were initially believed to be qualitatively as expected for a pure crystal, with the critical exponent ν, which describes the half width, clearly less than unity. The behaviour of the Oxford crystal is qualitatively different. The width of the scattering along both the [100] and [011] directions is always greater than the resolution and continues to decrease below T_c. It is always larger than that found in the Bell crystal and the temperature dependence is, for temperatures above T_c, nearly linear in $T - T_c$ unlike the behaviour of the Bell crystal.

Further analysis of the results can only be performed by assuming a form for the scattering cross-section. Initially this was taken to be a Lorentzian form as expected at transitions in pure systems;

$$S(\mathbf{Q}) = \frac{A}{\kappa^2+(q_y^2+q_z^2)/R^2+q_x^2} \qquad (1)$$

where the scattering vector $\mathbf{Q} = \mathbf{G} + \mathbf{q}_1 + \mathbf{q}$, and $\mathbf{G}$ is a reciprocal lattice vector. The anisotropy of the fluctuations was assumed to be such that the correlation length was different along [100] from that perpendicular to [100]. In principle, the correlation length is also anisotropic perpendicular to [100], but the large vertical resolution meant that the results were relatively insensitive to the correlation length perpendicular to the scattering plane. The results were fitted to eqn. 1 convoluted with the experimental resolution and added to a flat background to determine the amplitude, A, the inverse correlation range, κ, the anisotropy, R, and the background.

In the Bell crystal the Lorentzian form gave a good fit above 249K, and fairly reasonable fits ($\chi^2 \sim 2.5$) could be obtained above 248K. In the case of the Oxford crystal, all of the high resolution data for temperatures below 246K gave unsatisfactory fits to the Lorentzian form ($\chi^2 \sim 4$), as shown in Figure (7.2).

Since the Lorentzian form did not describe the results, fits were then performed to a Lorentzian squared form because this is found to describe the scattering in the random field Ising systems and because it is expected to occur in disordered systems;

$$S(\mathbf{Q}) = \frac{B}{(\kappa^2+(q_y^2+q_z^2)/R^2+q_x^2)^2} \qquad (2)$$

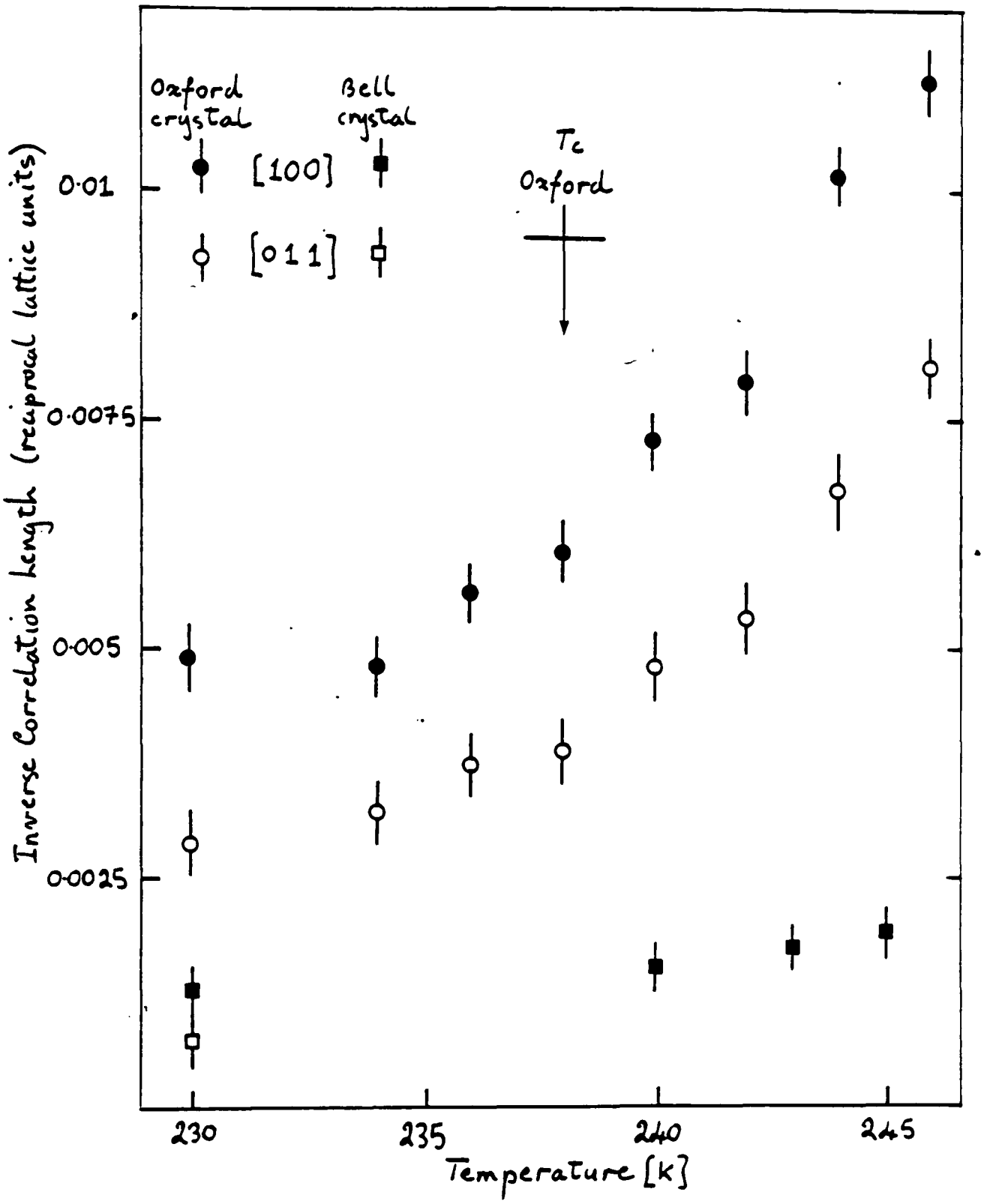

Figure 7.4 - The inverse correlation lengths from Lorentzian squared fits to the experimental profiles.

and also to the sum of a Lorentzian and Lorentzian squared functions. A good fit ($\chi^2 \backsim 1$), was obtained to all the data below 246K from the Oxford crystal using just a Lorentzian squared form, and no significant improvement was made on adding a Lorentzian term. The results are illustrated in Figure (7.2), and the resulting κ are shown in Figure (7.4). The anisotropy, R, can be obtained from Figure (7.4) and it is within error constant at 0.66, in reasonable agreement with the value obtained for the Bell crystal at high temperatures. The success of these fits prompted us to re-examine the fits to the Bell crystal. In particular the data taken below T_c, was fitted to a Lorentzian squared form and at the low temperature of 140K a good fit was obtained as shown in Figure (7.2), with the anisotropy parameter R = 0.61. Similar fits were obtained at other temperatures below 245K.

These results suggest that both crystals are, in fact, behaving in a very similar way; but that the concentration of impurities in the Oxford crystal is much larger. Further evidence for this comes from the lack of temperature dependence of the ordering wavevector in the Oxford crystal, which is evidence for a large defect concentration (Barthes-Regis et al, 1983). Finally Lavrencic and Scott (1981) have shown that T_c can be reduced by up to 10K in samples made fluorine deficient through heat treatment. Consequently we consider that the unexpected behaviour presented in this letter is due to the presence of defects and that these defects are most probably fluorine vacancies.

The results show that long range order is not established in these samples because the defects act as a random field by pinning the phase of the incommensurate modulation (Imry & Ma, 1975, Sham & Patton, 1976). The scattering profile at low temperatures is well described by a Lorentzian squared form as also found in the magnetic Ising systems. Unexpectedly there is a well-defined phase transition at a temperature that decreases with increasing impurity concentration. The results shown in Figure (7.1), and in chapter 6, strongly suggest that this transition is associated with an abrupt freezing of the system, as found at the metastability boundary in the Ising systems (Birgeneau et al, 1985), but which has not to our knowledge been predicted theoretically for systems with continuous symmetry. Finally, at temperatures above T_c, the scattering from the more disordered crystal has a Lorentzian squared contribution. Presumably this defect induced scattering is the origin of the 'central peak' observed above T_c by Cox et al (1979). We hope that these results will stimulate further work on the effect of random fields on systems with continuous symmetry, especially as this experiment suggests that the

behaviour is very similar to that of the Ising systems which have proven to be much more subtle than at first realised.

CHAPTER EIGHT

$RbCaF_3$: The 196K Antiferrodistortive Transition.

8.1) INTRODUCTION.

The antiferrodistortive perovskites, general formula AMX_3, constitute a very important structural family in the context of modern experimental studies of critical phenomena at structural phase transitions. These materials undergo one of the simplest possible examples of a unit-cell doubling (or antiferrodistortive) structural phase transitions from a cubic phase, with space group Pm3m, to a tetragonal phase with space group I4/mcm. The transition is connected to the condensation of a soft optic phonon at the R-point (or **q**=0.5,0.5,0.5) of the cubic Brillouinzone. This mode involves anti-phase rotations of corner-sharing MX_6 octahedra around cubic [100] axes in adjacent unit cells resulting in the characteristic, in-plane rotational distortion pattern shown in Figure (8.1). At T_c the atomic displacement pattern of the soft-mode 'freezes in' to the static structure of the low temperature phase, the rotation axis becoming the tetragonal 'c' axis. The rotation angle, phi, is the order parameter of the low temperature phase.

The most thoroughly examined member of the family is $SrTiO_3$, which undergoes a second-order transition at 105K, and it was in this material that the first experimental observation of a zone-boundary condensation was made, using inelastic neutron scattering (Shirane and Yamada 1969). The inadequacy of the simple soft-mode description of the phase transition soon, however, became apparent with the observation of the so-called 'central peak' by Riste et al (1971).

In addition to the inelastically scattered signal, corresponding to the softening phonon mode, a quasi-elastically scattered component was observed. This appeared some 70K above T_c and, as T_c was approached, critically diverged, eventually dominating the scattering spectrum close to T_c. Essentially identical scattering features were subsequently observed in the isomorphous perovskites $KMnF_3$ and $RbCaF_3$ (Rousseau et al 1976, Almairac et al 1977).

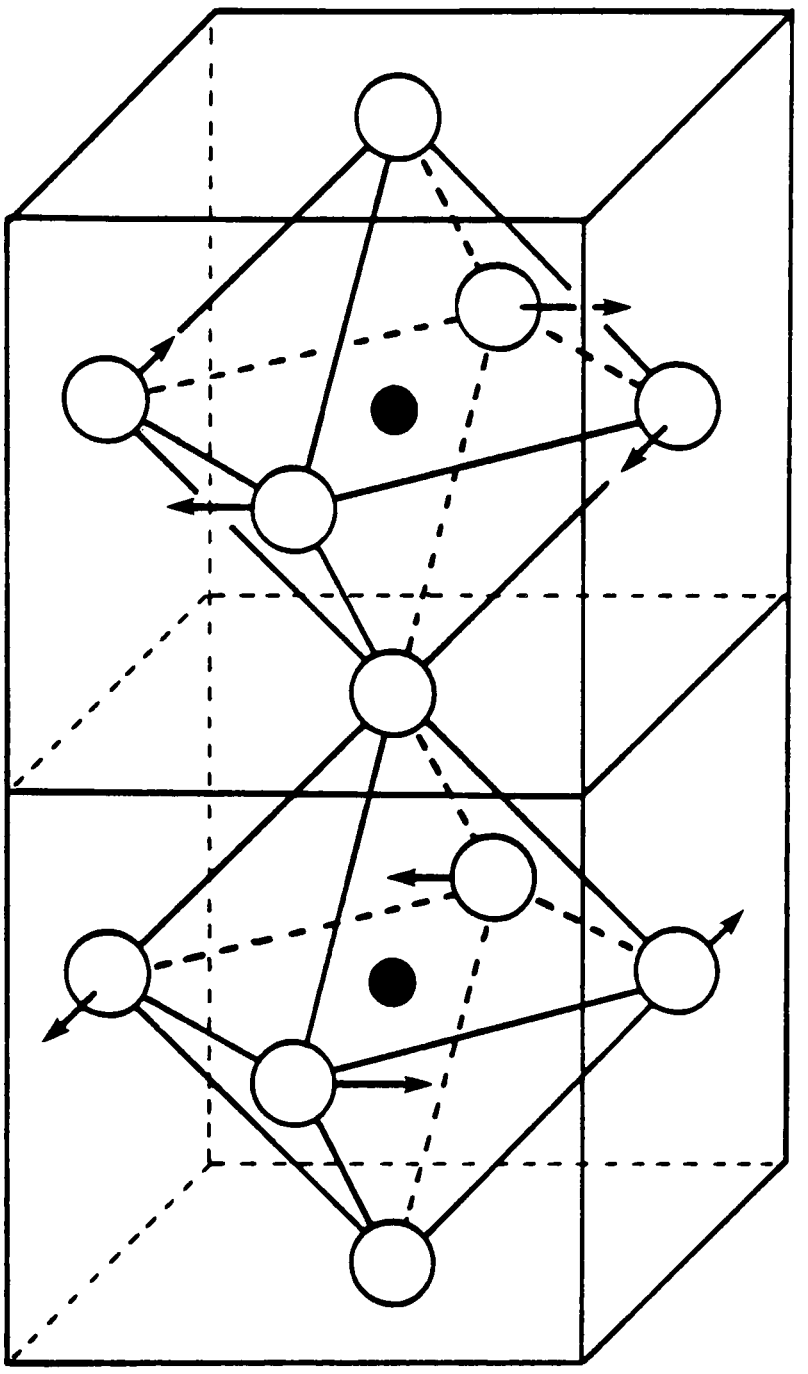

Figure 8.1 - The atomic displacement pattern of the R_{25} soft-mode in the antiferrodistortive perovskites, AMX_3. The MX_6 octahedra are shown. The A atoms occupying the cube-corner sites, are omitted for clarity.

The two-timescale response revealed by the inelastic neutron scattering measurements has been confirmed by a number of other experimental methods including EPR (Simon et al 1981, Buzare and Simon 1984) and light scattering (Bruce et al 1980) and several theoretical models were proposed to acount for the existence of this unexpected feature, as reviewed by Bruce and Cowley (1981). Broadly, these fall into two categories; those which consider the central peak to be an intrinsic feature of the pure material and those which consider it to be related to the presence of defects. The former models predict the existence of 'precursor clusters' within which the static displacements of the low temperature phase temporarily 'freeze in' above T_c and the experimentally observed long-timescale is acounted for by the relatively slow motion of the cluster walls.

The 'extrinsic' models (Halperin and Varma 1976) explain the existence of the central peak in terms of defects or impurities, introducing local distortions which couple to the order parameter and thereby stabilise small regions of the low temperature structure. The timescale is determined by the mobility of the defects.

Whatever the mechanism for their production, the existence of pre-cursor clusters of the tetragonal-phase structure above T_c in the antiferrodistortive perovskites is now a widely accepted and experimentally verified fact (Bruce et al 1980, Jex et al 1980, Buzare et al 1984). There are, however, a number of experimental features which remain puzzling.

The current theoretical models, outlined above, correctly predict the two-timescale response of the system but predict a single lengthscale for the correlations above T_c, that of the R_{25} soft-mode. X-ray scattering experiments, however, measure the quantity $S(\mathbf{Q})$ and are, therefore, insensitive to the two-timescale response of the system but can accurately measure the correlation length of the scattering features.

Darlington and O'Connor(1976) reported the existence of an intense, Bragg like scattering component at the R-point in $SrTiO_3$ in x-ray and Mossbauer scattering experiments. The scattering appeared to be surface specific and was interpreted as originating in a surface-stabilised tetragonal layer some 20μm thick at T_c+5K and critically growing into the bulk as T_c was approached. The existence of this layer was proposed as a plausible explanation for the quasi-elastically scattered 'central peak' but this was subsequently

disputed, on the evidence of non-surface specific neutron scattering measurements, by Cowley and Shirane(1978).

In $RbCaF_3$, Ridou et al(1980) reported x-ray scattering measurements which appeared to demonstrate the existence of very large (circa 2-6000Å) pre-cursor clusters of the tetragonal phase in the temperature range T_c to T_c+5K in high quality sample crystals. No attempt was made to examine the surface specificity of the observed scattering.

Very recently, Andrews(1986), using the Edinburgh triple-crystal x-ray spectrometer, carried out a detailed study of critical scattering and pre-transitional Bragg scattering in a number of samples of $SrTiO_3$. He observed a Q-resolution limited Bragg-like component above T_c at the cubic R-point. The feature was first visible some 6K above T_c, superimposed upon the broad, diffuse scattering from the softening R_{25} mode, and grew steadily in intensity as T_c was approached. The correlation length of the feature was estimated to be $\sim 10^4$Å but its intensity was found to be both sample and history dependent. Andrews concluded that it contained contributions from both bulk, defect stabilised regions and from a surface layer.

The existence of this, apparently sample dependent, feature seriously complicates any experimental study of critical effects in the antiferrodistortive perovskites. Its precise origin, to what extent it is representative of pure crystal behaviour and its relationship to the 'central peak' are still not well understood.

A preliminary x-ray scattering study of $RbCaF_3$ (Ryan and Gibaud, unpublished), which is structurally isomorphous with $SrTiO_3$ but differs in that the transition, at $\sim$196K, is slightly first-order, confirmed the existence of the narrow, Bragg like component above T_c. Unfortunately, efforts to examine this feature and to measure the critical exponents β, γ and ν were unsuccessful, partly because of the poor quality of the available sample crystals, which often consisted of a number of misorientated crystallites, and partly because of an inadequate understanding of the distribution of tetragonal domains within the sample.

In collaboration with Prof. J. Nouet, Universite du Maine, Le Mans, a very high quality $RbCaF_3$ sample crystal was subsequently prepared and the present work describes a high-Q-resolution experimental study of the x-ray scattering at the R-point of $RbCaF_3$ in the region of the 196K cubic to tetragonal structural phase transition.

8.2) SAMPLE CRYSTAL GROWTH AND PREPARATION.

The $RbCaF_3$ sample crystal was grown by the Bridgman-Stockbarger technique from a non-stoichiometric mixture of RbF and CaF_2 by Prof. J.Nouet Universite du Maine, Le Mans, France. It is notoriously difficult to grow highly perfect crystals of Rubidium compounds - the difficulty lies mainly in the low purity of commercially available starting materials containing Rubidium. The experience gained in our preliminary experimental study, using $RbCaF_3$ crystals which were originally believed to be very perfect but which were obviously far from perfect when examined using the triple-crystal x-ray spectrometer, had shown that crystals of exceptionally high quality were required.

The commercially obtained RbF was purified prior to serious crystal growth. This was achieved by growing a crystal of RbF from the melt, removing the bottom portion of the crystal and re-growing a new crystal from the top portion of the crystal. The process was repeated a number of times until the RbF crystal was as pure as possible.

$RbCaF_3$ growth was performed from the purified starting materials. The crystal was pulled from the melt at a speed of 1cm/24hr in a thermal gradient of 8° per cm. The boule was ~2.5cm in diameter and a large portion of it appeared optically very clear. The growth axis was directed along a cubic [100] direction.

The boule was sliced, with a diamond saw, perpendicular to the growth axis into a number of plates, between 1mm and 3mm thick. Two samples were chosen, one from the top end of the boule (crystal I), where the defect concentration was believed to be lowest, and one from the lower end of the boule (crystal II), where the defect concentration should be higher. The 'a' faces of both crystals were lapped to an optically perfect finish using 0.25μm diamond paste and then etched in conc. HCl to remove surface damage introduced by the polishing process and to relieve surface strain. Careful sample preparation is of absolutely fundamental importance to the sucess of a high-Ω-resolution x-ray scattering experiment as the x-ray penetration depth within the sample is, typically, much less than 100μm.

The sample crystals were then mounted on a film of cryo-con grease

(Air Products Co.Ltd.) on a high conductivity copper mounting block. The crystals were held in position by small amounts of Ge7031 varnish - in this way the mounting was as strain free as possible. To allow access to a cubic phase R-point the crystals were oriented with a [001] axis normal to the face and a [011] axis in the plane of the face.

8.3) THE X-RAY SPECTROMETER.

The experiments were carried out using the Edinburgh triple-crystal x-ray spectrometer with $CuK\alpha_1$ radiation from a rotating-anode source operating at 3KW with a focal spot size of $0.3x3.0mm^2$.

For the low-resolution measurements of the critical scattering from the R_{25} soft mode the instrument was fitted with pyrolytic graphite (0002) monochromator and analyser crystals giving a reciprocal space resolution of $\sim 2.0x10^{-2}\text{Å}^{-1}$ in the scattering plane and a resolution of $\sim 5x10^{-2}\text{Å}^{-1}$ in the vertical plane. For high resolution measurements the graphite crystals were replaced by perfect Si(111) crystals improving the resolution to $\sim 5x10^{-3}\text{Å}^{-1}$ in the scattering plane. A scintillation counter was used to detect the scattered signal.

The sample crystal was contained in an isothermal enclosure mounted on the cold stage of a closed-cycle cryo-refrigerator. The sample temperature was controlled with a stability of ±0.02K and an absolute accuracy of ±0.3K.

The x-ray beam incident upon the sample crystal was a narrow, vertical line, ~1.0mm high and ~0.1mm wide.

$\lambda/2$ contamination is a serious potential problem when working at cubic Brillouin zone boundary or corner points. With Si(111) collimation optics the problem does not exist because the Si(222) reflection (which would pass $\lambda/2$) is virtually absent. With graphite (0002) optics, however, the (0004) reflection is present and a $\lambda/2$ component is inevitable. The measurements described in this work were carried out at the cubic (0.5,0.5,3.5) position and $\lambda/2$ Bragg scattering from the (1,1,7) reflection is possible. To eliminate this possibility a pulse height analysis of the scattered beam was carried out and the $\lambda/2$ contribution was found to be negligible.

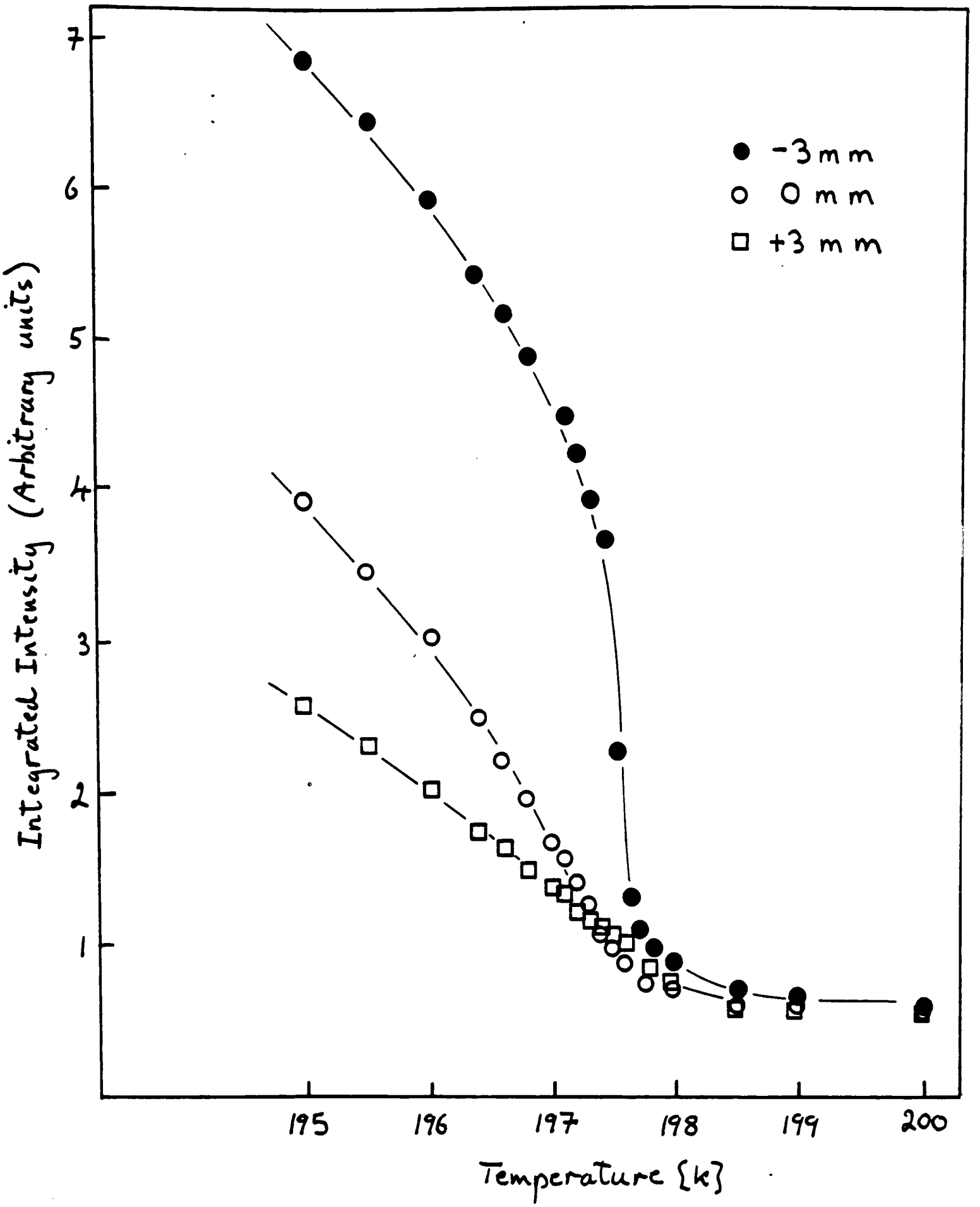

Figure 8.2 - The integrated intensity of the R-point scattering at three positions on the crystal face as the temperature was lowered through T_c.

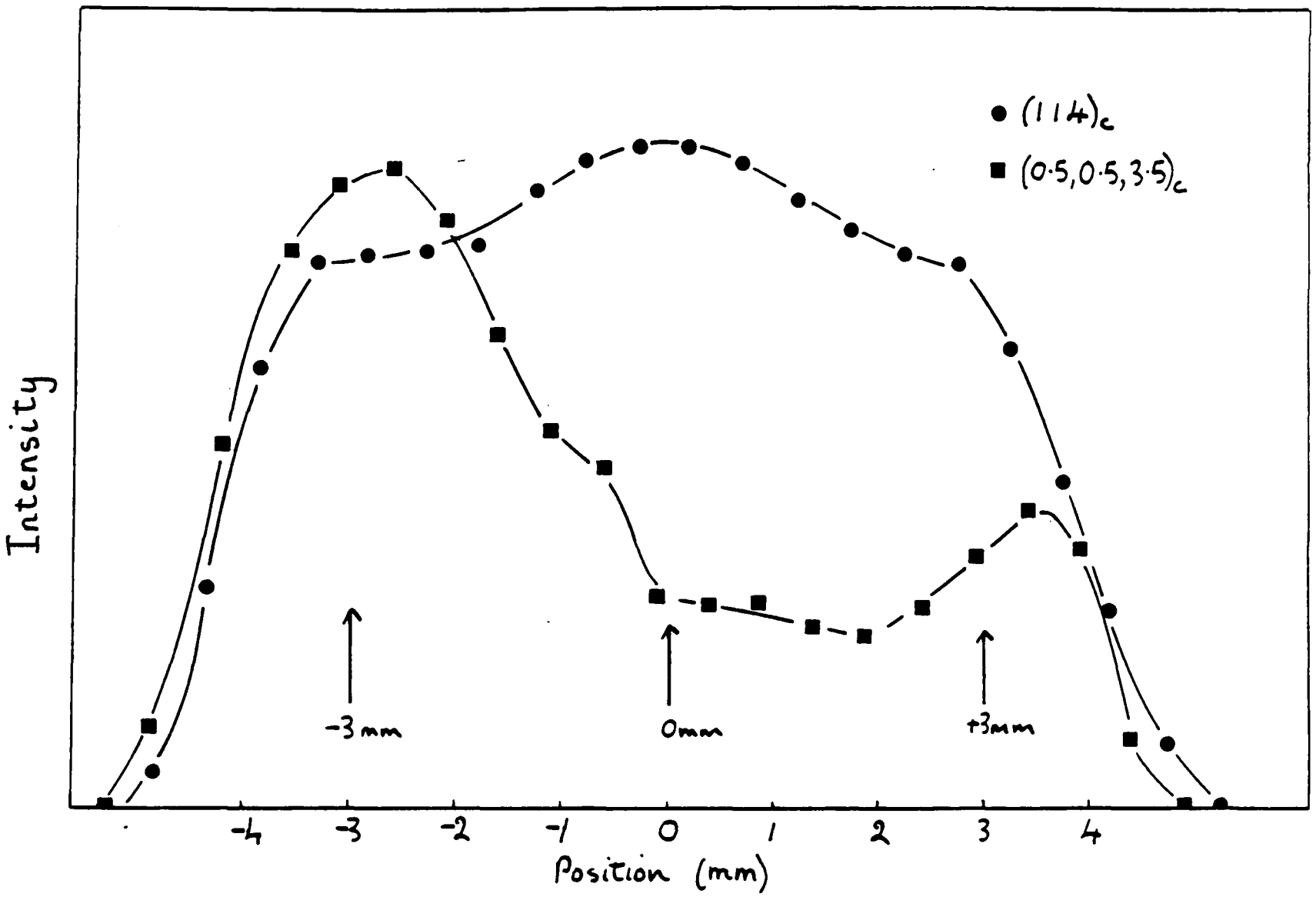

Figure 8.3 - The integrated intensity of the $(0.5,0.5,3.5)_c$ R-point reflection and the $(114)_c$ Bragg reflection at T_c - 2K as a function of position along the crystal face. The three points referred to in figure 8.2 are marked.

8.4) CRYSTAL QUALITY AND THE DOMAIN DISTRIBUTION BELOW T_c.

The quality of the two sample crystals was assessed by rocking-curve measurements of the $(004)_c$ cubic phase Bragg reflection. The measurements were made in the high-Q-resolution configuration. Crystal I has a mosaic distribution of ~0.006(1)° FWHH and crystal II a distribution of ~0.012(1)° FWHH. As expected, the crystal cut from the lower end of the boule is of poorer quality, although, by any normal standards, both crystals are of exceptionally high quality. The experimental effort was initially focussed on crystal I.

The crystal was approximately rectangular in shape ~4mm high, 8mm wide and 1.5mm thick. The intensity of the new, tetragonal phase Bragg peak which appears at the cubic R-point below T_c is directly related to the rotation of the fluorine octahedra and, thus, is a measure of the order parameter of the low temperature phase. To determine T_c, and measure the order parameter critical exponent, β, the integrated intensity at the cubic R-point, specifically $(0.5,0.5,3.5)_c$, was measured as a function of temperature at a number of positions along the crystal face in the low-Q-resolution mode. Three of the results are shown in Figure(8.2). The transition temperature, T_c, is 197.6(2)K.

Quite clearly, the behaviour differs very dramatically over the crystal face and any attempt to extract a meaningful critical exponent is doomed to failure. What are the possible explanations?

To check for possible instrumental effects the integrated intensities of the superlattice peak at $(0.5,0.5,3.5)_c$ and an adjacent Bragg peak (in fact the cluster of three tetragonal phase Bragg peaks) at $(1,1,4)_c$ were measured as a function of position along the sample face at T_c-2K. The results are shown in Figure(8.3). The intensity of the Bragg peak(s) remains almost constant along the crystal face, whereas the intensity of the superlattice peak varies substantially. The observed variation in the intensity of the superlattice peak is, clearly, a real effect.

The explanation lies in the domain structure of the tetragonal phase (Jona and Shirane 1962, Modine et al 1974). The tetragonal 'c' axis can develop along any of the cubic 'a' axes and, in a bulk sample, the expectation is that domains of the three possible tetragonal orientations will form with equal

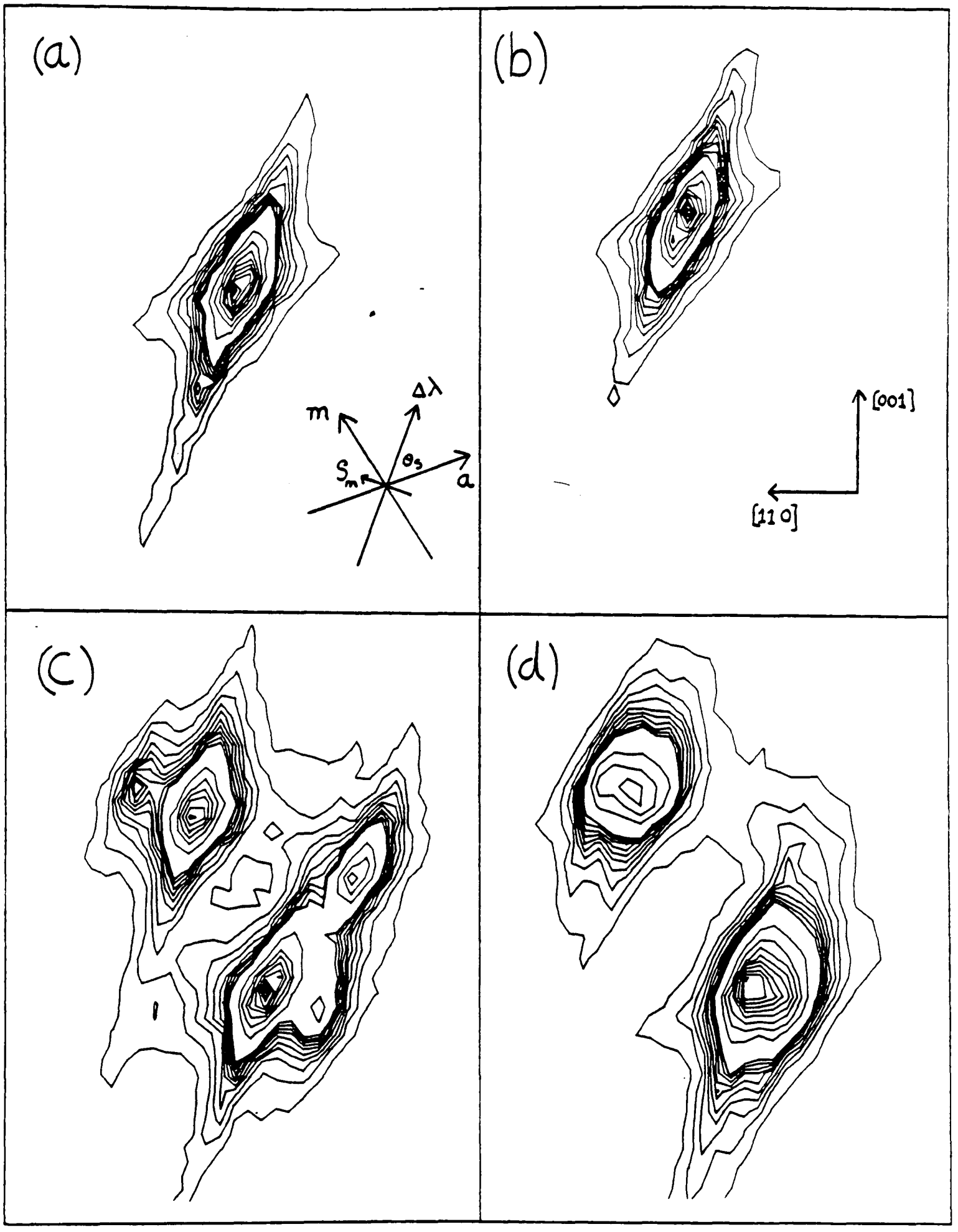

Figure 8.4 - Grid scans of the position $(114)_c$ above and below T_c in crystal I. (a) T_c + 3K at position 0mm. (b) T_c - 2K at position -3mm. (c) T_c - 2K at position 0mm. (d) T_c - 2K at position +3mm.

probability (Maetz, Mullner, Jex and Peters 1978). Our previous experience of antiferrodistortive phase transitions suggests that such domains can form on a macroscopic scale (see chapter 6), with potentially serious consequences for experiments sensitive to the domain structure. In this case, we expect three domain types to form; one with the tetragonal 'c' axis normal to the crystal face and two with their tetragonal 'c' axes in the plane of the face but inclined at 45° above and below the scattering plane. Bragg, or superlattice, reflections from the latter two domain types will appear superimposed in the present experimental configuration.

On this model, a Bragg reflection, of the cubic phase, should split into three, tetragonal-phase Bragg reflections. For example, the cubic Bragg peak $(1,1,4)_c$ forms three tetragonal-phase peaks, $(0,2,8)_t$, $(-3,5,2)_t$ and $(3,5,2)_t$; the latter pair being equivalent by symmetry. In this experimental configuration, the $(-3,5,2)_t$ and $(3,5,2)_t$ reflections lie just above and below the scattering plane and the relatively poor vertical resolution of the instrument allows both to be recorded simultaneously.

The situation is more complicated at the cubic R-point $(0.5,0.5,3.5)_c$ where three tetragonal superlattice peaks should appear below T_c, $(0,1,7)_t$, $(-3,4,1)_t$ and $(3,4,1)_t$; the latter two superimposed. The $(0,1,7)_t$ reflection, however, which originates in the tetragonal domain with the 'c' axis normal to the crystal face, is forbidden by the 'c' glide condition (0kl: k=2n) in the space group of the tetragonal phase. The observed superlattice intensity at any position on the crystal face is, therefore, directly related to the proportion of domains, in the sampled volume of crystal, with the tetragonal 'c' axis parallel to the crystal face.

Figures (8.2) and (8.3) show that at position -3mm, the crystal is predominantly composed of domains with the tetragonal 'c' axis parallel to the plane of the face, whilst, at position 0mm, the reverse is true.

To directly test this hypothesis, the instrument was reconfigured to the high-Q-resolution mode and grid-scans of the $(1,1,4)_c$ Bragg peak were performed at three positions, -3mm, 0mm and +3mm as the temperature was lowered through T_c. Scans recorded at T_c+3K and T_c-2K are shown in Figure (8.4). As with all of the grid-scans shown in this work, the contour intervals are arranged in two decades - 1% to 10% and 10% to 100% - to display weaker scattering features without allowing the contour plots to become dominated by

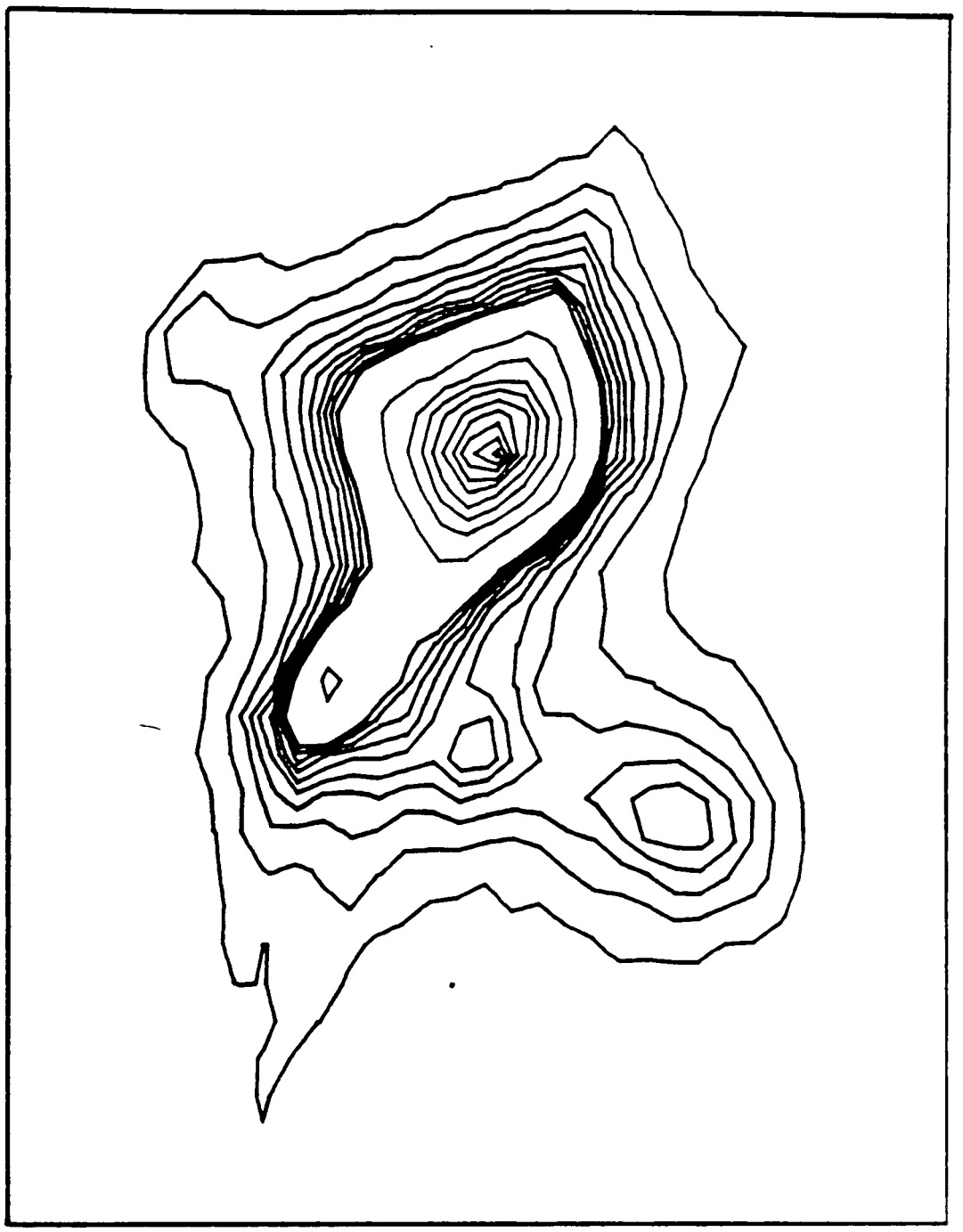

Figure 8.5 - Grid scan of the point $(114)_c$ at T_c - 1.4K in crystal II.

the strong features.

The results are, simultaneously, satisfying and confusing. In the cubic phase, a single, resolution-limited Bragg peak is visible. Scan (a) shows a typical Bragg peak at T_c + 3K, in fact at position 0mm. Below T_c, at position -3mm, the sampled volume is composed entirely of domains with the 'c' axis parallel to the crystal face whereas, at 3mm the crystal has formed roughly equal proportions of both domain types, as expected. At position 0mm, however, a much more complicated domain pattern is in evidence with, possibly, up to six Bragg peaks visible.

Leaving this complication for the time being (see section 8.4), it is clear that position -3mm is very suitable for studying critical scattering and the evolution of the tetragonal phase in this crystal.

The domain structure of crystal II was investigated in the same way with broadly similar results. In this case, the domain structure was considerably more homogeneous across the crystal face, Figure(8.5) shows a contour plot of the cluster of tetragonal phase Bragg reflections at the $(1,1,4)_c$ point at T_c-2K. Once again, as with position 0mm in crystal I, five Bragg peaks are visible but one is very much more intense than the others. The dominant Bragg peak, being closer to the origin of reciprocal space, is clearly the superposition of $(-3,5,2)_t$ and $(3,5,2)_t$ and shows that this part of crystal II is predominantly composed of domains with 'c' parallel to the crystal face.

Although it was impossible to find an area of the face of crystal II as completely 'monodomain' as the position -3mm on crystal I, a large part of the crystal face was ~95% 'monodomain' and, therefore, suitable for further study.

8.5) THE GEOMETRY OF DOMAINS IN THE TETRAGONAL PHASE.

The result shown in Figure (8.4), i.e that a single Bragg reflection of the cubic phase splits into a cluster of up to six tetragonal-phase Bragg reflections, was entirely unexpected. When crystal II showed almost identical behaviour (Figure 8.5) it became clear that this was a real effect and that the domain structure of the tetragonal phase was considerably more complicated than the simple model, described above, suggested.

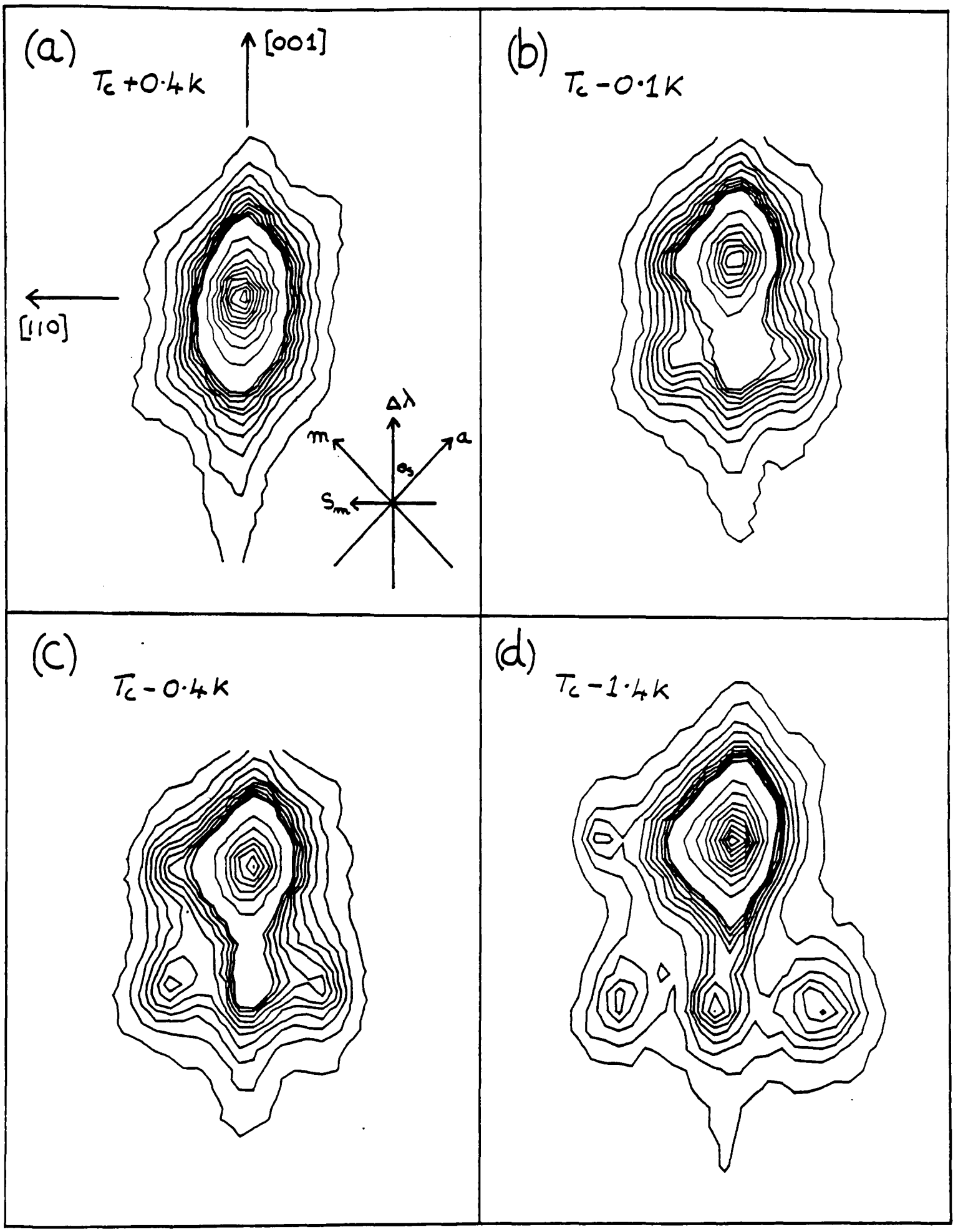

Figure 8.6 - Grid scans of the point $(004)_c$ in crystal II at (a) T_c + 0.4K. (b) T_c - 0.1K. (c) T_c - 0.4K. and (d) T_c - 1.4K.

Cubic

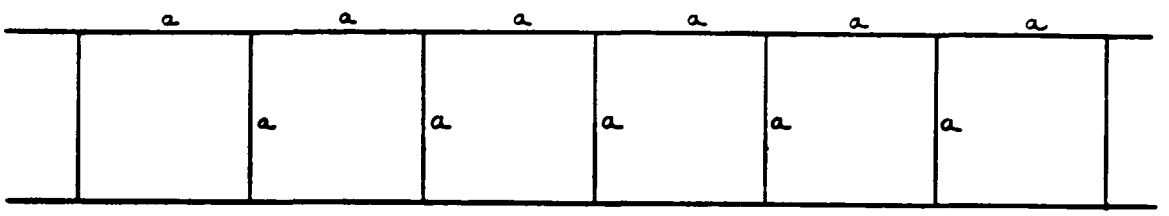

Figure 8.7 - A 2-d representation of the cubic-phase lattice and a corresponding cubic-phase reciprocal lattice point.

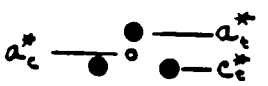

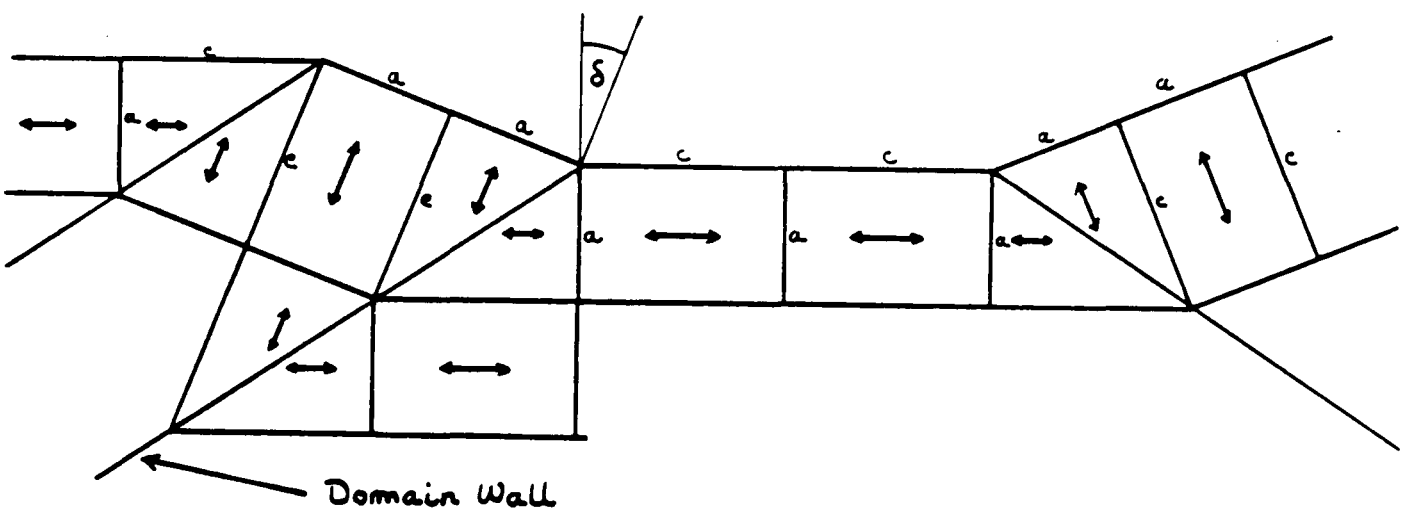
c
a
a
δ
c
c
a
a
a
a
a
a
a
a
a
a
a

Figure(8.6) shows a series of grid scans of the $(004)_c$ reciprocal lattice point as the temperature of crystal II was lowered through T_c. The single Bragg peak of the cubic phase evolves into a cluster of five Bragg peaks in the tetragonal phase, whereas, the simple model of the tetragonal phase predicts only two. Further grid scans, at a number of positions on the sample face, revealed a sixth Bragg peak, completing the symmetrical pattern of two rows of three peaks. Three of the peaks clearly originate in domains with the 'c' axis normal to the face and three in domains with 'c' parallel to the face.

The origin of this pattern becomes clearer on consideration of the manner in which the three possible tetragonal domains fit together within a bulk crystal. In fact, the following explanation is a logical extension of the domain model illustrated in Jona and Shirane (1962).

Figure(8.7) shows a 2-d representation of the prototype-cubic lattice with lattice parameter 'a', and a corresponding reciprocal lattice point '**a***'. At T_c, the tetragonal 'c' axis can develop along either of the cubic 'a' axes with equal probability. Suppose unit cell (1) develops the tetragonal axis parallel to the crystal face (an 'a' domain) and unit cell (2) normal to the face (a 'c' domain). The two tetragonal lattices must match onto one another at a domain wall.

Figure(8.8) shows how the domain matching is achieved. The domain wall is composed of strained, kite-shaped unit cells and, necessarily, the tetragonal 'c' directions are not exactly perpendicular. The presence of a single domain wall implies a macroscopic bend in the crystal and, clearly, this is unresonable. To retain its original shape, the crystal forms a pattern of alternating 'c' and 'a' domains. Note that, in this example, there are two distinct 'c' domain orientations, misoriented by by an angle δ, where δ is

$$\delta = 2(2\tan^{-1}(c/a)-90)^\circ$$

resulting in the corresponding arrangement of three, tetragonal reciprocal lattice points as shown.

It is, of course, equally likely that the crystal will form a 'c' domain, with the tetragonal axes parallel to the original cubic axes. In this case, two distinct 'a' domain orientations will appear, also misoriented by the angle δ, as shown in Figure(8.9).

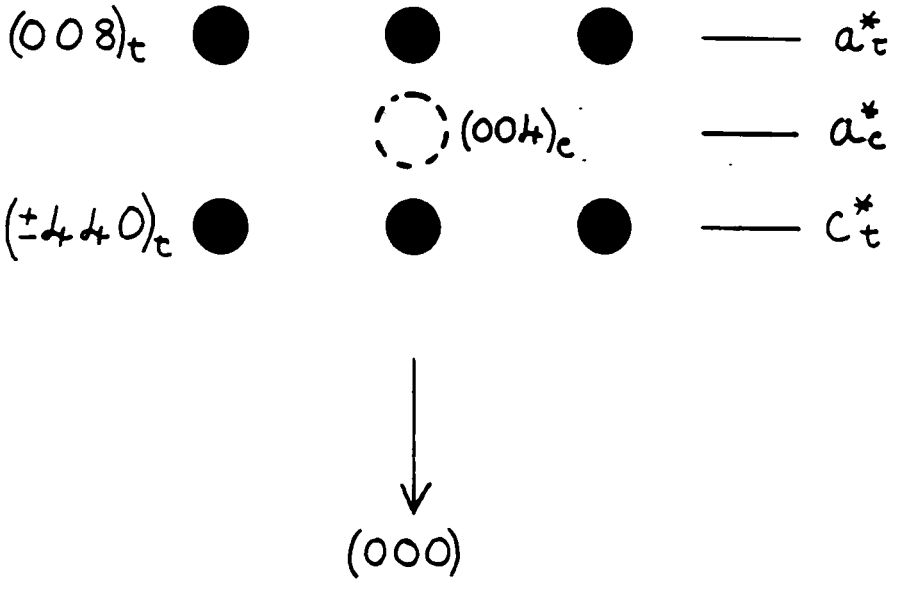

Figure 8.10 - The resulting cluster of six tetragonal-phase Bragg reflections from a poly-domain crystal. Note that in 3-dimensions it is possible to generate a cluster of up to fifteen Bragg reflections.

Combining these two pictures, we now have a pattern of tetragonal-phase Bragg peaks, Figure(8.10), very similar to the experimentally observed pattern in Figure(8.6). It should be noted that the two models described in Figures(8.8) and (8.9) are incompatible in a perfect crystal; their co-existence requires the presence of some kind of dislocation or crack.

Extending the model to three dimensions is quite straightforward. We rotate the 2-d example of Figure(8.8) by 90° about the tetragonal 'c' axis and find that we produce a cluster of 5 tetragonal-phase Bragg peaks. Performing the same operation on the model of Figure(8.9) and combining the two, we now have a cluster of 10 Bragg peaks. Adding the third tetragonal cell orientation, i.e. 'c' normal to the plane of the page, we create, at some general position in reciprocal space, a grand total of 15 tetragonal phase Bragg peaks! The author has no intention of even attempting to draw a figure illustrating this point.

Figures (8.4) and (8.5) show up to six peaks, and that is because several peaks superimpose in this scattering geometry.

The very important conclusion to be drawn from this exercise is that the domain structure of <u>any</u> perovskite, in the tetragonal phase, is extremely complicated. High-Q-resolution x-ray scattering techniques allow the experimentalist to examine the domain distribution within a particular sample crystal prior to embarking on a quantitative experimental study. A failure to do so will, almost certainly, introduce serious uncertainties into the experiment.

8.6) CRITICAL SCATTERING MEASUREMENTS.

The detailed study of the domain distribution described in section 8.5 revealed three distinct regions in crystal I. At one end of the crystal (position -3mm) there is an area which forms an entirely 'a' domain structure below T_c. In the centre of the crystal face there is an area with a very complex domain structure below T_c, and this possible signifies the existence of some kind of crack, flaw or strain, whilst, at the other end of the crystal there is an area which appears to form almost equal proportions of 'a' and 'c' domains.

In contrast, the domain distribution of crystal II (which is significantly less perfect than crystal I) is quite homogeneous. The crystal forms between

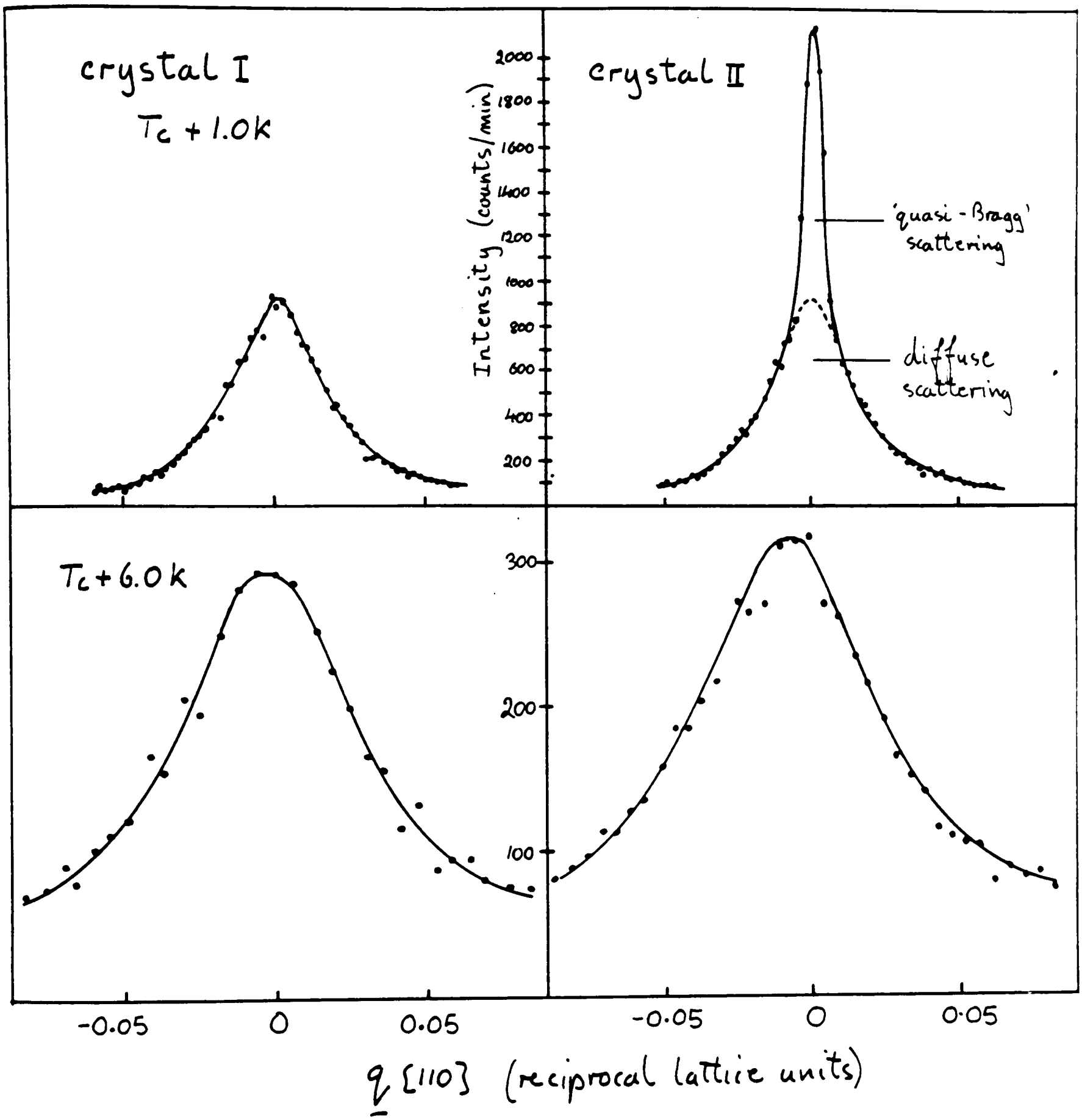

Figure 8.11 – Low-resolution (graphite monochromator and analyser) scans, along [110], through $(0.5,0.5,5.5)_c$ at T_c + 1K and T_c + 6K in crystals I and II. Note the appearance of a quasi-Bragg scattering component in crystal II at T_c + 1K.

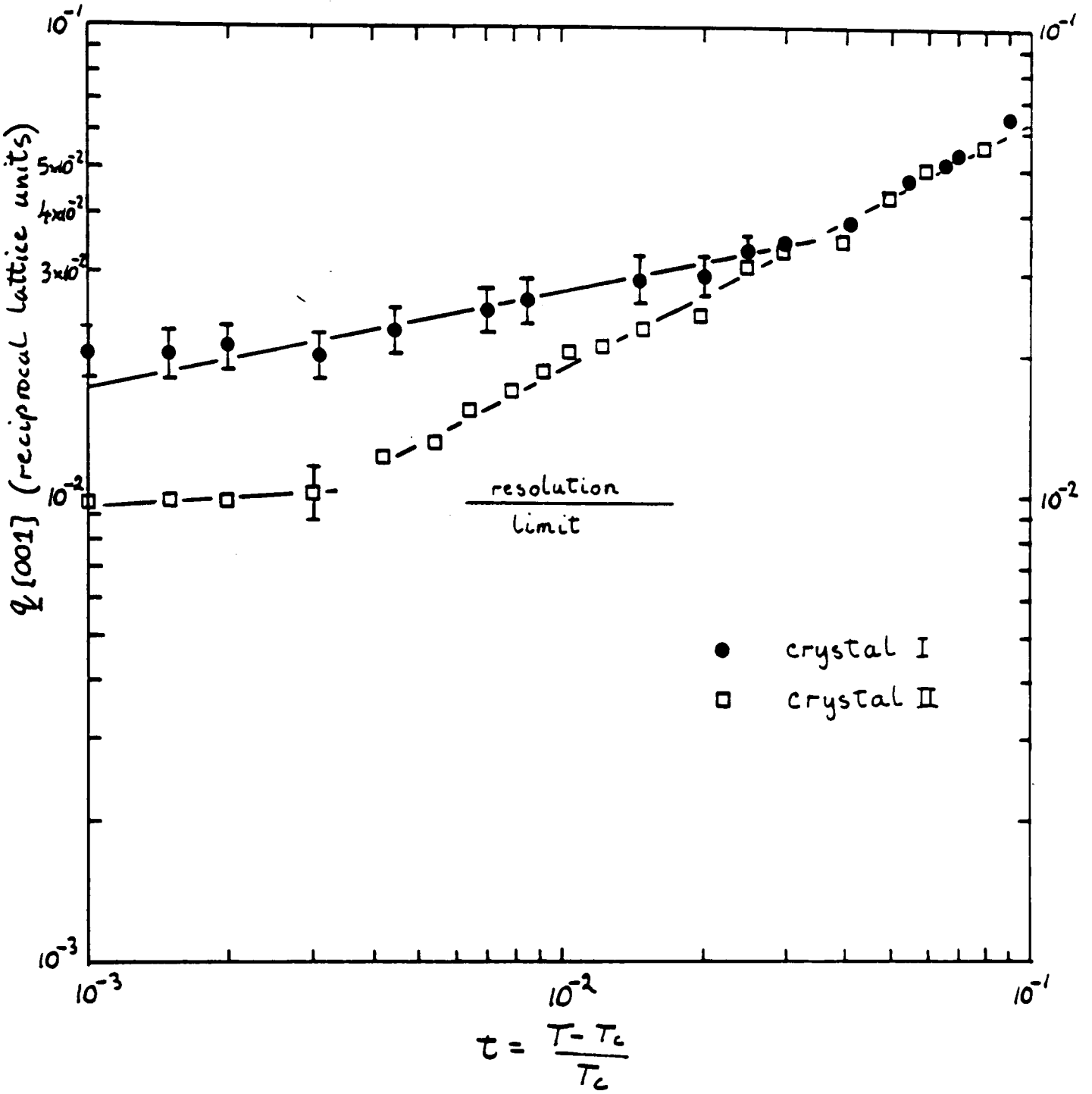

Figure 8.12 - A log-log plot of the measured wave-vector width in the [001] direction of the R-point diffuse scattering in crystals I and II. Note that, at temperatures above $\sim T_c$ + 4K, the behaviour of both crystals is identical but, close to T_c, a narrow component dominates the scattering spectrum in crystal II.

90% and 95% 'a' domains. The remainder of the experimental studies reported in this work were carried out at position -3mm in crystal I and position 0mm (the centre of the crystal face) in crystal II.

The critical exponents, γ and ν, describing the static susceptibility and correlation range, are obtained from measurements of the temperature dependence of the intensity and width of critical scattering from the R_{25} soft mode. Measurements of the critical scattering were carried out with the instrument operating, once again, in the low resolution mode with graphite (0002) monochromator and analyser crystals. Scans along the [001] and [110] directions were carried out in the temperature range T_c to T_c+30K in both crystals and some typical results are shown in Figure(8.11).

It is immediately apparent that the behaviour of both crystals is very similar at temperatures far from T_c but, as T_c is approached, a very significant difference develops. In crystal II a very narrow, Bragg like component appears, superimposed upon the broader, diffuse scattering from the R_{25} soft mode. This feature is completely absent in crystal I. Closer to T_c, the intensity of this feature increases continuously, eventually completely dominating the scattering spectrum.

The difference in behaviour of the two crystals is quite clearly illustrated in Figure(8.12) which shows the full width at half height of the measured scattering peak in the [001] direction as a function of temperature in both sample crystals. At temperatures above $\sim T_c$+4K the observed widths are essentially identical in both crystals. Closer to T_c, however, the Bragg like component emerges in crystal II until, at $\sim T_c$+1K, the FWHH measurement is dominated by its resolution-limited width.

Very significantly, crystal I shows no evidence whatsoever of this narrow component. The measured width of the scattering in crystal I decreases monotonically to T_c when a resolution-limited Bragg peak abruptly appears.

Cowley, Gibaud and Mitchell(1986) have sucessfully analysed the above data by modelling the observed scattering from crystal II as a superposition of a resolution limited Bragg peak and the broader, diffuse component. Within error, the critical exponents derived from the two separate data sets, crystal I and crystal II, are identical.

90% and 95% 'a' domains. The remainder of the experimental studies reported in this work were carried out at position -3mm in crystal I and position 0mm (the centre of the crystal face) in crystal II.

The critical exponents, γ and ν, describing the static susceptibility and correlation range, are obtained from measurements of the temperature dependence of the intensity and width of critical scattering from the R_{25} soft mode. Measurements of the critical scattering were carried out with the instrument operating, once again, in the low resolution mode with graphite (0002) monochromator and analyser crystals. Scans along the [001] and [110] directions were carried out in the temperature range T_c to T_c+30K in both crystals and some typical results are shown in Figure(8.11).

It is immediately apparent that the behaviour of both crystals is very similar at temperatures far from T_c but, as T_c is approached, a very significant difference develops. In crystal II a very narrow, Bragg like component appears, superimposed upon the broader, diffuse scattering from the R_{25} soft mode. This feature is completely absent in crystal I. Closer to T_c, the intensity of this feature increases continuously, eventually completely dominating the scattering spectrum.

The difference in behaviour of the two crystals is quite clearly illustrated in Figure(8.12) which shows the full width at half height of the measured scattering peak in the [001] direction as a function of temperature in both sample crystals. At temperatures above $\sim T_c$+4K the observed widths are essentially identical in both crystals. Closer to T_c, however, the Bragg like component emerges in crystal II until, at $\sim T_c$+1K, the FWHH measurement is dominated by its resolution-limited width.

Very significantly, crystal I shows no evidence whatsoever of this narrow component. The measured width of the scattering in crystal I decreases monotonically to T_c when a resolution-limited Bragg peak abruptly appears.

Cowley, Gibaud and Mitchell(1986) have sucessfully analysed the above data by modelling the observed scattering from crystal II as a superposition of a resolution limited Bragg peak and the broader, diffuse component. Within error, the critical exponents derived from the two separate data sets, crystal I and crystal II, are identical.

8.7) PRE-TRANSITIONAL BRAGG SCATTERING.

The behaviour of crystal II is very similar to the pre-transitional behaviour described by Andrews(1986) in $SrTiO_3$; a resolution limited Bragg-like peak, superimposed upon the broader critical scattering from the soft mode, first appearing several degrees above T_c and rapidly growing in intensity as T_c is approached. Significantly, though, the Bragg-like feature appears to be totally absent in the crystal I data!

To learn more about the nature and origin of the pre-transitional Bragg scattering component in crystal II, the instrument was, once again, reconfigured in the high-Q-resolution mode with Si(111) monochromator and analyser crystals. The objective of the experiment was to find the precise location of the feature in the reciprocal lattice, thereby identifying it as a cubic or tetragonal phase feature, and to measure (if possible) any additional wavevector width. Andrews(1986) has shown that the pre-transitional Bragg peak in $SrTiO_3$ has no additional wavevector width and so the correlations giving rise to it are ordered over many thousands of unit cells.

The experiment is technically very difficult, for two reasons. Firstly, the integrated intensity of the pre-transitional Bragg scattering feature is some four orders of magnitude less than that of a typical cubic-phase Bragg reflection. Secondly, the lattice parameter discontinuity from the cubic to the tetragonal phase is known to be very small, $\sim 9 \times 10^{-4}$Å (Ridou et al 1980). To ascertain whether the pre-transitional peak is located exactly at the cubic R-point (in which case it is an intrinsic feature of the cubic phase) or whether it is displaced from the R-point, and by how much, is experimentally very demanding.

Before presenting the experimental results we should recap, briefly, the crystallography of the phase transition. The reduction in symmetry at T_c is from the cubic space group Pm3m to the tetragonal space group I4/mcm. The transition is known to be slightly first-order and, at T_c, the tetragonal c/a ratio is ~ 1.0002 (Ridou et al 1980). The tetragonal 'c' axis can develop along any of the cubic axes with equal probability, and a simple model of the domain structure predicts the formation of three orthogonal tetragonal domains. A cubic-phase Bragg peak is, therefore, expected to decay into three

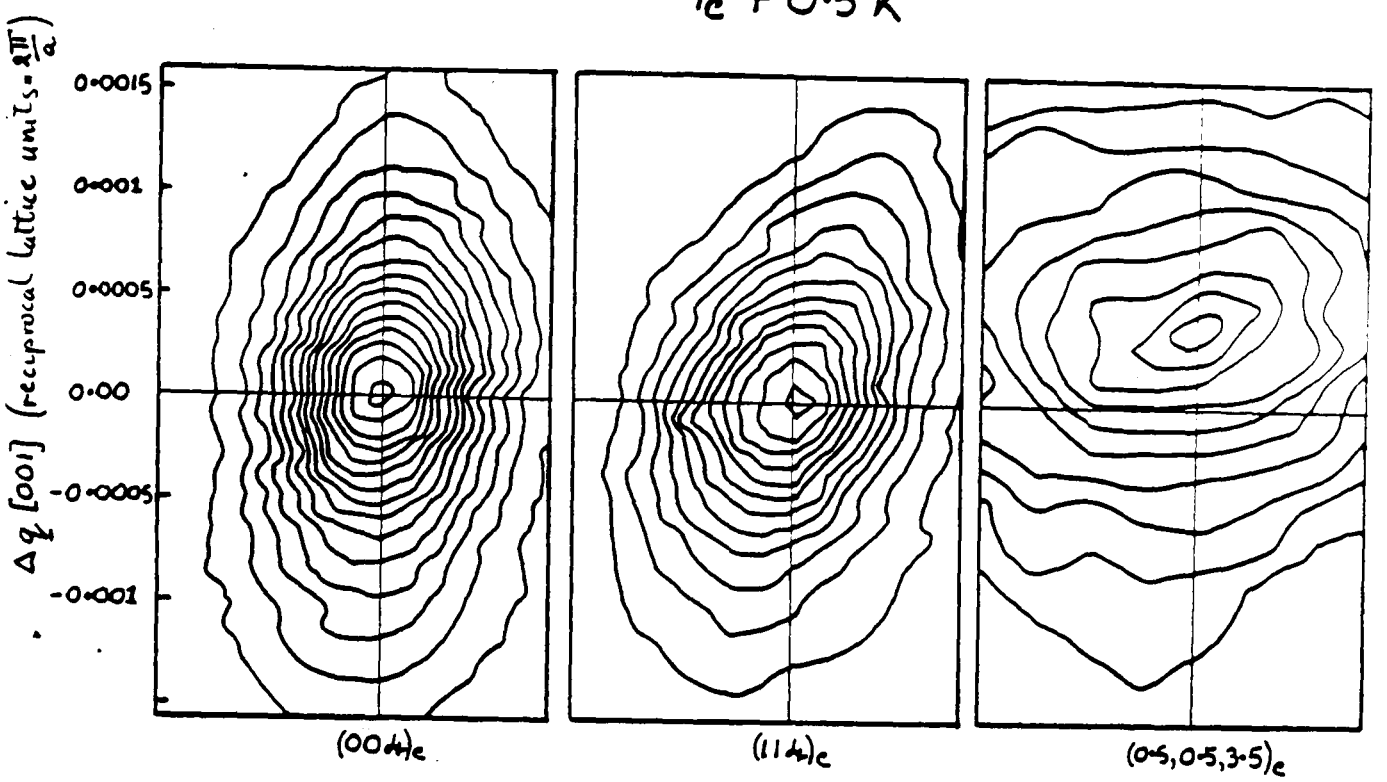

Figure 8.13 - High-resolution grid scans, with Si(111) monochromator and analyser crystals, of the $(114)_c$ and $(004)_c$ Bragg peaks and the $(0.5,0.5,3.5)_c$ R-point scattering at T_c+0.5K and T_c-0.2K.

tetragonal-phase Bragg peaks at T_C.

At the R-point examined in this experiment, $(0.5,0.5,3.5)_c$, three tetragonal-phase Bragg peaks should develop at T_c, namely $(0,1,7)_t$, $(-3,4,1)_t$ and $(3,4,1)_t$, indexed on the I4/mcm cell. However, $(0,1,7)_t$ is forbidden by the 'c-glide' condition in I4/mcm (0kl: k=2n), whilst $(-3,4,1)_t$ and $(3,4,1)_t$ appear superimposed. On this model, therfore, a single tetragonal-phase Bragg peak should be observed below T_c. In fact, as explained fully in section 8.5, the actual geometry of the domains in a real crystal is *considerably* more complicated than the above model would suggest. Rather than forming three orthogonal domain orientations in the tetragonal phase, giving rise to a cluster of three Bragg reflections, a real crystal forms up to *fifteen* domain orientations - resulting in a complicated cluster of up to *fifteen* tetragonal-phase Bragg reflections.

In this experiment considerable care was exercised to ensure that the area of sample crystal examined formed a simple domain pattern, comprised only of domains with the tetragonal 'c' axis in the plane of the face and giving rise only to the tetragonal Bragg reflections $(-3,4,1)_t$ and $(3,4,1)_t$ at the R-point.

The position, intensity and wave-vector width of the R-point scattering were measured by performing grid scans of the region around $(0.5,0.5,3.5)_c$ and of three reference cubic-phase Bragg reflections, $(0,0,4)_c$, $(1,1,4)_c$ and $(1,1,3)_c$, as the sample temperature was lowered through T_c. Typical sets of grid scans, recorded at T_c+0.5K and T_c-0.2K, are shown in Figure (8.13). It is immediately apparent that the pre-transitional scattering peak, at T_c+0.5K is clearly offset from the cubic R-point and is clearly broader, along both [110] and [001], than the two reference Bragg reflections shown. Below T_c, the scattering has developed into a true, tetragonal-phase Bragg reflection and the reference Bragg reflections have moved to their tetragonal positions, with indices $(\pm4,4,0)_t$, $(\pm3,5,2)_t$ respectively, in registry with the superlattice reflection. As expected, for tetragonal phase reflections with h+k>>l, the displacement is predominantly in the cubic [001] direction and its magnitude corresponds to a tetragonal c/a ratio of 1.00020(5).

The experimental results are summarised, graphically, in Figures (8.14), (8.15) and (8.16).

(i) Figure (8.14a) shows the measured displacement of the pre-transitional peak along the cubic [001] direction with respect to the cubic frame of reference defined by the trio of Bragg reflections. Within error, the

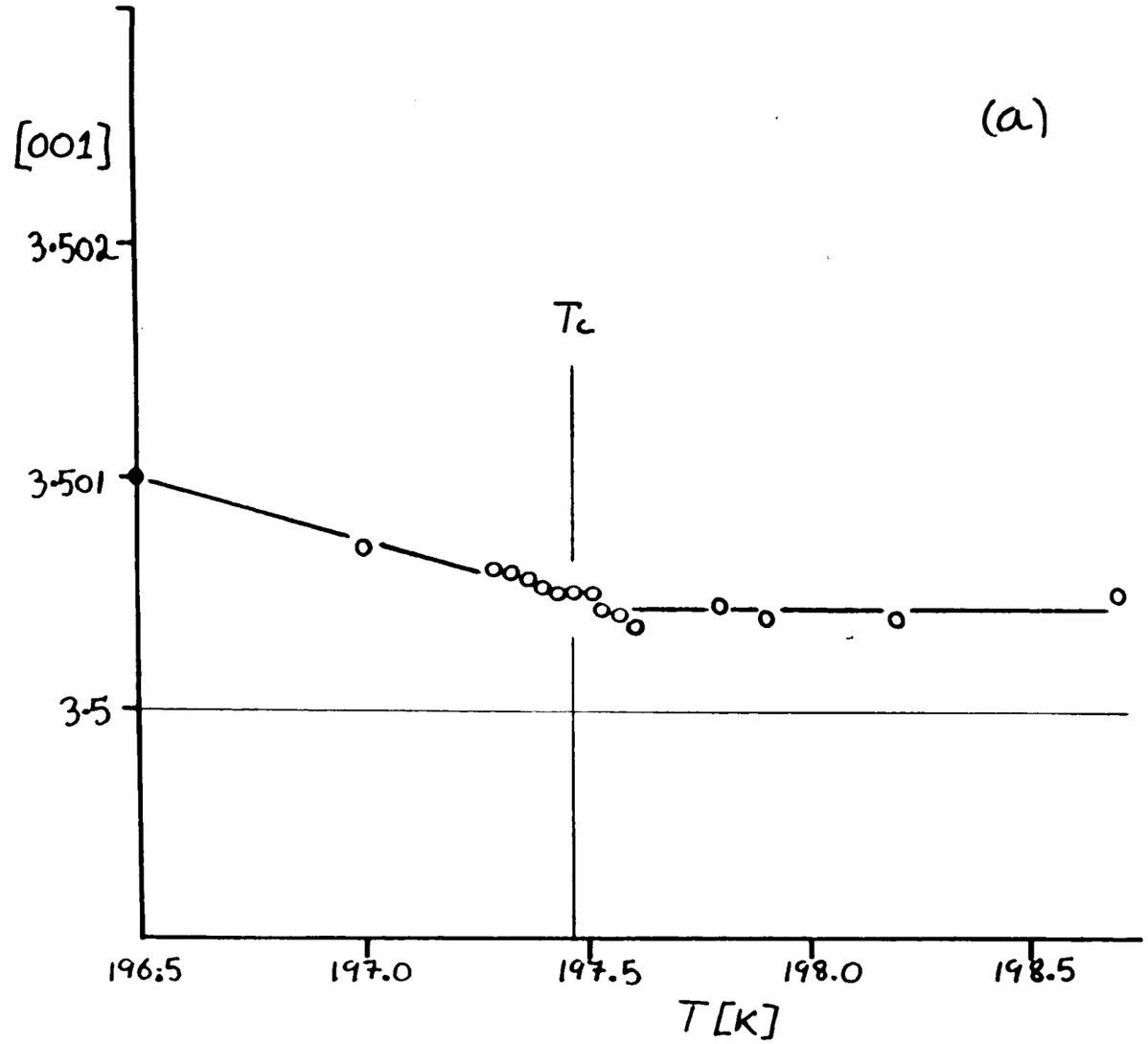

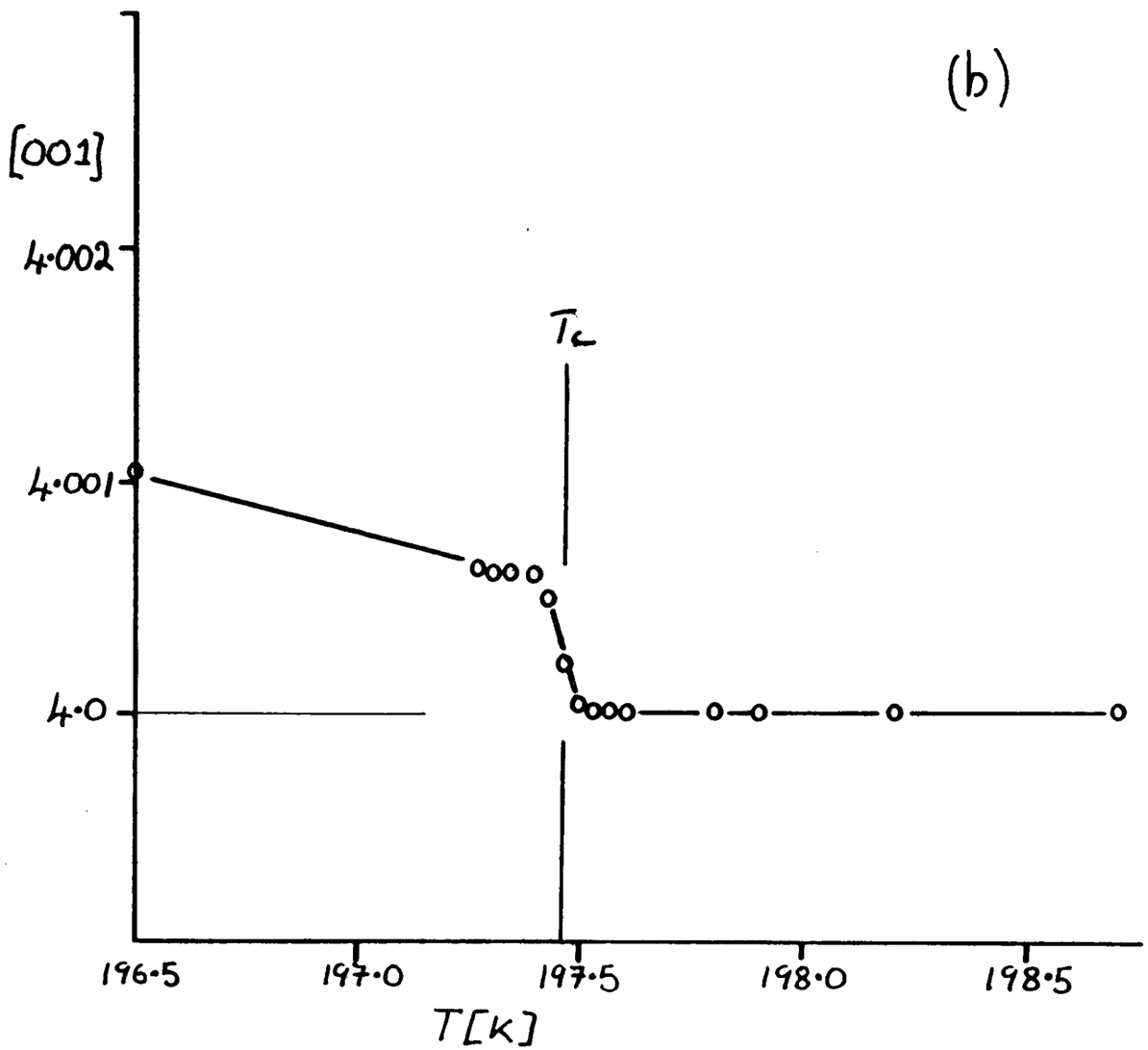

Figure 8.14 – (a) The measured position, along [001], of the pre-transitional scattering peak w.r.t the cubic frame of reference. (b) The measured position. along [001], of the $(114)_c$ Bragg peak w.r.t the cubic frame of reference.

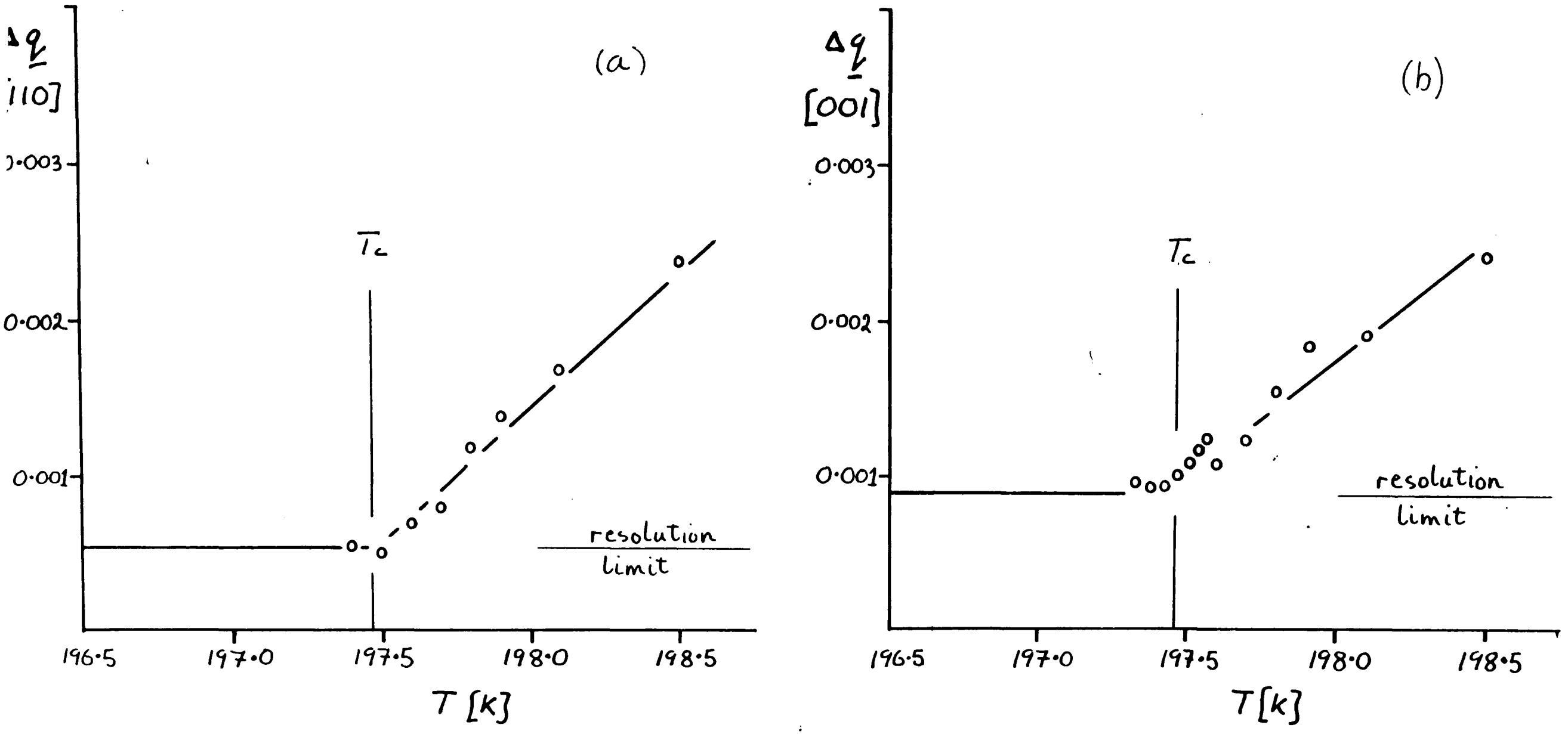

Figure 8.15 – The wave-vector width of the pre-transitional scattering peak (*a*) along [110] and (b) along [001].

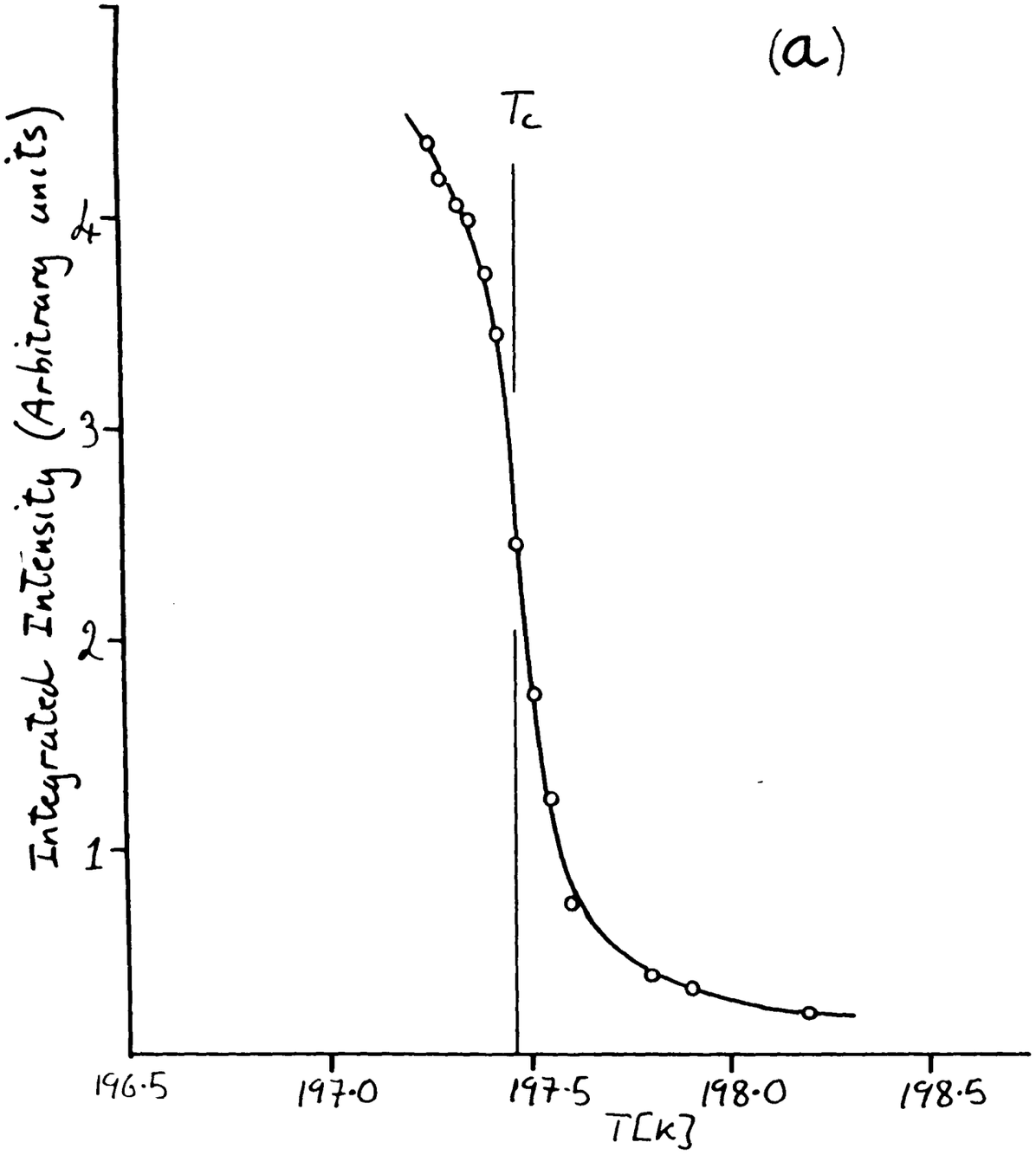

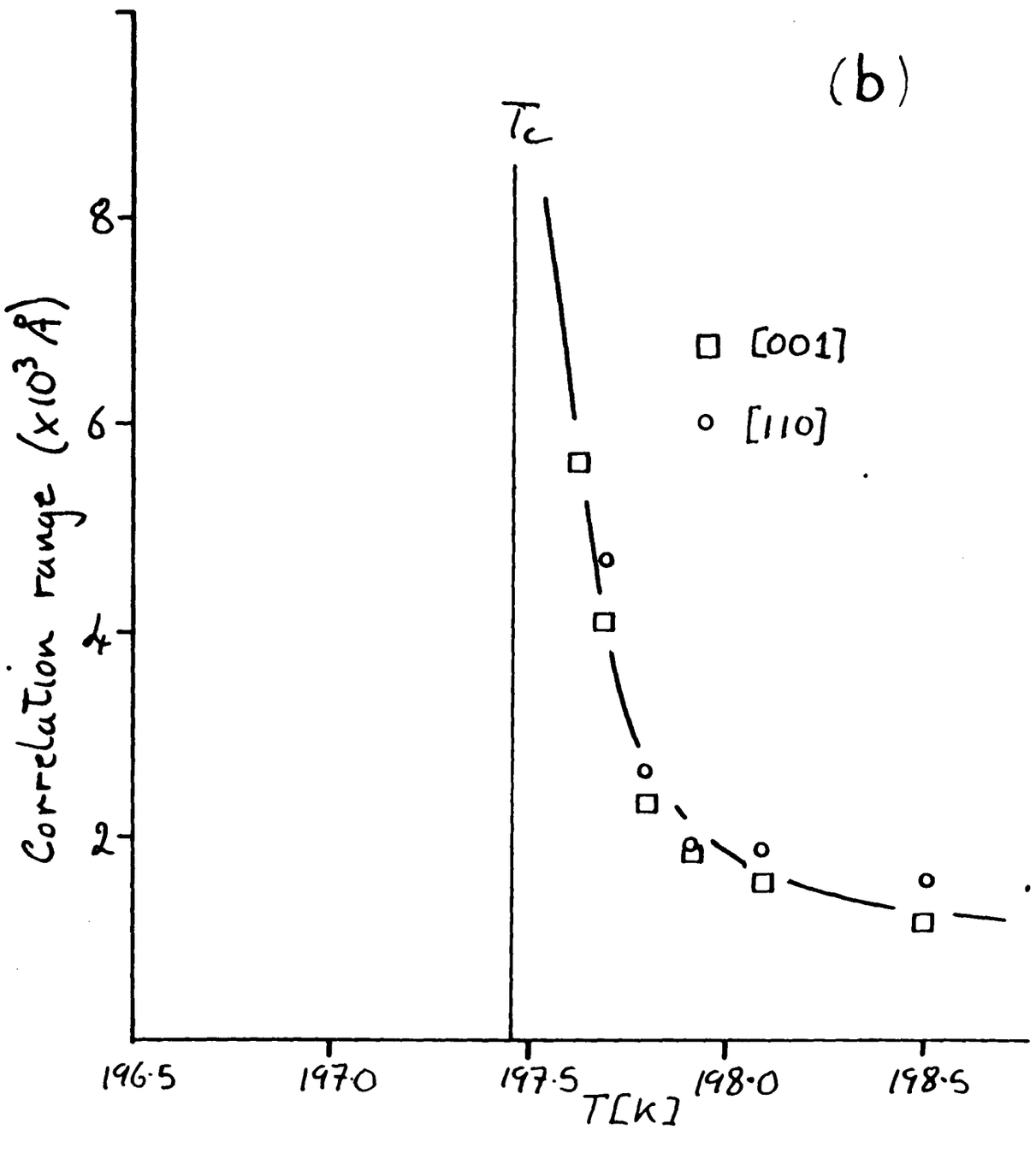

Figure 8.16 – (a) the integrated intensity of the R–point scattering. (b) the deconvolved correlation range o along [110] and □ along [001].

displacement is constant at 0.0004 reciprocal lattice units (i.e. 0.00056$Å^{-1}$) and does not alter perceptibly at T_c. In contrast, the Bragg reflections appear to jump discontinuously into registry with the new, superlattice reflection at T_c (Figure (8.14b)). Clearly, the pre-transitional scattering originates in parts of the sample crystal which have already transformed to the tetragonal phase whilst the bulk of the crystal remains cubic.

(ii) Figures (8.15a) and (8.15b) show the measured wave-vector widths of the pre-transitional scattering along [110] and [001]. The widths decrease continuously to the instrumental resolution limit at T_c. This behaviour contrasts quite sharply with the behaviour observed in $SrTiO_3$ by Andrews, where the pre-transitional scattering had no appreciable additional width, even at T_c+3K.

(iii) Figure (8.16a) shows the integrated intensity of the scattering which increases through T_c with no apparent discontinuity at the transition temperature, although it is possible that a small discontinuity would be masked by the temperature 'window' of the measurement (which is approximately equal to one temperature increment ~0.04K).

(iv) Finally, Figure (8.16b) shows the deconvolved correlation ranges in the [110] and [001] directions which are, respectively, parallel and perpendicular to the crystal surface. Within error, the correlation ranges are identical in both directions. Plotting the measured widths as inverse correlation length (κ) against reduced temperature ($(T-T_c)/T_c$) on a log/log scale shows that the results are well described by a power law relationship

$$\kappa = C((T-T_c) / T_c)^{\nu}$$

where T_c=197.4K, C=44Å and ν=0.68(2).

What clues do the above measurements provide to the origin of the pre-transitional scattering? Firstly, the temperature dependent width of the scattering rules out the possibility of a simple temperature gradient across the sampled area of crystal. Secondly, it is difficult to reconcile the lack of anisotropy in the measured correlation ranges, parallel and perpendicular to the surface, with the model of a critically growing surface layer. Thirdly, the apparent sample dependence (evidenced by Figures (8.11)and (8.12) and the study of $SrTiO_3$ by Andrews(1986)) suggests a connection with the defect

concentration or dislocation density.

The effect of defects on the static and dynamic critical behaviour of systems near displacive structural phase transitions has been considered by Halperin and Varma (1976). The precise effect depends upon the nature of the defect, whether it is mobile or fixed and whether the local symmetry is broken or maintained, but, under certain circumstances, the strain field around a defect can couple to the order parameter and thereby stabilise clusters of the low-temperature phase. The theoretical model predicts that the lengthscale of these clusters is limited by the correlation length of the system, a conclusion apparently in conflict with the two experimentally observed lengthscales, described above. The theoretical model, however, considers only point defects accompanied by an isotropic strain field. A real, mosaic crystal, on the other hand, almost certainly contains dislocations which extend over many thousands of unit cells and it is quite possible that this may account for the unexpectedly long correlation lengths.

If this, defect-stabilised pre-cursor cluster model is correct we are left with a picture of rather large (~2000Å diameter at T_c+1K), tetragonal-phase clusters existing in a cubic matrix, which grow in size as T_c is approached, eventually encompassing the entire crystal.

The intensity of the pre-transitional scattering, on this model, is governed by the structure factor of the superlattice reflection and the volume of the tetragonal clusters. The structure factor is directly related to the order-parameter of the low temperature phase, i.e. the rotation angle of the CaF_6 octahedra, and there is good evidence from structural studies of the tetragonal phase that this is strongly coupled to the tetragonal strain.

From Figure (8.14b) it appears that the tetragonal strain is constant from T_c to T_c+1.5K, then the observed integrated intensity above T_c, (Figure (8.16a)) as a fraction of its value at T_c, should measure the relative volumes of the cubic and tetragonal phase regions within the crystal. But at this point we encounter a paradox: both the intensity variation of the superlattice reflection and its diverging correlation length indicate a *continuous* evolution from a predominantly cubic phase to a wholly tetragonal phase whilst the zone-centre reflections exhibit a *discontinuous* jump to their tetragonal-phase positions at T_c! In other words, the transition appears to be second-order at the zone-boundary and first-order at the zone-centre.

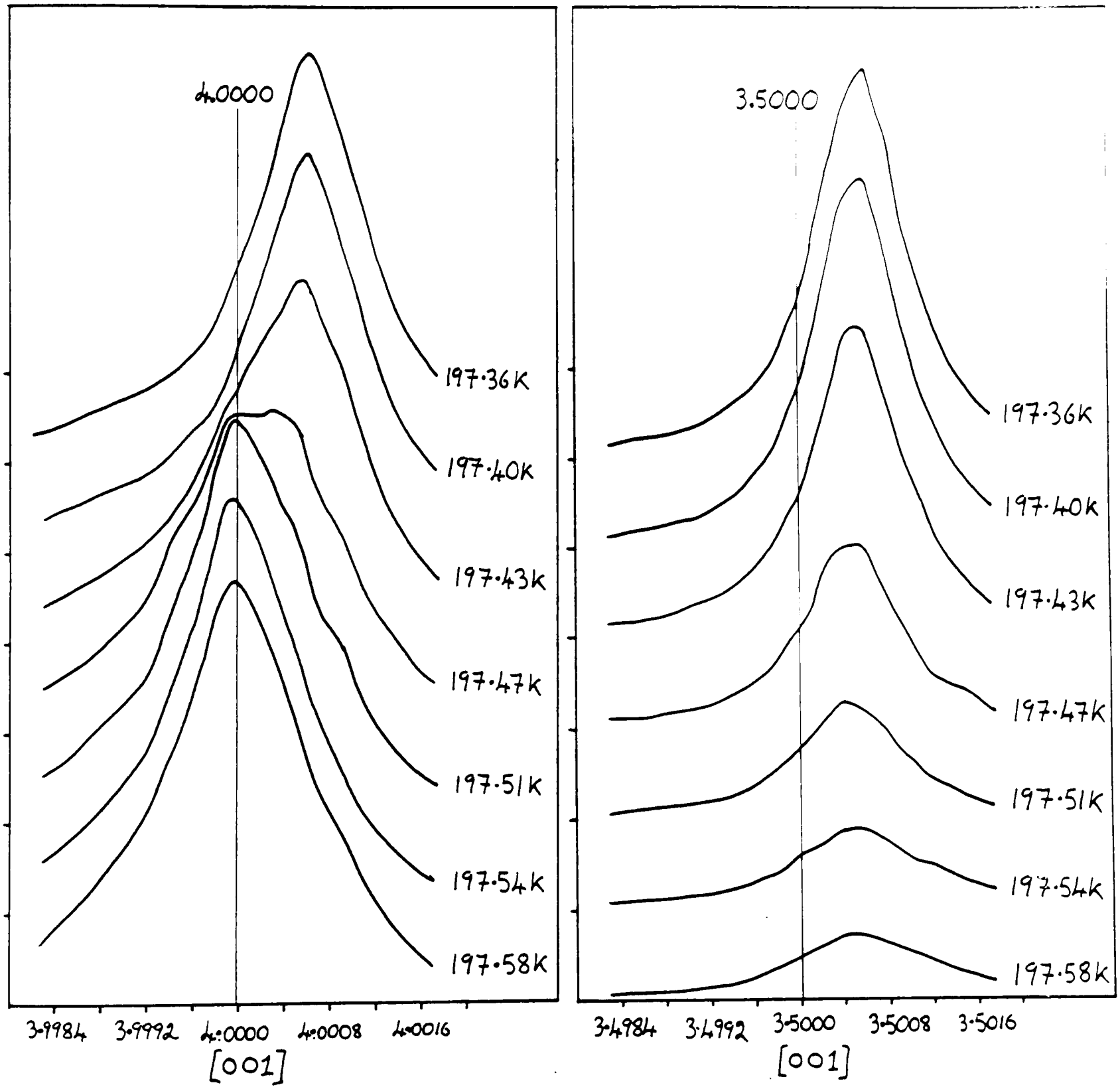

Figure 8.17 – Scan profiles, along [001] of the scattering at $(114)_c$ and $(0.5,0.5,3.5)_c$ as the temperature is lowered through T_c.

A somewhat clearer picture can be obtained by an examination of the scan profiles of the $(114)_c$ Bragg reflection and $(0.5,0.5,3.5)_c$ zone-boundary point shown in Figure (8.17). The figure shows a series of scans, in the [001] direction, as the temperature was lowered through T_c. The pre-transitional scattering peak is clearly visible, offset from the R-point, and continuously evolving into a true, tetragonal-phase superlattice Bragg peak below T_c. The $(114)_c$ Bragg reflection, on the other hand, is centered on the cubic reciprocal lattice point above T_c and, even at T=197.54K, when the intensity of the superlattice peak indicates that some 25% of the bulk of the crystal has the tetragonal structure, no asymmetry is evident in the Bragg peak. At T=197.46K, the tetragonal phase clearly encompases some 50% of the crystal and this is quite clearly reflected in both the profile of the (114) Bragg reflection and the intensity of the superlattice peak. Below T_c, there is an obvious asymmetry in the profile of the $(3,5,2)_t$ Bragg peak until 197.36K, when the ordering curve of Figure (8.16a) shows that the crystal is fully tetragonal.

Why is there no obvious asymmetry above T_c? The answer may lie in a remarkable similarity between the behaviour of this (defect influenced) system and the defect dominated behaviour observed at the commensurate-incommensurate transition in $BaMnF_4$, described in Chapters 6 and 7 of this thesis. To briefly recap the $BaMnF_4$ observations, at ~247K $BaMnF_4$ undergoes a second-order transition from a normal phase, with space goup $A2_1am$, to an incommensurate phase in which the symmetry of the average structure is monoclinic ($P2_1$) and the crystal forms twin domains. A crystal in which the incommensurate modulation wave was pinned by impurities or defects showed a depressed T_c and enhanced critical scattering which continuously evolved into an incommensurate phase satellite peak as the temperature was lowered though T_c. Above T_c, critical scattering measurements showed that fluctuations corresponding to <u>both</u> low temperature phase, monoclinic domains were present in equal poportions in the bulk cystal but at T_c there was an abrupt freezing of the system into <u>one</u> of the two possible monoclinic domains.

A closer inspection of the Bragg peak profiles, shown in Figure (8.17), shows that the width of the $(114)_c$ reflection above T_c is larger than the coresponding tetragonal phase peak $(3,5,2)_t$, below T_c. Significantly, the widths of this peak and the new superlattice Bragg peak, $(3,4,1)_t$, are identical.

A possible explanation for the lack of asymmetry in the Bragg

reflections above T_c is that pre-cursor clusters, or fluctuations, with all of the possible tetragonal orientations are present in equal quantities, but at T_c the portion of the crystal sampled in the experiment abruptly freezes into a single domain orientation. Scattering from clusters of the 'unfavourable' domain oientation above T_c is, of course, invisible at the zone-boundary because of the c-glide absence condition: but at the zone-centre, scattering from both tetragonal pre-cursor domains appears with equal weight. As discussed in chapter 7, with particular reference to $BaMnF_4$, this abrupt freezing of the system at T_c is very similar to the behaviour observed at the metastability boundary in the, much studied, dilute Ising 'antiferromagnetic systems (Birgeneau et al 1985).

There are two, obvious, experimental tests of this hypothesis. The first is to extend the Bragg peak profile measurements of Figure (8.17) to higher temperatures and follow the temperature dependence of the Bragg peak width through T_c. The second is to examine the scattering at an R-point where scattering from all of the possible domains is allowed by the space group of the low-temperature phase. In this case, pre-transitional scattering peaks corresponding to pre-cursor clusters of both domain orientations should be visible above T_c, but at T_c, as the system freezes into the low-temperature domain structure, the intensity of one peak should diminish as the other increases.

The author intends to carry out these measurements as soon as possible.

CONCLUSIONS.

This experimental, high-resolution x-ray scattering study has produced a wealth of new information on the 196K antiferrodistortive phase transition in $RbCaF_3$; information which is, to the best of the author's knowlege, unattainable by any other experimental technique. In section 8.5, the domain structure of $RbCaF_3$ in the tetragonal phase (and, by implication, that of all of the tetragonal perovskites) was shown to be considerably more complicated than the generally accepted model suggests. A correct interpretation of the results described in the subsequent sections depends *crucially* on the detailed knowlege of the domain distribution and geometry contained in section 8.5. The

low-Q-resolution measurements of the R_{25} soft-mode scattering, described in section 8.6 revealed a sample-dependent quasi-Bragg scattering component superimposed upon the broader diffuse scattering from the soft-mode, and it is the nature and origin of this quasi-Bragg scattering component with which the present work is concerned. The diffuse scattering from the R_{25} soft mode has been analysed and the results will be described in detail by Cowley et al(1986).

Section 8.7 describes a very detailed, high-Q-resolution, examination of the nature of this pre-transitional quasi-Bragg scattering component in the region of T_c. The results are consistent with the formation of metastable pre-cursor clusters of the tetragonal-phase structure close to T_c and their existence appears to be related to the presence of defects or dislocations. The lengthscale of the clusters is, at first, rather surprising. Current theoretical models predict that certain types of defect *can* stabilise clusters of the low-temperature phase but the size of the cluster is limited by the correlation length of the soft-mode. The experimentally observed clusters are, however, larger than the theory predicts by almost one order of magnitude. However, the models consider only point defects. The experiments, on the other hand, reveal a correlation between the mosaicity of the crystal and the occurence of these, rather large, pre-cursor clusters. This appears to suggest that dislocations, wich may extend over many thousands of unit cells, rather than point defects, play a major role in the establishment of pre-cursor clusters with a spatial extent of several thousands of Ångstroms.

As T_c is approached, the clusters grow continously in extent but, at T_c, there is an abrupt freezing of the system into the ordered domain structure of the low-temperature phase. This behaviour is remarkably similar to the behaviour observed in other materials undergoing structural phase transitions under the influence of random fields and may well turn out to be a general feature of all phase transitions in impure materials.

Unfortunately, .the above measurements give no absolute indication of the exact type or concentration of defects within the two sample crystals. The conclusion, that the presence of large pre-cursor clusters is connected to the crystal quality, is based on rocking-curve measurements of the mosaic spread of each crystal. On the basis of this measurement, both crystals would normally be considered to be of very high quality and their behaviour would normally be considered to be representative of a pure crystal. The surprising aspect of these results is that the critical behaviour of a crystal with a mosaic spread of the

order of 0.01° should be, quite drastically, altered by the presence of defects.

It is of some interest to consider the other reported observations of pre-transitional Bragg scattering in the light of the above conclusions. Very few authors, in fact, report sufficient details of sample preparation or characterisation. Of the few who do, Andrews(1986) and Darlington and O'Connor(1976) examined $SrTiO_3$ and Ridou et al (1980) examined $RbCaF_3$. Andrews $SrTiO_3$ sample had a measured mosaic spread of ~0.02°, and so was relatively far from perfect. The intensity of the feature was strongly dependent upon the method of sample preparation, being strongest in samples with surface layers damaged by polishing. Darlington and O'Connor did not report a measurement of the crystal mosaic spread but their samples were mechanically polished, a process which, as demonstrated by Andrews, inevitably introduces a damaged surface layer. In both of the above experimental studies, the intensity of the quasi-Bragg scattering component was reduced in annealed sample crystals.

Ridou et al, on the other hand, examined mechancally polished $RbCaF_3$ crystals and reported a careful assesment of the crystal quality. The crystal examined in the experiment had a bulk mosaic spread, measured by γ ray diffractometry, of 0.012° but a mosaic spread of ~0.017° when measured by x-ray diffractometry. The difference was, probably correctly, accounted for by the existence of a damaged surface layer. Large pre-cursor clusters were observed.

Recalling that the present experimental study has revealed evidence of large, pre-cursor clusters in a sample crystal with a mosaic spread of ~0.012° but no evidence of similar clusters in another crystal, from the same source, prepared in an identical manner, but with a measured mosaic spread of ~0.005°, the above observations are quite consistent. Very recently, highly perfect, flux grown samples of $SrTiO_3$ have become available. A comparative study of ultrasonic attenuation near the 105K phase transition in two sample crystals, one flux grown and the other grown by the more conventional Verneuil technique, has revealed sample dependent differences which the authors attribute to the presence of strain fields around defects in the Verneuil-grown sample (Fossum and Fossheim, 1985). Significantly, the phase transition in the flux-grown sample appeared to be slightly first-order. It would be interesting to examine such a sample using the high-$\mathbf{Q}$-resolution x-ray scattering technique and to compare the results with Andrews' study of a Verneuil-grown sample.

Conclusions

The principle purpose of this thesis was to explore some of the possible applications of the high-Q-resolution x-ray scattering technique in the field of structural phase transitions in crystalline solids. To this end, we have reviewed related work carried out by a number of research groups, we have discussed, in some detail, the x-ray optical factors determining the instrumental resolution in Q space and we have presented experimental studies of structural phase transitions in three materials, Ag_3AsS_3, $BaMnF_4$ and $RbCaF_3$.

In each case, the uniquely-high resolving power of the triple-crystal instrument has revealed new, and in some respects surprising, aspects of the phase transitions in these materials.

In proustite, for instance, we have demonstrated the existence of a (previously unsuspected) incommensurate phase and conducted an extremely detailed investigation of the temperature dependence of the wave-vector of the incommensurate modulation. As well as showing the nature of the incommensurate phase to be considerably more subtle than was first expected, the measurements also revealed a very long time constant for the ordering process. The ordering may be associated with the presence of mobile defects which pin the phase of the modulation wave, thereby inhibiting the establishment of long-range order. This phenomenon merits further, more detailed study.

In $BaMnF_4$ we have, for the first time, directly measured the magnitude of the monoclinic distortion angle of the average structure in the low-temperature incommensurate phase. This measurement has cleared up a longstanding uncertainty. The study also revealed remarkable similarities between the behaviour of an impure $BaMnF_4$ sample crystal and the behaviour observed in the, much studied, Random Ising Antiferromagnets.

The investigation of $RbCaF_3$ has revealed a remarkably complicated domain structure in the tetragonal phase which, by implication, must be common to all of the perovskite family and which can introduce serious complications into experimental studies which are sensitive to the domain structure. The experiment also revealed an apparent connection between the presence of large pre-cursor clusters of the tetragonal phase above T_c and the sample crystal quality.

In fact, a recurring theme of this thesis is the role played by defects. It has long been accepted, or at least suspected, that defects play an important role in modifying the behaviour of materials near phase transitions. A number of theoretical models have been proposed to describe the effect of defects but their role has, to a large extent, been neglected.

The, perhaps surprising but certainly significant, conclusion which has emerged from the experimental work presented in this thesis is that defect-influenced behaviour is seen in sample crystals which would, by any normal standards, be regarded as highly perfect.

Clearly, if substantial progress is to be made in experimental studies of structural phase transitions in crystalline solids, the problem of defects, impurities and crystal quality must be overcome. This can be achieved by improving the techniques of crystal growth and sample characterisation and trying to gain a clearer theoretical and experimental understanding of the way in which real defects influence the critical behaviour of real crystals.

Abdikamalov B A, Ivanov V I, Shekhtman V Sh and Shmyt'ko I M (1978) Sov.Phys. Solid State **20**, 1711

Alexander L E and Smith G S (1962) Acta Cryst. **15**, 983

Alexander L E and Smith G S (1964) Acta Cryst. **17**, 1195

Alexander L E and Smith G S (1964) Acta Cryst. **17**, 447

Allen S (1985) private communication and Phase Transitions, in press

Allison S K and Williams J H (1930) Phys.Rev. **35**, 149

Almairac R, Rousseau M, Gesland J Y, Nouet J and Hennion B (1977) J.Physique **38**, 1429

Als-Neilsen J, Birgeneau R J, Kaplan M, Litster J D and Safinya C R (1977) Phys.Rev.Lett. **39**, 1668

Als-Nielsen J and Pershan P S (1983) Nucl.Instr.Meth. **208**, 545

Als-Nielsen J, Birgeneau R J, Kaplan M, Litster J D and Safinya C R (1977) Phys.Rev.Lett. **39**, 352

Als-Nielsen J, Litster J D, Birgeneau R J, Kaplan M, Safinya C R, Lindegaard-Andersen A and Mathiesen B (1980) Phys.Rev. B**22**, 312

Andrews S R (1986) J.Phys.C: Solid State Phys. in press.

Andrews S R and Cowley R A (1985) J.Phys.C: Solid State Phys. **18**, 6427

Andrews S R and Cowley R A (1986) J.Phys.C: Solid State Phys. in press.

Andrews S R and Mashiyama H (1983) J.Phys.C: Solid State Phys. **16**, L247

Bacon G E and Pease R S (1955) Proc.Roy.Soc. London A**230**, 359

Barthes-Regis M, Almairac R, St-Gregoire P, Fillippini C,Steigenberger U, Nouet J and Gesland Y (1983) J.Physique Lettres **44**, L829

Belanger D P, King A R, and Jaccarino V (1985) Phys.Rev. B**31**, 4538

Belyaev A D, Gololobov Yu P, Machulin V F, Miselyuk E G and Nekrasova I M (1984) Sov.Phys. Solid State **26**, 820

Birgeneau R J, Cowley R A, Shirane G and Yoshizawa H (1984) J.Stat.Phys. **34**, 817

Birgeneau R J, Cowley R A, Shirane G and Yoshizawa H (1985) Phys.Rev.Lett. **54**, 2147

Bjerrum-Moller H and Neilsen M (1969) Acta Cryst. **25**, 547

Bleif H-J, Cowley R A and Nelmes R J (1982) J.Phys.C: Solid State Phys. **15**, L201

Bohr J, Feidenhans'l R, Neilsen M, Toney M, Johnson R L and Robinson I K (1985) Phys.Rev.Lett. **54**, 1275

Bondar A V, Vikhnin V S, Ryabchenko S M, Yachmenev V E (1983) Sov.Phys. Solid State **25**, 1497

Bonse U and Hart M (1965) Appl.Phys.Lett. **7**, 238

Brinkman W F, Fisher D S and Moncton D E (1982) Science **217**, 693

Bruce A D and Cowley R A (1981) *Structural Phase Transitions* London:Taylor and Francis

Bruce A D, Taylor W and Murray A F (1980) J.Phys.C: Solid State Phys. **13**, 483

Burbank R D (1964) Acta Cryst. **17**, 434

Buzare J Y and Simon P (1984) J.Phys.C: Solid State Phys. **17**, 2681

Cochran W (1960) Adv.Phys. **9**, 387

Cochran W (1963) Rep.Prog.Phys. **16**, 1

Cochran W (1969) Adv.Phys. **18**, 157

Cochran W and Kartha G (1956) Acta Cryst. **9**, 941

Cooper M J and Nathans R (1967) Acta Cryst. **23**, 357

Cowley J M (1981) 'Diffraction Physics' (Amsterdam)

Cowley R A and Shirane G (1978) J.Phys.C: Solid State Phys. **11**, L939

Cowley R A, Birgeneau R J, Shirane G and Yoshizawa H (1984) in *Multicritical Phenomena* ed. R. Pynn, Plenum (New York).

Cowley R A, Bleif H-J, Andrews S R and Nelmes R J (1983) Physica **120**B, 267

Cowley R A, Mitchell P W and Gibaud A - to be submitted.

Cowley R A, Yoshizawa H, Shirane G and Birgeneau R J (1985) Z.Phys. B**58**, 15

Cox D E, Shapiro S M, Cowley R A, Eibschutz M and Guggenheim H J (1979) Phys.Rev.B **19**, 5754

Cox D E, Shapiro S M, Nelmes R J, Ryan T W, Bleif H-J, Cowley R A, Eibschutz M and Guggenheim H J (1983) Phys.Rev.B **28**, 1640

D'Amico K L, Moncton D E, Specht E D, Birgeneau R J, Nagler S E and Horn P M (1984) Phys.Rev.Lett. **53**, 2250

Darlington C N W and O'Connor D A (1976) J.Phys.C: Solid State Phys. **9**, 3561

Darlington C N W, Fitzgerald W J and O'Connor D A (1975) Phys.Lett. **54**A, 35

Darwin C G (1914) Phil.Mag. **27**, 325

Davey S C, Budai J, Goodby J W, Pindak R and Moncton D E (1984) Phys.Rev.Lett. **53**, 2129

Davidov D, Safinya C R, Kaplan M, Dana S S, Schaetzing R, Birgeneau R J and Litster J D (1979) Phys.Rev. B**19**, 1657

De Gennes P D (1974) *The Physics of Liquid-Crystals* Oxford U.P. London.

Dederichs P H (1971) Phys.Rev. B**4**, 1041

Dresselhaus M S and Dresselhaus G (1981) Adv.Phys. **30**, 139

Du Mond J W M (1937) Phys.Rev. **52**, 872

Dvorak V and Fousek J (1980) Phys.Stat.Sol.(a) **61**, 99

Eisenberger P and Marra W C (1981) Phys.Rev.Lett. **46**, 1081

Eisenberger P, Alexandropoulos N G and Platzman P M (1972) Phys.Rev.Lett. **28**, 1519

Engel P and Nowacki W (1966) Neues.Jahrb.Mineral.Monatsch. **8**, 181

Erbil A, Kortan A R, Birgeneau R J and Dresselhaus M S (1983) Phys.Rev. B**28**, 6329

Erhart P and Schilling W (1973) Phys.Rev. B**8**, 2604

Ewen P S, Taylor W and Paul G L (1983) J.Phys.C: Solid State Phys. **16**, 6475

Fisher M E (1968) Phys.Rev. **176**, 257

Fishman S and Aharony A (1979) J.Phys.C:Solid State Phys. **12**, L729

Fjaer E, Cowley R A and Ryan T W (1985) J.Phys.C: Solid State Phys. **18**, l41

Fleming R M, Moncton D E and McWhan D B (1978) Phys.Rev. B**18**, 5560

Fleming R M, Moncton D E, Axe J D and Brown G S (1984) Phys.Rev. B**30**, 1877

Fleming R M, Moncton D E, McWhan D B and DiSalvo F J (1980) Phys.Rev.Lett. **45**, 576

Fleury P A, Scott J F and Worlock J M (1968) Phys.Rev.Lett. **21**, 16

Fossum J O and Fossheim K (1985) J.Phys.C: Solid State Phys. **18**, 5549

Fujii Y and Yamada Y (1971) J.Phys.Soc.Japan **30**, 1676

Gibaud A and Ryan T W - to be submitted.

Golovko U A and Levanyuk A P (1983) *Light scattering near phase transitions* ed. A.Levanyuk and H.Z.Cummins (North Holland, New York)

Griffiths R B (1970) Phys.Rev.Lett. **24**, 1497

Guerard B v, Grasse D and Peisel J (1980) Phys.Rev.Lett. **44**, 262

Halperin B and Varma C M (1976) Phys.Rev. B**14**, 4030

Harada J, Axe J D and Shirane G (1971) Phys.Rev. B**4**, 155

Hardcastle S E, Misenheimer M E and Zabel H (1983) Rev.Sci.Instrum. **54**, 206

Harker D (1936) J.Chem.Phys. **4**, 381

Heiney P A, Birgeneau R J, Brown G S, Horn P M, Moncton D E and Stephens P W (1982) Phys.Rev.Lett. **48**, 104

Hidaka M and Scott J F (1984) Physica B and C **123**, 291

Horn P M, Birgeneau R J, Heiney P and Hammonds E M (1979) Phys.Rev.Lett. **41**, 961

Huang K (1947) Proc.Roy.Soc. London A**190**, 122

Iida A (1979) Phys.Stat.Sol. (a)**54**, 701

Iida A and Kohra K (1979) Phys.Stat.Sol. (a)**51**, 533

Imry Y and Ma S (1975) Phys.Rev.Lett. **35**, 1399

James R W (1948) *The Optical Principles of the Diffraction of X-Rays* G. Bell and Sons. London.

Jex M, Maetz J and Mullner M (1980) Phys.Rev. B**21**, 1209

Jona F and Shirane G (1962) *Ferroelectric Crystals* Macmillan, New York.

Keve E T, Abramams S C and Bernstein J L (1969) J.Chem.Phys. **51**, 4928

Khasanov S S, Shekhtman V Sh and Shmyt'ko I M (1984) Sov.Phys. Solid State **26**, 572

Kjaer K, Neilsen M, Bohr J, Lauter H J and McTague J P (1982) Phys.Rev. B**26**, 5186

Kjems J K, Passel L, Taub H, Dash J G and Novaco A D (1976) Phys.Rev. B**13**, 1446

Kortan A R, Erbil A, Birgeneau R J and Dresselhaus M S (1982) Phys.Rev.Lett. **49**, 1427

Ladell J and Spielberg N (1966) Acta Cryst. **21**, 103

Lavrencic B B and Scott J P (1981) Phys.Rev. B**24**, 2711

Le Guillou J C and Zinn-Justin J (1980) Phys.Rev. B**21**, 3976

Levstik A, Blinc R, Kadaba P and Cizikov S (1975) Bull.Am.Phys.Soc **20**, 558

Lines M E and Glass A M (1977) *Principles and Applications of Ferroelectrics and Related Materials* Clarendon Press, Oxford.

Lomov A A, Zaumseil P and Winter U (1985) Acta Cryst. A**41**, 223

McMillan W L (1971) Phys.Rev. A**4**, 1238

McTague J P, Als-Nielsen M, Bohr J and Neilsen M (1982) Phys.Rev. B**25**, 7765

McWhan D B, Moncton D E, Fleming R M and DiSalvo F J (1980) Phys.Rev.Lett.

45, 269

Maetz J, Mullner M, Jex H and Peters K (1978) Sol.St.Commun. **28**, 555

Marion G, Almairac R, Lefebvre J and Ribet M (1981) J.Phys.C: Solid State Phys. **14**, 3177

Marra W C, Eisenberger P and Cho A Y (1979) J.Appl.Phys. **50**, 6927

Marra W C, Fuoss P H and Eisenberger P (1982) Phys.Rev.Lett. **49**, 1169

Mathieson A McL (1982) Acta Cryst. A**38**, 378

Mathieson A McL (1983a) Acta Cryst. A**39**, 79

Mathieson A McL (1983b) J.Appl.Cryst. **16**, 257

Mathieson A McL (1984) Acta Cryst. A**40**, 355

Mathieson A McL (1985) Acta Cryst. A**41**, 309

Merril J J and Du Mond J W M (1961) Ann.Phys. **14**, 166

Mochrie S G J, Sutton M, Birgeneau R J, Moncton D E and Horn P M (1984) Phys.Rev. B**30**, 263

Modine F A, Sonder E, Unruh W P, Finch C B and Westbrook R D (1974) Phys.Rev. B**10**, 1623

Moncton D E and Brown G S (1983) Nucl.Instr.Meth. **208**, 579

Moncton D E and Pindak R (1979) Phys.Rev.Lett. **43**, 701

Moncton D E, Pindak R, Davey S C and Brown G S (1982) Phys.Rev.Lett. **49**, 1865

Moncton D E, Stephens P W, Birgeneau R J. Horn P M and Brown G S (1981) Phys.Rev.Lett. **46**, 1533

Nelmes R J, Howard C J, Ryan T W, David W I F, Schultz A J and Leung P C W (1984) J.Phys.C: Solid State Phys. **17**, L861

Nelmes R J, Kuhs W F, Howard C J, Tibballs J E and Ryan T W (1985) J.Phys.C: Solid State Phys. **18**, L711

Nelmes R J, Meyer G M and Tibballs J E (1982) J.Phys.C: Solid State Phys. **15**, 59

O'Hara C, Shorrocks N M, Whatmore R W and Jones O (1982) J.Phys.D: Applied Phys. **15**, 1289

Ocko B M, Kortan A R, Birgeneau R J and Goodby J W (1984) J.Physique **45**, 113

Patel J R (1975) J.Appl.Cryst. **8**, 186

Pisarev R V, Krichevtzov B B, Markovin P A, Korshunov O Yu and Scott J F (1983) Phys.Rev.B **28**, 2677

Pynn R, Fujii Y and Shirane G (1983) Acta Cryst. A**39**, 38

Rees D C (1982) Acta Cryst. A**38**, 201

Reid J S (1981) Acta Cryst. A**37**, 382

Ridou C, Rousseau M and Freund A (1980) Sol.St.Commun. **35**, 723

Riste T, Samuelsen E J, Otnes K and Feder J (1971) Sol.St.Commun. **9**, 1455

Robinson I K (1983) Phys.Rev.Lett. **50**, 1145

Robinson I K - private communication.

Rousseau M, Nouet J, Almairac R and Hennion B (1976) J.Physique Lett. **37**, L33

Ryan T W (1986) J.Phys.C: Solid State Phys. in press.

Ryan T W, Gibaud A and Nelmes R J (1985) J.Phys.C: Solid State Phys. **18**, 5279

Ryan T W, Cowley R A and Andrews S R (1986) J.Phys.C: Solid State Phys. in press.

Ryan T W, Nelmes R J and Gibaud A - to be submitted.

Safinya C R, Kaplan M, Als-Nielsen J, Birgeneau R J, Davidov D, Litster J D, Johnson D L and Neubert M E (1980) Phys.Rev. B**21**, 4149

Schoenborn B P (1983) Acta Cryst. A**39**, 315

Scott J F (1979) Rep.Prog.Phys. **12**, 1055

Scott J F, Habbal F and Hidaka M (1982) Phys.Rev.B **25**, 1805

Semak D G, Mikhal'ko I P, Popik Y V, Bercha D M, Nebola I I, Golovei M I, Gurzan M I (1975) Sov.Phys.Semicond. **8**, 823

Sham L J and Patton B R (1976) Phys.Rev. B**13**, 3151

Shapiro S M, Axe J D, Shirane G and Riste T (1972) Phys.Rev. B**6**, 4332

Shapiro S M, Cowley R A, Cox D E, Eibschutz M and Guggenheim H J (1976) *Proceedings of the Conference on Neutron Scattering*, ed. R.M.Moon (NTIS,Springfield,Virginia 22161)

Shirane G and Yamada Y (1969) Phys.Rev. **177**, 858

Simon P, Buzare J Y, Rousseau M, Leble A and Fayet J C (1981) Ferroelectrics **36**, 451

Skalyo J, Frazer B C and Shirane G (1970) Phys.Rev. B**1**, 278

Smolenskii G A, Sinii I G, Prokhorova S D, Godovikova A A, Laikho R, Levola T, Karaemyaki E (1981) Sov.Phys. Solid State **23**, 1178

Specht E D, Sutton M, Birgeneau R J, Moncton D E and Horn P M (1984) Phys.Rev. B**30**, 1589

Stedman R (1968) Rev.Sci.Instrum. **39**, 878

Stephens P W, Heiney P, Birgeneau R J and Horn P M (1979) Phys.Rev.Lett. **43**, 47

Terauchi H and Yamada Y (1972) J.Phys.Soc.Japan **33**, 446

Terauchi H, Takenaka H and Shimaoka K J.Phys.Soc.Japan **39**, 435

Van Hove L (1954) Phys.Rev. **95**, 249

Villain J (1985) in *Scaling Phenomena in Disordered Systems* ed. R.Pynn, Plenum (in press).

Warren B E (1941) Phys.Rev. **59**, 693

Werner S A (1972) Acta Cryst. A**28**, 143

Wilson K G (1971) Phys.Rev. B**4**, 3174

Witz J (1969) Acta Cryst. A**25**, 30

Yamada Y and Yamada T (1966) J.Phys.Soc.Japan **21**, 2167

Yoshizawa H, Cowley R A, Shirane G and Birgeneau R J (1985) Phys.Rev. B**31**, 4348

Zacharaisen W H (1945) *Theory of X-Ray Diffraction in Crystals* New York.

Zaumseil P and Winter U (1982) Phys.Stat.Sol. (a)**70**, 497

X-ray- and neutron-diffraction measurements on $BaMnF_4$

D. E. Cox and S. M. Shapiro
Brookhaven National Laboratory, Upton, New York 11973

R. J. Nelmes, T. W. Ryan, H. J. Bleif,* and R. A. Cowley
Department of Physics, University of Edinburgh, Mayfield Road, Edinburgh EH9 3JZ, Scotland

M. Eibschütz and H. J. Guggenheim
Bell Laboratories, Murray Hill, New Jersey 07974

(Received 7 January 1983)

X-ray- and neutron-diffraction measurements on powder and single-crystal samples of $BaMnF_4$ have failed to show any evidence for the distortion with wave vector, in reciprocal-lattice units, $\vec{q} = (0.4, 0, 0.5)$ recently reported by Scott, Habbal, and Hidaka. The distorted phase which is observed below 247 K is described by a wave vector $\vec{q} = (\zeta, 0.5, 0.5)$ with ζ incommensurate. There is a small ($\sim 1\%$) increase in the magnitude of ζ as the temperature is lowered to 100 K, and the detailed temperature dependence of ζ is found to be different on heating and on cooling. The low-temperature distortion is characterized by a single wave vector $\vec{q} = (\zeta, 0.5, 0.5)$ rather than by a pair of wave vectors $(\zeta, 0.5, 0.5)$ and $(\zeta, -0.5, 0.5)$.

I. INTRODUCTION

The structural properties of $BaMnF_4$ are unusual and ıave attracted considerable interest over the past few years, s described in a review by Scott.[1] At about 250 K the ma-erial undergoes a phase transition from an orthorhombic tructure with space group $A2_1am$ ($a = 5.9845$ Å, $= 15.098$ Å, $c = 4.2216$ Å at 298 K). The nature of the ɔw-temperature phase was studied in detail by some of the resent authors[2] using neutron-diffraction techniques. The esults showed that this phase was distorted from the high-emperature phase by a displacement with a wave vector, in eciprocal-lattice units, $\vec{q} = (0.392, 0.5, 0.5)$. This phase ʻas unusual in that it remained incommensurate down to ıe lowest temperatures and that the wave vector of the dis-ɔrtion did not change with temperature within the resolu-on of the experiment.

More recently Scott, Habbal, and Hidaka[3] have reported ɔecific-heat measurements, and more briefly some iezoelectric resonance studies, and x-ray-, neutron-, and lectron-diffraction measurements on $BaMnF_4$. On the asis of the results from the first two techniques, they con-ude that there are two transitions, at 247 and 255 K. The iffraction measurements showed many samples to exhibit a isordered $P2_12_12_1$ structure, which was attributed to a par-cular type of stacking fault in which the MnF_6 chains are acked antiparallel along the b axis. Unlike the sample with ıe usual $A2_1am$ structure, these disordered samples ıowed no structural phase transition between 77 and 570 .

Samples with the $A2_1am$ structure were studied by Scott *al.* below 250 K, and x-ray and electron scattering data ıowed superlattice reflections at a wave vector $\vec{q} = (0.4, 0, 5)$, corresponding to a commensurate unit cell $5a \times b \times 2c$ ith respect to the room-temperature cell. However, neu-on scattering results showed reflections of the type $= (0.392, 0.5, 0.5)$, in agreement with our earlier work.[2] his led Scott *et al.* to suggest that the neutron scattering ises from magnetic reflections due to short-range spin or-ering at 250 K.

This explanation seems unlikely to us in view of our earlier detailed measurements both at the structural transition around 250 K and the magnetic transition at 26 K, but in view of the discrepancy, and the suggestion of Scott *et al.*, that there is another phase between 247 and 255 K which is incommensurate,[4] we have performed further neutron studies and new x-ray-diffraction measurements with improved resolution to elucidate the nature of the structural phase transition in $BaMnF_4$. In Sec. II we describe our results and show that both x-ray- and neutron-diffraction results for our specimens of $BaMnF_4$ are consistent with our earlier measurements and inconsistent with those of Scott *et al.*[3] We then report on measurements of the temperature dependence of the modulation wave vector $\vec{q}$ and on the structure of the incommensurate phase, which is shown to have a form such that in each domain only one of the modes $\vec{q}_1 = (0.392, 0.5, 0.5)$ or $q_3 = (0.392, -0.5, 0.5)$ describes the wave vector of the modulation (the notation is that of Ref. 2). In Sec. III the results are summarized and discussed.

II. EXPERIMENTAL

The measurements were performed mostly on the same powder and single-crystal specimens used in our earlier study. The single crystals were grown at Bell Laboratories from zone melted materials and several different specimens were studied. One crystal was also grown by similar techniques at the Clarendon Laboratory, Oxford. In our studies no difference was observed in the results obtained from these various specimens.

The experiments were performed using neutron-diffraction techniques at the Brookhaven National Laboratory High-Flux Beam Reactor (HFBR), x-ray powder measurement at Brookhaven, and x-ray single-crystal measurements at Edinburgh University. These latter measurements were performed partly with an Enraf-Nonius CAD-4 four-circle diffractometer and partly with a high-resolution two-circle x-ray spectrometer with an Elliott 15-kW rotating

anode generator as the x-ray source and a Si monochromator to provide a very well-collimated incident beam.

Initially a search was made for a modulation wave vector $\vec{q} = (0.4, 0, 0.5)$ using neutron-diffraction techniques and the x-ray four-circle diffractometer. No evidence was found for any intensity at the corresponding wave-vector transfers using x-ray-diffraction techniques. Initially some scattering was observed in the neutron-diffraction experiment for a wave vector $\vec{Q} = (2.39, 0, 0.5)$ (Ref. 5) but this was found to arise from a small second crystal in the sample misoriented by about 4° with respect to the main crystal and is not characteristic of a true single crystal.

X-ray-powder-diffraction measurements were made on an an automated General Electric XRD5 diffractometer with Cu $K\alpha$ radiation at a number of temperatures between 20 – 295 K. Below 250 K, several small satellite reflections characteristic of the modulation $\vec{q} = (0.39, 0.5, 0.5)$ were observed in the low angle region of the pattern in the range $2\theta = 20° - 40°$, with intensities typically of the order of 1% of those of the fundamental peaks. A careful search was made for superlattice peaks characteristic of the (0.4, 0, 0.5) modulation reported by Scott *et al.*, but none could be detected in this region within the experimental sensitivity, which was about 0.02% of the intensity of the fundamental reflections.

The intensity of the x-ray scattering from the strongest incommensurate peak (which actually consists of two overlapping reflections) from the power sample is shown in Fig. 1. This is clearly very similar to the neutron-diffraction results shown in Fig. 12 of Ref. 2, and we therefore conclude that the incommensurate structure with $\vec{q} = (0.392, 0.5, 0.5)$ scatters both neutrons and x rays in a similar way, and hence that the scattering cannot be of magnetic origin.

A detailed study of the temperature dependence of the satellite wave vector was performed on single crystals with both neutron- and x-ray-diffraction techniques. In both cases measurements were made of two satellite reflections corresponding to $\vec{q} = (\zeta, 0.5, 0.5)$ and $(-\zeta, 0.5, 0.5)$ so as to obtain the wave vector ζ as accurately as possible by taking the difference in the reciprocal-lattice positions. The

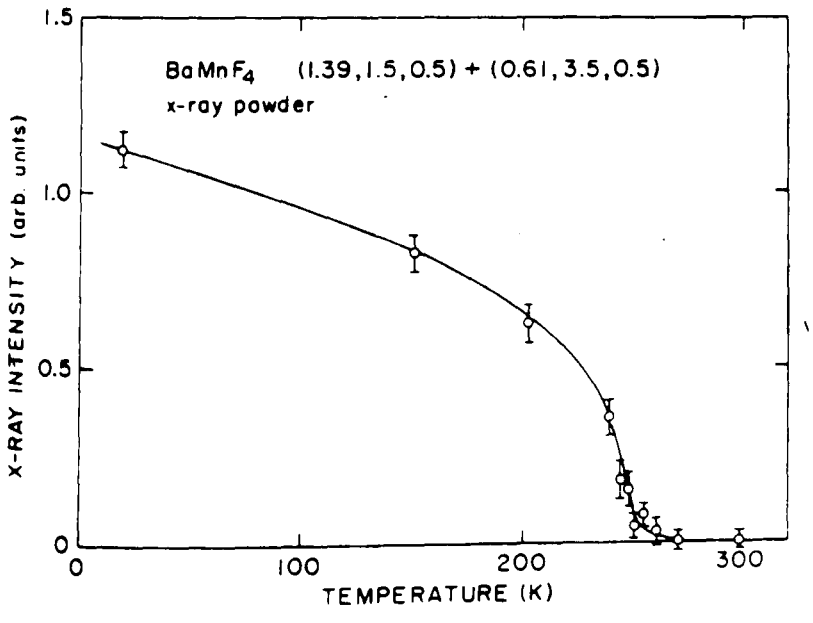

FIG. 1. Temperature dependence of the x-ray intensity of an incommensurate peak consisting of two overlapping satellites in a polycrystalline sample of $BaMnF_4$. The behavior is similar to that shown by neutron diffraction in Fig. 12 of Ref. 2.

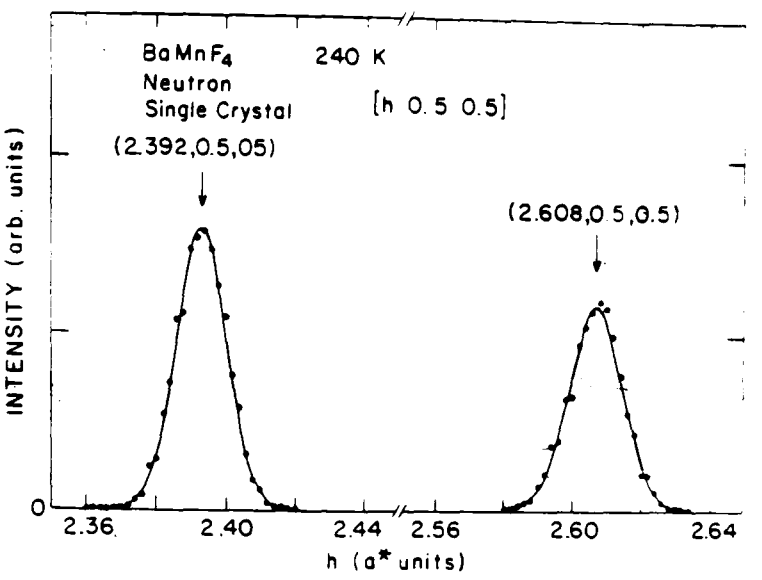

FIG. 2. Neutron scattering from a single crystal of $BaMnF_4$ at 240 K at two satellite positions.

results of typical scans are shown in Figs. 2 and 3. The results for the temperature dependence of the wave vector are summarized in Fig. 4.

It is quite clear from Figs. 3 and 4 that slightly different wave vectors ζ were obtained in the x-ray-diffraction measurements on heating and cooling. On cooling, the wave vector ζ slowly but steadily increases from about 0.390 to 0.394, but on heating ζ remains largely independent of temperature until the temperature is close to T_c. Although the lower-resolution neutron scattering measurements were not performed in such systematic detail, they are broadly consistent with the x-ray results. The width of the incommensurate reflections along ζ (Fig. 3) is also somewhat larger than the experimental resolution as shown by the results for

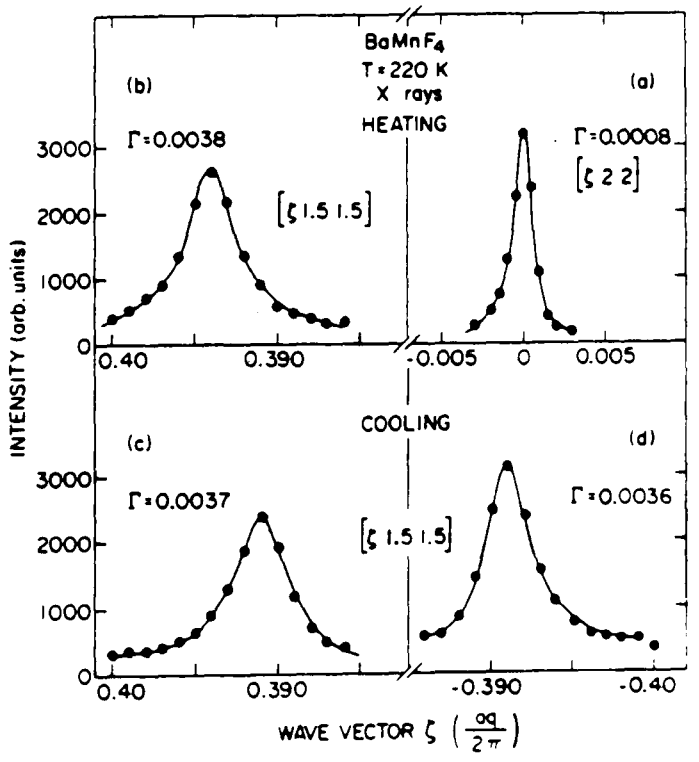

FIG. 3. X-ray scattering from $BaMnF_4$ at $T = 220$ K. (a) Bragg peak showing resolution. (b) Satellite measured on heating. (c) and (d) Satellite measured on cooling. Γ is the full width at half maximum and the vertical scales of parts (a) and (b) are different.

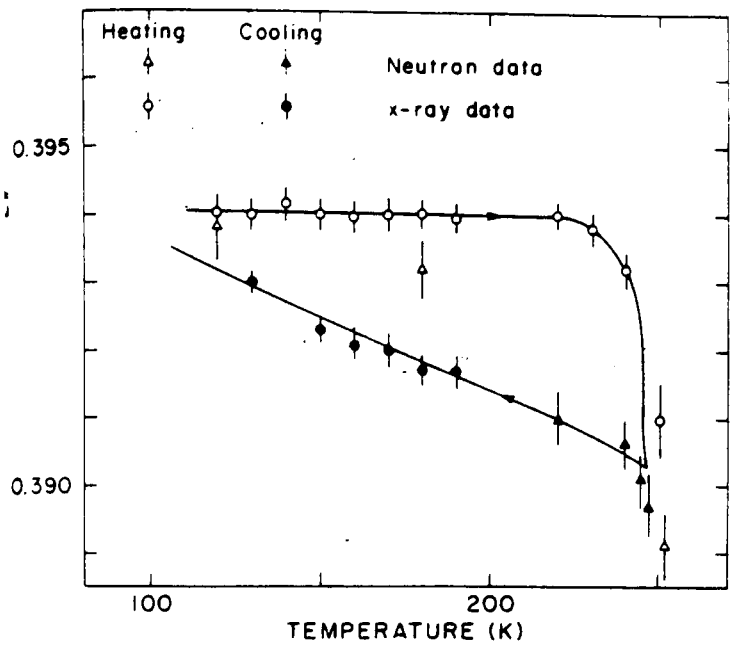

G. 4. Temperature dependence of ζ of the incommensurate vector $(\zeta, 0.5, 0.5)$ in $BaMnF_4$.

agg reflection suggesting that the incommensurate phase ssible pinned by defects.

ıe nature of the scattering was found to change abruptly 17 K as revealed by the width of the satellite reflection n in Fig. 5. No evidence was found for a second phase ition at 255 K.

our earlier work[2] we showed that the low-temperature e of $BaMnF_4$ might be either of type (i) in which the icement ϕ_1 associated with wave vector $\vec{q}_1 = (0.39, 0.5,$ was the same as ϕ_2, the displacement associated with $(0.39, -0.5, 0.5)$, or of type (ii) in which either ϕ_1 or zero. These two structures have different types of d-order satellite reflections because domains of type ill show reflections for $\vec{q}_1 + \vec{q}_3 = \vec{q}_7 = (0.78, 0, 1)$ as is for $2\vec{q}_1$ and $2\vec{q}_3$, whereas for type (ii) single scatter- ocesses cannot give rise to scattering for the wave vectors with $\vec{q} = \vec{q}_7$ and only scattering from $2\vec{q}_1$ and $2\vec{q}_3$ would be present.

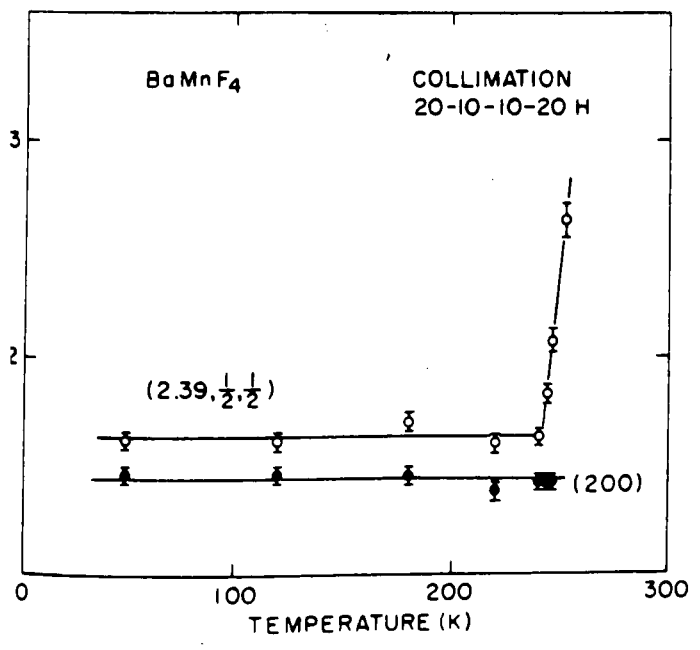

5. Neutron scattering measurement of the widths of an in- surate reflection and a nearby fundamental reflection as a of temperature.

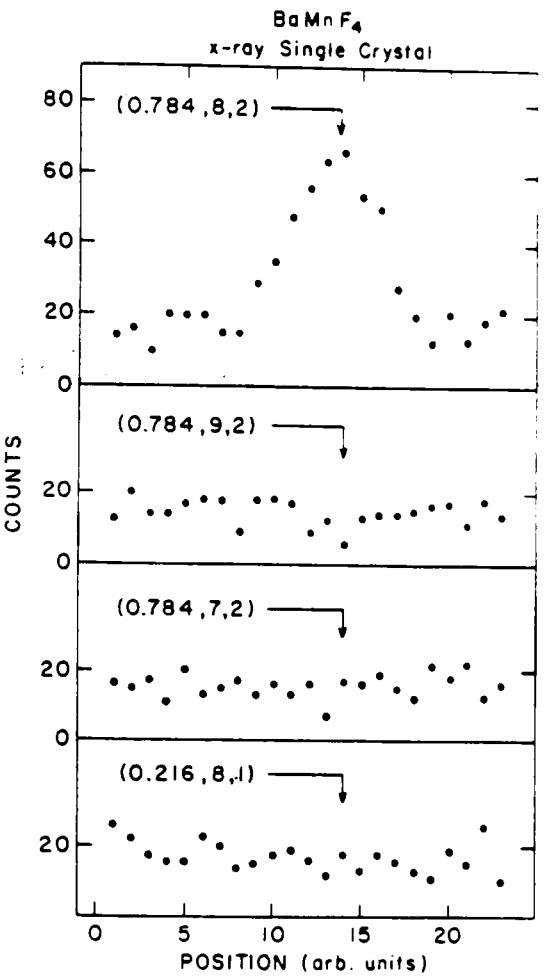

FIG. 6. X-ray scans through possible second-order satellite reflections in $BaMnF_4$.

The scattering at a large number of second-order satellite reflection positions has been measured using the CAD-4 x-ray-diffraction instrument. Some typical scans are illustrated in Fig. 6 and the measured intensities along two lines in reciprocal space are given in Table I. Clearly, there is no intensity for $\vec{Q} = \vec{\tau} + \vec{q}_7$ but there is substantial intensity at the positions $\vec{Q} = \vec{\tau} + 2\vec{q}_1$. ($\tau$ is a reciprocal-lattice vector.) We conclude that the low-temperature structure is of type (ii) in which the distortion is characterized by only a single pair of wave vectors $\pm\vec{q}_1$ in each domain.

III. DISCUSSION AND CONCLUSIONS

Firstly, we have found no evidence of distortions characterized by a wave vector $\vec{q} = (0.4, 0, 0.5)$ as reported by Scott *et al.*[3] The distorted phase observed in our samples is characterized by a wave vector $\vec{q} = (0.39, 0.5, 0.5)$ in both neutron- and x-ray-diffraction measurements, and so this scattering cannot be of magnetic origin as suggested by Scott *et al.*[3] We are unable to account for the discrepancy between the x-ray and neutron results reported by these authors. In addition, we find no evidence of two transitions in our diffraction measurements, in contradiction to the results of Scott *et al.*[3] Of course, there is always the possibility of a distortion with a very different wave vector and amplitude too small to be observed by powder-diffraction techniques, but we consider this to be unlikely.

Secondly, we have measured the temperature dependence

TABLE I. Intensities (arbitrary units) of second-order satellite reflections along the lines (0.216, k, l) and (0.784, k, l).

h	k	l	I	h	k	l	I
0.216	7	1	625 ± 50	0.216	6	1	32 ± 44
0.216	9	1	215 ± 40	0.216	8	1	−36 ± 40
0.216	11	1	247 ± 42	0.216	10	1	10 ± 38
0.216	13	1	161 ± 36	0.216	12	1	−13 ± 36
0.784	2	2	65 ± 45	0.784	3	2	−32 ± 43
0.784	4	2	137 ± 43	0.784	5	2	−9 ± 41
0.784	6	2	170 ± 42	0.784	7	2	−4 ± 39
0.784	8	2	585 ± 47	0.784	9	2	−85 ± 38
0.784	10	2	61 ± 39	0.784	11	2	−45 ± 34
0.784	12	2	259 ± 38				

of the incommensurate wave vector in $BaMnF_4$. Slightly different results are obtained on heating and cooling as also found[6] in other insulating incommensurate systems.[7] Furthermore, the linewidth of the scattering is larger than the resolution width, showing that the incommensurate phase is not properly periodic. This behavior suggests that the incommensurate phase in $BaMnF_4$ may be pinned by defects. However, the affect of defects in phase transitions is not clearly understood, especially so in incommensurate systems where there is some evidence that they play a more significant role.[7,8] We plan to investigate their role in more detail by studying samples where defects are admitted in a controlled manner.

Thirdly, we have determined the structure of the low-temperature phase to be of type (ii) in which the distortion is described by a single wave vector, either $\vec{q} = (0.39, 0.5, 0.5)$ or $(0.39, -0.5, 0.5)$. As pointed out by Golovko and Levanyuk,[9] the structure of the low-temperature phase is then monoclinic with an xy strain. No evidence of this distortion was found in the measurements so its amplitude must be small and is of opposite sign in the different domains, which presumably make up the sample at low temperatures.

ACKNOWLEDGMENTS

Work at Brookhaven National Laboratory was supported by the Division of Materials Sciences, U.S. Department of Energy, under Contract No. DE-AC02-76CH00016, and that at Edinburgh by the United Kingdom Science and Engineering Research Council.

---

*Permanent address: Hahn-Meitner Institut für Kernforschung Berlin, D-1000 Berlin 39, West Germany.

[1]J. F. Scott, Rep. Prog. Phys. 42, 1055 (1979).
[2]D. E. Cox, S. M. Shapiro, R. A. Cowley, M. Eibschütz, and H. G. Guggenheim, Phys. Rev. B 19, 5754 (1979).
[3]J. E. Scott, F. Habbal, and M. Hidaka, Phys. Rev. B 25, 1805 (1982).
[4]J. F. Scott, F. Habbal, and M. Hidaka, Bull. Am. Phys. Soc. 26, 303 (1981).
[5]D. E. Cox, S. M. Shapiro, M. Eibschütz, and H. J. Guggenheim, Bull. Am. Phys. Soc. 26, 303 (1981).
[6]R. M. Fleming, P. E. Moncton, D. B. McWhan, and F. J. DiSalvo, Phys. Rev. Lett. 45, 546 (1980).
[7]K. Hamano, Y. I. Keda, T. Fujimoto, K. Ema, and S. Hirotsu, J. Phys. Soc. Jpn. 49, 2278 (1980).
[8]B. B. Lavrenic and J. F. Scott, Phys. Rev. B 24, 2711 (1981).
[9]U. A. Golovko and A. P. Levanyuk, in *Light Scattering Near Phase Transitions*, edited by A. Levanyuk and H. Z. Cummins (North-Holland, New York, 1983).

J Phys C Solid State Phys, 17 (1984) L861–L865. Printed in Great Britain

LETTER TO THE EDITOR

A neutron and x-ray diffraction study of the phase transitions in proustite (Ag_3AsS_3) between 35 K and room temperature

R J Nelmes†, C J Howard†‡, T W Ryan†, W I F David§, A J Schultz‖ and P C W Leung‖

† Department of Physics, University of Edinburgh, Mayfield Road, Edinburgh EH9 3JZ, UK

§ Rutherford Appleton Laboratory, Chilton, Didcot, Oxford OX11 0QX, UK

‖ Chemistry and Materials Science & Technology Divisions, Argonne National Laboratory, Argonne, Illinois 60439, USA

Received 6 August 1984

Abstract. The techniques of time-of-flight neutron diffraction and high-resolution x-ray diffraction have been used to show that the second-order transition on cooling proustite (Ag_3AsS_3) through ~61 K is to an incommensurate phase, with a further transition to a commensurate phase at ~49 K.

The material proustite (Ag_3AsS_3) has attracted considerable interest over the past ten years, principally because of its realised and probable optical and electronic applications (Bardsley *et al* 1969, O'Hara *et al* 1982). The room-temperature structure of proustite was investigated by Harker (1936) and Engel and Nowacki (1966), and found to have space group R3c (C_{3v}^6). Other phases have since been discovered at low temperatures: there is a second-order transition at ~58 K (reported values range from 56 K to 60 K) and a first-order transition at ~27 K (reported values range from 24 K to 30 K), first detected in NQR spectra by Baisa *et al* (1973) and subsequently by a variety of other experimental techniques (briefly summarised by Ewen *et al* 1983). Smolenskii *et al* (1979, 1982) have suggested that Raman scattering spectra show a further transition at 200 K, but this seems not to be confirmed by a later detailed study (Ewen *et al* 1983). Very recently Bondar *et al* (1983) have found evidence in NQR spectra for two distinct phases between the previously known transitions at ~27 K and ~58 K: they confirm the second-order transition at ~58 K (they obtain 60 K), but then find another small but distinct first-order change in the spectra at 49 K in addition to the abrupt change at ~27 K. From the character of their spectra, they argue that the phase between 49 K and 60 K is incommensurate.

No very clear picture has yet emerged as to the structural nature of these phase transitions. In the most recent structural work, Allen (1984) has now succeeded in showing the phase below 27 K to be monoclinic, with space group Cc (C_s^4), but he was unable to reach any definite conclusion about the phase (or phases) between 27 K and

‡ On leave from the AAEC Research Establishment, Lucas Heights, NSW, Australia

0022-3719/84/320861+05 $02.25

58 K. The balance of evidence appeared to be in favour of space group R3 (C_3^4) in this range (Allen 1984, Taylor *et al* 1984), but Allen was unable to detect any breaking of the *c*-glide absence conditions (of R3c) in x-ray photographs.

We report here on neutron and x-ray diffraction experiments we have recently carried out with the aim of clarifying this unresolved problem and investigating the proposed incommensurate phase. The neutron experiment was performed on the single-crystal diffractometer (SCD), described by Schultz *et al* (1984), at the Argonne National Laboratory pulsed-source (IPNS): the problem of searching for weak changes in a diffraction pattern is well suited to the ability of the pulsed-source SCD, with its area detector and time-of-flight analysis, to survey reciprocal space with good signal-to-noise sensitivity. The x-ray experiment was performed in Edinburgh on a high-resolution, two-circle diffractometer mounted on a rotating-anode source with a primary beam of Si(111)-monochromated Cu $K\alpha_1$ x-rays. The same single-crystal sample of proustite was used for both experiments, and was from the same source as the samples used in the Raman scattering studies of Ewen *et al* (1983).

In the neutron-diffraction study, performed first, attention was concentrated on the reflections which are absent in space group R3c but allowed in R3. Adopting hexagonal indices, these are the $(hh\bar{0}l)$ reflections with $l \neq 2n$. (The R lattice imposes the condition that $-h + k + l = 3n$ for a general $(hkil)$ reflection, and so $h + l = 3n$ in the $hh\bar{0}l$ plane.) Data were first recorded at 66 K, above the 58 K transition, and then at 38 K: each run, at one orientation of the sample crystal, took about six hours. This proved sufficient to detect additional weak peaks in the $hh\bar{0}l$ plane at 38 K. These were followed, on warming back towards the transition, in runs at 48 K and 54 K; and they disappeared when the temperature was raised above 58 K again, to 61 K. Figure 1(*a*) shows part of the $hh\bar{0}l$ plane from one of the runs at 61 K. The ridges are Debye–Scherrer powder-diffraction rings from the aluminium radiation shield in the cryostat. Otherwise the only distinct features are the Bragg reflections allowed in this plane for space group R3c: namely $(9\bar{9}00)$, $(6\bar{6}00)$, $(11\bar{1}10\bar{2})$, $(8\bar{8}02)$, $(5\bar{5}02)$, $(10\bar{1}00\bar{4})$ and $(7\bar{7}04)$. There appears to be some extremely weak scattering at the position of some *c*-glide absent reflections, like $(7\bar{7}01)$ and $(9\bar{9}03)$, which was thought to be possibly attributable to multiple scattering. Figure 1(*b*) shows the same part of the $hh\bar{0}l$ plane from one of the runs made after again cooling the sample below the transition, to 35 K. The additional peaks reappeared, and can be seen located in pairs around each *c*-glide absence position—most clearly, in this figure, around $(9\bar{9}03)$. The very weak scattering at some of the *c*-glide absence positions remains (e.g. at $(9\bar{9}03)$).

A computer peak search through all the 35 K data, covering a region of reciprocal space around and including the $hh\bar{0}l$ plane, revealed new weak peaks around many of the Bragg reflections in this region. These satellite peaks were all at one or more of the six positions $(h \pm \delta, k \mp \delta, \ldots, l \pm \delta)$, $(h \pm \delta, k, \ldots, l \mp \delta)$ and $(h, k \mp \delta, \ldots, l \mp \delta)$ around any $(hkil)$ allowed by the R lattice, with δ close to $\frac{1}{3}$. In the $hh\bar{0}l$ plane, the only satellites strong enough to be detected around reflections with $l \neq 2n$ (i.e. the *c*-glide absent reflections) were at the two positions lying *in* the plane—namely $(h \pm \delta, \bar{h} \mp \delta, 0, l \pm \delta)$—whilst for reflections with $l = 2n$ the detected satellites were restricted to the other four, out-of-plane, positions. In the planes adjacent to $hh\bar{0}l$ ($h\bar{h}\ldots 1l$ and $hh\ldots\bar{1}1l$) the reverse was true.

The x-ray experiment was then carried out to investigate these findings in more detail and with higher reciprocal-space resolution. Measurements were made by reflection from a polished flat face of the sample, which was carefully oriented with one of the $hh\bar{0}l$ planes in the (horizontal) scattering plane of the diffractometer. The sample was first

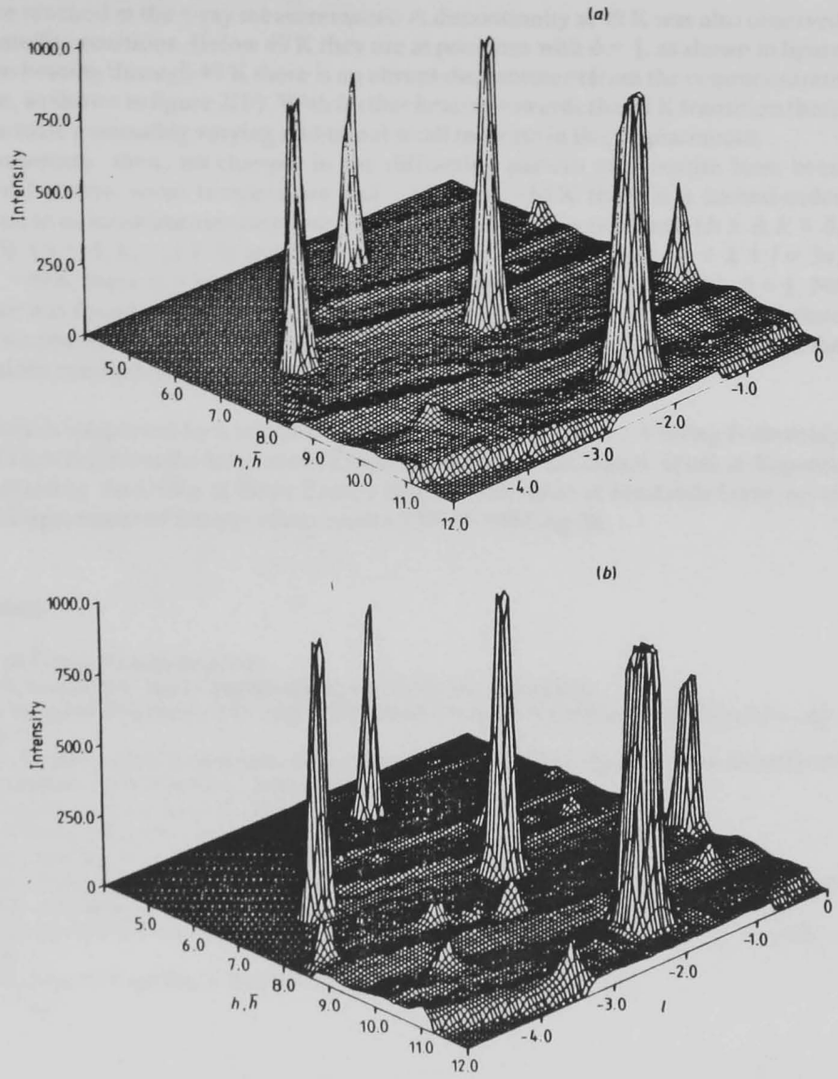

Figure 1. Recorded neutron-diffraction intensity as a function of position in part of the $hh\bar{l}0l$ reciprocal lattice plane of proustite: (*a*) at 61 K; (*b*) at 35 K.

cooled to 48 K, and the features revealed by the neutron-diffraction experiment were found to be reproduced: i.e. satellites at $(h \pm \delta, \bar{h} \mp \delta, 0, l \pm \delta)$ around the *c*-glide absence positions ($l \neq 2n$), generally somewhat weaker peaks at the *c*-glide absence positions themselves, and no detectable satellites in the $hh\bar{l}0l$ plane around any of the ten strong Bragg reflections ($l = 2n$) accessible to measurement. On raising the temperature the satellite intensities decreased, and disappeared at 61 ± 1 K. But the peaks at $hh\bar{l}0l$, $l \neq 2n$, were unaltered, clearly persisting well above 61 K: this was unexpected because it suggested that the true space group is R3 above as well as below the 58 K transition.

In scans made below 58 K it was found: (i) that there was detectable intensity at all

of the ten *c*-glide absence positions accessible to measurement; and (ii) that the intensities generally increased towards the higher index positions. Two of the strongest 'absent' reflections, $(\bar{3}309)$ and $(3\bar{3}09)$, were scanned as the temperature was raised, in steps of 10 K, up to room temperature. The intensities of both reflections simply decreased smoothly with increasing temperature, and remained plainly detectable, though very weak, at room temperature. Hence, either the true space group was R3 even at room temperature or the observed intensity arose from $\lambda/2$ or multiple scattering. A direct test for a weak $\lambda/2$ component was made first, by reducing the x-ray generator voltage to 16 kV: the relative intensities were unaltered. To test for multiple scattering some separate x-ray measurements were made subsequently, at ~45 K, with the same experimental arrangement except that Mo $K\alpha_1$ x-rays were used. With the shorter wavelength there were several 'absent' reflections accessible to measurement for which it was possible to rotate the sample around the scattering vector. The intensities of all these reflections displayed the strong orientation dependence characteristic of multiple scattering, and it was concluded that the true symmetry of proustite at room temperature, and down to and below the 58 K transition, is R3c.

Attention was next turned (in the main experiment, with Cu $K\alpha_1$ x-rays) to the temperature dependence of the satellite intensities and positions below the 58 K transition. On cooling below 61 ± 1 K, the intensity was found to rise linearly to 49 ± 1 K, where the rate of increase of the intensity with cooling approximately doubled. This larger linear temperature dependence was maintained down to 37 K, the lowest tem-

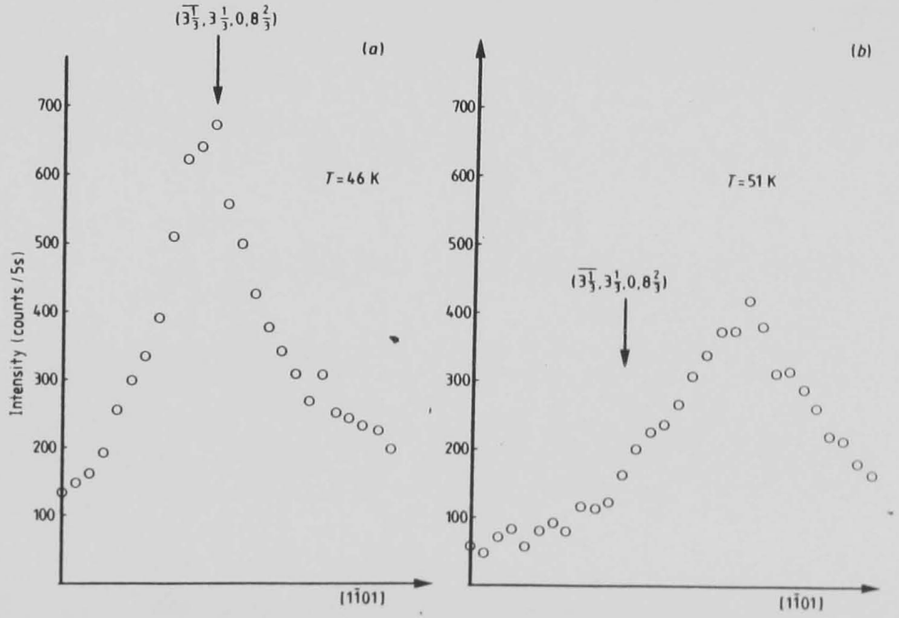

Figure 2. X-ray diffraction scans through the satellite reflection in the vicinity of $(\bar{3} - \delta, 3 + \delta, 0, 9 - \delta)$: (*a*) at 46 K; (*b*) at 51 K; along the direction $[1\bar{1}01]$ towards $(\bar{3}309)$. The arrow on each scan marks the commensurate position $(\bar{3}\frac{1}{3}, 3\frac{1}{3}, 0, 8\frac{2}{3})$. In (*b*) the peak is displaced to the point $(\overline{3.32}, 3.32, 0, 8.68)$ in the scan. (But note that these measurements do not establish that the displacement is exactly along the scan direction.)

perature reached in the x-ray measurements. A discontinuity at 49 K was also observed in the satellite positions. Below 49 K they are at positions with $\delta = \frac{1}{3}$, as shown in figure 2(*a*). On heating through 49 K there is an abrupt displacement from the commensurate position, as shown in figure 2(*b*). With further heating towards the 58 K transition there appears to be a smoothly varying additional small increase in this displacement.

In summary, then, no changes in the diffraction pattern of proustite have been detected between room temperature and ~61 K; at ~61 K there is a second-order transition to an incommensurate phase which has satellite reflections near $(h \pm \delta, k \mp \delta, . , l \pm \delta)$, $(h \pm \delta, k, . , l \mp \delta)$ and $(h, k \mp \delta, . , l \mp \delta)$, with $\delta \sim \frac{1}{3}$ and $-h + k + l = 3n$; and at ~49 K there is a further transition to a commensurate phase, with $\delta = \frac{1}{3}$. No evidence was found for any other change in symmetry at these transitions. The nature of the two phases below ~61 K, and of the transition between them, is in accord with the conclusions reached by Bondar *et al* (1983) from their NQR measurements.

This work is supported by a research grant (to R J Nelmes) and a Visiting Fellowship (for C J Howard) from the Science and Engineering Research Council. Work at Argonne is supported by the Office of Basic Energy Sciences (Division of Materials Sciences) of the US Department of Energy under contract W-31-109-Eng-38.

References

Allen S 1984 *Phase Transitions* in press
Baisa D F, Bondar A V, Rez I S and Abezgauz I A 1973 *Ukr. Fiz. Zh.* **18** 1550
Bardsley W, Davies P H, Hobden M V, Hulme K F, Jones O, Pomeroy W and Warner J 1969 *Opto-electronics* **1** 29–31
Bondar A V, Vikhnin V S, Ryabchenko S M and Yachmenev V E 1983 *Sov. Phys.–Solid State* **25** 1497–1501
Engel P and Nowacki W 1966 *Neues. Jahrb. Mineral. Monatsch.* **8** 181
Ewen P J S, Taylor W and Paul G L 1983 *J. Phys. C: Solid State Phys.* **16** 6475–90
Harker D 1936 *J. Chem. Phys.* **4** 381
O'Hara C, Shorrocks N M, Whatmore R W and Jones O 1982 *J. Phys. D: Appl. Phys.* **15** 1289–99
Schultz A J, Srinivasan K, Teller R G, Williams J M and Lukehart C M 1984 *J. Am. Chem. Soc.* **106** 999–1003
Smolenskii G A, Sinii I G, Kuz'minov E G and Godovikov A A 1979 *Sov. Phys. Solid State* **21** 1343–8
Smolenskii G A, Sinii I G, Prokhorova S D, Kuz'minov E G and Godovikov A A 1982 *Sov. Phys.–Crystallogr.* **27** 82–5
Taylor W, Ewen P J S and Han I 1984 *Ferroelectrics* **55** 83–6

J. Phys. C: Solid State Phys., 18 (1985) L41–L46. Printed in Great Britain

LETTER TO THE EDITOR

X-ray diffraction study of incommensurate $\{N(CH_3)_4\}_2CoCl_4$—consequences of radiation damage

E Fjaer†, R A Cowley and T W Ryan
Department of Physics, University of Edinburgh, Mayfield Road, Edinburgh EH9 3JZ, UK

Received 27 September 1984

Abstract. The sequence of incommensurate/commensurate phases occurring in TMATC-Co around room temperature was studied by means of x-ray diffraction. The results changed during the course of the experiment, due to radiation damage caused by the x-ray beam. The changes included a pinning of the modulation wave into components with different wavevectors, and a lowering as well as a smearing of the normal to incommensurate transition temperature

Tetramethylammonium tetrachlorocobaltate—TMATC-Co for short—undergoes several phase transitions at and below room temperature (Sawada *et al* 1978). The material has attracted interest lately because of the sequence of incommensurate and commensurate phases which occur when it is cooled (Hasebe *et al* 1980, Shimizu *et al* 1980, Marion 1981, Tsuchida *et al* 1982). At normal atmospheric pressure an incommensurate phase is followed on cooling by a ferroelectric commensurate phase which then becomes incommensurate again (Sawada *et al* 1978, Hasebe *et al* 1980).

The modulation wavevector has previously been studied by means of x-ray diffraction by Hasebe *et al* (1980) and Marion (1981). The results are in general agreement with one another although they differ somewhat in detail. Some problems with a lack of reproducibility were noticed by Hasebe *et al*, who obtained their best results when a small AC field was applied to the crystal.

We here report results from a high-intensity x-ray diffraction study of the modulation in the temperature region of the incommensurate phases. The results were found to change dramatically during the course of the experiment, deviating increasingly from those reported by Hasebe *et al* (1980). We argue that the reason is that radiation damage to the sample is caused by the x-ray beam. This illustrates that the properties of materials with incommensurate phases are particularly susceptible to the presence of defects, and that materials containing hydrogen are particularly prone to damage by x-rays, as similar effects have not been observed in similar experiments on Rb_2ZnCl_4 (Andrews and Mashiyama 1983) and $BaMnF_4$ (Cox *et al* 1983).

Single crystals of TMATC-Co were grown by slow evaporation at 34 °C from an aqueous solution containing a stoichiometric proportion of $N(CH_3)_4Cl$ and $CoCl_2 6H_2O$.

† Permanent address: Department of Physics, The Norwegian Institute of Technology, N-7034 Trondheim-NTH, Norway.

0022-3719/85/020041+06 $02.25

A (100) face of a crystal of size 4 × 5 × 8 mm was ground and polished with diamond powder. The crystal was mounted in a variable-temperature cryostat on a two-circle diffractometer so as to allow for scans in the $(h0l)$ plane. A rotating anode tube provided high-intensity Cu Kα radiation, with a graphite monochromator for some of the measurements and a flat silicon monochromator for the rest.

As the experiment was not initially designed to monitor the radiation dose, no precautions were taken to ensure a uniform dose over the scattering volume. The doses given in the following paragraph are therefore only estimates, indicating a weighted average of the doses for each part of the scattering volume (the weighting factor being proportional to the contribution made to the observed scattering).

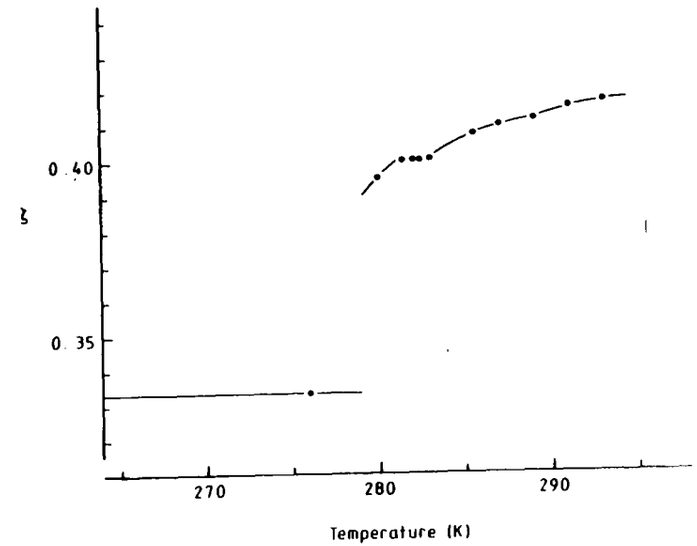

Figure 1. Modulation wavenumber ζ versus temperature at $(5, 0, \zeta)$ for radiation doses less than 0.1 Mrad.

Our measurements initially agreed with the previously reported behaviour of the modulation wavevector (Hasebe *et al* 1980, Marion 1981). Figure 1 shows the modulation wavevector obtained from scans along $(5, 0, \zeta)$ at a spot on the crystal not previously irradiated. The curve, tentatively drawn through the rather sparse set of data, indicates that the modulation wavenumber ζ decreases with temperature through the incommensurate region, temporarily locks in at $\zeta = \frac{3}{8}$ and finally at $\zeta = \frac{1}{3}$. By assuming a temperature dependence of

$$I \propto (T_1 - T)^{2\beta} \qquad (2\beta = 0.75) \tag{1}$$

(Hasebe *et al* 1980, Marion 1981) for the integrated intensity I of the satellite, we estimated the incommensurate transition temperature T_1 to be $T_1 = 294.4 \pm 0.3$ K.

Later measurements with the x-ray beam incident on the same part on the crystal did not give the same results. After a while, the satellite peak splits into several peaks, each of which was pinned at a fixed wavevector. The wavevectors of the peaks in the scattering

are illustrated in figure 2, indicating the presence and positions of the peaks throughout the temperature range. Apart from $\zeta = \frac{1}{3}$ and possibly $\zeta = 0.416 \approx \frac{5}{12}$, the positions are not related to any reasonable commensurate value. In particular, it is surprising that the modulation characterised by $\zeta = \frac{2}{5}$ no longer appears at any temperature, although this commensurate phase was initially present between two incommensurate phases, figure 1.

The relative balance between the various peaks was clearly dependent on the recent thermal history of the sample. In general, however, it was found that the balance shifted towards lower wavenumbers with decreasing temperature, as did the original satellite intensity in the initial measurements. As an example, the relative intensity in each peak, as found during slow heating/cooling ($\frac{1}{2}$ – 1 degree per hour) starting well outside the initially incommensurate region, is shown in figure 3. Notice that, on cooling, the modulation jumps from $\zeta = 0.405$ to $\zeta = \frac{1}{3}$ at 278 K where, on heating, the modulation jumps back to $\zeta = 0.390$, bearing at least some resemblance to the original lock-in transition. The modulations at $\zeta = 0.416$ and 0.423 seem on the other hand to be quite unaffected by this transition.

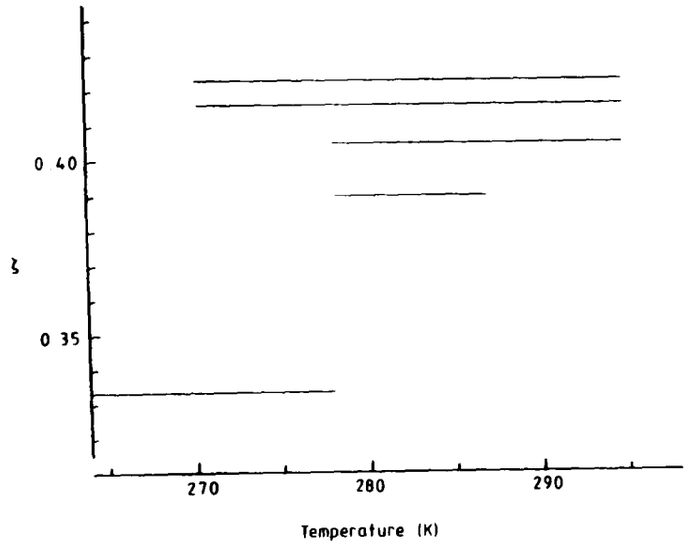

Figure 2. Modulation wavenumber ζ versus temperature at $(5, 0, \zeta)$ for radiation doses greater than 1.5 Mrad.

A clear indication that the pinning of the satellite is due to the x-ray radiation is seen in figure 4. Curve (*a*) shows the $(5, 0, \zeta)$ satellite profile at 281.4 K (i.e. inside the intermediate $\zeta = \frac{2}{5}$ phase), after the exposed volume of the crystal has acquired a dose of ~0.2 Mrad. The peak at $\zeta = 0.405$ is seen to dominate, although a minor part of the scattering is still left at the initially expected position $\frac{2}{5}$, possibly due to the non-uniform irradiation. Curve (*b*) was recorded immediately afterwards and at the same temperature, but with the crystal translated by 0.5 mm sideways in the beam, thereby exposing a previously unexposed region. The satellite is now a single peak accurately positioned at $\zeta = \frac{1}{3}$, as we would expect for a pure crystal.

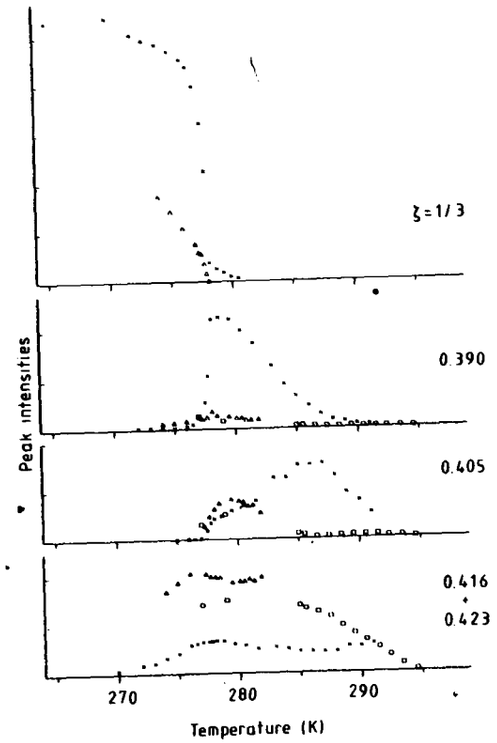

Figure 3. Peak intensities of the pinned modulations at $(5, 0, \zeta)$ versus temperature. Symbols are as follows: crosses, heating run, radiation dose 4–4.5 Mrad; triangles, cooling run, dose 1.5–3 Mrad; squares, cooling run, dose 5–5.5 Mrad.

The integrated intensity of the scattering at $(5, 0, \zeta)$ was studied in particular in the vicinity of the incommensurate transition. Figure 5 shows the integrated intensity versus temperature as obtained on a cooling run after a dose of ~5 Mrad. A subsequent heating run showed no significant difference. It is clear that equation (1) with $2\beta = 0.75$ is no longer a good description of the observations. However, formula (1) with $2\beta = 0.75$, modified to allow for a normal distribution of the transition temperature T_1, gave a very satisfactory fit to the data. The fitted curve is shown in figure 5 as a solid line. The average transition temperature was found to be $\langle T_1 \rangle = 293.72 \pm 0.03$ K and the standard deviation $\sigma_{T_1} = 1.28 \pm 0.06$ K.

Our x-ray diffraction results initially agreed with results previously obtained for this material. However, continued exposure with the same scattering volume gave very different results. We believe that the results, in particular figure 4, show that the changes arise from damage to the crystal inflicted by the x-ray beam.

The results show that in the irradiated sample the modulation wave is pinned to particular wavenumbers. This is known to happen when impurities are present in incommensurate systems (Mashiyama *et al* 1982), and has also been observed and ascribed to radiation damage by others (Moudden *et al* 1983, Durand *et al* 1984). It is

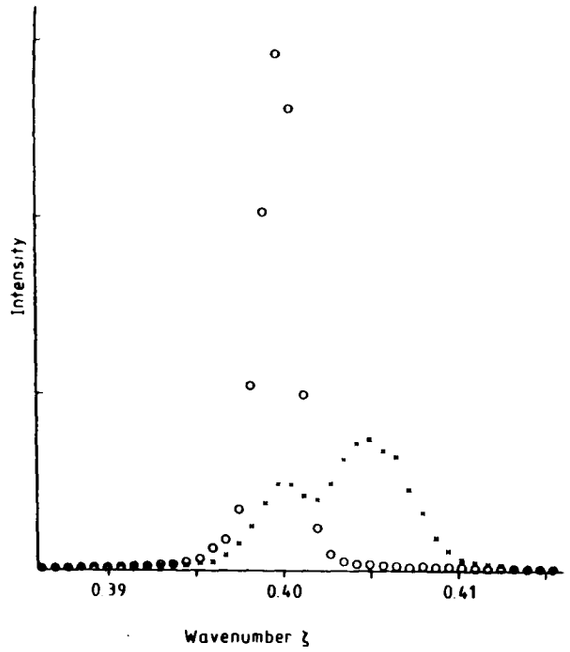

Figure 4. Intensity versus wavenumber ζ for $(5, 0, \zeta)$ at 281.4 K: (*a*) radiation dose 0.2 Mrad; (*b*) radiation dose less than 4 krad

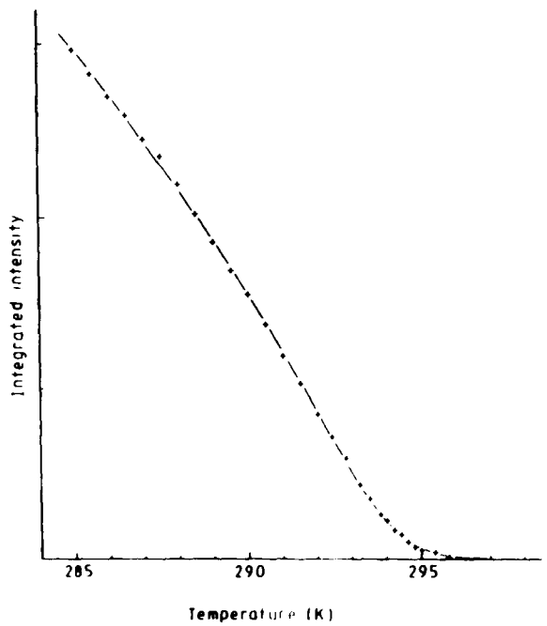

Figure 5. Integrated intensity versus temperature at $(5, 0, \zeta)$. Radiation dose 5–5.5 Mrad

possible that the differences in detail between the works of Hasebe *et al* (1980) and Marion (1981) can be ascribed to the same effect. It is further seen from our results that several pinned modulations of different wavenumbers may be present simultaneously, thus revealing a metastability in the irradiated sample. The pinned modulations are in a varying degree affected by the original phase transitions in the system.

We have also seen that the incommensurate transition temperature T_1 is affected by the changes in the crystal. A general shift downwards, from $T_1 = 294.4 \pm 0.3$ K to $\langle T_1 \rangle = 293.72 \pm 0.03$ K for a dose of $\simeq 5$ Mrad, seems to occur. The spread of T_1, described by the standard deviation σ_{T_1}, may partly be ascribed to non-uniform irradiation, but it seems as if a genuine spread in T_1 may be another consequence of the accumulated irradiation. It has been suggested (Sham and Patton 1976) that a lowering as well as a smearing of the transition temperature are effects that are likely to occur as consequences of impurities in an incommensurate system.

In conclusion these measurements have shown that x-ray irradiation of TMATC-Co modifies the properties of the incommensurate phase and effectively prohibits a detailed study of the phase transitions in this material with x-rays. Since similar effects have not been seen in x-ray experiments on Rb_2ZnCl_4 and on $BaMnF_4$, we suspect that incommensurate materials containing hydrogen are particularly susceptible to these effects.

This work was supported by the Science and Engineering Research Council and by the Royal Norwegian Council for Scientific and Industrial Research.

References

Andrews S R and Mashiyama H 1983 *J. Phys. C: Solid State Phys.* **16** 4985–96
Cox D E, Shapiro S M, Nelmes R J, Ryan T W, Bleif H J, Cowley R A, Eibschutz M and Guggenheim H J 1983 *Phys. Rev.* B **28** 1640–3
Durand D, Dénoyer F, Currat R and Vettier C 1984 to be published
Hasebe K, Mashiyama H and Tanisaki S 1980 *J. Phys. Soc. Japan Lett.* **49** 1633–4
Marion G 1981 *J. Physique* **42** 469–72
Mashiyama H, Tanisaki S and Hamano K 1982 *J. Phys. Soc. Japan* **51** 2538–44
Moudden A H, Moncton D E and Axe J D 1983 *Phys. Rev. Lett.* **51** 2390
Sawada S, Shiroishi Y, Yamamoto A, Takashige M and Matsuo M 1978 *Phys. Lett.* **67A** 56–8
Sham L J and Patton B R 1976 *Phys. Rev.* B **13** 3151–3
Shimizu H, Kokubo N, Yasuda N and Fujimoto S 1980 *J. Phys. Soc. Japan* **49** 223–9
Tsuchida K, Imaizumi S, Abe R and Suzuki I 1982 *J. Phys. Soc. Japan* **51** 2199–204

J. Phys. C: Solid State Phys. 18 (1985) 2793–2798. Printed in Great Britain

The structure of the glass phase in $Rb_{1-x}(NH_4)_xH_2PO_4$

R A Cowley†, T Ryan† and Eric Courtens‡

† Department of Physics, University of Edinburgh, Mayfield Road, Edinburgh EH9 3JZ, UK

‡ IBM Zurich Research Laboratory, 8803 Rüschlikon, Switzerland

Received 12 October 1984

Abstract. X-ray measurements on the glass state of $Rb_{1-x}(NH_4)_xH_2PO_4$ have been made for $x = 0.78, 0.75, 0.72, 0.68$ and 0.49. The results show short-range antiferroelectric ordering for $x > 0.70$ which disappears on warming above 60 K. There is also evidence for a tendency to order with a wave-vector, $\boldsymbol{q} = (\zeta, 0, 0)$, with $\zeta \sim 0.35a^*$. The tendency increases with decreasing x and largely disappears on warming above 160 K.

Systems in which there are competing interactions have attracted a great deal of interest recently. A structural analogue of the magnetic spin glasses is the mixed system formed from ferroelectric RbH_2PO_4 and antiferroelectric $NH_4H_2PO_4$. Single crystals of this mixed system, $Rb_{1-x}(NH_4)_xH_2PO_4$, have been grown for all values of x, and have been studied by birefringence and dielectric measurements (Courtens 1982, 1983, 1984). For small values of x, $x < 0.22$, the crystals become ferroelectric at low temperatures and have a similar structure to that of ferroelectric RbH_2PO_4. For large values of x, $x > 0.8$ the crystals have an antiferroelectric transition similar to that in $NH_4H_2PO_4$. In the intermediate range $0.22 < x < 0.8$, optical and dielectric measurements show that the crystals remain tetragonal down to the lowest temperatures although the crystals show evidence of long relaxation times (Courtens 1984) and other behaviour which is characteristic of systems with competing interactions.

In this paper we report on x-ray diffuse scattering measurements on five samples in this intermediate 'glass' range with $x = 0.49, 0.68, 0.72, 0.75$ and 0.78. X-ray measurements on a sample of $x = 0.35$ have also been performed by Courtens *et al* (1984) and more recently on samples with $x = 0.8, 0.7$ and 0.6 by Iida and Terauchi (1983), by Terauchi *et al* (1984), and by Hayase *et al* (1985). We shall compare our results with theirs later.

The measurements were performed on crystals in the form of (100) plates of size about $3 \times 3 \times 1\ mm^3$. The crystals were mounted with GE7031 varnish to the variable-temperature stage of a closed cycle cryostat. The temperature could be varied between 7 K and 300 K and held constant to ± 0.02 K. The crystals were then mounted on a two-axis x-ray diffractometer. A Marconi–Elliott rotating anode tube gave an intense source of Cu $K\alpha$ radiation and a pyrolytic graphite monochromator was used to collimate the incident beam. Another pyrolytic graphite monochromator was used to define the x-ray beam scattered by the sample. The diffractometer could be controlled to perform scans

0022-3719/85/142793+06 $02.25

along predetermined directions in reciprocal space. All of the crystals had a tetragonal structure on cooling down to 7 K.

Measurements were made of the scattering at 7 K in the neighbourhood of antiferroelectric Bragg points $(h\,0\,l)$ with $h + l$ odd. Scattering with a similar form and temperature dependence was observed around each of these positions and typical scans through $(6\,0\,\bar{1})$ are shown in figure 1. For $x = 0.78$, the scans along h have the resolution width (FWHM), $0.0225 \pm 0.001\ a^*$, but along l the observed width $0.041 \pm 0.003\ c^*$ is significantly larger than the resolution width of $0.017 \pm 0.002\ c^*$. In the crystal with $x = 0.75$, the intensity is much reduced and both of these widths are larger: $0.060 \pm 0.003\ a^*$ and $0.21 \pm 0.02\ c^*$. The intensity is further reduced and the widths increased with $x = 0.72$, while for $x = 0.67$, there is no observable antiferroelectric scattering. This decrease in the tendency towards antiferroelectric ordering when x is less than 0.8 is surprisingly rapid.

The temperature dependence of the scattering observed with a wave-vector transfer $(6\,0\,\bar{1})$ is illustrated in figure 2. For $x = 0.78$ the scattering decreases rapidly when the temperature is raised above 50 K and disappears for temperatures above 58 K. For smaller values of x the decrease in the intensity occurs over a wider range of temperature and shows a more rounded behaviour. The widths of the scattering are illustrated in figure 3, which shows that the widths are independent of temperature for temperatures below 40 K, but that the widths then begin to increase. Even in the case of $x = 0.78$, the width increases for temperatures just above 50 K, well below any 'phase transition'

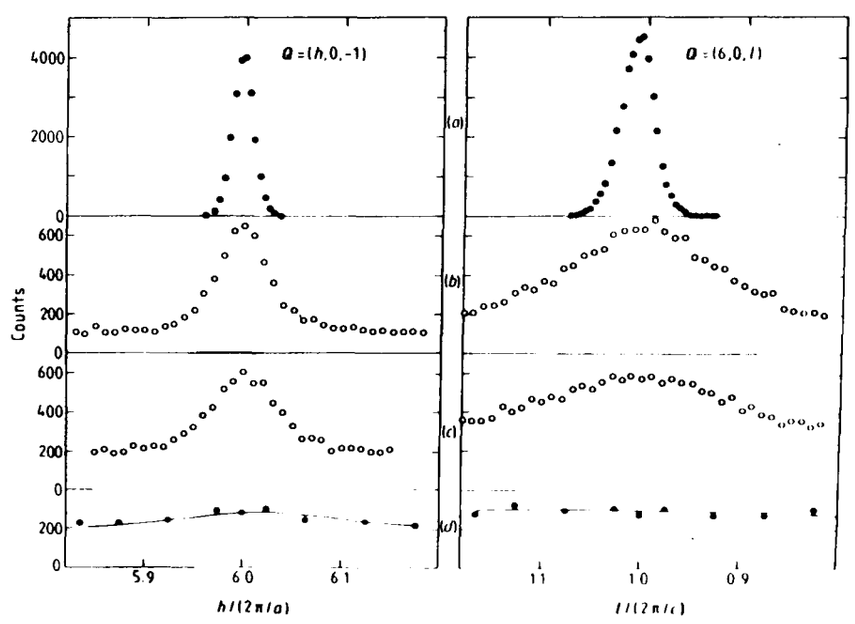

Figure 1. The scattering as a function of wavevector transfer in the neighbourhood of the $(6\,0\,\bar{1})$ antiferroelectric Bragg peak. The temperature was 7.0 K and the values of x in $Rb_{1-x}(NH_4)_xH_2PO_4$ and times were (*a*) $x = 0.78$, $t = 5$ s, (*b*) $x = 7$ s, $t = 60$ s, (*c*) $x = 0.72$, $t = 120$ s, (*d*) $x = 0.68$, $t = 250$ s. The results show the destruction of antiferroelectric order as x decreases.

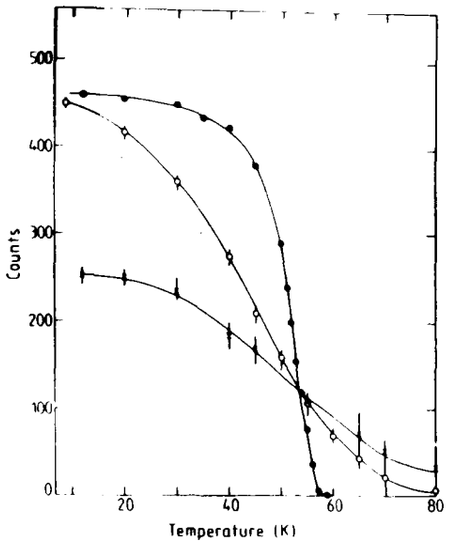

Figure 2. The temperature dependence of the intensity observed with the diffractometer set at a wavevector transfer of $(6\,0\,\bar{1})$ for ●, $x = 0.78$, $t = 0.5$ s; ○, $x = 0.75$, $t = 50$ s, ×, $x = 0.72$, $t = 100$ s.

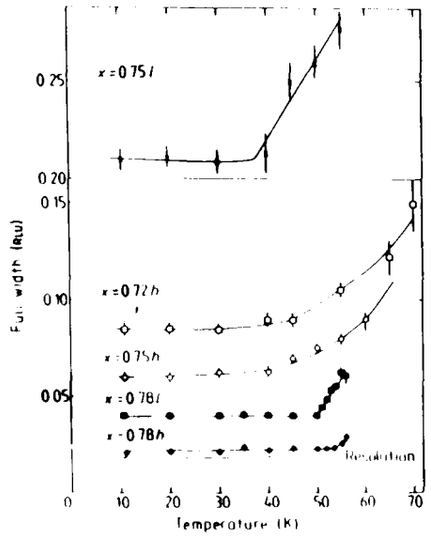

Figure 3. The temperature dependence of the widths of the distributions shown in figure 1. These give approximately the inverse correlation range of the antiferroelectric correlations in reciprocal lattice units (RLU) for $x = 0.78$, 0.75 and 0.72.

which might be suggested by the temperature dependence, figure 2. These results are qualitatively similar to the effects observed due to random fields in destroying the long-range order in antiferromagnetic materials in field cooled experiments (Hagen *et al* 1983).

The results for $x = 0.78$, shown in figures 1, 2 and 3, are the results of heating the sample steadily after one particular cooling. When the sample was recooled, the scattering was different in that the width along l varied between $0.03\,c^*$ and $0.07\,c^*$ dependent upon the particular conditions, while the intensity varied to give a nearly

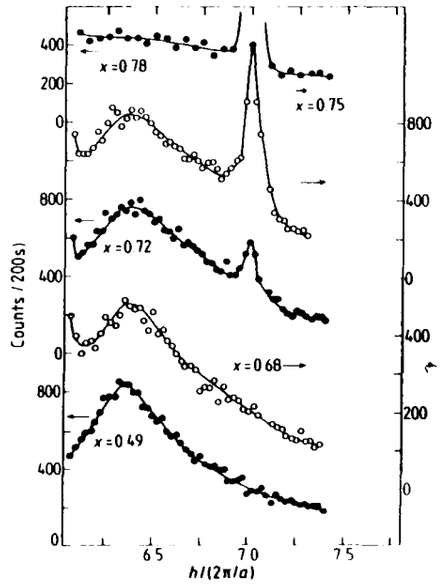

Figure 4. The wavevector dependence of the scattering observed for wavevectors along the line $(h\,0\,\bar{2})$ for $x = 0.78$, 0.75, 0.72, 0.67 and 0.49 at 7 K.

constant integrated intensity. This lack of reproducibility is characteristic of systems with metastable states and competing interactions.

Besides the antiferromagnetic ordering, evidence was also found for a broad diffuse peak in the scattering along the a^* direction. This broad peak in the scattering occurred for each concentration although as shown in figure 4, it was most well defined for $x = 0.49$ and had almost disappeared as a peak for $x = 0.78$. The wavevector of the maximum was about $0.35\,a^*$ for $x = 0.75$ and 0.68, and was slightly smaller, $0.32\,a^*$, for $x = 0.49$. The temperature dependence of this scattering is illustrated in figure 5 which shows that there is still a fairly well defined maximum at 120 K but that by 160 K it has largely disappeared.

The results for the scattering from the antiferroelectric correlations are consistent with those of Iida and Terauchi (1982), of Terauchi *et al* (1984), and of Hayase *et al* (1985) for $x = 0.7$, although ours are considerably more detailed as a function of wavevector, temperature and concentration.

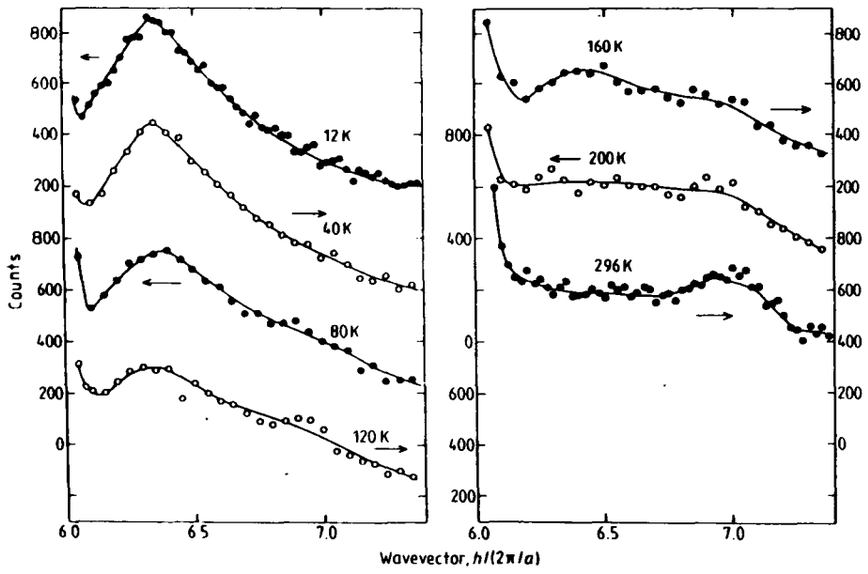

Figure 5. The temperature dependence of the scattering observed for wavevectors along the line $(h\,0\,\bar{2})$ for $x = 0.49$. Similar behaviour is observed for $x = 0.67, 0.72$ and 0.75.

The results show that short-range antiferroelectric correlations are present at low temperatures for $0.68 < x < 0.78$ and that these correlations persist up to about 60 K. The correlations are of greater spacial extent in the *ab* plane than in the *c* direction. We do not understand why these correlations occur for only such large values of x, as it would seem reasonable to expect the antiferroelectric correlations to persist for considerably smaller values of x.

The results shown in figures 4 and 5 are more unexpected. They can be compared with the observation by Courtens *et al* (1984) of somewhat broadened peaks with a wavevector $0.25\,a^*$ for $x = 0.35$, which could not be observed above 50 K. Since the much broader peaks in figure 5 persist up to 120 K, it is unlikely that they result from the same ferroelectric correlations. The persistence of the peaks to 120 K suggests that they may be associated with ordering of the NH_4 ions because NMR measurements (Courtens 1983) suggest that the reorientation of the NH_4 ions is by then very slow. Figure 4 shows that this scattering is reduced when $x = 0.78$ and there are nearly fully developed antiferroelectric correlations. It is of interest that at 80 K when there are no longer any antiferroelectric correlations, figure 2, there is a peak in the scattering for wavevectors close to $(6.35, 0, -2)$. The origin of these peaks in the scattering is clearly by no means yet understood. They clearly persist throughout much of the 'glass' phase and correspond to correlations being frozen below about 120 K. Further measurements are in progress to elucidate the nature of this scattering.

Acknowledgment

This work was supported by the Science and Engineering Research Council.

References

Courtens E 1982 *J. Physique Lett.* **43** L199
—— 1983 *Helv. Phys. Acta* **56** 705
—— 1984 *Phys. Rev. Lett.* **52** 69
Courtens E, Rosenbaum T F, Nagler S E and Horn P M 1984 *Phys. Rev.* B **29** 515
Hagen M, Cowley R A, Satija S K, Yoshijawa H, Shirane G and Birgeneau R J 1983 *Phys. Rev.* B **28** 2602
Hayase S, Futamura T, Sakashita H and Terauchi H 1985 to be published
Iida S and Terauchi H 1983 *J. Phys. Soc. Japan* **52**
Terauchi H, Futamura T, Nishihata Y and Iida S 1984 *J. Phys. Soc. Japan* **53** 483

J. Phys. C: Solid State Phys. 18 (1985) L711–L716. Printed in Great Britain

LETTER TO THE EDITOR

Structural ordering below T_c in KDP and DKDP

R J Nelmes†, W F Kuhs‡, C J Howard†§, J E Tibballs†‖ and T W Ryan†

† Department of Physics, University of Edinburgh, Mayfield Road, Edinburgh EH9 3JZ, UK

‡ Institut Laue–Langevin, Avenue des Martyrs, 38042 Grenoble Cedex, France

Received 3 June 1985

Abstract. High-resolution neutron diffraction studies have been carried out on KH_2PO_4 at 1 K, 10 K and 20 K below T_c (123 K), and on 95% deuterated $K(D_xH_{1-x})_2PO_4$ at 2 K, 6 K and 10 K below T_c (224 K). The results show that in both cases the structural ordering is homogeneous: the temperature dependence of the proton (deuteron) ordering is the same, within error, as that of the heavy-atom displacements. And the temperature dependence of this structural ordering is the same as that of the spontaneous polarisation.

The neutron diffraction studies by Bacon and Pease (1953, 1955) established that the structural phase transition on cooling KH_2PO_4 (KDP) from its tetragonal para-electric phase (space group $I\bar{4}2d$) to its orthorhombic ferroelectric phase (space group Fdd2) involves:

(i) ordering of the protons in the short O–H–O bonds, almost in the xy plane, connecting neighbouring PO_4 groups; and

(ii) relative displacement of the K and P atoms along the z axis—the direction of the spontaneous polarisation, P^s.

We have previously made more detailed diffraction studies of the temperature and pressure dependence of the tetragonal-phase structure of KDP and its deuterated form, DKDP (Tibballs *et al* 1982, Nelmes *et al* 1982, Tibballs and Nelmes 1982); and recently we established that—like the deuteron distribution in DKDP (Nelmes *et al* 1982)—the proton distribution in KDP is clearly two-peaked above T_c (Kuhs *et al* 1983). But since the work of Bacon and Pease there has not been any more accurate study of the ferroelectric-phase structure, except the x-ray diffraction work on DKDP at $T_c - 10$ K by Nakano *et al* (1974). In particular, there is no information as to how the structure changes with temperature in the range just below T_c, where it is expected to be only partially ordered.

We now report results obtained from high-resolution neutron diffraction data collected from KDP about 1 K, 10 K and 20 K below T_c (123 K), and from 94.6(6)% deuterated (Nelmes *et al* 1982) DKDP about 2 K, 6 K and 10 K below T_c (224 K). Measurements of P^s (Samara 1973, Chabin and Gilletta 1977) suggest that over these

§ On leave from AAEC Research Establishment, Lucas Heights, NSW 2232, Australia

‖ Now at Senter for Industriforskning, Blindern, Oslo 3, Norway

0022-3719/85/240711+06 $02.25

temperature ranges the ordering of KDP varies from ~60% at $T_c - 1$ K to ~95% at $T_c - 20$ K, and that of DKDP from ~75% at $T_c - 1$ K to ~95% at $T_c - 10$ K.

All six experiments were carried out on the D8 and D9 four-circle diffractometers at the Institut Laue–Langevin, Grenoble. The single-crystal samples were maintained in an almost completely monodomain state by the application of ~400 V mm^{-1} electric field between electrodes painted on the c faces. The first experiments to be done were the two at $T_c - 10$ K. In both cases a neutron wavelength of ~0.70 Å was chosen, and full three-dimensional data were collected out to $(\sin\theta)/\lambda = 1.2$ Å^{-1}, giving about 1300 independent reflections altogether. Analysis of these data sets showed that a higher resolution would be required to study in detail the ~60% ordered structure anticipated for KDP at 1 K below T_c: accordingly data for that experiment were measured with a neutron wavelength of ~0.55 Å, out to a $(\sin\theta)/\lambda$ limit of 1.6 Å^{-1}. In this case a sufficient number of independent reflections (~1200) was obtained by collecting complete data out to 1.6 Å^{-1} in the ($hk0$), ($h0l$), ($0kl$) and (hhl) layers of the orthorhombic reciprocal lattice, and only the stronger general (hkl) reflections. This same procedure was then adopted for the remaining three experiments.

Temperature stability was monitored by use of a thermocouple in thermal contact with the sample base. For the first two experiments (i.e. at $T_c - 10$ K) the recorded variation was within ±0.5 K; for the subsequent experiments the stability was improved to ±0.15 K. The absolute value of the temperature, relative to T_c, was obtained for the experiments at $\sim T_c - 1$ K by careful measurement of the angular separation, $2u_{xy}$, between a strong ($hh0$) reflection and the weak 'side' peak attributable to the very small amount (<1%) of the sample that remained in the reverse-poled state. For KDP, this measured angle was then compared with values of $u_{xy} = (2\tan^{-1}(a/b) - 90)^0$ as a function of temperature derived from the accurate lattice parameter measurements by Kobayashi *et al* (1971); for DKDP we made our own high-resolution x-ray diffraction measurements of u_{xy} as a function of temperature (unpublished). Table 1 shows the temperatures thus obtained, after taking account of the known hysteresis and of the effect of the applied field on T_c (Kobayashi *et al* 1971, Uesu *et al* 1974). The temperatures given in table 1 are relative to the value of T_c on heating (appropriate to data collection in the low-temperature phase) with the field applied. Because du_{xy}/dT is too small to employ this technique successfully at the lower temperatures, they could not be

Table 1. The values obtained at the given experiment temperatures for the degree of proton (deuteron) ordering, the displacement Δz(K) of the K atom along z relative to the P atom, and the distortion (Δ(P–O): see the text) of the PO_4 groups, compared with the temperature dependence of the spontaneous polarisation (Samara 1973, Chabin and Gilletta 1977) for: (*a*) KH_2PO_4; and (*b*) 95% deuterated $K(D_xH_{1-x})_2PO_4$.

Temperature	P^s (μC cm^{-2})	H(D) ordering (%)	Δz(K) (Å)	Δ(P–O) (Å)
(*a*) KDP				
$T_c - 1.3(3)$ K	3.25(15)	63.6(6)	0.0672(7)	0.0375(7)
$T_c - 10(0.5)$ K	4.6(1)	86.8(8)	0.0970(7)	0.0532(7)
$T_c - 20(1)$ K	4.85(5)	91.8(8)	0.1025(14)	0.0560(8)
(*b*) DKDP				
$T_c - 1.8(6)$ K	5.25(20)	84.6(4)	0.1149(14)	0.0600(10)
$T_c - 5.8(6)$ K	5.80(5)	93.1(4)	0.1267(14)	0.0666(9)
$T_c - 10(1)$ K	6.00(3)	96.0(2)	0.1298(7)	0.0693(6)

determined so directly: they were obtained simply by adjusting the temperature controller relative to its reading at T_c (with the field applied). Careful measurement of the width of the 'side' peak just below T_c, where du_{xy}/dT is at its maximum, showed the thermal gradient across the samples to be $\leqslant 1$ K for both KDP and DKDP. The errors given for the experiment temperatures in table 1 include estimates of the temperature stability and of the uncertainty in the determination of the temperature relative to T_c (see above), but exclude the thermal gradient. This is because the structural parameters obtained from the experiments are themselves averaged over the same thermal gradient. So the average sample temperature is the relevant quantity provided the ordering is sensibly linear over a range of 1 K: the P^s measurements of Chabin and Gilletta (1977) show that that is the case.

After standard data reduction, all reflection intensities were corrected for absorption, and for one- and two-phonon TDS; they were then used for least-squares refinement of positional and harmonic thermal parameters, and anisotropic extinction parameters. These corrections and refinements, and the mapping presented later, were all carried out with the PROMETHEUS suite of crystallographic programs (Zucker *et al* 1983).

In the refinements, the proton distribution was represented by two overlapping gaussian functions, one on each of the two proton sites, δ apart, in the O–H–O bonds ($\delta \sim 0.34$ Å for KDP and ~0.45 Å for DKDP): see Nelmes *et al* (1982). Above T_c, the two sites are related by the two-fold axis of $I\bar{4}2d$ and so are equally occupied, 50:50. Below T_c, one of the sites becomes increasingly occupied at the expense of the other: for a refined distribution of $X:(100-X)$ the degree of ordering is $2(X-50)\%$, and $X \rightarrow 100$ as $T \rightarrow 0$ K. As the protons order in this way onto sites closer to, say, the 'upper' two oxygens (O2) of each PO_4 group, the P atoms displace along the z axis towards the 'lower' two oxygens (O1) of the group. Hence the bond length P–O2 becomes increasingly larger than P–O1, by an amount Δ(P–O). Relative to the oxygen framework, there is also an oppositely directed, and nearly equal, displacement of the K atoms along z, by a total amount Δz(K) relative to the P atoms. Table 1 shows the refined values of the H (or D) ordering, Δz(K) and Δ(P–O) at the given experiment temperatures. The table also includes values for the spontaneous polarisation P^s at these temperatures, taken from the measurements by Samara (1973) and by Chabin and Gilletta (1977). The lattice parameters used to calculate the tabulated values of Δz(K) and Δ(P–O) were obtained from Kobayashi *et al* (1970, 1971) for KDP, and from Nakano *et al* (1974) and Uesu *et al* (1974) for DKDP—with allowance for the effect of the applied field. The full details of the experiments (i.e. of the effect of the applied field on the estimation of u_{xy}, P^s and the lattice parameters; of the evaluation of elastic constants for the TDS corrections; of how account has been taken of varying estimates in the literature for DKDP deuteration levels; and of the least-squares refinements, including values for all the refined structural parameters) will be published in a separate comprehensive account of this work by Kuhs *et al* (1985).

The central purpose of this Letter is to examine whether or not P^s, the H(D) ordering, Δz(K) and Δ(P–O) have the same temperature dependence. Figure 1(*a*) shows the curve of P^s versus temperature for KDP (Samara 1973, Chabin and Gilletta 1977) compared in turn with the temperature dependence of the refined proton ordering, Δz(K) and Δ(P–O) values in table 1. The H order values have been plotted by accepting Samara's (1973) estimate of 5.10 μC cm^{-2} for the fully saturated magnitude of P^s: the H order at $T_c - 20$ K then corresponds to 91.8(8)% (see table 1) of 5.10 μC cm^{-2}, and so on. The Δz(K) and Δ(P–O) values have been plotted by normalising them to the P^s curve at $T_c - 20$ K, where the rate of change with temperature is very small. Figure 1(*b*) shows

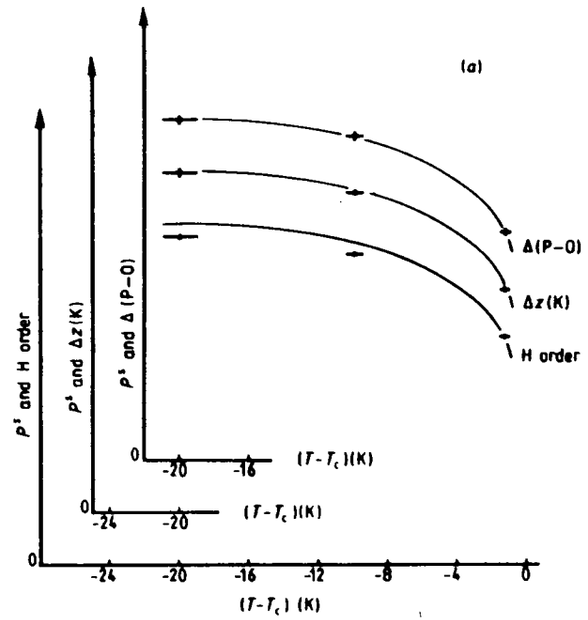

Figure 1. The temperature dependence of: (i) the refined proton (deuteron) ordering, (ii) the displacement Δz(K) of K along z relative to P, and (iii) the distortion Δ(P–O) of the PO_4 groups in (*a*) KH_2PO_4 and (*b*) 95% deuterated $K(D_xH_{1-x})_2PO_4$, compared with the temperature dependence of P^s, the spontaneous polarisation (Samara 1973, Chabin and Gilletta 1977), shown by the full curves. The vertical axis is in arbitrary units: the actual magnitudes of the H(D) ordering, Δz(K), Δ(P–O), and P^s are given in table 1, and the way they have been scaled together for this figure is explained in the text.

the results for DKDP, plotted in the same way, using the P^s measurements of Samara (1973) on ~91%† deuterated DKDP and his fully saturated value of 6.20 μC cm^{-2}.

Of the four quantities compared, only the H(D) ordering yields an absolute magnitude for the degree of order attained at each temperature: the values of P^s, Δz(K) and Δ(P–O) can be expressed in percentage terms only on the basis of some estimate of their fully saturated values (as Samara 1973 has done, by extrapolation, for P^s: see above). But that is not an impediment to a comparison of the *relative* temperature dependences, which can be seen to be remarkably similar, with just one minor departure: the proton ordering in KDP displays a slightly less rapid saturation with cooling than do P^s, Δz(K) and Δ(P–O). Figure 2 shows the refined (model) proton distribution function as it

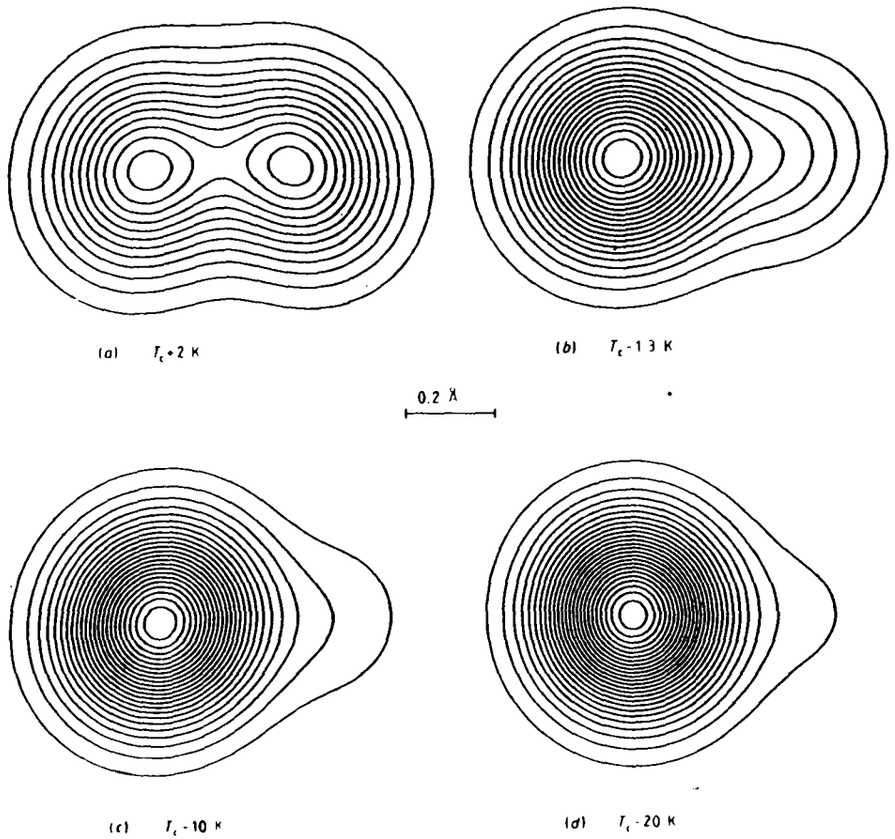

Figure 2. Sections through the refined proton distribution in KH_2PO_4 at: (*a*) T_c + 2 K (Kuhs *et al* 1983); (*b*) T_c – 1 3 K; (*c*) T_c – 10 K; (*d*) T_c – 20 K. In each case the section contains (i) the line H H joining the two proton sites and (ii) the line at constant *z* perpendicular to H H. (In relation to (*a*) note that Kuhs *et al* (1983) published a *Fourier* map of the proton distribution at T_c + 2 K. What is shown here is the refined *model* distribution derived from the same data.) The contours are all equally spaced on a common arbitrary scale.

† The small difference between this value (judged from the quoted T_c of 219 8(1)K) and the 95% of our samples is not expected to affect the *form* of P^s versus T.

progressively orders from 50 : 50 disorder at T_c + 2 K (Kuhs *et al* 1983) to nearly complete (96 : 4) order at T_c – 20 K. Without other information it is not possible to decide whether the remaining asymmetry at T_c – 20 K is wholly disorder (as assumed for simplicity here) or partly an intrinsic anharmonicity. The latter does in fact seem the more likely, because the proton in an O–H · · · O bond is in a (relatively) shallow asymmetric potential. (This is less true for the deuteron in O–D · · · O because of the greater O · · · O separation and the greater mass of the deuteron.) We believe this is the most probable explanation for the slightly, but significantly, low degree of the refined H ordering at T_c – 20 K compared with P^s and the heavy-atom displacements.

The results displayed in figures 1 and 2 represent the most complete and accurate study yet made of the onset of order, at the microscopic level, for the KDP-type transition. From these results we conclude that the structural ordering in KDP and DKDP is homogeneous: the progressive ordering of the proton (deuteron), on cooling below T_c, shows the same temperature dependence as that of the heavy-atom displacements down to well below T_c. Furthermore, the structural ordering follows the same temperature dependence as the spontaneous polarisation P^s. That this need not be the case is shown by recent work on the phenomenologically similar transition in $PbHPO_4$, where the proton ordering has the same temperature dependence as P^s but the heavy-atom displacements apparently do not (Lockwood *et al* 1985).

Further work will be required to ascertain to what extent, if any, the proton distribution in KDP may remain asymmetric (because of anharmonicity) even when fully ordered.

We are pleased to thank Mr J Archer for invaluable technical support. We gratefully acknowledge the support of a Visiting Fellowship (C J Howard) and a Research Associateship (J E Tibballs) from the Science and Engineering Research Council, and also a collaborative research grant from NATO.

References

Bacon G E and Pease R S 1953 *Proc. R. Soc.* A **220** 397–421
—— 1955 *Proc. R. Soc.* A **230** 359–81
Chabin M and Gilletta F 1977 *Ferroelectrics* **15** 149–54
Kobayashi J, Uesu Y and Enomoto Y 1971 *Phys. Status Solidi* b **45** 293–304
Kobayashi J, Uesu Y, Mizutani I and Enomoto Y 1970 *Phys. Status Solidi* a **3** 63–9
Kuhs W F, Nelmes R J and Howard C J 1985 in preparation
Kuhs W F, Nelmes R J and Tibballs J E 1983 *J. Phys. C: Solid State Phys.* **16** L1029–32
Lockwood D J, Ohno N, Nelmes R J and Arend H 1985 *J. Phys. C: Solid State Phys.* **18** L559–66
Nakano J, Shiozaki Y and Nakamura E 1974 *Ferroelectrics* **8** 483–4
Nelmes R J, Meyer G M and Tibballs J E 1982 *J. Phys. C: Solid State Phys.* **15** 59–75
Samara G A 1973 *Ferroelectrics* **5** 25–37
Tibballs J E and Nelmes R J 1982 *J. Phys. C: Solid State Phys.* **15** L849–53
Tibballs J E, Nelmes R J and McIntyre G J 1982 *J. Phys. C: Solid State Phys.* **15** 37–58
Uesu Y, Tanaka T and Kobayashi J 1974 *Ferroelectrics* **7** 247–9
Zucker U H, Perenthaler E, Kuhs W F, Bachmann R and Schulz H 1983 *J. Appl. Crystallogr.* **16** 358

J Phys C: Solid State Phys. 18 (1985) L1023–L1030. Printed in Great Britain

LETTER TO THE EDITOR

Structural evidence for centre-of-mass motion in the ferroelectric fluctuation of KDP and DKDP

R J Nelmes†, W F Kuhs‡, C J Howard†§, J E Tibballs†‖ and T W Ryan†

† Department of Physics, University of Edinburgh, Mayfield Road, Edinburgh EH9 3JZ, UK

‡ Institut Laue–Langevin, Avenue des Martyrs, 38042 Grenoble Cedex, France

Received 12 August 1985

Abstract. Using high-resolution neutron diffraction data, the thermal vibration amplitudes of the K, P and O atoms, and the positions of the H(D) atoms have been determined as a function of temperature near T_c for KH_2PO_4 (KDP) and 95%-deuterated $K(D,H_{1-x})_2PO_4$ (DKDP). The data were collected from KDP at 2 K above T_c (123 K) and at 1, 10 and 20 K below T_c, and from DKDP at 2 K above T_c (224 K) and at 2, 6 and 10 K below T_c. The results show changes in some thermal amplitudes and in the H(D) positions, at and below T_c, that strongly support a model of the ferroelectric fluctuation revised to include a local fluctuation of the centre of mass along the ferroelectric axis.

The pattern of atomic displacements in the critical fluctuation near the ferroelectric transition in KH_2PO_4 (KDP) and KD_2PO_4 (DKDP) was first determined from diffuse neutron scattering measurements on DKDP at $T_c + 4$ K by Skalyo *et al* (1970). They obtained the results illustrated in figure 1. The D atoms move between two sites separated by $2D_a$ in the xy plane and by $2D_z$ along z, where z is the direction of the fourfold axis in the tetragonal paraelectric phase. As the D atoms move onto sites near the 'upper' O atoms of each PO_4 group (i.e. D_1 and O_2 in figure 1), the P atoms move 'down' along z by P_z and the K atoms move 'up' by K_z, as shown by the arrows in figure 1(*a*). The displacement of the O atoms along z, O_z, was found to be very small. The magnitudes of P_z, K_z, O_z and D_z obtained by Skalyo *et al* (1970) are given in table 1, column 4 scaled to a value of 0.224 Å for D_a taken from the structural study of DKDP at $T_c + 5$ K by Nelmes *et al* (1982). These displacements were in good general agreement with the structural displacements found in the ferroelectric phase of KDP by Bacon and Pease (1955), with one important exception: whereas the D atoms moved along z in phase with the P atom in the ferroelectric mode (figure 1; table 1, column 4), the structural displacement of the H atom below T_c in KDP was in the opposite sense. At that time no structural information was available for DKDP, and Skalyo *et al* (1970) suggested this disagreement might simply indicate a difference between KDP and DKDP in their ferroelectric mode displacements.

However, subsequent neutron diffraction studies of the crystal structure of DKDP (and KDP) above T_c by Nelmes *et al* (1982) revealed further discrepancies:

§ On leave from the AAEC Research Establishment, Lucas Heights, NSW 2232, Australia.

‖ Now at the Senter for Industriforskning, Blindern, Oslo 3, Norway.

0022-3719/85/321023 + 08 $02.25 © 1985 The Institute of Physics

(i) the D sites, well resolved by the high resolution of the diffraction data, were found to be separated along z by only 0.058(3) Å, much less than the value of $2D_z$ of 0.184(16) Å obtained by Skalyo *et al* (1970); and

(ii) the T-dependence found for u^{33}(K) and u^{33}(P), the mean square thermal amplitudes of K and P along z, suggested that K_z should be much smaller than P_z.

These observations led to a re-analysis of the diffuse neutron scattering data, and the collection and analysis of new diffuse x-ray scattering data for DKDP at $T_c + 2$ K by Bleif *et al* (1982). These authors showed that a much improved fit to the data was achieved by allowing a local fluctuation of the centre of mass along z, with amplitude Δ_z, as a component of the ferroelectric mode. The results of their re-analysis of the neutron data (from Skalyo *et al* 1970) are given in table 1, column 3. The centre of mass moves in phase with the P atom, thus increasing the total z amplitude of P and decreasing that of K, in agreement with the conclusions noted under (ii) above. Also D_z is reduced substantially, though it still remains larger than expected from the structural studies.

The diffuse x-ray scattering measurements for DKDP made by Bleif *et al* (1982), and similar measurements for KDP by Cowley *et al* (1983) have recently been analysed further by Andrews and Cowley (1986). Their results are given in table 1, columns 1–2, where the quoted standard deviations apply to the relative magnitudes: the absolute values are sensitive to the approximations inherent in establishing a scale. In the case of DKDP the refined displacements were indirectly scaled to the D_a-value of 0.224 Å by fixing P_z at −0.080 Å (see table 1 and Bleif *et al* 1982). For KDP the absolute magnitudes were scaled by comparing the relative strengths of the ferroelectric mode and acoustic mode scattering in KDP and DKDP (Andrews and Cowley 1986). The x-ray work does not, of course, yield values for H_z and D_z.

Just above T_c the overall thermal amplitudes of the K and P atoms, along z, are expected to be

$$u^{33}(\mathrm{K}) = u_i^{33}(\mathrm{K}) + K_z^2 \qquad u^{33}(\mathrm{P}) = u_i^{33}(\mathrm{P}) + P_z^2 \tag{1}$$

where u_i^{33}(K) and u_i^{33}(P) are the 'intrinsic' thermal amplitudes in the absence of the ferroelectric mode motion. The revised model for the mode, incorporating the centre-of-mass motion, can then be seen to predict a large decrease in u^{33}(P) but only a very small change in u^{33}(K) on cooling through T_c, whereas the purely optic mode derived by Skalyo *et al* (1970) would predict approximately equal decreases in both parameters (see table 1). Figure 1 and table 1 also show that, in the revised model, a large part of D_z is due to the centre-of-mass motion. As long-range order is established below T_c, the local centre-of-mass motion is expected to freeze out. Hence the progressive ordering of the D atom onto one of its sites below T_c (Nelmes *et al* 1985)—say D_1 at the expense of D_2 in figure 1(*b*)—should then be accompanied by a movement of the D_1 site towards the O . . . O line, whereas the purely optic mode model of Skalyo *et al* (1970) would predict no such displacement (as they noted: see above).

The revised model is thus open to test by diffraction studies. In this Letter we report results obtained from high-resolution neutron diffraction measurements carried out to test the above predictions by determining the K, P (and O) thermal parameters, and the location of the H and D sites, as a function of temperature through T_c. Data were collected from KDP at 2 K above T_c (123 K) and at 1.3, 10 and 20 K below T_c; and from DKDP at 2 K above T_c (224 K) and at 1.8, 5.8 and 10 K below T_c. The DKDP was known to be 94.6(6)% deuterated (Nelmes *et al* 1982). Measurements of the spontaneous polarisation, P_s, show that the ordering of KDP varies from ~35% at T_c to ~95% at

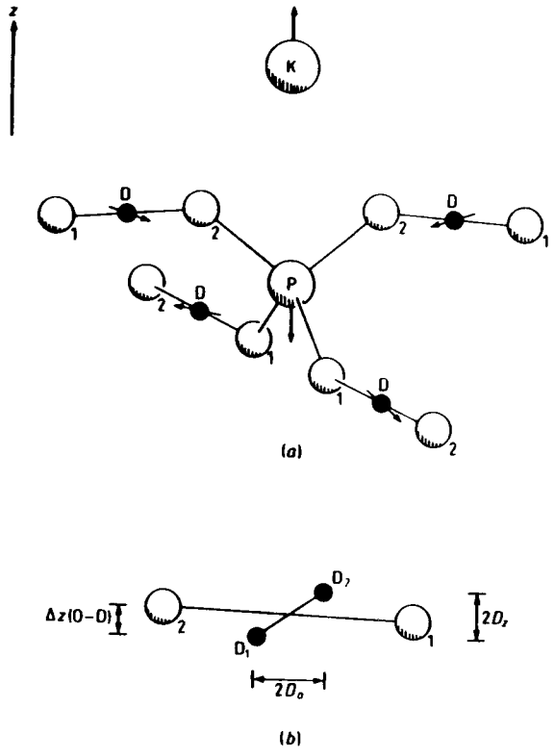

Figure 1. The ferroelectric mode displacements determined by Skalyo *et al* (1970) for DKDP at T_c + 4 K are shown in (*a*), omitting the very small displacements of the O atoms along *z* and their *xy* displacements. The positions of the two D sites in the O–TD–TO bonds are illustrated in (*b*): the *z* separation of the sites, $2D_z$, is exaggerated.

Table 1. Ferroelectric mode amplitudes along *z* in KDP and DKDP for the K, P, O and H(D) atoms in units of 10^{-1} Å. The values in columns 1–3 include a local centre-of-mass motion along *z* of amplitude Δ_z, whereas those in column 4 are with Δ_z constrained to be zero.

	X-ray data Andrews and Cowley (1986)		Neutron data	
	KDP 1	DKDP 2	Bleif *et al* (1982) DKDP 3	Skalyo *et al* (1970) DKDP 4
P_z	51(1)	80‡	83(8)	46(5)
K	10(1)	12(1)	7(10)	55(4)
O	21(1)	−18(2)	22(3)	7(4)
H, D		-	44(7)	−92(8)
Δ	19(1)	−24(1)	27(4)	0

‡ This amplitude was fixed at the mean of the two slightly different values obtained from a phonon model and a pseudo-spin model by Bleif *et al* (1982).

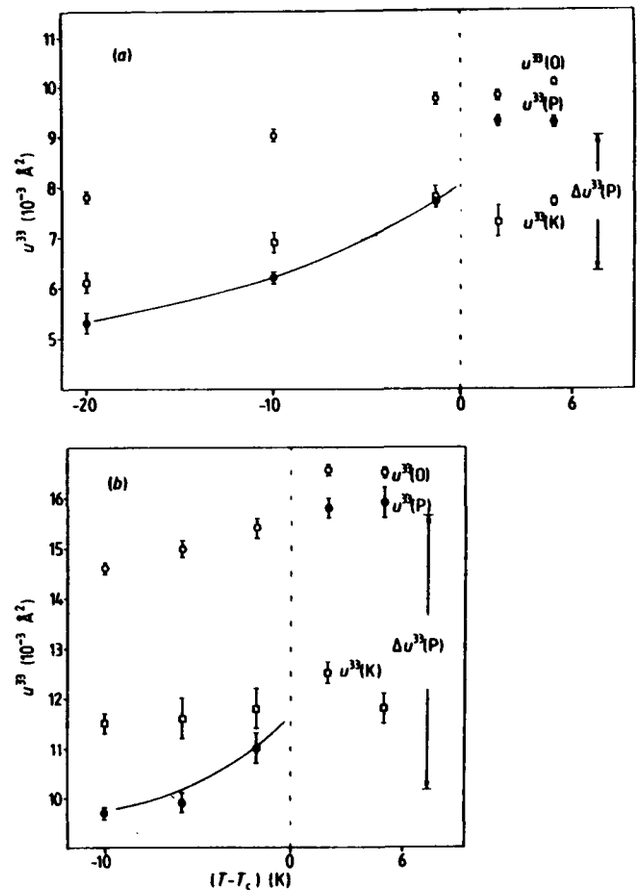

Figure 2. The values obtained for the mean square thermal motion along the *z* axis, u^{33}, as a function of temperature for the K atom (□), the P atom (●) and the O atom (○) in (*a*) KDP and (*b*) DKDP. For the O atoms below T_c the mean value of u^{33}(O) is shown (the two independent values are just within the given error bars for KDP, but are separated by 2.5 times the error bars for DKDP). The dotted lines show variation proportional to the absolute temperature; the full curves are guides to the eye for the *T*-dependence of u^{33}(P) below T_c. The discontinuities Δu^{33}(P) are discussed in the text.

T_c − 20 K, and that of highly deuterated DKDP varies from ~65% at T_c to ~95% at T_c − 10 K (Samara 1973, Chabin and Gilletta 1977). Any changes associated with the transition should then have their onset abruptly at T_c and become almost completed (saturated) over the temperature ranges of the two sets of experiments.

All eight experiments were carried out on the D8 and D9 four-circle diffractometers at the Institut Laue–Langevin, Grenoble. Below T_c, the single-crystal samples were maintained in an almost completely monodomain state by the application of a 400 V mm^{-1} electric field between electrodes painted on the *c* faces. Data were collected out to $\sin(\theta/\lambda) = 1.2$ Å^{-1} in the experiments at T_c − 10 K and out to $\sin(\theta/\lambda) = 1.6$ Å^{-1} in all the other experiments. We have already used these same data sets to study the onset of structural ordering below T_c in KDP and DKDP (Nelmes *et al* 1985), and further experimental details are given in the report of that study. All reflection intensities were

corrected for absorption, and for one- and two-phonon TDS, before being used for least-squares refinement of positional and harmonic thermal parameters, and of anisotropic extinction parameters. The data collected previously from KDP and DKDP at $T_c + 5$ K (Nelmes *et al* 1982) had not been corrected for TDS and these were completely re-analysed in the same way. (Values quoted from the Nelmes *et al* (1982) in this Letter are as obtained in the re-analysis.) The corrections and refinements were all carried out with the PROMETHEUS suite of crystallographic programs (Zucker *et al* 1983).

The refined values of the mean-square thermal amplitudes of the O, P and K atoms, along z, are shown in figure 2. (Values for all the other refined structural parameters, together with full details of the experiments and analysis, will be published in a separate comprehensive account by Kuhs *et al* (1985).) The most striking feature is the sharp fall in u^{33}(P) at T_c, larger in DKDP than in KDP, followed by a further decrease in the ordering range below T_c. On the basis of (1) we can estimate P_z by extrapolating from the value of u^{33}(P) at $T_c - 20$ K for KDP (at $T_c - 10$ K for DKDP) back to T_c, proportionally to the absolute temperature: the differences marked Δu^{33}(P) on figure 2 can then be identified with P_z^2. (This procedure will slightly underestimate P_z because the structural ordering is not quite complete at $T_c - 20$ K in KDP or $T_c - 10$ K in DKDP, as shown by Nelmes *et al* (1985). However, the difference is negligible within the inherent approximations.) The estimates thereby obtained are 0.050(5)Å and 0.075(3)Å for P_z in KDP and DKDP, respectively, in good agreement with the values for the revised model in table 1, columns 1–3. For both materials the K_z-values for the revised model imply an additional amplitude of only ~ 0.0001 Å^2 in u^{33}(K) above T_c, and hence no detectable change is expected at T_c within the uncertainties of the structural measurements. This is seen to be so, except for the slightly elevated value of u^{33}(K) at $T_c - 1.3$ K in KDP, for which we have no definite explanation at present. For the O atoms there is the complication that below T_c there are two independent atoms, O_1 and O_2 in figure 1. Based on the mean values of u^{33}(O) at $T_c - 20$ K (KDP) and $T_c - 10$ K (DKDP), there are small changes at T_c corresponding to O_z-amplitudes of ~ 0.02 Å for KDP and ~ 0.03 Å for KDP, in approximate agreement with the values in table 1, columns 1–3.

Further information about the nature of the ferroelectric mode can be extracted from a comparison between the amplitudes in the mode and the static (structural) displacements, relative to the centre of mass, that are established in the ferroelectric phase. For example, if the ferroelectric mode involved simply a pseudo-spin-like fluctuation of all the atoms between the two opposite ferroelectric configurations, then the fully saturated displacements of mean atomic positions would be equal to the optic mode components of the fluctuation. Relevant mode amplitudes and structural displacements are set out in table 2. First, in columns 1–4 in the table, the x-ray results of Andrews and Cowley (1986) from table 1 have been separated into two components: the centre-of-mass, or acoustic mode, amplitude (A), and the optic mode amplitude (O) derived by subtracting Δ_z from the overall amplitudes P_z, K_z, O_z and H_z (D_z). For H and D the overall amplitudes have been taken to be half the site separation along z obtained from the structural studies at $T_c + 5$ K (Nelmes *et al* 1982). Then, in column 5, the purely optic mode amplitudes derived by Skalyo *et al* (1970) are reproduced. Finally, the almost saturated displacements from the structural studies at $T_c - 20$ K (KDP) and $T_c - 10$ K (DKDP) are given in columns 6 and 7.

It can be seen that the structural displacements of the heavy atoms do not distinguish decisively between the two models of the mode above T_c—i.e. with and without the centre-of-mass motion. The models are in accord in having a small O_z(O) optic mode amplitude and so they both predict a very small displacement for the O atoms, in

Table 2. Columns 1–4 show the ferroelectric mode amplitudes along z in KDP and DKDP separated into the centre-of-mass, or acoustic mode, component (A) and the optic mode component (O). Column 5 shows the purely optic mode components of Skalyo *et al* (1970). Columns 6 and 7 show the structural displacements along z relative to the centre of mass in KDP at $T_c - 20$ K and in DKDP at $T_c - 10$ K. All values are in units of 10^{-3} Å. Within error, the separate structural displacements of the two independent O atoms are the same as their mean values (marked with asterisks) given here.

	KDP		DKDP		DKDP		KDP	DKDP
	O	A	O	A	O			
	1	2	3	4	5		6	7
P_z	−32(1)	−19(1)	−56(1)	−24(1)	−46(5)	P	−59(2)	−76(2)
K_z	29(1)	−19(1)	36(2)	−24(1)	55(4)	K	42(2)	56(2)
O_z	−2(1)	−19(1)	6(2)	−24(1)	−7(4)	O	1(2)*	−1(2)*
H_z/D_z	2(2)	−19(1)	−5(2)	−24(1)	−92(8)	H/D	22(3)	32(2)

agreement with the structural results. The values obtained for the P and K displacements agree better with the revised model insofar as the P displacement is found to be larger than that of K, in both KDP and DKDP; but the absolute magnitudes of the displacements are larger than the optic mode amplitudes of both models. (This difference in magnitudes—whereas, as shown, the changes in the u^{33} thermal parameters of P and K agree well with the P_z and K_z amplitudes just above T_c—suggests that the heavy-atom behaviour is more phonon-like than purely pseudo-spin-like.) We are then left with the structural displacements of the H and D atoms: they displace in the same direction as the K atoms (table 2, columns 6 and 7), rather than the direction of the P atoms as expected for the Skalyo *et al* (1970) model. It is on this crucial feature of the structural displacements in table 2 that we focus attention.

In the structural refinements the H and D distributions were represented by two overlapping gaussian functions, one on each of the two H(D) sites (e.g. D_1 and D_2 in figure 1 (b)). It is the large xy amplitude of the H(D) atoms ($2D_a \sim 0.5$ Å in figure 1 (b)) that makes it possible to resolve the two sites in this way, and thereby gain the important advantage of being able to measure the H(D) z amplitudes above T_c directly (as the z separation of the sites) despite their small size†. There are then differences between the interpretations applied to changes in the H(D) and heavy-atom distributions at and below T_c. The following two are important here.

(i) The freezing out of the ferroelectric mode motion of H(D) is observed as the progressive ordering onto one site (say, D_1 in figure 1(b)) at the expense of the other (D_2), whereas for K, P and O it is observed in the reduction of u^{33}. (For H and D the u^{33} thermal parameter is simply the mean square amplitude about each site—i.e., u_1^{33} in (1)—and, as then expected, does not show any discontinuity at T_c.)

(ii) Table 2 shows that in the revised model almost all of the z motion of the O and H(D) atoms is attributable to the centre-of-mass motion, Δ_z. For the O atom, as for P and K, the freezing out of any centre-of-mass motion will simply be part of the change in u^{33} under (i) above, and could not be unambiguously distinguished from the freezing out of optic mode motion. However, for the H (D) atoms the freezing out of centre-of

† The much larger z amplitude of P in DKDP still gives a site separation, $2P_z = 0.16$ Å, too small to be resolved in a diffraction experiment, quite apart from the evidence (above) that a simple two-site distribution may not be appropriate for the heavy atoms

Table 3. The values obtained at the given experimental temperatures for the z separation of the H (D) atoms from the adjacent O atom, in units of 10^{-3} Å, for (*a*) Δz(O–H) in KDP and (*b*) Δz(O–D) in DKDP (see figure 1(*b*)). The $T_c + 5$ K results are from Nelmes *et al* (1982). The values are also expressed as a proportion (%) of their estimated fully ordered magnitude, as explained in the text, and compared with the spontaneous polarisation, P^s, expressed the same way from measurements by Samara (1973) and Chabin and Gilletta (1977).

(*a*) KDP		$T_c - 20$ K	$T_c - 10$ K	$T_c - 1.3$ K	$T_c + 5$ K
Δz(O–H)		8(2)	9(2)	16(2)	28(2)
	(%)	95	90(10)	57(10)	0
P^s	(%)	95(1)	90(2)	64(3)	0
(*b*) DKDP		$T_c - 10$ K	$T_c - 5.8$ K	$T_c - 1.8$ K	$T_c + 5$ K
Δz(O–D)		4(1)	7(2)	11(2)	38(1)
	(%)	97	89(6)	77(6)	0
P^s	(%)	97(0.5)	94(1)	85(3)	0

mass motion would be manifested as a movement of the increasingly occupied H(D) site along z relative to the mean position of the adjacent O atom—changing the separation labelled Δz(O–D) in figure 1(*b*), and the equivalent Δz(O–H) in KDP.

An analysis of the T-dependence of the H(D) distributions can thus afford important additional information. The study of the onset of structural ordering by Nelmes *et al* (1985) has already shown that the progressive ordering of the H and D atoms onto one site—(i) above—has the same T-dependence as P^s. We restrict attention here to (ii), the T-dependence of the H- and D-site locations.

Table 3 gives the refined values of Δz(O–H) and Δz(O–D) at $T_c + 5$ K (Nelmes *et al* 1982) and the three temperatures below T_c. The study of structural ordering (Nelmes *et al* 1985) shows KDP at $T_c - 20$ K to be 95(1)% ordered and DKDP at $T_c - 20$ K to be 97(1)% ordered. If the values of Δz(O–H) and Δz(O–D) at these temperatures are taken to represent 95% and 97%, respectively, of the fully saturated changes, the two values closer to T_c can also be expressed in relative percentage terms and compared with the T-dependence of P^s, expressed likewise (see Nelmes *et al* 1985). Clearly Δz(O–H) and Δz(O–D) both change significantly on cooling below T_c and, within the (quite large) errors, do so with the same T-dependence as P^s (table 3). Whilst the Δz(O–H, D) changes incorporate the displacements of the O atoms as their ferroelectric mode motion freezes out, this can be seen from table 2 to be a very small component†. Thus the remaining, much larger, part of the changes in Δz(O–H) and Δz(O–D) must be attributed to the loss of a centre-of-mass component in H_z and D_z below T_c, and thus affords direct evidence for the presence of this component in the ferroelectric mode.

Hence, the changes both in the u^{33} thermal parameters of the heavy atoms and also in the relative displacements of the H (D) atoms along z, on cooling through T_c, strongly support a model of the ferroelectric mode that includes a fluctuation of the centre of mass along z in phase with the optic mode motion of the P atom. For KDP the structural results agree with the revised mode amplitudes (tables 1 and 2) and suggest a simple two-

† Because the optic mode motion of the O atoms is very small the changes in Δz(O–H, D) are close to the H (D) structural displacements in table 2.

site (pseudo-spin) behaviour of the H atom coupled to a more phonon-like behaviour of the heavy atoms. Below T_c the H atom orders within error onto the location of one of its two tetragonal-phase sites (Nelmes *et al* 1985), just displaced along z as the local centre-of-mass motion is lost: in fact, almost all of the z motion of H in KDP above T_c is attributable to the centre-of-mass motion†. For DKDP there is a similar agreement between the structural results and the revised mode amplitudes, with the exception of the D atom. As already noted, the magnitude 0.044(7)Å obtained for D_z by Bleif *et al* (1982) is significantly larger than the 0.029(1)Å obtained in structural studies at both $T_c + 5$ K (Nelmes *et al* 1982) and $T_c + 2$ K (this work). Also, the almost saturated structural displacement along z of 0.032(2)Å + 0.001(2)Å for D relative to O (see table 2) is significantly larger than the predicted relative displacement of 0.024(1)Å − 0.006(2)Å from the $D_z(A)$ and $O_z(O)$ amplitudes in table 2‡. (The same comparison shows very good agreement in KDP.) These are small, but puzzling and significant, discrepancies that merit further investigation.

Finally, we note that Andrews and Cowley (1986) made measurements of diffuse x-ray scattering from the 'walls' separating oppositely poled domains in polydomained crystals of KDP and DKDP below T_c; and analysis of the data yielded the surprising conclusion that the frozen-in displacements, relative to the centre of mass of the whole crystal, include the local centre-of-mass fluctuations. That is to say, oppositely poled domains are displaced $2\Delta_z \sim 0.04$ Å relative to each other along z. However, even if accurate diffraction data could be obtained from a polydomained crystal they would be insensitive to this effect, because coherent elastic scattering from different domains adds as intensities not as (phased) amplitudes. Our results apply to a freezing in of the ferroelectric mode motions within a single domain, whether that is one of many in a polydomained crystal or—as in our experiment—the whole crystal.

We are pleased to thank J Archer for invaluable technical support and R A Cowley for several helpful discussions of the analysis and results. We gratefully acknowledge the support of a Visiting Fellowship (C J Howard) and a Research Associateship (J E Tibballs) from the Science and Engineering Research Council, and also a collaborative research grant from Nato.

References

Andrews S R and Cowley R A 1986 *J. Phys. C: Solid State Phys.* in press
Bacon G E and Pease R S 1955 *Proc. R. Soc.* A **230** 359–81
Bleif H-J, Cowley R A and Nelmes R J 1982 *J. Phys. C: Solid State Phys.* **15** L201–6
Chabin M and Gilletta F 1977 *Ferroelectrics* **15** 149–54
Cowley R A, Bleif H-J, Andrews S R and Nelmes R J 1983 *Physica* B **120** 267–9
Kuhs W F, Nelmes R J and Howard C J 1985 in preparation
Nelmes R J, Kuhs W F, Howard C J, Tibballs J E and Ryan T W 1985 *J. Phys. C: Solid State Phys.* **18** L711–6
Nelmes R J, Meyer G M and Tibballs J E 1982 *J. Phys. C: Solid State Phys.* **15** 59–75
Samara G A 1973 *Ferroelectrics* **5** 25–37
Skalyo J, Frazer B C and Shirane G 1970 *Phys. Rev.* B **1** 278–86
Zucker U H, Perenthaler E, Kuhs W F, Bachmann R and Schulz H 1983 *J. Appl. Crystallogr.* **16** 358

† At $T_c - 1.3$ K in KDP the z separation of the two H sites, $2H_z$, is 0.019(7) Å. This suggests that the separation of the two configurations becomes less as one of them becomes more occupied at the expense of the other, which seems physically plausible. In all other cases, the position of the less occupied H(D) site is insufficiently well determined to follow the T dependence of H_z (D_z) below T_c with useful precision.

‡ A comparison based on the larger value of D_z obtained from the neutron data only increases the disagreement.